

THE EFFECT OF REGULAR AND RANDOM
ARRAYS OF PINNING CENTRES ON
VORTICES IN SUPERCONDUCTORS



THE UNIVERSITY
of MANCHESTER

A THESIS SUBMITTED TO THE UNIVERSITY OF MANCHESTER
FOR THE DEGREE OF DOCTOR OF PHILOSOPHY
IN THE FACULTY OF SCIENCE

By

Adolfo Zamora Ramos

Department of Physics and Astronomy

March 2001

ProQuest Number: 10834155

All rights reserved

INFORMATION TO ALL USERS

The quality of this reproduction is dependent upon the quality of the copy submitted.

In the unlikely event that the author did not send a complete manuscript and there are missing pages, these will be noted. Also, if material had to be removed, a note will indicate the deletion.



ProQuest 10834155

Published by ProQuest LLC (2018). Copyright of the Dissertation is held by the Author.

All rights reserved.

This work is protected against unauthorized copying under Title 17, United States Code
Microform Edition © ProQuest LLC.

ProQuest LLC.
789 East Eisenhower Parkway
P.O. Box 1346
Ann Arbor, MI 48106 – 1346

✓

✕
Th 22779

JOHN RYLANDS
UNIVERSITY
LIBRARY OF
MANCHESTER

Contents

Abstract	5
Declaration and Copyright Notice	7
Autobiographical Note	8
Acknowledgements	9
1 Introduction	10
1.1 Equilibrium Properties of Conventional Superconductors	11
1.1.1 Ideal Type-I Superconductors	12
1.1.2 Ideal Type-II Superconductors	14
1.2 Nonequilibrium Effects and Fluctuations	17
1.2.1 Transport Currents and Pinning	17
1.2.2 Thermal Fluctuations	19
1.3 High- T_c Superconductors	20
1.3.1 Structure	21
1.3.2 Effect of Fluctuations	24
1.3.3 Pinning of Vortex Lines	25
1.4 Overview	27
2 Theoretical Approach	29
2.1 Ginzburg-Landau Theory of Superconductivity	30
2.1.1 Thermodynamic Equilibrium Solutions: GL Equations	31

2.1.2	The Lowest Landau Level Approximation	37
2.1.3	Effective Temperature Parameter	39
2.2	Lawrence-Doniach Model	40
2.2.1	The LLL Approximation for the LD Model	42
2.3	Limits of the LLL Approximation	44
2.4	Fluctuations about the LLL Approximation	46
3	Numerical Studies on the Spherical Thin-Film	49
3.1	Clean Thin-Film	50
3.1.1	Zero Temperature Properties: Numerical Calculations	51
3.1.2	Finite Temperature Properties: Computer Simulations	62
3.2	Pinning Due to Random Disorder	71
3.2.1	The System at $T = 0$	73
3.2.2	The System at $T > 0$	75
3.3	Pinning Imposed by a Periodic Substrate	78
3.3.1	Commensurate Case	81
3.3.2	Incommensurate Case	98
3.4	Discussion	104
4	Simulations on the Spherical Layered-Superconductor	108
4.1	Clean Layered-Superconductor	109
4.1.1	Physical Properties and Order-Parameter Ratios	110
4.1.2	Vortex Positions, Structure and Correlations	112
4.2	Pinning by a Random Substrate of Columnar Defects	118
4.2.1	Basic Quantities	121
4.2.2	Structure and Vortex Correlations	123
4.3	Pinning by a Periodic Substrate of Columnar Defects	126
4.3.1	Commensurate Case	127
4.3.2	Incommensurate Case	138
4.4	Discussion	143

Conclusions	146
A Notation, Conventions and Derivations	149
A.1 Notation and Conventions	149
A.2 Landau Levels	152
A.3 LLL Calculations on Energy Terms	156
A.3.1 Expansion Coefficients Representation	157
A.3.2 Energy Differences	164
A.3.3 First Order Derivatives	167
A.4 The Integral $J_{p,q,l}^m$ and its Reduced Form $I_{q,l}^m$	172
A.5 LD-LLL Energy Function in Terms of the Original Variables	174
A.6 Physical Properties in the LLL Approximation	175
References	180

Abstract

UNIVERSITY OF MANCHESTER

ABSTRACT OF THESIS submitted by **Adolfo Zamora Ramos** for the Degree of Doctor of Philosophy and entitled **The Effect of Regular and Random Arrays of Pinning Centres on Vortices in Superconductors.**

Month and Year of Submission: March 2001.

This thesis presents a numerical investigation on the properties of high-temperature superconductors (HTSCs) in a magnetic field with and without disorder. It first introduces a model with spherical geometry based on the Ginzburg-Landau (GL) theory that has been used before to study disorder-free thin-film superconductors within the lowest Landau level (LLL) approximation. Finite-temperature properties are consistent with a single vortex-liquid phase extending to the whole of the mixed-phase which freezes to the vortex lattice only at $T = 0$ (in agreement with previous studies on the same geometry). Finite-size effects on the ground states are seen and the existence of magic numbers with icosahedral symmetry that have lower energy is confirmed. When random impurities are added, the vortex system is frozen to an amorphous-solid phase in its ground state, while at finite temperatures it behaves effectively as a glass. If, instead of random disorder, a regular substrate of pinning centres is imposed then the behaviour of the system seems to be determined by the parameter B/B_Φ , where B is the magnetic induction (proportional to the density of flux lines) and B_Φ is proportional to the density of pinning centres. At the matching

field, $B/B_\Phi = 1$, a low temperature region in which phase coherence exists is observed. This is separated by a line of continuous, XY -type, phase transitions from a state with no phase coherence. The same diagram seems to describe the case $B/B_\Phi > 1$, but with the pinning strength g scaled to a higher value. For this case a novel vortex quasi-lattice is observed at the ground state in the strong pinning regime.

In the second part, the investigation is extended to the case of a strongly-anisotropic layered HTSC using the Lawrence-Doniach (LD) model and also again the LLL approximation. The magnetic field is, once again, applied in the direction perpendicular to the layers (i.e. along the c -axis). All systems with and without columnar defects in the c -direction show a sharp first-order transition below which pancake-vortices are coupled in all layers, but above which are decoupled. The phase above the transition is just a liquid of decoupled pancake-vortices, but the low temperature behaviour is dominated by pinning effects. In the case without point and columnar pins, our investigation confirms that the highly correlated low-temperature phase behaves effectively as a crystal. For the system in presence of randomly-distributed columnar defects, a low-temperature vortex glass can be observed. No signature of a sharp transition to the vortex liquid exists suggesting that the system just crosses over to liquid behaviour when decoupling takes place. This is not in agreement with the expected continuous transition from the theory of pinning by correlated disorder. The question whether the vortex glass is in fact a Bose-glass remains to be answered. Finally the sample with a regular array of columnar defects is considered. As in its thin-film counterpart, the behaviour of the system appears to depend strongly on B/B_Φ and not on whether the pinning substrate and the vortex lattice are commensurate or incommensurate. The low temperature phase of the $B/B_\Phi = 1$ case is consistent with the Mott insulator, and the mechanism for the system to achieve it seems to be setting of lattice-like vortex ordering within each layer and then inter-layer coupling (the last simultaneous with flux-line trapping by columnar defects). For weak enough pinning the system at $B/B_\Phi > 1$ shows no qualitative difference to the pure case. This suggests the absence of a Bose-glass phase in this case down to low temperatures.

Declaration and Copyright Notice

No portion of the work referred to in this thesis has been submitted in support of an application for another degree or qualification of this or any other university or other institution of learning.

Copyright in text of this thesis rests with the Author. Copies (by any process) either in full, or of extracts, may be made **only** in accordance with instructions given by the Author and lodged in the John Rylands University Library of Manchester. Details may be obtained from the Librarian. This page must form part of any such copies made. Further copies (by any process) of copies made in accordance with such instructions may not be made without permission (in writing) of the Author.

The ownership of any intellectual property rights which may be described in this thesis is vested in the University of Manchester, and may not be made available for use by third parties without the written permission of the University, which will prescribe the terms and conditions of any such agreement.

Further information on the conditions under which disclosures and exploitation may take place is available from the Head of the Department of Physics and Astronomy.

Autobiographical Note

The author was born and educated in Mexico City until the completion of his B.Sc. in Physics. This was done with a project on the Renormalization Group Theory at the “Universidad Nacional Autónoma de México” in October 1996. Since then he has been engaged in the research leading to the degree of Doctor of Philosophy at the University of Manchester.

Acknowledgements

First of all I would like to thank my supervisor, Professor Mike Moore, for introducing me to the field of High- T_c Superconductivity and rather specially for reminding me to rely only on fundamental principles. This has motivated much of the work presented in this manuscript.

Secondly, I would like to express my gratitude to the many colleagues and friends with whom I have had interactions during my stay in Manchester: Fernando Rojas Iñíguez, Agustín Sabio Vera, Ntoi P. Rapapa, Varagorn Pipuntchonlathee, Janis Gravelis, Anne Kienappel and Suzinne Kim. I am also grateful to Antonio Pérez Garrido and Ulugbek Abdurakhmanov for assistance with numerical data (and Antonio's Fortran code) to generate some pretty pictures appearing on some pages.

Finally, I acknowledge financial support for this investigation from the "Consejo Nacional de Ciencia y Tecnología" (CONACyT) in Mexico.

I dedicate this thesis to my Family, who have been supporting me all the time.

Chapter 1

Introduction

Superconductivity is a property of many metals, alloys and other compounds in which the sample is able to conduct electrical currents with no measurable dissipation. The property of *perfect conductivity* was first found and later was *perfect diamagnetism* discovered. However, none of these characteristics completely define the phenomenon. Superconductivity stands for a more general property which results from the condensation of the electrons in a sample into a phase of bosonic states showing quantum coherence on a *macroscopic* scale. The macroscopic magnetic properties of the sample determine the class it corresponds to, either type-I or type-II superconductor.

In this chapter we will introduce the equilibrium properties of conventional type-I and type-II superconductors as observed in experiments and explained mainly by the phenomenological theories, though some comments on the microscopic BCS theory will also be made. For simplicity, the *ideal*¹ superconductor will be considered first. Then, the nonequilibrium effects of transport currents and crystal lattice impurities, as well as thermal fluctuations, will be added to the conventional picture. Next, a review of the strongly anisotropic high- T_c superconductors (HTSCs) will be given. It is worth mentioning that this introductory chapter is not intended to be either exhaustive or extensive, but describe the essential superconducting characteristics required to

¹In this context ideal superconductor stands for a material with a perfect crystal-lattice structure and zero demagnetization factor when an external magnetic field is applied. Examples are a long cylinder in a magnetic field parallel to its axis, or a sheet (or “half space”) with the magnetic field parallel to the plane of symmetry.

understand this thesis. For a fairly complete review of the subject the reader is addressed to Refs. [1, 2, 3, 4, 5], but for a “quickstart” on this manuscript is advised to become familiar with the notation here by reading Section A.1 in Appendix A. The treatment, in the following, will be mostly chronological emphasizing the “nature” of the results (i.e. theoretical, experimental or both), but not going into rather specific details. Whenever appropriate relevant references will be cited instead. The chapter concludes with an overview of the rest of this thesis.

1.1 Equilibrium Properties of Conventional Superconductors

The story of superconductivity up to date can be divided into two main periods: The first one starting with its discovery in conventional low- T_c materials (in 1911) and ending before the discovery of the high- T_c copper-oxide compounds when an essentially complete description of the phenomenon was achieved by the results arising from the phenomenological theory of Ginzburg and Landau (GL) [6] and the microscopic theory of Bardeen, Cooper and Schrieffer (BCS) [7]. The second period started with the discovery of the high- T_c cuprates (in 1986) and is still extending nowadays. This section is intended to describe in sufficient detail the physics of the conventional low- T_c superconductors mostly in an applied magnetic field \mathbf{H} and sometimes also subject to a sufficiently weak transport current density \mathbf{j} . Without loosing generality, we will sometimes refer to the magnitudes H and j of the vectors \mathbf{H} and \mathbf{j} as the applied magnetic field and transport current density respectively. Unless otherwise stated, through the whole of this section we will be considering ideal samples (both crystal structure and sample geometry) which in practical terms correspond to extrapolations of the cleanest specimens found in nature. These classical superconductors are materials which can be accurately described by the mean field solutions of the appropriate statistical field theory, which in this thesis will be taken as that of Ginzburg and Landau. Realistic nonequilibrium effects and fluctuations will be presented in Section 1.2, and are needed to complete the picture of the real low- T_c superconductors.

1.1.1 Ideal Type-I Superconductors

Superconductivity was first found experimentally as a property of some metals (and later of some alloys). H. Kamerlingh Onnes [8], in his experiments on mercury (Hg) in 1911, found a drop in the d.c. electrical resistance of the metal to a value $< 10^{-6} \Omega$ as the sample was cooled below 4.3 K. The “narrow” temperature interval (< 0.1 K) over which the resistance “vanished” suggested a transition to a perfect conducting state that soon was called *superconductivity*. The temperature at which the “transition” to the superconducting state occurs, which is material dependent, is called *the transition temperature* and denoted T_c . Years later, in 1914, Kamerlingh Onnes [9] also discovered that superconductivity can be destroyed by a sufficiently strong magnetic field; but that it will reappear when the applied magnetic field is removed. Apart from transport phenomena, thermodynamic properties were measured in subsequent years. Discontinuities in the magnetization curve (see Figure 1.1(a)) and in the entropy difference of the metals were reported. This attracted theoreticians to apply thermodynamics in a phenomenological way [10, 11, 12] to describe the transition between normal and superconducting states. However the electrodynamical properties were rarely described until the work of F. London and H. London [13] when the experimental results of W. Meissner and R. Ochsenfeld [14] had already confirmed the reversibility of the normal-superconducting (N-S) phase transition. Meissner and Ochsenfeld found that, at temperatures lower than T_c , a superconducting sample expels completely a sufficiently “weak” applied magnetic field H from its bulk, independently of the history of the cooling-magnetization process. This complete *flux exclusion* from the bulk of the sample is usually referred to as the *Meissner effect* and it leads to the thermodynamical reversibility of the H - T phase diagram of an ideal type-I superconductor (see Figure 1.1(b)). In ideal conditions, namely a pure-metallic sample of a macroscopic size and a long-cylindrical shape in an applied magnetic field H parallel to its axis (i.e. demagnetization factor $D_f = 0$), the phase diagram consists of two phases: A lower T and H “pure superconducting state” (Meissner phase) characterized by perfect conductivity and perfect diamagnetism, and a higher T and H “normal metal

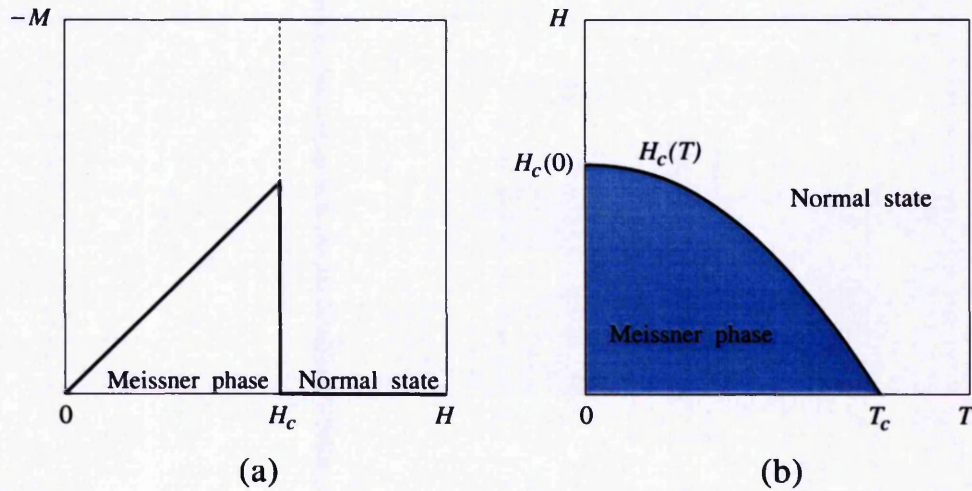


Figure 1.1: Equilibrium properties of ideal type-I superconductors (schematic). (a) Magnetization curve. (b) H - T phase diagram.

state" (Normal state) characterized by finite electrical resistance and total flux penetration. The line of phase transitions $H_c(T)$ is called the *thermodynamical critical field* and experimentally has been found to be approximately described by the relation $H_c(T) = H_c(0)[1 - (T/T_c)]^2$, where $H_c(0)$ is the thermodynamical critical field at zero temperature and T_c the transition temperature. It is known, from both experiments and theories, that $H_c(T)$ is a line of *first order* phase transitions at any finite temperature below T_c with discontinuities in the entropy, magnetization, etc. However, the transition at $T = T_c$ ($H = 0$) turns out to be *continuous*.

To describe these phenomena F. and H. London [13, 15] introduced a phenomenological theory based on a set of two empirical electrodynamical partial differential equations which gave qualitative account of most of the electrodynamical properties of the metallic superconducting compounds (later classed as type-I). Both perfect conductivity and perfect diamagnetism were described as well as the magnetic linear response. The physical nature of the Meissner effect, namely the fact that screening supercurrents flow on the surface of the samples producing an antiparallel field inside the sample which cancels the applied magnetic field, also appeared from the equations. The length scale for the penetration of the surface supercurrents was given by the London *penetration depth* $\lambda_L = (m/4\mu_0 n_s e^2)^{1/2}$, where n_s is the density of

superconducting electrons and m and e the mass and charge of the electron respectively. Shape dependent effects in non-ideal samples [16, 17] as well as the effects of transport currents are also described quantitatively within this theory. An extension of the London-London (L-L) theory was given by Pippard [18] in 1953 (L-L-P theory). Pippard introduced a non-local relation for the density of superconducting current, \mathbf{j}_s , in terms of the vector potential $\mathbf{A}(\mathbf{r})$, which provided a quantitatively satisfactory description of conventional superconductivity and at the same time introduced a length scale for variations of the coherence in the electronic behaviour called the *coherence length* ξ .

1.1.2 Ideal Type-II Superconductors

The fundamental nature of type-II superconductivity was first realised in the early experiments of Shubnikov [19] in 1937. His work on single-crystal samples of lead-indium and lead-thallium alloys showed that an ideal specimen in a uniform magnetic field parallel to its axis does not exhibit total flux exclusion, except for very low fields. The study of the magnetization curves, $M = M(H)$, of those ideal samples revealed a large region of applied fields where the curve loses its linear behaviour, changing slope and finally vanishing at a “strong” field (see Figure 1.2(a)).

This phenomenon was unnoticed for theoreticians at the time. However, it was clear that such a nonlinear magnetic behaviour is not contained in the Londons’ theory, though it can be regained from the L-L-P theory in the limit $\lambda_L \gg \xi$. The first theory to give proper account of this behaviour was proposed by Ginzburg and Landau (GL) [6] in 1950. This powerful phenomenological theory, which is based on Landau’s general theory of continuous phase transitions and includes quantum effects, will be described in detail in chapter 2 as it is the theoretical framework used throughout this thesis. Here we will quote some relevant results only. First of all, the GL theory introduces naturally the fundamental length scales: the penetration depth $\lambda_{GL}(T) = (m\beta/4\mu_0 e^2 |\alpha|)^{1/2}$ and the coherence length $\xi_{GL}(T) = (\hbar^2/2m|\alpha|)^{1/2}$. Their ratio, $\kappa = \lambda_{GL}/\xi_{GL}$, called the GL parameter, is independent of temperature within this theory. Flux quantization: $\Phi = N\Phi_0$, where $\Phi_0 = h/2|e|$ is the flux quantum and

N a positive integer, also appears naturally. Moreover, a major step of this theory comes from the consideration of the surface energy of a normal-superconducting (N-S) interface, σ_{ns} . Unlike the London theory, in which this surface energy is always positive (because of the condition of constant order parameter n_s), the surface energy of a N-S interface can be either positive or negative in the GL theory. Ginzburg and Landau noticed this fact in their paper without going any further. It was Abrikosov [20] in 1957 who pointed out the physical consequences of this fact and proposed a criterion for the classification of superconductors into type I and type II according to the value of their GL parameter.

Abrikosov established that type-II superconductors are characterised by the value of the GL parameter $\kappa > 1/\sqrt{2}$ for which the surface energy of a N-S interface is negative and therefore the total energy of the sample in a magnetic field is reduced by the creation of new interface boundaries. This way the appearance of normal regions in the interior of a specimen placed in a magnetic field is energetically favorable even for $H < H_c$ and the material splits into a fine-scale mixture of superconducting and normal regions, the arrangement being such as to give the maximum possible boundary area. Such a state is called *mixed phase* in which *magnetic vortices* penetrate the sample. Each vortex line carries a flux quantum Φ_0 and its structure consists of a core region of radius $\approx \xi$, in which superconductivity is suppressed, and an electromagnetic region of radius $\approx \lambda$ about which supercurrents flow. In equilibrium conditions the vortices form a regular vortex lattice with a finite density of these vortex lines across the whole field range $H_{c1}(T) < H < H_{c2}(T)$ (see Figure 1.2(b)). Such a lattice has been observed experimentally using the so-called decoration technique [21] in which small ferromagnetic particles deposited on the surface of a superconductor arrange themselves in a periodic magnetic structure due to the vortices. On the other hand, type-I superconductors are characterised by the value of the GL parameter $\kappa < 1/\sqrt{2}$ for which the surface energy of a N-S interface is positive and then the total energy of the sample in a magnetic field is the lowest for the minimum number of interface boundaries. Thus, an ideal type-I superconducting sample is either in its normal or superconducting state, depending on the strength of the effective magnetic field acting

on it (regaining the H - T phase diagram of the ideal type I superconductor, Figure 1.1(a)).

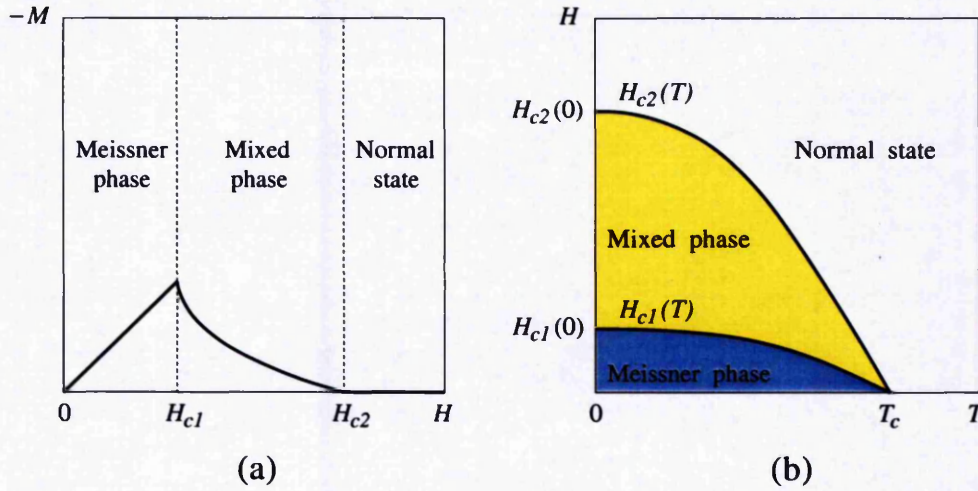


Figure 1.2: Equilibrium properties of ideal type-II superconductors (schematic). (a) Magnetization curve. (b) H - T phase diagram.

From his mean-field solution to the GL theory, Abrikosov found that there are two critical fields which play the important roles in the ideal type-II materials (H_{c1} and H_{c2}). In this scenario the *upper critical field* $H_{c2}(T)$ is a line of continuous phase transitions below which nucleation of the superconducting phase starts, with the size of a nucleation region of the order of ξ . Above it superconductivity is destroyed in the bulk of the sample, though a *surface superconductivity* in a layer of thickness ξ still remains up to a *surface nucleation field* given by $H_{c3} \simeq 1.69H_{c2}$ [22]. The *lower critical field* $H_{c1}(T)$ is also a line of continuous phase transitions, below which the Meissner phase is still possible. The thermodynamical critical field, $H_c(T)$, plays no important role in type-II superconductors. It is worth noticing that the original GL theory of superconductivity describes “accurately” the properties of conventional superconductors only near T_c . For instance, the expressions for the critical fields H_{c1} and H_{c2} are linear in T and not parabolic as in the experimental H - T phase diagram of Figure 1.2(b). Also, the GL theory was derived from the microscopic BCS theory in the limit $T \rightarrow T_c$ by Gor’kov [23]. The BCS theory is known to give a remarkably complete description of conventional low- T_c superconductivity, including the pairing mechanism

of the electrons. For the description of ideal conventional superconductors, both type I and type II, the mean field approximation of the GL theory provides a sufficiently good account of both the thermodynamical and electrodynamical N-S properties for most purposes.

1.2 Nonequilibrium Effects and Fluctuations

Real superconducting samples are rarely found to have perfect crystal lattice structures; the consequences of high current densities in them need to be considered for practical applications. The effects of crystal lattice defects and transport currents are known to be two of the most important effects in realistic superconducting samples and will be treated next. Also the effects of thermal fluctuations in conventional low- T_c samples will be described. The aim of this section is to complete the phenomenological scheme of the real conventional low- T_c superconductors that was started in Section 1.1. Again, neither exhaustive nor extensive treatment is intended, but just enough arguments and references to “argue” the physics involved.

1.2.1 Transport Currents and Pinning

In the ideal case of the conventional low- T_c superconductors a perfect vortex lattice is possible because the repulsion interaction of the vortices in the mixed phase, which in absence of a transport current are the only forces acting on the vortex system, compensate each other as to produce a zero net force on every single vortex. The situation changes when a bulk transport current \mathbf{j} is applied in a direction different to the vortex axis direction $\hat{\Phi}_0$. In this case the vortices move under the action of the *Lorentz force* $\mathbf{F}_L \propto \mathbf{j} \times \Phi_0$ and if we assume a perfect crystal lattice structure of the material, then this force is only “opposed” by the *viscous drag force* $\mathbf{F}_v = -\eta\mathbf{v}$, which originates from the electric field generated in the region around a vortex core. The parameter η in the previous expression is the viscous drag coefficient and \mathbf{v} is the vortex velocity. Magnetic flux motion under an external current will, then, result in the appearance of an electric field $\mathbf{E} = -\bar{\mathbf{v}} \times \bar{\mathbf{B}}$, where $\bar{\mathbf{v}}$ is the mean vortex velocity

and \bar{B} the mean magnetic induction acting on the superconductor. This vortex motion will lead to energy dissipation through the process of *flux-flow* and will drive the type-II superconductor to a *resistive state*. Experimental evidence of voltage generation under flux motion has been reported in the work of Giaever [24].

In a real conventional type-II superconductor, where a perfect crystal lattice is by no means possible, crystal lattice imperfections such as voids, dislocations, grain boundaries, non-superconducting precipitates, inhomogeneities, etc. act as *pinning centres* to impede motion of vortex lines [25, 26]. The local changes of the superconductor arising from these defects result in position-dependence of the free energy of the flux lines. The difference between the free energy of a flux line in the pinning centre and in the surrounding medium characterizes the strength of the pinning centre. Depending on the strength of the pinning interactions, type-II superconductors are classed as *soft* (“weak” pinning) or *hard* (“strong” pinning). The last class is the most useful in technological applications as they are the materials which can transport more electrical current without measurable dissipation.

The different phenomena which can occur from the interplay of the Lorentz force, viscous drag force and pinning forces depend on the strength of their interactions. The strength of the pinning force controls the maximum *critical current density*, j_c , that a superconductor can carry without dissipation. For current densities $j < j_c$, the pinning force is able to stop the vortex motion produced by the electric field generated in the regions around the vortex cores. However, for current densities $j > j_c$, the Lorentz and viscous drag forces overcome the pinning force resulting in dissipation through the flux-flow process.

Pinning forces may act either individually, on a single vortex line, or collectively as a bulk pinning force density. The distribution of these pinning forces through the sample is, in general, random. To provide a phenomenological description of the behaviour of hard superconductors, the concept of the *critical state* was introduced by Bean [27] and Kim *et al.* [28], which reduced the variables to a single material-sensitive property: the mean pinning force density F_p . A more sophisticated statistical approach was suggested by Labusch [29] in 1969. In this work, Labusch considered

an array of rigid vortices in the presence of pinning centres distributed randomly. A decade later, Larkin and Ovchinnikov [30] considered the approximation where each individual pinning force is sufficiently weak in comparison to the Lorentz force (called weak pinning theory). An important result from this theory is that the coherent contribution of weak individual pinning forces may lead to a sufficiently strong pinning regime.

The physical mechanism for pinning has a different nature depending on the type of defect. Macroscopic defects like grain boundaries pin vortices due to electromagnetic effects, but the interaction between vortices and voids is due to the difference of condensation energy. The effectiveness of the vortex pinning usually depends on the geometry of the samples and it becomes optimal when the sample length scale (e.g. layer thickness, if layered structure or thin film) is of the order of the penetration depth. Pinning due to voids is most effective when they are long (columnar or plane) defects of lateral size of order ξ . In practice, pinning forces provide the unique mechanism to minimize dissipation caused by vortex motion and therefore they are very important in technological applications. Thermal fluctuations, however, play an important role in the resistive state of type-II superconductors as will be described below.

1.2.2 Thermal Fluctuations

Pinning effects make it possible for type-II superconductors to carry a bulk current density with practically no dissipation. However, a sample carrying a macroscopic transport current is in a state which is thermodynamically metastable. At finite temperatures the vortex lines will tend to move under a flux gradient by activated jumps across the pinning barriers. This thermally activated phenomenon is known as *flux creep* and was first introduced by Anderson [31] and by Anderson and Kim [32]. In the flux-flow regime, for current density $j > j_c$, the resistivity is already non-zero. Furthermore, the flux-creep phenomenon manifests itself in the existence of a finite resistivity even for transport current densities $j < j_c$. Vortex jumping from one pinning centre to another usually happens in vortex bundles because of intervortex interaction. In the experiments of Beasley *et al.* [33] this amount was estimated to

be between 10 and 100 fluxoids at low fields and approximately one fluxoid near H_{c2} . The theory of flux creep suggests the existence of a non-zero resistivity at any finite temperature. This behaviour is usually referred to as thermally activated flux flow (TAFF). The thermally activated resistivity predicted by the theory is exponentially small at low temperatures but it becomes more pronounced at higher temperatures. In conventional low- T_c superconductors these aspects are in general irrelevant but they put severe limitations on the use of high- T_c superconductors in large-scale applications as will be explained in Section 1.3. Other thermal processes present in practical superconducting wires which lead to a degradation effect in superconducting solenoids are the so-called thermal instabilities [34].

The effects of thermal fluctuations play a crucial role in the lack of truly perfect conductivity of type-II superconductors at any finite temperature and also in the remains of supercurrents above T_c . These effects cannot be described within the mean field approximation of the GL theory and are known to modify the phase diagram in high temperature superconductors where they produce the vortex liquid phase. The first numerical estimation of the fluctuation contribution to the heat capacity of conventional superconductors in the vicinity of T_c was done by Ginzburg [35] in 1960. He showed that superconducting fluctuations increase the heat capacity above the transition temperature and smear it up. Recent reviews on fluctuation phenomena in superconductors can be found for temperatures close to T_c in Ref. [36] and over the mixed state in Ref. [37] and references therein.

1.3 High- T_c Superconductors

Unlike conventional low- T_c superconductors, for which a reasonable complete description has been achieved in terms of both microscopic and phenomenological theories, the more “recently” discovered high- T_c materials continue being a focus of research, especially to find the mechanism responsible for their superconductivity and to enhance their magnetic, mechanical and thermodynamic properties to make them suitable for technological applications. This section will be devoted to the description of

the general picture of the high- T_c superconductors, which are a class of type-II superconductors with rather peculiar characteristics: periodic layered structures, strong anisotropies in electronic transport, strong thermal fluctuations caused by the “high” transition temperatures ($T_c \sim 100$ K), short coherence lengths, etc. These “extreme” superconducting properties are believed to introduce new phases in the vortex state and here will be described within the phenomenological “melting scenario”. The possibility of real technological applications relies mostly on the efficiency of pinning effects. Currently, a major development in this area has emerged with the introduction of precise irradiation techniques using heavy ions. This important pinning mechanism will be described at the end of this section.

1.3.1 Structure

After the discovery of the phenomenon of superconductivity in 1911, one of the most challenging tasks to physicists and material scientists has been to find superconducting materials with the highest possible transition temperature, T_c . Lacking of definite guidelines to predict materials with high T_c , an empirical search has been the most effective one. In 1986 Bednorz and Müller [38] made a remarkable discovery. While carrying out experiments in superconducting oxides, trying to raise the T_c of the compounds by enhancing the electron-phonon interaction through the Jahn-Teller effect, they achieved superconductivity at around 30 K in the Ba-La-Cu-O system. This is the first class of copper-oxide materials (also called cuprates). The material they used was La_2CuO_4 in which Ba, Sr or Ca were introduced to replace some of the La. The superconducting phase was found to crystallize in the K_2NiF_4 structure, which is a layered perovskite with strongly anisotropic crystal structure.

Several months later groups in the United States [39] and China [40] announced the discovery of superconductivity above 77 K in the Y-Ba-Cu-O (YBCO) system. The resistance drop started at 90 K and completed at 80 K and the Meissner effect was also confirmed in these compounds below 90 K. Later the superconducting transition was sharpened and enhanced to between 98 K and 94 K. The identification of the phase responsible for the superconductivity lead to the chemical formula $\text{YBa}_2\text{Cu}_3\text{O}_{7-\delta}$ and

to the evidence for a layered structure. This crystal structure is an oxygen-defect perovskite and is very anisotropic. Cu–O planes (superconducting layers) and linear Cu–O chains along the b axis were found to exist (see Figure 1.3(b)). With the stoichiometry and the general structure of the superconducting phase determined, a new class of superconductors derived from the YBCO system.

In 1988 many new compounds and classes of compounds were discovered. Notable among these were the Bi–Sr–Cu–O and the Bi–Sr–Ca–Cu–O (BSCCO) compounds, with transition temperatures up to 115 K, and the Tl–Ba–Ca–Cu–O (TBCCO) compounds, with transition temperatures up to 125 K. The general formula for the Bi compounds is $\text{Bi}_2\text{Sr}_2\text{CaCu}_2\text{O}_{8+\delta}$. Figure 1.3(a) shows a section of the crystal structure of $\text{Bi}_2\text{Sr}_2\text{CaCu}_2\text{O}_8$. T_c increases with increasing number of CuO_2 planes in the elementary unit cell which is the general rule for all cuprate compounds.

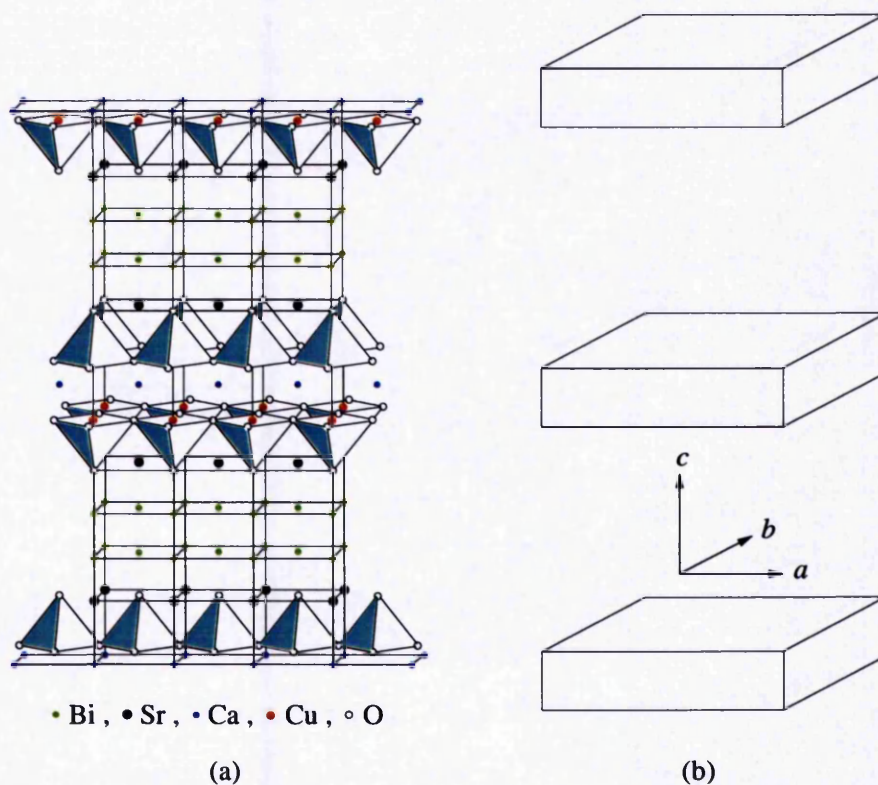


Figure 1.3: Typical Cu–O layered structure of HTSCs. (a) Crystal structure of $\text{Bi}_2\text{Sr}_2\text{CaCu}_2\text{O}_8$. (b) Superconducting Cu–O layers. [Adapted from Ref. [5].]

With time the discovery of other cuprates has resulted in a large number of superconducting compounds. In some of them a T_c of greater than 130 K has been achieved [41]. A more complete list of superconducting materials and their critical temperatures can be found in Ref. [42]. The known high- T_c materials are found to have many different structures with variety of chemical substitutions but all of them share the characteristic presence of copper oxide layers (see Figure 1.3(b)).

It is universally accepted that the mechanism responsible for superconductivity is the pairing of electrons. However, the question of the pairing mechanism in high- T_c superconductors is still controversial. The microscopic BCS theory [7] proposes the phonon mediated attraction between electrons, which seems to describe properly the properties of conventional low- T_c superconductors. However, discrepancies with experiments raise the doubt whether the same result holds for high- T_c oxides. The so called *s*-wave gap requires that the electron-electron interaction is attractive, while an unconventional *d*-wave gap can take advantage of a repulsive interaction. Many types of experiments have been carried out aimed at probing the symmetry of the gap function, including tunnelling, absorption of microwaves, Raman spectroscopy and Josephson junction measurements [43, 44, 45]. Most of them are consistent with the *d*-wave pairing; even the phase-sensitive Josephson junction measurements [46]. However, these experiments do not necessarily prove a pure *d*-wave symmetry. It may possibly be a manifestation of a more complicated anisotropy related to repulsive interactions at some regions of the Fermi surface [47].

In the absence of a microscopic theory of high- T_c superconductivity the only successful descriptions are phenomenological. There are models based both on the London theory and the Ginzburg-Landau theory. To describe the less anisotropic compounds such as YBCO, the anisotropic GL theory is employed. This approach is a generalization of the conventional GL theory to include anisotropic materials [48]. To describe highly anisotropic materials like BSCCO and TBCCO, where the coherence length is much smaller than the distance between adjacent Cu-O planes and therefore can be treated as a system of two dimensional layers with a weak interaction between them, the Lawrence-Doniach (LD) model [49] is appropriate. This model assumes

the GL equations in each layer and introduces a parameter for the coupling between layers. An important result from the LD model is that the perpendicular current is the Josephson current provided the interlayer coupling is weak. For strong interlayer coupling the anisotropic GL theory is recovered. The experimental manifestation of extremely strong anisotropy in BSCCO was the discovery of the so-called intrinsic Josephson effect in this compound [50] where there are Josephson weak links from a Cu–O double layer to its neighbouring double layers.

The structure of the vortex lines in layered high- T_c superconductors with weak Josephson interaction is very peculiar. The vortex line is a stack of two-dimensional “pancake” vortices in different layers [51, 52, 53]. The weakness of attractive interaction between the pancakes from different layers results in a strong reduction of the shear modulus of the vortex lattice along the layers as well as large effects due to thermal fluctuations. The existence of the pancake vortices has been established experimentally. A relatively recent review of the status of the phenomenological theories of high- T_c superconductivity was given by Blatter *et al.* [54]. The macroscopic magnetic properties of the cuprates are very different from those of conventional type-II superconductors. Apart from the extreme anisotropies and small coherence lengths, the effects of thermal fluctuations and pinning produce very unusual superconducting behaviour close to T_c .

1.3.2 Effect of Fluctuations

The fact of large thermal fluctuations and strong anisotropies is believed to introduce new vortex phases in the phase diagram of the high- T_c cuprates [55, 56]. Their phenomenological H – T phase diagram, as proposed by Blatter [54], shows important new features. In the absence of pinning the mixed state is split into a *vortex lattice* and a *vortex liquid* (see Figure 1.4(a)). Below a certain temperature the vortex system will freeze into a vortex lattice phase in which resistivity is exponentially small. Above this temperature the vortex system is in a vortex liquid state (the flux-flow state) with a resistance of the order of the normal-state resistance. Another feature, closely related to the vortex lattice–vortex liquid transition, is the experimentally observed

irreversibility line which provides a boundary between reversible and irreversible magnetic behaviour of a superconductor. In conventional superconductors, the vortex liquid phase is confined to a very narrow region near H_{c2} , with the irreversibility line essentially coinciding with $H_{c2}(T)$. Enhanced thermal fluctuations, smaller coherence length and large anisotropy of the cuprates lead to an observable vortex liquid region in these materials. In addition, when the effects of pinning are considered (see Figure 1.4(b)) the upper vortex-liquid phase is split into an *unpinned vortex liquid* phase and a region of *pinned vortex liquid* below. In this case the melting transition is from a vortex glass phase to a pinned vortex liquid, except at temperatures close to T_c where the transition is from the vortex glass phase to the unpinned vortex liquid regime. Notice the two branches of the melting line in every phase diagram, the high field and the low field ones, which are essentially the irreversibility lines. The regions of vortex liquid, either pinned or unpinned, are phases of flux-flow resistivity. Thus, a truly superconducting state with essentially zero resistivity exists only in the vortex lattice (or vortex glass) regime, at temperatures below the melting point. On heating, at higher temperatures, the vortex glass melts into a pinned vortex liquid. Then there is a crossover to the unpinned vortex liquid phase with resistance of the order of magnitude of the normal-state resistance.

In high- T_c superconductors, either considering the effects of pinning or not, the upper critical field H_{c2} is no longer a line of continuous phase transitions (as for conventional type-II superconductors) but a crossover between the superconducting and normal states. As Figure 1.4(b) shows, the effects of pinning may reduce the vortex liquid phase (flux-flow region), so that higher magnetic fields or greater transport current densities can be carried with less dissipation. The state of research on pinning mechanisms is of great interest so as to make copper-oxide compounds practical in technological applications.

1.3.3 Pinning of Vortex Lines

Apart from strong thermal fluctuations, which become very important at temperatures close to T_c , strong anisotropy and weak random pinning play a crucial role in

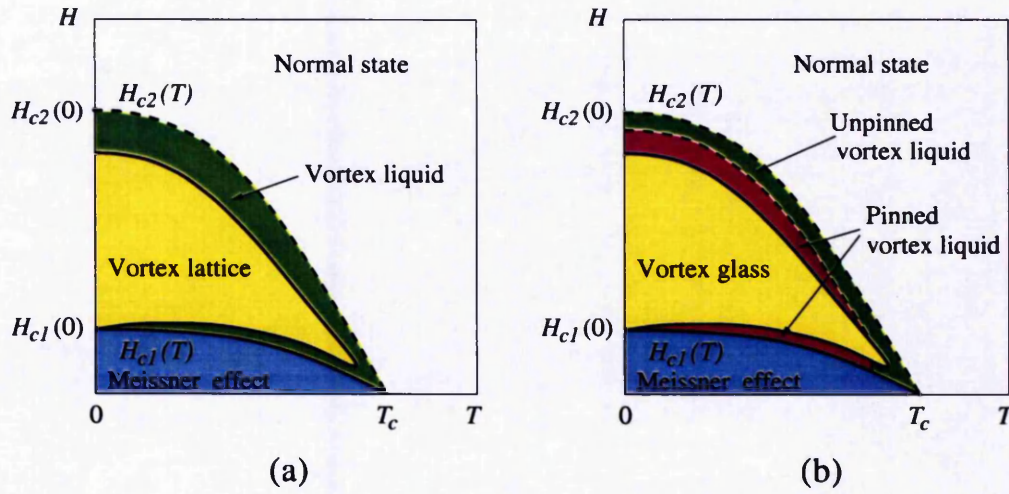


Figure 1.4: Phenomenological phase diagram for an anisotropic HTSC in the flux-lattice melting scenario (schematic). (a) Including thermal fluctuations only. (b) Including both thermal fluctuations and weak disorder (pinning).

the macroscopic magnetic properties of the cuprates [57]. The pinning properties are consequences both of the small coherence length and on the fact that the pinning centres in high- T_c materials are mainly provided by point defects, e.g. oxygen vacancies. The randomness of the pinning is due to the disorder in oxygen vacancy positions that may arise from slight deviations from the complicated stoichiometry and depends strongly on doping. If there is a magnetic field parallel to the Cu–O planes, additional intrinsic pinning exists due to the interaction of the vortex lines with the periodic potential created by the planes. Another source of pinning, which leads to degradation of the critical current in bulk high- T_c superconductors, is the grain boundaries. Because of the very short coherence length, the grain boundaries act like very weak Josephson junctions, strongly attenuating the maximum supercurrent that can be transported across the boundary. In practice, as it is extremely difficult to fabricate “defect free” samples, grain boundaries make it hard for bulk polycrystalline samples to have technologically significant critical current densities at fields above H_{c1} . This sets a limit on the magnetic applications of high- T_c superconductors. The problem, however, has been avoided by growth of highly textured samples and oriented thin films. The currently achieved maximum critical current densities in Y–Ba–Cu–O at 77 K are of the

order of 10^7 Acm^{-2} in thin films and of 10^5 Acm^{-2} in bulk polycrystalline samples. The upper critical fields are of the order of 10^2 – 10^3 T depending on the direction of the magnetic field relative to the ab planes [2].

For practical applications the useful regime is that of the vortex glass phase where practically zero resistivity exists. In YBCO the vortex glass temperature of 77 K corresponds to a field of about 4 T. This provides a restriction on the practical use of the YBCO compound. In the more anisotropic BSCCO and TBCCO the flux lattice melting temperature falls to about 30 K. In order to increase this temperature, considerable efforts are being directed towards flux-pinning enhancement by creation of strong-pinning centres. Due to the two-dimensional nature of vortices in these materials the pinning defects should represent the columns perpendicular to the Cu–O layers. Such columnar defects are at present produced, for example, by irradiation of BSCCO and TBCCO samples with high-energy ions and have started to be studied theoretically. Results show that periodic arrays [58] of these columnar defects provide a more efficient mechanism than arrays of randomly distributed columns [59]. The periodicity of the columnar defect substrate and the vortex lattice play an important role as more efficient pinning is achieved when both lattices are commensurate. Also, pinning effects by a periodic lattice of columnar defects (perpendicular to the Cu–O planes) are most effective when the direction of the applied magnetic field is parallel to the columns. Results from numerical simulations of high- T_c superconducting thin films and layered systems will be presented in this thesis in support of these facts.

1.4 Overview

The effects of pinning through point or columnar defects in strongly anisotropic high- T_c superconductors is the work that this thesis addresses. The theoretical framework is that of the phenomenological GL theory within the Lowest Landau Level (LLL) approximation. Both the thin-film limit of the GL theory and the LD model for the description of the layered system are described in Chapter 2.

Within this theoretical approach, numerical simulations on some physical properties of the vortex state are presented for both the thin superconducting film and the strongly anisotropic high- T_c superconductor. Throughout the whole of this thesis the numerical simulations are based on the Metropolis Monte-Carlo algorithm. A numerical study of ground-state and finite-temperature properties of the thin-film HTSC is given in Chapter 3. The cases when the superconducting sample is ideally clean as well as when it contains crystal lattice defects (random disorder) are described first. Then, the presence of pinning centres forming a periodic lattice is considered for the case when this “periodic substrate” and the vortex lattice are either commensurate or incommensurate.

An extension of the two-dimensional study to consider a periodic layered superconductor is presented in Chapter 4. The clean sample and the one containing columnar defects are studied at non-zero finite temperature. Two important cases are reviewed for the system with columnar defects: The first one when the pinning columns are distributed randomly throughout the sample as in the first experiments on heavy-ion irradiated high- T_c superconductors. The second, when the columnar defects form a periodic substrate. Again, the cases when this periodic lattice and the vortex lattice are either commensurate or incommensurate are studied. The thesis ends with conclusions and a proposition for further work. A discussion section in each chapter summarizes the main points of chapters 3 and 4. Appendices are given to provide notation and derivations for important results.

Chapter 2

Theoretical Approach

In order to describe the properties of high- T_c superconductors (HTSCs), some of them outlined in the introduction, we use the phenomenological Ginzburg-Landau (GL) theory of superconductivity as the starting point. Our interest is focused towards thin films and copper-oxide samples, so both the thin film limit of the GL theory and the Lawrence-Doniach (LD) model of layered superconductors will be introduced. Also, as the main interest is towards strongly anisotropic HTSCs, the use of the LD model will be justified.

First, the GL theory of superconductivity will be introduced as a general *statistical field theory*. Then, the order parameter configurations describing thermodynamic equilibrium will be shown to satisfy the GL equations with appropriate boundary conditions. Special cases of these equations will be solved next: First the simplest case of uniform solutions (called mean field approximation (MFA) within the GL theory [60]) which derives naturally in the description of type-I superconductors; and then we go on to study nonuniform solutions near H_{c2} . This gives rise to type-II behaviour and introduces the Landau level (LL) solutions for constant microscopic magnetic flux \bar{B} . The lowest Landau level (LLL) approximation is used and a scaling is performed so as to give a GL energy functional in terms of a two-dimensional effective temperature parameter α_T . The thin film limit is then taken and a final form for the “free energy” is obtained. Afterwards the LD model for layered superconductors is introduced; first in a general context and then within the LLL approximation (in terms of α_T). The

chapter ends with discussions on fluctuations and the limits of the LLL approximation.

2.1 Ginzburg-Landau Theory of Superconductivity

The problem of calculating physical observables for superconducting materials within a framework containing fluctuations was solved by Ginzburg and Landau [6] in 1950. They introduced a phenomenological *free energy functional*, based on Landau's general theory of continuous phase transitions, from which thermodynamical and electrodynamical quantities are calculated directly. The physical meaning of this theory relies on important assumptions. First, it is assumed that the behaviour of the electrons in a superconducting material can be described by a spatially varying complex order parameter $\psi(\mathbf{r})$, whose squared modulus is equal to the density of superconducting electrons: $n_s = |\psi(\mathbf{r})|^2$. From Landau's theory of continuous phase transitions (LTCPT) [17], this "effective wave function" $\psi(\mathbf{r})$, will have the property of being zero in the "disordered phase" (normal phase) and non-zero in the "ordered phase" (superconducting state).

The second assumption, which also follows from the LTCPT, is that near the transition temperature T_c the equilibrium properties of a superconductor in an applied magnetic field \mathbf{H} can be described in terms of the GL energy functional

$$\mathcal{H}[\psi, \mathbf{A}] = \int d^3r \left[\alpha |\psi|^2 + \frac{\beta}{2} |\psi|^4 + \frac{1}{2m} |\mathbf{D}\psi|^2 + \frac{1}{2\mu_0} |\mathbf{B} - \mu_0 \mathbf{H}|^2 \right], \quad (2.1)$$

where the integration is extended over the volume of the sample. Here $\mathbf{B} = \nabla \times \mathbf{A}$ is the microscopic flux density and $\mathbf{D} = -i\hbar\nabla - 2e\mathbf{A}$ the gauge invariant derivative operator. α and β are the usual phenomenological parameters which, for temperatures near T_c , can be approximated by $\alpha(T) = \alpha'(T_c)(T - T_c)$ with $\alpha'(T_c) > 0$ and $\beta > 0$ (constant). The last three constants: μ_0 , m and e are the permeability of the vacuum and, the mass of the Cooper pair¹ and the charge of the electron ($e = -|e|$),

¹Throughout the whole of this thesis we consider the usual convention of writing explicitly the charge of the Cooper pair, $2e$, directly in all expressions involving it; and for consistency set the mass $m = 2m_e$, where m_e is the electronic mass.

respectively.

Considering the GL energy functional as a Hamiltonian, the statistical field theoretical problem is centred on the partition function

$$Z(T, \mathbf{H}) = \int \mathcal{D}[\psi] \mathcal{D}[\mathbf{A}] \exp(-\mathcal{H}[\psi, \mathbf{A}]/k_B T), \quad (2.2)$$

where the functional integrations $\mathcal{D}[\psi]$ and $\mathcal{D}[\mathbf{A}]$ extend to all possible configurations of the complex order parameter and the vector potential in a fixed gauge.

Given the value of the partition function for a temperature and applied magnetic field (and the other parameters: α , β , etc.), the thermal average of a physical observable “ X ” is given by

$$\langle X(T, \mathbf{H}) \rangle = \frac{1}{Z(T, \mathbf{H})} \int \mathcal{D}[\psi] \mathcal{D}[\mathbf{A}] X[\psi, \mathbf{A}] \exp(-\mathcal{H}[\psi, \mathbf{A}]/k_B T). \quad (2.3)$$

It is well known [61] that an exact analytical calculation of a partition function and thermal average is only possible for very few statistical models. Containing all possible configurations of the “complex field” $\psi(\mathbf{r})$ and the vector potential \mathbf{A} , the GL partition function and thermal average of a physical observable in Eqs. (2.2) and (2.3) are rather more complicated than those and thus it is not possible to think of an exact analytical solution. However, at low temperatures, a “good enough” estimation can be obtained by concentrating on the “saddle point configurations”.

2.1.1 Thermodynamic Equilibrium Solutions: GL Equations

Calculating exact values of physical observables from Eqs. (2.2) and (2.3) is not only analytically impossible but also numerically difficult. The crucial problem is the infinite number of possible configurations that both the order parameter $\psi(\mathbf{r})$ and vector potential $\mathbf{A}(\mathbf{r})$ can take. To go one step forward one focuses only on the configurations which contribute the most to the partition function (2.2). These are given by the functions (ψ_0, \mathbf{A}_0) for which the GL energy functional has its saddle point [62]. Therefore, they are found by minimization of the GL energy functional (2.1) with

respect to both $\psi^*(\mathbf{r})$ and $\mathbf{A}(\mathbf{r})$.² This gives the GL equations

$$\alpha\psi + \beta|\psi|^2\psi + \frac{1}{2m}\mathbf{D}^2\psi = 0, \quad (2.4)$$

$$\mathbf{j}_s \equiv \frac{1}{\mu_0}\nabla \times (\nabla \times \mathbf{A}) = \frac{e}{m}[\psi^*\mathbf{D}\psi + \psi(\mathbf{D}\psi)^*], \quad (2.5)$$

where the superconducting current density \mathbf{j}_s has been introduced and the indices “0” have been dropped from ψ_0 and \mathbf{A}_0 . Notice that these equations should be valid at any point inside the superconducting sample and must be subject to boundary conditions. In general, for a superconductor-normal (S-N) interface, the boundary condition is [4]

$$\frac{1}{i\hbar}\mathbf{D}\psi \cdot \hat{\mathbf{n}} = \lambda_b\psi, \quad (2.6)$$

with $\hat{\mathbf{n}}$ a unit vector normal to the S-N boundary and λ_b a non-zero real constant which can be calculated from the microscopic theory. In the particular case of a superconductor-insulator (S-I) interface, $\lambda_b = 0$.

The condition (2.6) is consistent with the fact that the normal component of the superconducting current, $\mathbf{j}_s \cdot \hat{\mathbf{n}}$, is zero across the S-N interface since no nondissipative current can flow in a normal metal. Moreover, in the S-I interface case ($\lambda_b = 0$), the fact that the normal component of the magnetic induction $\mathbf{B} \cdot \hat{\mathbf{n}}$ is continuous, is also regained. This completes the general scheme of the thermodynamic equilibrium solutions for the GL theory. In the following we consider particular cases of this problem.

Uniform Solutions

The simplest solution of the GL equations is for the case of uniform superconductors: $\psi(\mathbf{r}) = \text{constant}$ with $\mathbf{A}(\mathbf{r}) = \mathbf{0}$. From Eq. (2.4) one derives the solution for the order parameter across the volume of the sample

$$|\psi_u|^2 = \begin{cases} 0 & \text{if } T > T_c, \\ -\alpha/\beta & \text{if } T < T_c, \end{cases} \quad (2.7a)$$

$$(2.7b)$$

²It is worthwhile noticing that minimization of the energy functional with respect to $\psi(\mathbf{r})$ gives just the complex conjugate of Eq. (2.4).

which correspond to the normal and superconducting phases respectively. On the other hand, Eq. (2.5) gives the superconducting current density

$$\mathbf{j}_s = \mathbf{0}, \quad (2.8)$$

regardless of the applied magnetic field \mathbf{H} . The *thermodynamical critical field* $H_c(T)$, is obtained by the condition $\mathcal{H}[\psi_u, \mathbf{0}] = 0$ ($T < T_c$)³ and equals

$$H_c(T) = \frac{|\alpha|}{(\mu_0\beta)^{1/2}}. \quad (2.9)$$

We notice that this equation gives a linear dependence on $T - T_c$ of H_c , which is accurate only near T_c . It is worth mentioning that the fact of assuming $\mathbf{A}(\mathbf{r}) = \mathbf{0}$, means $\mathbf{B} = \mathbf{0}$ in the bulk of the superconductor.

Characteristic Length-Scales

Let us derive expressions for the important length scales in a superconductor within the thermodynamic equilibrium approach. The first characteristic length ξ can be introduced by writing the GL equation (2.4) in the following form

$$-\xi^2 \nabla^2 \tilde{\psi} - \tilde{\psi} + \tilde{\psi} |\tilde{\psi}|^2 = 0, \quad (2.10)$$

where we have assumed $\mathbf{B}=\mathbf{0}$ inside the sample, chosen the vector potential as $\mathbf{A}=\mathbf{0}$ and introduced the dimensionless function $\tilde{\psi} = \psi/|\psi_u|$ ($T < T_c$). This defines the *coherence length* $\xi(T)$ by the equation

$$\xi(T) = \left(\frac{\hbar^2}{2m|\alpha|} \right)^{1/2}. \quad (2.11)$$

From Eq. (2.10) it is clear that $\xi(T)$ indeed measures the range of variation of $\tilde{\psi}$ (i.e. the smallest distance over which the order parameter ψ can have a large fractional change).

The second characteristic length, λ , can be introduced by considering electromagnetic effects ($\mathbf{A} \neq \mathbf{0}$) in the current density GL equation (2.5). Consider a superconductor in a magnetic field \mathbf{H} that produces a “weak” magnetic induction $\mathbf{B} = \nabla \times \mathbf{A}$

³In other formulations [63] the GL free energy $\mathcal{H}[\psi, \mathbf{A}]$ of Eq. (2.1) is associated directly with the difference in the Gibbs free energies of the superconducting and normal phases, $G_s[\psi, \mathbf{A}] - G_n[\psi, \mathbf{A}]$, which makes evident the condition $\mathcal{H}[\psi_u, \mathbf{0}] = 0$.

across the sample. In this case the order parameter $\psi(\mathbf{r})$ varies slowly and, to first approximation, can be taken as the superconducting uniform solution ψ_u ($T < T_c$). Replacing ψ by ψ_u ($T < T_c$) into Eq. (2.5) gives

$$\frac{1}{\mu_0} \nabla \times (\nabla \times \mathbf{A}) = -\frac{4e^2}{m} |\psi_u|^2 \mathbf{A}. \quad (2.12)$$

Taking $\nabla \times$ on the previous equation (using Maxwell's equation $\nabla \cdot \mathbf{B} = 0$) and using expression (2.7b) we can write

$$\nabla^2 \mathbf{B} = \frac{1}{\lambda^2} \mathbf{B}, \quad (2.13)$$

with the penetration depth defined by

$$\lambda(T) = \left(\frac{m\beta}{4\mu_0 e^2 |\alpha|} \right)^{1/2}, \quad (2.14)$$

which characterizes the range of variation of the magnetic induction \mathbf{B} .

The ratio of these quantities, called the GL parameter (already mentioned in the introduction), is a constant within the GL theory given by

$$\kappa = \frac{\lambda(T)}{\xi(T)} = \left(\frac{m^2 \beta}{2e^2 \hbar^2 \mu_0} \right)^{1/2}. \quad (2.15)$$

This parameter characterizes different materials and moreover its value determines whether a superconductor is type I or II, as explained in Chapter 1.

Non-uniform Solutions near H_{c2} within the MFA

Considering general non-uniform solutions to the GL equations (2.4) and (2.5) for arbitrary temperatures and magnetic fields is not a trivial matter. Fortunately they can be found around certain important limits. In the case of applied fields “just below” H_{c2} and temperatures “very close” to T_c (necessary condition for GL energy to be valid), the superconducting condensate has “just appeared” and therefore the squared modulus of the order parameter, $|\psi(\mathbf{r})|^2$, is “nearly zero”. In this case the cubic term in Eq. (2.4) is small and can be neglected leading to the eigenvalue equation

$$\frac{1}{2m} \mathbf{D}^2 \psi(\mathbf{r}) = -\alpha \psi(\mathbf{r}), \quad (2.16)$$

which is formally equivalent to the time-independent Schrödinger equation for a particle of charge $2e$ and mass m in a magnetic induction field $\mathbf{B} = \nabla \times \mathbf{A}$. Notice that

the energy eigenvalues are given by $-\alpha$ and that the solutions depend on \mathbf{B} , but must be gauge invariant.

With this consideration and the fact that for slowly varying wave functions $\psi(\mathbf{r})$ (which is accurate close enough to H_{c2}) the supercurrents are nearly zero, we can approximate the microscopic flux density \mathbf{B} by its constant mean value across the sample $\bar{\mathbf{B}}$.⁴ This means that the vector potential \mathbf{A} can be chosen as a function of the spatial coordinates, \mathbf{A}_0 , such that $\nabla \times \mathbf{A}_0 = \bar{\mathbf{B}}$. It is shown in Appendix A.2 that if $\bar{\mathbf{B}} = \bar{B}\hat{\mathbf{k}}$ and we consider solutions on the plane perpendicular to the magnetic induction, then in Landau's gauge: $\mathbf{A}_0 = -\bar{B}y\hat{\mathbf{i}}$ (for which $\nabla \cdot \mathbf{A}_0 = 0$) a set of normalized eigenfunctions is given by

$$\psi_{n,k_x}(x, y) = \mathcal{N}_n \exp \left[ik_x x - \frac{1}{2} \left(\frac{y - k_x l_m^2}{l_m} \right)^2 \right] H_n \left(\frac{y - k_x l_m^2}{l_m} \right), \quad (2.17)$$

where $H_n(x)$ is the Hermite polynomial of order $n = 0, 1, 2, \dots$; $l_m = (\hbar/2|e|\bar{B})^{1/2}$ the mean distance between magnetic vortices (called the magnetic length) and $\mathcal{N}_n = [\pi^{1/4} l_m^{1/2} L_x^{1/2} \sqrt{2^n n!}]^{-1}$ for the finite-sized system (in the infinite case it takes the value $\mathcal{N}_n = [\pi^{3/4} l_m^{1/2} \sqrt{2^{n+1} n!}]^{-1}$) as explained in Appendix A.2. $\hbar k_x$ are the continuous eigenvalues of the momentum operator $\hat{p}_x = -i\hbar\partial/\partial x$.

These are the Landau levels (LL), within the Landau gauge, with energy eigenvalues ($-\alpha(n) = E_n$) given by

$$-\alpha = \frac{2|e|\bar{B}\hbar}{m} \left(n + \frac{1}{2} \right). \quad (2.18)$$

Notice that the degree of degeneracy of each level is infinite because for each energy index n the momentum in x direction, $\hbar k_x$, can take any real value from $-\infty$ to $+\infty$. These solutions apply in the two-dimensional limit only. For the case of the bulk superconductor in the presence of a uniform magnetic induction along the z -axis see the first footnote in Appendix A.2.

Another particular geometry, which will be of interest in the rest of this thesis, is that of a sphere of radius R with a radial magnetic induction $\mathbf{B}(\mathbf{r}) = (\bar{B}R^2/r^2)\hat{\mathbf{r}}$. Near H_{c2} , this will be again approximated by its mean value across the sample, $\bar{\mathbf{B}} = \bar{B}\hat{\mathbf{r}}$,

⁴From now on we will use the notation \bar{X} to represent spatial average $(1/V) \int d^d r X(\mathbf{r})$ of the quantity $X(\mathbf{r})$ over the d -dimensional "volume" under consideration, V .

where $\bar{B} = B(R)$. The gauge is now chosen as $\mathbf{A}_0 = (\bar{B}R^2/r) \tan(\theta/2) \hat{\phi}$, which again is such that $\nabla \cdot \mathbf{A}_0 = 0$. In this case the normalized energy eigenfunctions in spherical polar coordinates are found to be

$$\psi_{n,q,N}(\theta, \phi) = \mathcal{N}_{n,q,N} e^{iq\phi} \sin^q(\theta/2) \cos^{N-q}(\theta/2) P_n^{(q, N-q)}(\cos \theta), \quad (2.19)$$

where $P_n^{(q, N-q)}(x)$ are the Jacobi polynomials and $\mathcal{N}_{n,q,N}$ is the normalization constant (see Appendix A.2). These LL on the sphere are again labeled by the index $n = 0, 1, 2, \dots$; and the degeneracy of each level is labeled by the angular momentum eigenvalue $q = -n, -n+1, \dots, n+N$, with N the total number of flux tubes penetrating the sphere. Notice that the degeneracy of each level is $N+1+2n$.

The energy eigenvalues, $-\alpha(n) = E_n$, in this geometry are now

$$-\alpha = \frac{2|e|\bar{B}\hbar}{m} \left(\frac{n(n+N+1)}{N} + \frac{1}{2} \right). \quad (2.20)$$

Once again these solutions apply in the two-dimensional limit only. For the case of the bulk superconductor in the presence of the radial magnetic induction $\bar{\mathbf{B}} = \bar{B}\hat{\mathbf{r}}$ see the second footnote in Appendix A.2. Notice that these energy levels are quadratic in n and not linear as in the plane geometry, Eq. (2.18). Figure 2.1 illustrates this fact. However, in the limit $N \rightarrow \infty$, when the sphere tends to a plane, the excited energy levels on the sphere are lowered and those on the plane are recovered.

The eigenvalue solutions in both cases, Eqs. (2.18) and (2.20), can be solved for \bar{B} (which to first approximation can be replaced by $\mu_0 H$). Both cases show that the highest field for which superconductivity occurs corresponds to $n = 0$. This defines the upper critical field as

$$H_{c2}(T) = \frac{m|\alpha|}{\hbar\mu_0|e|}. \quad (2.21)$$

In a similar fashion, the lower critical field can be defined by making physical considerations in the London limit ($|\psi| \approx \text{constant}$). The result is

$$H_{c1}(T) = \frac{\hbar|e\alpha|}{m\beta} \ln \kappa, \quad (2.22)$$

for $\kappa \gg 1$. It is worthwhile noticing that within the MFA of the GL theory both critical fields have linear dependence on $T - T_c$, which is valid only near the MF critical point $(T, H) = (T_c, H_{c2})$.

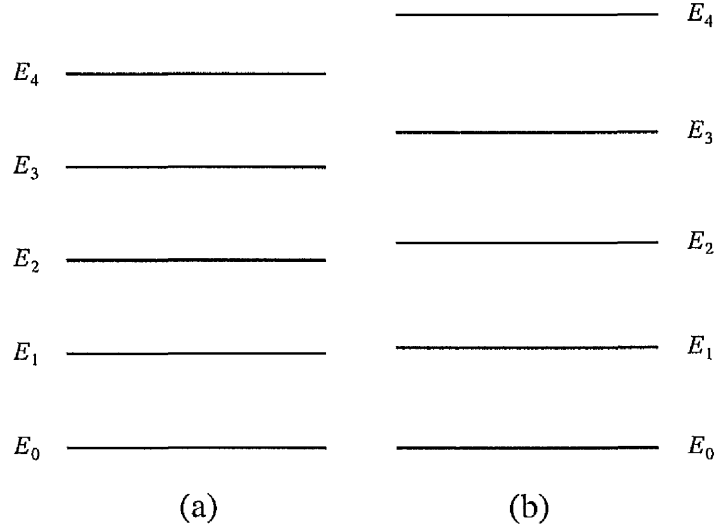


Figure 2.1: First five energy Landau-levels on two different geometries. (a) For a flat plane. (b) In a spherical shell.

2.1.2 The Lowest Landau Level Approximation

In order to consider the possibility of a vortex lattice, as argued in the introduction, we need to be able to obtain periodic solutions for the order parameter $\psi(\mathbf{r})$ over the region $H_{c1} < H < H_{c2}$ (Figure 1.2(b)). As explained above, for applied magnetic fields which are “slightly lower” than the upper critical field H_{c2} the vector potential can be fixed to a value \mathbf{A}_0 and therefore its fluctuations can be neglected. In a similar fashion, the superconducting condensate will be “properly” described by the eigenfunctions corresponding to the lowest energy eigenvalue: $n = 0$ in Eqs. (2.17) and (2.19). These lowest energy eigenfunctions are called the lowest Landau levels (LLL) and periodic solutions are constructed by taking linear combinations of the degenerate eigenfunctions of the LLL. In the plane geometry with $\bar{\mathbf{B}} = \bar{B}\hat{\mathbf{k}}$, the order parameter is expanded as⁵

$$\psi_L(x, y) = Q \sum_{k_x} c_{k_x} \psi_{k_x}(x, y), \quad (2.23)$$

⁵To compact notation, in the following the index “0” (corresponding to $n = 0$) will be dropped from all LLL expressions containing it. For instance $\psi_{k_x} \equiv \psi_{0,k_x}$ and $\psi_{q,N} \equiv \psi_{0,q,N}$; and the same for the normalization constants $\mathcal{N} \equiv \mathcal{N}_0$ and $\mathcal{N}_{q,N} \equiv \mathcal{N}_{0,q,N}$.

with energy eigenvalue $-\alpha = |e|\bar{B}\hbar/m$, normalized LLL eigenfunctions $\psi_{k_x}(x, y)$ [given in Eq. (2.17) with $n = 0$] and complex coefficients c_{k_x} . Q is a real parameter, fixed so as to give a simple temperature dependence of the energy functional. Analogously in the spherical geometry with $\bar{\mathbf{B}} = \bar{B}\hat{\mathbf{r}}$, the order parameter is given by

$$\psi_L(\theta, \phi) = Q \sum_{q=0}^N v_q \psi_{q,N}(\theta, \phi), \quad (2.24)$$

with the same energy eigenvalue $-\alpha = |e|\bar{B}\hbar/m$, normalized LLL eigenfunctions $\psi_{q,N}(\theta, \phi)$ [given in Eq. (2.19) with $n = 0$], complex expansion coefficients v_q and $Q = (\Phi_0 k_B T / \beta d_0 \bar{B})^{1/4}$ chosen so as to give a simple temperature dependence to the energy functional in the thin-film limit.

Putting the LLL expansion of Eq. (2.23) into the current density GL Eq. (2.5) it is possible to show [64] that the contribution of the supercurrents to the magnetic induction (within the LLL subspace) is given by the *first Abrikosov's identity* [20]

$$\mathbf{B} = \mu_0 \mathbf{H} - \frac{e\hbar\mu_0}{m} |\psi_L|^2 \hat{\mathbf{k}}. \quad (2.25)$$

Then, introducing Eqs. (2.23) and (2.25) into the GL energy functional, Eq. (2.1), the LLL energy functional is found to be

$$\mathcal{H}[\psi_L, \mathbf{A}_0] = \int d^3r \left[\alpha_H |\psi_L|^2 + \frac{\beta_\kappa}{2} |\psi_L|^4 + \frac{\hbar^2}{2m} \left| \frac{\partial \psi_L}{\partial z} \right|^2 \right], \quad (2.26)$$

with $\alpha_H = \alpha + |e|\hbar\mu_0 H/m$ and $\beta_\kappa = \beta(1 + 1/2\kappa^2)$. The upper critical field in the LLL approximation is defined by $\alpha_H = 0$. Notice the dimensional reduction in the derivative term to only variations on the order parameter along the direction of the applied magnetic field.

In fact, by looking for spatially averaged configurations of $|\psi_L|^2$, $\overline{|\psi_L|^2}$, which minimise the LLL energy in Eq. (2.26) we see that the positive contribution in the last term will be removed if ψ_L is z -independent. This justifies the set of z -independent Landau level eigenfunctions considered in Eq. (2.17). In this case Eq. (2.26) reads

$$\mathcal{H}[\psi_L, \mathbf{A}_0] = V \overline{|\psi_L|^2} \left[\alpha_H + \frac{1}{2} \beta_\kappa \beta_{A,L} \overline{|\psi_L|^2} \right], \quad (2.27)$$

where the LLL Abrikosov ratio $\beta_{A,L} = \overline{|\psi_L|^4} / \overline{|\psi_L|^2}^2$ has been introduced and V denotes the volume of the sample. Differentiation of this equation with respect to $\overline{|\psi_L|^2}$ shows

that the energy will be minimum when $|\overline{\psi_L}|^2 = -\alpha_H/\beta_\kappa\beta_{A,L}$ ($\alpha_H \leq 0$), and in that case

$$\mathcal{H}_{\min}[\psi_L, \mathbf{A}_0] = -\frac{\alpha_H^2}{2\beta_\kappa\beta_{A,L}}V, \quad (2.28)$$

which shows that the lowest value of $\beta_{A,L}$ will also minimise the free energy. The Abrikosov ratio [20] is in fact defined for general configurations of the order parameter as $\beta_A = |\overline{\psi}|^4/|\overline{\psi}|^2$ and it achieves its minimum value of $\beta_A = 1.15959527\cdots$ for a triangular lattice [65].

2.1.3 Effective Temperature Parameter

A convenient expression for the GL energy functional can be obtained by rescaling the order parameter and spatial coordinates in the following way

$$\psi_L = (|\alpha_H|/\beta_\kappa)^{1/2}\tilde{\psi}_L \quad (2.29)$$

$$(x, y) = \rho^{1/2}(\tilde{x}, \tilde{y}) \quad (2.30)$$

$$z = \xi_H \tilde{z}, \quad (2.31)$$

where we have introduced the rescaled variables denoted by the tilde on them and the scaling parameters $\rho = \pi\hbar/|e|\mu_0 H$ and $\xi_H = (\hbar^2/2m|\alpha_H|)^{1/2}$. Introducing Eqs. (2.29)–(2.31) into Eq. (2.26) and defining the *effective temperature parameter* in three dimensional samples as

$$\alpha_T^{(3D)} = \left(\frac{\pi\hbar^2}{\beta_\kappa|e|\mu_0 H k_B T \sqrt{2m}} \right)^{2/3} \alpha_H, \quad (2.32)$$

the GL-LLL energy functional becomes

$$\mathcal{H}_{(3D)}[\tilde{\psi}_L] = |\alpha_T^{(3D)}|^{3/2} k_B T \int d^3\tilde{r} \left[\text{sgn}(\alpha_T^{(3D)}) |\tilde{\psi}_L|^2 + \frac{1}{2} |\tilde{\psi}_L|^4 + \left| \frac{\partial \tilde{\psi}_L}{\partial \tilde{z}} \right|^2 \right]. \quad (2.33)$$

In the thin film limit, where the thickness d_0 of the film is less than the coherence length, with a magnetic field applied perpendicular to the film a two dimensional effective temperature parameter can be defined by

$$\alpha_T = \left(\frac{\pi\hbar d_0}{\beta_\kappa|e|\mu_0 H k_B T} \right)^{1/2} \alpha_H, \quad (2.34)$$

and the GL-LLL energy can be written as

$$\mathcal{H}_{2D}[\tilde{\psi}_L] = |\alpha_T|^2 k_B T \int d^2\tilde{r} \left[\text{sgn}(\alpha_T) |\tilde{\psi}_L|^2 + \frac{1}{2} |\tilde{\psi}_L|^4 \right]. \quad (2.35)$$

This equation will be used in most of the calculations involving the GL-LLL energy of the clean thin-film superconductor, so the subindex $2D$ will be changed in favour of “c” (for clean). To avoid confusion between the original and scaled variables, we will keep the notation with the tildes for the scaled variables. We notice, for example, that within this LLL scaling the order parameter on the plane will be written as

$$\tilde{\psi}_L(x, y) = \tilde{Q} \sum_{k_x} c_{k_x} \psi_{k_x}(x, y), \quad (2.36)$$

where \tilde{Q} is another scaled parameter and the rest of symbols are the same as in Eq. (2.23). Analogously the LLL expansion on the sphere, within this scaling, will be given by

$$\tilde{\psi}_L(\theta, \phi) = \tilde{Q} \sum_{q=0}^N v_q \psi_{q,N}(\theta, \phi), \quad (2.37)$$

with $\tilde{Q} = |2\pi/\alpha_T|^{1/2}$ and the rest of the expression completely analogous to Eq. (2.24). It is proved in Appendix A.5 that within the thin-film limit of HTSCs, the scaled form of the GL-LLL formulation in Eq. (2.35) is equivalent to the original GL-LLL formulation, Eq. (2.1), for $\mathbf{B} = \mu_0 \mathbf{H}$. Finally it is worthwhile remarking that $\alpha_T = 0$ corresponds to the line $H_{c2}(T)$ and $\alpha_T \rightarrow \pm\infty$ when $T \rightarrow \infty$ and $T \rightarrow 0$ respectively.

2.2 Lawrence-Doniach Model

To describe the properties of superconductors with layered structures we use a model introduced by Lawrence and Doniach (LD) [49] which is based on the GL theory of superconductivity (Section 2.1). In this model, layered superconductors are represented by a stacked array of “two-dimensional” superconducting thin films. Within each layer, labeled by the index n , the order parameter ψ_n is a complex function of the two-dimensional vector position across the layer; and adjacent layers are coupled together via Josephson tunnelling. The model can, therefore, be defined in terms of

an energy functional similar to the GL energy functional in Eq. (2.1). For a system of M layers in an applied magnetic field \mathbf{H} , perpendicular to the layers, the LD energy functional is written as

$$\mathcal{H}_{LD} = \sum_{n=1}^M d_0 \int d^2r \left[\alpha |\psi_n|^2 + \frac{\beta}{2} |\psi_n|^4 + \frac{1}{2m_{\perp}} |\mathbf{D}_{\perp} \psi_n|^2 + \frac{\hbar^2}{2m_{\parallel} s^2} |\psi_{n+1} - \psi_n|^2 + \frac{1}{2\mu_0} |\mathbf{B} - \mu_0 \mathbf{H}|^2 \right], \quad (2.38)$$

with $\mathbf{B} = \nabla \times \mathbf{A}$ the magnetic induction in which the gauge satisfies $\nabla \cdot \mathbf{A} = 0$ and we have introduced the directions: “parallel” and “perpendicular” relatives to the applied magnetic field.⁶ We have also introduced the gauge invariant derivative operator on the layers (and therefore perpendicular to the magnetic flux): $\mathbf{D}_{\perp} \equiv \hat{\mathbf{B}} \times \mathbf{D} = -i\hbar \nabla_{\perp} - 2e\mathbf{A}_{\perp}$, where $\hat{\mathbf{B}}$ is a unit vector in the direction of the magnetic induction field. The anisotropy in electronic transport is introduced by the different masses m_{\perp} and m_{\parallel} along and perpendicular to the layers respectively. The layers of thickness d_0 are equally spaced by a distance s and periodic boundary conditions on the order parameter $\psi_{M+1} = \psi_1$ are assumed.

With this energy functional as Hamiltonian, the statistical field theoretical approach in this model is based on the partition function

$$Z_{LD}(T, \mathbf{H}) = \int \prod_{n=1}^M \mathcal{D}[\psi_n] \mathcal{D}[\mathbf{A}] \exp(-\mathcal{H}_{LD}/k_B T), \quad (2.39)$$

and the thermal average of physical observables “ X ”; given by

$$\langle X(T, \mathbf{H}) \rangle = \frac{1}{Z_{LD}(T, \mathbf{H})} \int \prod_{n=1}^M \mathcal{D}[\psi_n] \mathcal{D}[\mathbf{A}] X[\psi_n, \mathbf{A}] \exp(-\mathcal{H}_{LD}/k_B T). \quad (2.40)$$

To tackle this problem, again, the thermodynamic equilibrium solutions are undertaken which leads to the set of M ($n = 1, 2, \dots, M$) LD mean field equations

$$\alpha \psi_n + \beta |\psi_n|^2 \psi_n + \frac{1}{2m_{\perp}} \mathbf{D}_{\perp}^2 \psi_n - \frac{\hbar^2}{2m_{\parallel} s^2} [\psi_{n+1} - 2\psi_n + \psi_{n-1}] = 0, \quad (2.41)$$

⁶In general the integrand of the coupling term between layers is given by [66]

$$\frac{\hbar^2}{2m_{\parallel} s^2} \left| \psi_{n+1} \exp \left(-\frac{2ie}{\hbar} \int_{ns}^{(n+1)s} dx_{\parallel} A_{\parallel} \right) - \psi_n \right|^2,$$

where dx_{\parallel} represents the spatial coordinate along the direction of the applied magnetic field and A_{\parallel} the component of the vector potential in the same direction. Within the approximations in this thesis the exponential factor is just 1, so we write directly the LD energy functional as in Eq. (2.38).

$$\mathbf{j}_s \equiv \frac{1}{\mu_0} \nabla \times (\nabla \times \mathbf{A}) = \frac{e}{m_\perp} [\psi_n^* \mathbf{D}_\perp \psi_n + \psi_n (\mathbf{D}_\perp \psi_n)^*], \quad (2.42)$$

which couple the order parameter in adjacent layers, but leave the current equations independent. This is valid as long as the magnetic field is applied perpendicular to the layers.

Once again the problem is completed by imposing boundary conditions. The periodic boundary conditions for the order parameter on the layers are given by

$$\psi_{M+1} = \psi_1, \quad (2.43)$$

$$\psi_0 = \psi_M, \quad (2.44)$$

and the coupled superconductor-medium (S-M) boundary conditions written as

$$\left(\frac{1}{i\hbar} \mathbf{D}_\perp \psi_n - \frac{\psi_{n+1} - \psi_n}{s} \hat{\mathbf{B}} \right) \cdot \hat{\mathbf{n}} = \lambda_b \psi_n, \quad (2.45)$$

with $\hat{\mathbf{n}}$ and $\hat{\mathbf{B}}$ unit vectors: normal to the S-M boundary and parallel to the magnetic flux, respectively. λ_b is a non-zero real constant for S-N interfaces but $\lambda_b = 0$ for S-I interfaces (as in Section 2.1.1).

By considering the S-I interface between a superconducting layer and the insulating medium adjacent to it, in this case of magnetic flux normal to the superconducting layers, the condition $\psi_{n+1} = \psi_n$ follows immediately from Eq. (2.45). In such a case the LD equations for the order parameter in Eq. (2.41) automatically decouple leading to a set of n identical GL equations [as in Eq. (2.4)] whose solutions “near” H_{c2} in each layer are given by the Landau levels [as in Eqs. (2.17)-(2.20)].

2.2.1 The LLL Approximation for the LD Model

By the considerations explained just above, and the conclusions on the lowest Landau level (LLL) approximation in Section 2.1.2, periodic solutions can be constructed in each layer n of a LD layered superconductor by taking linear combinations of the LLL energy eigenfunctions. For the case of magnetic induction in the z -axis direction, $\bar{\mathbf{B}} = \bar{B} \hat{\mathbf{k}}$, the order parameter becomes

$$\psi_{n,L}(x, y) = Q \sum_{k_x} c_{n,k_x} \psi_{k_x}(x, y), \quad (2.46)$$

where the expansion coefficients c_{n,k_x} are complex numbers and Q the same real constant as in Eq. (2.23). The energy eigenvalue is $-\alpha = (|e|\overline{B}\hbar/m_\perp) + (\hbar^2 k_z^2/2m_\parallel)$ (see the first footnote in Appendix A.2) and the normalized LLL eigenfunctions, $\psi_{k_x}(x, y)$, given in Eq. (2.17) with $n = 0$.

In the case of $\overline{\mathbf{B}} = \overline{B}\hat{\mathbf{r}}$, however, the order parameter is given by

$$\psi_{n,L}(\theta, \phi) = Q \sum_{q=0}^N v_{n,q} \psi_{q,N}(\theta, \phi), \quad (2.47)$$

with energy eigenvalue $-\alpha = (|e|\overline{B}\hbar/m_\perp) + (\hbar^2 k^2/2m_\parallel)$ (see the second footnote in Appendix A.2), normalized LLL eigenfunctions $\psi_{q,N}(\theta, \phi)$ [given in Eq. (2.19) with $n = 0$], complex coefficients $v_{n,q}$ and Q the same constant as in Eq. (2.24).

The set of decoupled current density LD Eqs. (2.42) implies that the contribution of the supercurrents to the magnetic induction (within the LLL subspace) is, again, given by Eq. (2.25) for each layer n . Therefore, replacing ψ_L by $\psi_{n,L}$ (where $n = 1, 2, \dots, M$ and the index L stands as an abbreviation for LLL) and m by m_\perp in Eq. (2.25), and introducing this as well as Eq. (2.46) into the LD energy functional, Eq. (2.38), the LD-LLL energy functional can be reduced to

$$\mathcal{H}_{LD}[\psi_{n,L}] = \sum_{n=1}^M d_0 \int d^2r \left[\alpha_H |\psi_{n,L}|^2 + \frac{\beta_\kappa}{2} |\psi_{n,L}|^4 + \frac{\hbar^2}{2m_\parallel s^2} |\psi_{n+1,L} - \psi_{n,L}|^2 \right], \quad (2.48)$$

with the definitions of α_H and β_κ slightly modified by the change m by m_\perp (see the end of Section 2.1.2). The dimensional reduction to variations on the LLL order parameter only along the direction of the applied magnetic field is evident as before.

A final form for the LD-LLL energy functional can be obtained by rescaling the order parameter and spatial coordinates (x, y) as in Eqs. (2.29) and (2.30) [but replacing m by m_\perp] and the interlayer spacing by

$$s = \xi_H \tilde{s}, \quad (2.49)$$

where $\xi_H = (\hbar^2/2m_\parallel|\alpha_H|)^{1/2}$. In terms of the two dimensional effective temperature parameter, Eq. (2.34), the LD-LLL energy functional becomes

$$\mathcal{H}_{LD}[\tilde{\psi}_{n,L}] = |\alpha_T|^2 k_B T \sum_{n=1}^M \int d^2\tilde{r} \left[\text{sgn}(\alpha_T) |\tilde{\psi}_{n,L}|^2 + \frac{1}{2} |\tilde{\psi}_{n,L}|^4 + \frac{1}{\tilde{s}^2} |\tilde{\psi}_{n+1,L} - \tilde{\psi}_{n,L}|^2 \right]. \quad (2.50)$$

with the periodic boundary conditions defined by $\tilde{\psi}_{M+1,L} = \tilde{\psi}_{1,L}$. In a similar fashion to the two-dimensional case, this equation will be used in all calculations involving the LD-LLL energy of the clean layered superconductors, so the LD subindex will be exchanged by “c”. Once again we will keep the tildes to avoid confusing scaled and original parameters.

As in the thin-film case, we notice that the scaled LLL order parameter in each layer of the layered superconductor with plane geometry becomes

$$\tilde{\psi}_{n,L}(x, y) = \tilde{Q} \sum_{k_x} c_{n,k_x} \psi_{k_x}(x, y), \quad (2.51)$$

and in the spherical geometry

$$\tilde{\psi}_{n,L}(\theta, \phi) = \tilde{Q} \sum_{q=0}^N v_{n,q} \psi_{q,N}(\theta, \phi), \quad (2.52)$$

with $\tilde{Q} = |2\pi/\alpha_T|^{1/2}$, and the rest of the expressions completely analogous to those in Eqs. (2.46) and (2.47), respectively.

2.3 Limits of the LLL Approximation

The LLL approximation, as outlined before, relies on two essential assumptions: One is the fact that fluctuations in the vector potential \mathbf{A} should be vanishingly small, and therefore its value could be fixed to a value \mathbf{A}_0 such as to give a constant magnetic induction, $\bar{\mathbf{B}} = \nabla \times \mathbf{A}_0$, across the whole mixed phase of the type-II superconductor. Despite the fact that the microscopic flux density indeed varies on lengths of the scale of λ (so as to produce the vortex lattice), in HTSCs (with their $\kappa \gg 1$) this variation is slow in comparison with lengths of the scale of ξ and therefore the field in fact seems uniform. The second assumption is that the GL order parameter, $\psi(\mathbf{r})$, should be properly described by a linear combination of the degenerate set of LLL solutions to Eq. (2.16), with \mathbf{A} replaced by \mathbf{A}_0 (and m by m_\perp in the LD model). We expect this to be valid as long as the system is kept at low enough temperatures, where thermal fluctuations are small, and sufficiently high magnetic fields such that the energy levels are not closely spaced.

The range of validity of the first assumption can be quantified, within the MFA, in terms of the magnetic penetration depth λ , which measures variations in the magnetic flux, and the magnetic length l_m which is the mean distance between vortex lines. It is clear then that the approximation $\bar{\mathbf{B}} = \nabla \times \mathbf{A}_0$ will be valid as long as $\lambda/l_m \gg 1$. Using expressions from above we can write this condition as $\kappa(H/H_{c2}) \gg 1$, which shows that, for extreme type-II superconductors (as HTSCs are) with their large $\kappa \sim 100$ values, the approximation holds for a wide range of applied magnetic fields; breaking down only at very low fields.

The second assumption involves the term in the energy scale $|\alpha_H|$, that weights the quadratic contributions of the LLL order parameter to the GL energy functional in Eq. (2.26), and the energy separation of the LLs, $2e\mu_0 H \hbar/m$. A simple criterion for the validity of the assumption of retaining only the lowest level should be $|\alpha_H| \ll 2e\mu_0 H \hbar/m$, which obviously holds “near” H_{c2} because $\alpha_H = 0$ at exactly the upper critical field. However, for weak applied magnetic fields H the condition does not hold anymore and the energy contribution of the next LL becomes important. Another way to see the same fact is that at very low fields the LLs are closely spaced and strongly coupled through the quartic energy term; therefore the LLL approximation is expected to break down. At these very low fields, where the intervortex spacing is large compared to the vortex core size ξ , the variations in $|\psi|$ can be neglected and only the phase of the order parameter needs to be taken into account. This leads to the London limit of the GL theory [54, 67] where phase fluctuations play the important role over amplitude fluctuations in the order parameter ψ .

A more strict quantitative analysis of the range of validity of the LLL approximation has been given by Tešanović *et al.* [68]. The authors of this work have estimated that for fields $H < H_{c2}/3$ the effect of the second LL becomes relevant. Other investigations [69] suggest that the region of validity of the LLL approximation is that surrounding the H_{c2} line away from the zero field transition temperature regime. Nevertheless, in practice the LLL approximation is generally applied in situations beyond these criteria and the results are found to be qualitatively correct.

2.4 Fluctuations about the LLL Approximation

Abrikosov's [20] MFA of the GL theory argues that the $H_{c2}(T)$ field in bulk type-II superconductors (with $\kappa \gg 1$) is a line of continuous phase transitions. This work, however, neglects a rather important ingredient in the statistical physics of the problem, namely the effect of fluctuations. It was Ginzburg [35] in 1960 who first considered the effect of fluctuations about the transition temperature T_c . In his work, Ginzburg concluded that the mean field properties remain practically unchanged for bulk type-II superconductors, though they may play an important role in constrained geometries as thin films or others. Years later, more sophisticated approaches were carried out aimed at determining the nature of the transition at H_{c2} . A summary of these works is outlined below.

On the high-temperature side, where the quartic contributions to the energy functional in Eq. (2.1) are small compared to the quadratic ones, Ruggeri and Thouless (RT) [63] considered the effect of the LLL order parameter fluctuations $\delta\psi$ on the free energy. In this work, RT calculated a perturbation series of the free energy, defined analogously to the Helmholtz potential ($F = -k_B T \ln Z$, with Z the partition function in Eq. (2.2) and \mathcal{H} the LLL energy functional in Eq. (2.26)), in terms of the perturbation parameter β_κ . They performed this high-temperature series expansion in Feynman diagrams up to sixth order and used Padé approximants to extrapolate the series to low temperatures in a systematic manner. The result of their investigation is that no singularity at any finite temperature is found, indicating that the MF "transition" at H_{c2} becomes a "crossover" when order parameter fluctuations are included.

The renormalization scheme within this expansion is set up by the expression for the renormalized "mass". In three-dimensional samples, it is [63]

$$\alpha_R^{(3D)} = \alpha_H + \frac{\beta_\kappa |e| \bar{B} k_B T \sqrt{2m}}{\pi \hbar^2 \sqrt{\alpha_R^{(3D)}}}, \quad (2.53)$$

while in "two-dimensional" thin films is [63]

$$\alpha_R^{(2D)} = \alpha_H + \frac{2\beta_\kappa |e| \bar{B} k_B T}{\pi d_0 \hbar \alpha_R^{(2D)}}. \quad (2.54)$$

The use of these expressions has the advantage of reducing considerably the number of terms to every order in the perturbation series, but most importantly it “shifts” the transition temperature and makes the terms in the new series finite.

After this work, more investigations have been carried out within this renormalization scheme [70, 71] aimed at evaluating various quantities in two and three dimensions. The result is again that fluctuations in the order parameter drive the MF phase transition at H_{c2} to a crossover. In other investigation, Brezin, Nelson and Thiaville (BNT) [72] show that the high temperature renormalization procedure of this LLL free energy leads to an upper critical dimension $d_c = 6$, above which the exponents of the MFA become exact and at and below which fluctuations cannot be neglected. BNT perform expansions in $\epsilon = 6 - d$, with d the dimensionality of the sample, using a functional renormalization group (FRG) method. Their result to order ϵ is that no stable fixed point exists and this is interpreted as that fluctuations drive the continuous phase transition at H_{c2} to a first-order transition. More recent studies [73] have confirmed the absence of a stable fixed point in the FRG, although a fixed point is found when quenched random disorder is included. This is in agreement with the expectation that pinning effects may restore the continuous phase transition [74].

On the low temperature side, the pioneering work of Eilenberger [75] set up the framework for the study of fluctuations below the upper critical field H_{c2} in conventional low- T_c superconductors. In this investigation, Eilenberger considered small fluctuations $\delta\psi$ about the triangular-lattice ground state ψ_Δ of vortices. He concluded that the “mean square” $|\delta\psi|^2$ of these fluctuations becomes of the same magnitude as $|\psi_\Delta|^2$ when the applied field satisfies $(H_{c2} - H)/H_{c2} \leq 10^{-4}$ to 10^{-5} . This means that for conventional low- T_c superconductors the MFA of the GL theory is expected to break down at fields sufficiently near to H_{c2} ; though fluctuations in HTSCs are known to be much more severe. Eilenberger also showed that the triangular-lattice ground state ψ_Δ is stable against small fluctuations about H_{c2} and suggests that the vortex crystal melts at fields slightly below H_{c2} . Among more modern approaches, a non-perturbative investigation of the correlations in two-dimensional thin films in the vortex liquid regime [76] shows that the correlation length only diverges at $T \rightarrow 0$,

which implies that the vortex state remains a liquid except at zero temperature. Other investigations [77] show that thermal fluctuations in systems of dimensionality $d \leq 3$ destroy the phase coherence of the vortex state at any finite temperature. This means that if there is any vortex lattice freezing, this state must have long-range correlations of the vortex positions and density, but short-range phase coherence. If only a relevant length scale is assumed to describe both phase order and crystalline order in the system, perturbative calculations around zero temperature [78] predict zero temperature vortex-freezing at $d \leq 3$.

Chapter 3

Numerical Studies on the Spherical Thin-Film

The method we will adopt from now on for the study of superconducting properties is completely based on computer simulations and numerical calculations using generalizations of the GL-LLL model described in Sections 2.1.2 and 2.1.3.

This chapter is aimed at describing the effect of random and regular arrays of pinning centres in thin-film HTSCs, so extensions of the GL-LLL model for each case are presented and their consequences investigated. Our numerical study starts by introducing the appropriate form of the pure-system energy function suitable for numerical work. Then some relevant ground-state properties are obtained from energy minimizations. In order to go into the finite-temperature regime the simulation method is presented. This allows us to find thermal averages of many quantities of interest. An analogous treatment for the system in presence of both random and regular arrays of pinning centres is followed in subsequent sections, with special attention paid to the finite temperature properties. In this part we mainly present our results. A discussion aimed at summarising and comparing this investigation with other works is given at the end of the chapter. It is worth mentioning that most of the relevant expressions, just commented upon throughout this chapter, are derived (in general for the case of a layered system containing M layers) in Appendix A.

3.1 Clean Thin-Film

To carry out the numerical investigation of the physical properties of an ideally clean superconducting thin-film we start by defining the model we will rely on: “The thin-film superconductor with spherical geometry” as described before [79, 80, 81, 82, 83, 84, 85].

First of all we assume a superconducting spherical-shell of thickness d_0 and average radius $R \gg d_0$ in a radial magnetic field, defined by the vector potential $\mathbf{A} = (\overline{B}R^2/r) \tan(\theta/2) \hat{\phi}$, which arises from the geometrical centre of the sphere. As we suppose the film to be of a strongly anisotropic HTSC, we assume that it has a description in terms of the GL-LLL model outlined in Sections 2.1.2 and 2.1.3. In this case we can write $B = \overline{B} \approx B(R)$ across the film and use the GL-LLL energy functional in Eq. (2.35) with the scaled order parameter expanded in terms of the LLL energy eigenfunctions in the spherical geometry as

$$\tilde{\psi}_L(\theta, \phi) = \tilde{Q} \sum_{q=0}^N v_q \psi_{q,N}(\theta, \phi), \quad (3.1)$$

where $\tilde{Q} = |2\pi/\alpha_T|^{1/2}$ and $\{\psi_{q,N}\}$ is the LLL eigenspace composed by the $N+1$ orthonormal complex functions [86]

$$\psi_{q,N} = \mathcal{N}_{q,N} e^{iq\phi} \sin^q(\theta/2) \cos^{N-q}(\theta/2), \quad (3.2)$$

with the normalization factor $\mathcal{N}_{q,N} = [(N+1)C_N^q/4\pi R^2]^{1/2}$ and $C_N^q = N!/q!(N-q)!$ the binomial coefficient. By introducing the LLL expansion for the order parameter of Eq. (3.1) into the energy functional of Eq. (2.35), and calculating the integrals over the surface of the two-dimensional sphere of radius R ,¹ the energy functional of the pure system (per unit of thermal energy $k_B T$) is reduced to a function of $N+1$

¹The geometrical consideration of the scaling must be taken into account when performing the integration. This gives a factor $1/2\pi$ in front of each term which appears from the surface-element scaling $d^2\tilde{r} = \frac{1}{2\pi}d^2r$ and the fact that the LLL eigenfunctions satisfy

$$\int d^2r \psi_{p,N} \psi_{q,N}^* = \delta_{p,q},$$

with $d^2r = R^2 \sin\theta d\theta d\phi$ and $\delta_{p,q}$ the Kronecker delta function.

complex variables $(v_0, v_1, \dots, v_N) = \mathbf{v}$ given by [79]

$$\frac{\mathcal{H}_c(\mathbf{v})}{k_B T} = \alpha_T \sum_{q=0}^N |v_q|^2 + \sum_{p,q,r,s=0}^N \mathcal{W}_{pqrs} v_p v_q v_r^* v_s^* \delta_{p+q,r+s}, \quad (3.3)$$

where the subindex “c” stands for “clean” and the coefficient of the quartic term is defined as

$$\mathcal{W}_{pqrs} = \frac{(N+1)^2}{2N(2N+1)} \left[\frac{C_N^p C_N^q C_N^r C_N^s}{C_{2N}^{p+q} C_{2N}^{r+s}} \right]^{1/2}. \quad (3.4)$$

In these expressions the magnetic length $l_m = (\Phi_0/2\pi\bar{B})^{1/2}$ is taken as the unit to measure lengths and in these units $R^2 = N/2$ with N the number of magnetic vortices.

The quartic energy term can still be resummed to give the final expression for the energy function [81]

$$\frac{\mathcal{H}_c(\mathbf{v})}{k_B T} = \alpha_T \sum_{q=0}^N |v_q|^2 + \frac{1}{2N} \sum_{p=0}^{2N} |U_p(\mathbf{v})|^2, \quad (3.5)$$

where the quadratic form on the complex coefficients v_q is given as

$$U_p(\mathbf{v}) = N\gamma_{p,2N} \sum_{q=0}^N \mathcal{N}_{q,N} \mathcal{N}_{p-q,N} \Theta(p-q) \Theta(N-p+q) v_q v_{p-q}, \quad (3.6)$$

with the prefactor $\gamma_{r,s}$ defined as $\gamma_{r,s} = 2\pi/[(s+1)C_s^r]^{1/2}$ and $\Theta(x)$ the Heaviside step function: $\Theta(x) = 1$ if $x \geq 0$, and 0 otherwise. This resummation is of great use for better computer efficiency.

Equation (3.5), therefore, provides the form of the energy function of the pure superconducting-film suitable for numerical studies. In the following sections we describe our investigation on this ideally pure thin-film model.

3.1.1 Zero Temperature Properties: Numerical Calculations

The zero-temperature properties of vortices in the clean superconducting thin-film are found by minimization of the free energy in Eq. (3.5) as a function of the order parameter coefficients \mathbf{v} . We carry out the numerical minimization by using an implementation of the “*variable metric method*” (also called *quasi Newton*) given by Broyden-Fletcher-Goldfarb-Shanno as described in Ref. [87]. This method is known to find the exact minimum of a quadratic form after L line minimizations (where L is

the number of real variables the function \mathcal{H} depends upon) and uses the gradient of the function which is also provided. We rewrite the energy function of Eq. (3.5) given in terms of the complex variables \mathbf{v} to depend upon their real and imaginary parts (\mathbf{x}, \mathbf{y}) and introduce its analytic gradient calculated in Appendix A.3.3.1. In practice each run is started either with a low-energy initial configuration \mathbf{v} taken from Monte Carlo Simulations (to be described later on in this Chapter) or with a random one. After the first run the presumed minimum configuration is inserted as an initial one and the code is not stopped until the configuration no longer changes. In the case of using a random initial configuration this procedure is repeated several hundred times (depending on system size) and the configuration giving the lowest energy stored. From this we determine several other physical properties.

Basic Quantities

The physical property obtained directly from numerical minimization of $\mathcal{H}(\mathbf{v})/k_B T$ is, of course, the ground state energy. Here, and for every ground state energy product of energy minimization appearing in following sections, we use E_0 to denote the minimum of $\mathcal{H}_{\text{total}}/k_B T$ at a fixed α_T (usually -13). Therefore, E_0 in this clean thin-film superconductor is just the minimum of $\mathcal{H}_c/k_B T$ at $\alpha_T = -13$, with \mathcal{H}_c taken from Eq. (3.5). Figure 3.1(a) shows our results of E_0/N for system sizes $12 \leq N \leq 230$. We remark that the numerical values of this quantity depend on the value chosen for α_T , but no change in qualitative behaviour of the plot as a whole is observed for fixed negative α_T .

Another quantity of interest, which allows us to make contact with previous studies, is the Abrikosov ratio defined (for the thin-film) as

$$\beta_A = \frac{|\overline{\psi}|^4}{|\psi|^2}, \quad (3.7)$$

with a LLL expression taken from Eq. (A.135) at $M = 1$. Figure 3.1(b) shows the Abrikosov ratio as a function of the number of vortices, N . Our results are consistent with those of Dodgson [83] up to a small numerical discrepancy for $N > 100$. We also observe that the “magic numbers” (so called by Dodgson): 12, 32, 72, 132, ... give the

lowest energy and Abrikosov-ratio values in a small neighbourhood around them.

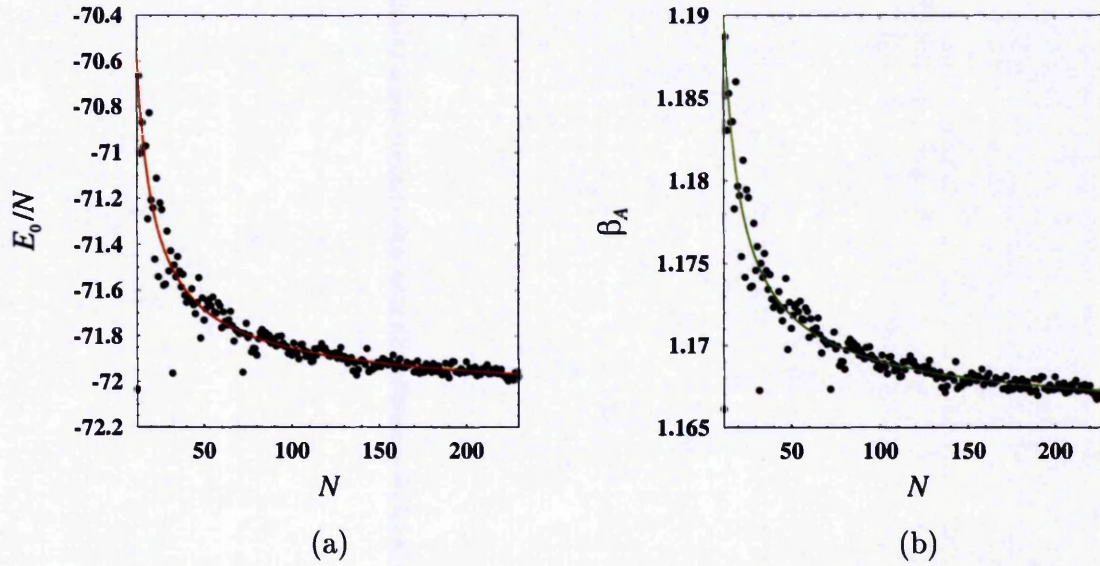


Figure 3.1: Ground-state properties of the clean thin-film superconductor with spherical geometry. [shown along with hyperbolic fits.] (a) Energy per vortex. (b) Abrikosov ratio.

In addition to these quantities, we have also calculated the average magnetization (per vortex), defined as²

$$\frac{1}{N}\mathcal{M} = \frac{4\pi R^2}{Q^2} \frac{1}{N} \overline{|\psi|^2}, \quad (3.8)$$

and the specific heat (at constant applied magnetic field and number of particles) per vortex given by

$$\frac{1}{N}C = \frac{1}{N} \frac{\partial \langle \mathcal{H} \rangle}{\partial T}. \quad (3.9)$$

Expressions in the LLL approximation for these quantities can be obtained from Eqs. (A.133) and (A.131) by dropping all indices depending on n and setting $M = 1$. It is noticeable that both the magnetization (or better to say “minus the magnetization”) and specific heat have the same qualitative behaviour as the energy ground-state and minimum Abrikosov-ratio (compare Figs. 3.2 and 3.1). In all four cases we find a

²In this definition \mathcal{M} is equal to the magnitude of the electrodynamic average magnetization $(1/\mu_0)\mathbf{B} - \mathbf{H} = \overline{\mathbf{M}}$ (taken from the first Abrikosov’s identity in Eq. (2.25)) multiplied by the factor $4\pi R^2 m/Q^2 |e|\hbar$.

satisfactory fit to the data by a power law function, with the asymptotes shifted, of the form $f(N) = A(N - N_0)^B + f_0$. (also shown in each plot.)

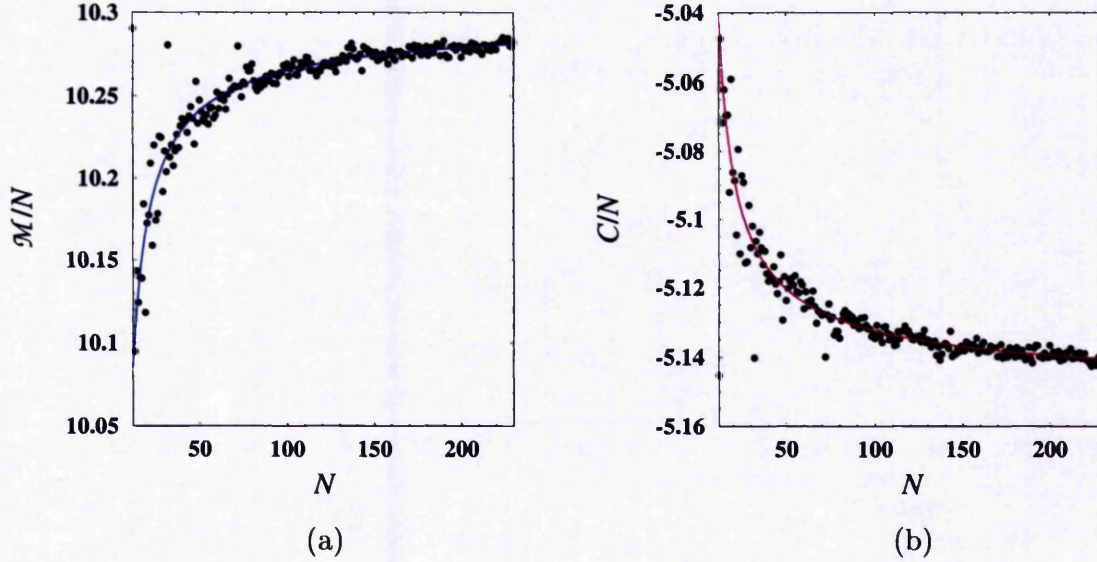


Figure 3.2: Ground-state properties of the clean thin-film superconductor with spherical geometry. [shown along with hyperbolic fits.] (a) Magnetization per vortex. (b) Specific heat per vortex.

From the nonlinear fit in each plot we determine the parameters B , N_0 and f_0 (the last giving the asymptotic values in the thermodynamic limit). In all cases the value of the exponent is $B \approx -0.70$ while $N_0 \approx 4.85$ (independent of α_T). Both the average energy and specific heat values are relative to the α_T chosen, but neither the average magnetization nor the Abrikosov ratio are. For instance at $\alpha_T = -13$ we obtain: $(E_0/N) \rightarrow -72.102 \pm 0.05446$ and $(C/N) \rightarrow -5.15014 \pm 0.003889$ as $N \rightarrow \infty$. These shall be compared to values for non-pure samples later on. The asymptotic value for the magnetization per vortex that we found is $(\mathcal{M}/N) \rightarrow 10.3003 \pm 0.007782$, and that for the Abrikosov ratio is $\beta_A \rightarrow 1.16504 \pm 0.000872$ as $N \rightarrow \infty$. This value is just between 3.9% and 5.4% greater than $\beta_{A,\min} = 1.15959527 \dots$ for a perfect triangular lattice, and is fairly consistent with the value obtained using $N \sim O(10^3)$ by Dodgson [83].

Vortex Positions on the Spherical Superconductor

The vortex positions are, by definition, the zeroes of the order parameter ψ along the whole of the mixed phase. Within the LLL approximation of the GL theory they are just the solutions to the equation³

$$\tilde{\psi}_L(\theta, \phi) = 0. \quad (3.10)$$

By taking the appropriate expressions, Eqs. (3.1) and (3.2), the equation reads

$$\tilde{Q} \cos^N(\theta/2) \sum_{q=0}^N v_q \mathcal{N}_{q,N} e^{iq\phi} \tan^q(\theta/2) = 0. \quad (3.11)$$

Here we realise that performing the change of complex variable

$$\zeta = 2R e^{i\phi} \tan(\theta/2), \quad (3.12)$$

with $\zeta = \xi + i\eta$ and R a positive real constant, the equation becomes

$$\tilde{Q} \cos^N(\theta/2) \sum_{q=0}^N a_{q,N} \zeta^q = 0, \quad (3.13)$$

where we have defined the complex coefficients $a_{q,N} = v_q \mathcal{N}_{q,N} / (2R)^q$.

Now a couple of comments on the change of complex variable in Eq. (3.12). First, from simple geometrical considerations we can identify it with the stereographic projection described in Figure 3.3. Secondly, since this stereographic projection makes the point to infinity be $\theta \rightarrow \pi$, this sets the bounds for θ as $0 \leq \theta < \pi$. Within this range and in the mixed phase the inequality: $\tilde{Q} \cos^N(\theta/2) \neq 0$ holds. Therefore the vortex positions simply become the roots of the polynomial $\sum_{q=0}^N a_{q,N} \zeta^q$. Notice, however, that $\zeta = \xi + i\eta$ is a point on the complex plane $\xi-\eta$, and not on the sphere. To be able to locate the vortex positions on the sphere we just reverse the stereographic projection. That is, we apply the inverse transformation of Eq. (3.12), which can be

³This is equivalent to finding the solutions of

$$\psi_L(\theta, \phi) = 0,$$

as $\tilde{\psi}$ and ψ differ only in a nonzero factor for finite temperatures below the upper critical field.

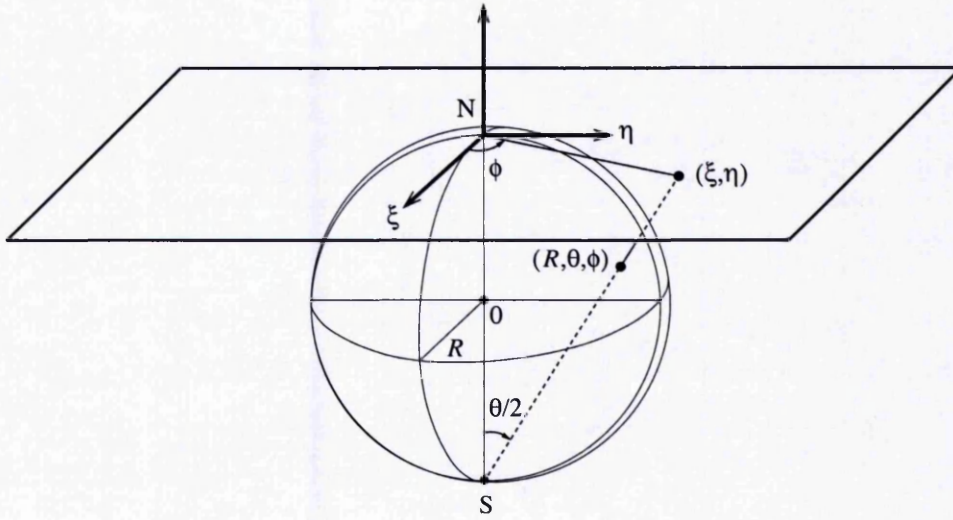


Figure 3.3: Stereographic projection with respect to the south pole, S.

written as

$$\phi = \arctan(\eta/\xi), \quad (3.14)$$

$$\theta = 2 \arctan(\sqrt{\xi^2 + \eta^2}/2R). \quad (3.15)$$

By using a numerical routine to find roots of polynomials with complex coefficients based on the *Method of Laguerre* [87] we obtain the vortex positions on the clean thin-film superconductor for system sizes $12 \leq N \leq 230$. As in the work of Dodgson [83] we find that at zero temperature the vortices stay on the vertices of the highly symmetric polyhedra (projections on the sphere of the icosadeltahedra)⁴ but only for $N(p, q) = 10(p^2 + pq + q^2) + 2$ with $p, q = 1, 2, \dots$ (with the exception of $N(1, 0) = 12$). Examples of these (for $q = 1, p = 0, 1, 2, \dots$) are shown in Fig. 3.4. Although Dodgson [83] suggests that the ground states of system sizes $N(p, 0)$, $p = 2, 3, \dots$ should have icosahedral symmetry, we find examples in this set ($N = 42, 92, 162$, etc.) with no icosahedral symmetry which have lower energy than the icosahedrally

⁴The icosadeltahedra are polyhedra composed of equilateral triangles which contain 12 five-fold vertices located at the vertices of an icosahedron (shown in Fig. 3.4(a)). This is commonly called icosahedral symmetry. From geometrical arguments one can see that these polyhedra have exactly $F(p, q) = 20(p^2 + pq + q^2)$ triangular faces (previously noticed by Dodgson) and $E(p, q) = 30(p^2 + pq + q^2)$ edges.

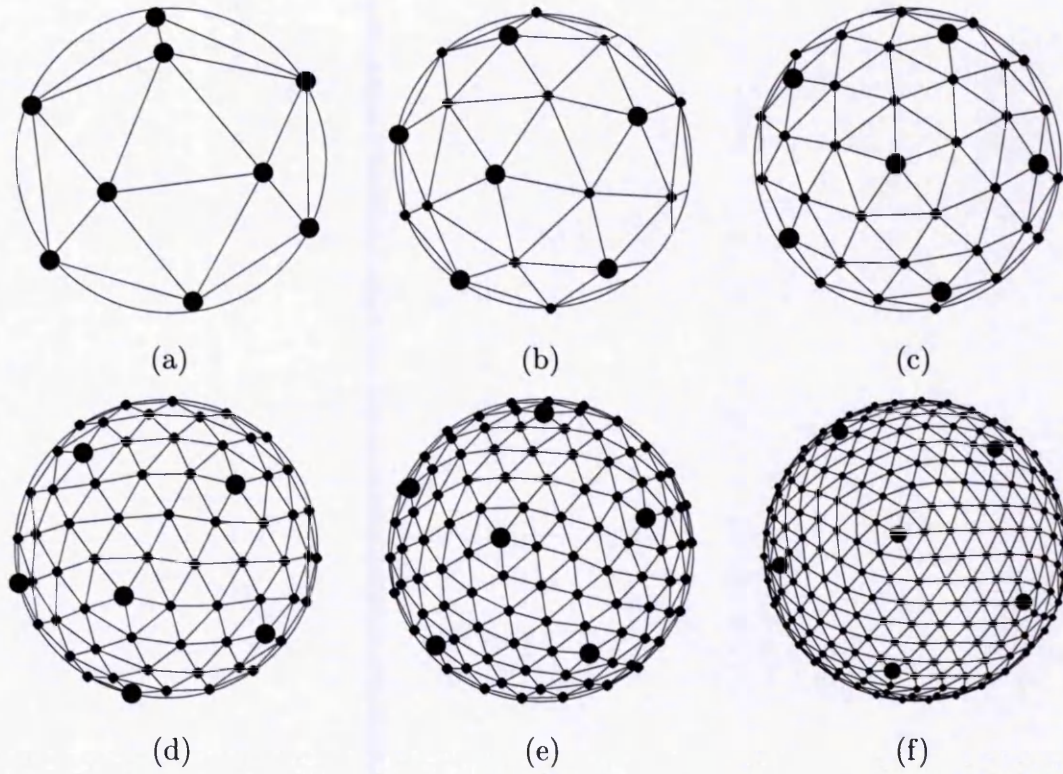


Figure 3.4: Ground-state vortex positions of the spherical thin-film HTSC without disorder for system sizes $N(p, 1)$. (a) $N(0, 1) = 12$. (b) $N(1, 1) = 32$. (c) $N(2, 1) = 72$. (d) $N(3, 1) = 132$. (e) $N(4, 1) = 212$. (f) $N(6, 1) = 432$. (Notice the icosahedral symmetry.)

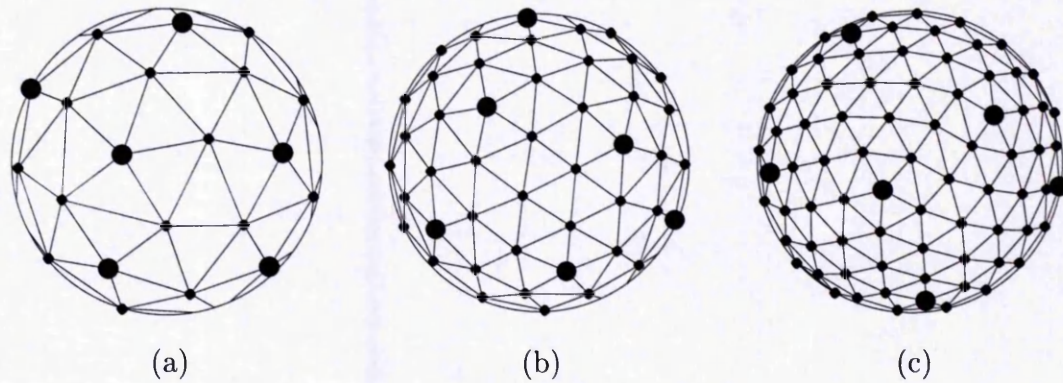


Figure 3.5: Ground-state vortex positions of the spherical thin-film HTSC without disorder for system sizes $N(p, 0)$. (a) $N(2, 0) = 42$. (b) $N(3, 0) = 92$. (c) $N(4, 0) = 162$. (Notice the absence of icosahedral symmetry.)

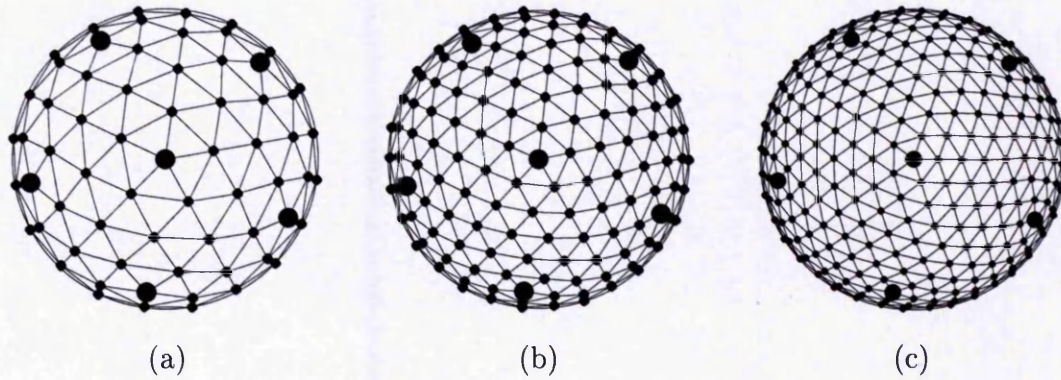


Figure 3.6: Ground-state vortex positions of the spherical thin-film HTSC without disorder for system sizes $N(p, p)$. (a) $N(2, 2) = 122$. (b) $N(3, 3) = 272$. (c) $N(4, 4) = 482$. (Notice the icosahedral symmetry.)

symmetric ones (see Figure 3.5). This suggests that the ground states of *all* system sizes $N(p, 0)$, $p = 2, 3, \dots$ are not projections on the sphere of the icosadeltahedra.

On the other hand, we can still find ground states of system sizes $N(p, p)$, $p = 2, 3, \dots$ for which the icosahedral symmetry is reestablished (i.e. no other state without icosahedral symmetry found has lower energy). This is shown in Fig. 3.6. Systems sizes in this set, however, do not have significantly lower energy-values than nearby N as shown in Fig. 3.1(a). All these results (when seen from plots of E_0/N or β_A in Fig. 3.1(a,b)) seem to indicate that the only magic numbers $N(p, q) = 10(p^2 + pq + q^2) + 2$ with the optimum properties (i.e. “much lower” energy than several neighbouring N , as the isolated points in Fig. 3.1.) are just those with $N(p, 1)$, $p = 0, 1, 2, \dots$. This could explain why system sizes other than these (irrespective of whether the ground state is icosahedrally symmetric or not) fail to give significantly lower Abrikosov ratio (or E_0/N) than nearby N .

Other Quantities

In addition to finding the vortex positions on the sphere, we have also looked at the stereographic projection of such points (see Figure 3.7). In these plots the origin $(\xi, \eta) = (0, 0)$ and the unit circle $\xi^2 + \eta^2 = 1$ are projections of the north pole “N” and equator of the sphere as shown in Figure 3.3.

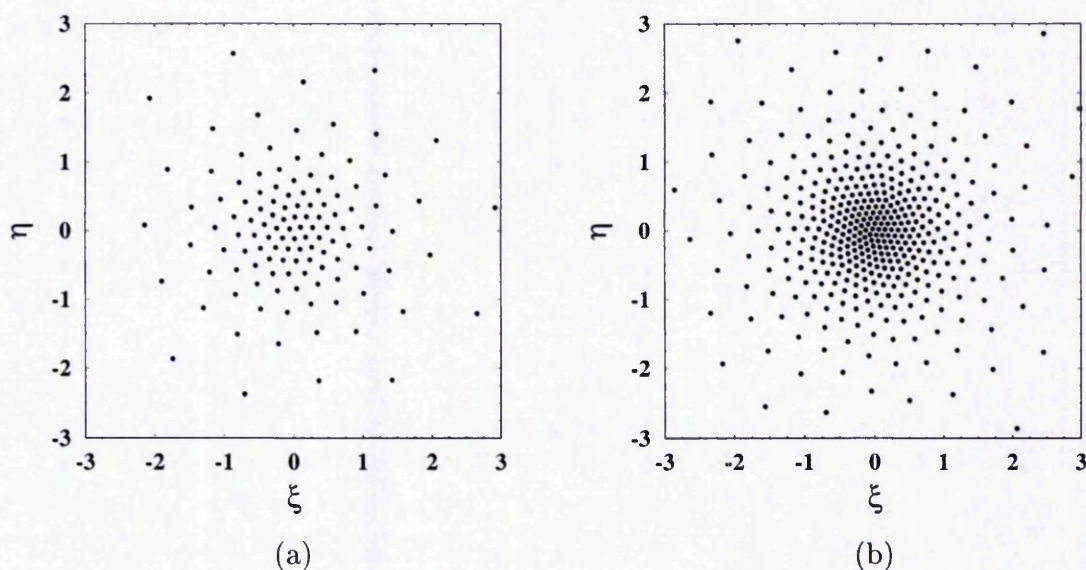


Figure 3.7: Stereographic projection of the vortex positions in the ground state of the clean thin-film superconductor. (a) For $N = 132$. (b) For $N = 432$.

By calculating the density-density correlation function in momentum space of the projected points we are able to determine the structure factor defined as [60]

$$S(\mathbf{k}) = \frac{1}{N} \left\langle \sum_{i,j=1}^N e^{-i\mathbf{k} \cdot (\mathbf{x}_i - \mathbf{x}_j)} \right\rangle, \quad (3.16)$$

where $\{\mathbf{x}_i = (\xi_i, \eta_i)\}$ are the positions (on the stereographic plane) of the N “particles” composing the medium. For two-dimensional systems this function is commonly plotted as a contour plot on the k_x - k_y plane. Here we have chosen to parametrise the wave vector \mathbf{k} using polar coordinates so that $\mathbf{k} = (k_x, k_y) = (k \cos \phi, k \sin \phi)$. In practice we discretize both variables k and ϕ so as to obtain the structure factor at each point of the grid $\mathbf{k}_{r,s} = (k_r \cos \phi_s, k_r \sin \phi_s)$, with $r = 1, 2, \dots, N_k$ and $s = 1, 2, \dots, N_\phi$. We have chosen $(N_k, N_\phi) = (1000, 192)$ for high resolution graphics and $(N_k, N_\phi) = (100, 48)$ for lower resolution, with wave-vector magnitudes $0 \leq k \leq 10$. (and azimuth angle-range $0 \leq \phi < 2\pi$.)

In addition to the structure factor, $S(\mathbf{k})$, we have defined a rotationally averaged structure function as

$$\Delta(k) = \frac{1}{2\pi} \int_0^{2\pi} d\phi S(\mathbf{k}), \quad (3.17)$$

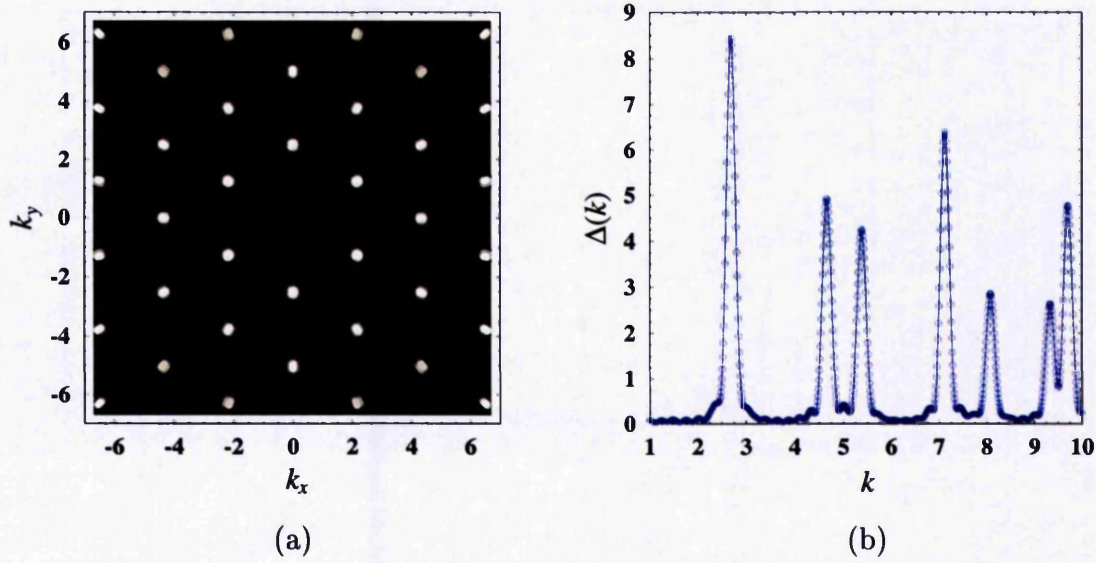


Figure 3.8: Scattering for a perfect triangular-lattice of $N = 100$ sites and lattice spacing $(4\pi/\sqrt{3})^{1/2}$. (a) Structure factor. (b) Rotationally averaged structure function. [shown along with spline fit.]

with a discrete expression given in terms of $\mathbf{k}_{r,s}$ (above) and the angular average replaced by $(1/N_\phi) \sum_{s=1}^{N_\phi}$. Both of these structure functions have, in general, a “spiky” (or oscillating) form reaching local maxima at the reciprocal lattice vectors (or magnitudes) when a lattice is observed. These are usually referred to as Bragg-peaks. Here, as a pattern to compare the results of our investigations, we present plots of the structure functions $S(\mathbf{k})$ and $\Delta(k)$ for a perfect triangular lattice of spacing $(4\pi/\sqrt{3})^{1/2} \approx 2.693547$ with $N = 100$ lattice sites (see Figure 3.8). Notice that in both figures we have omitted the peak at $\mathbf{k} = \mathbf{0}$ (the 0th peak). This is a common practice that will be used throughout this work. We will also be concentrating on the first non-zero peak (the first peak), which is represented by the central hexagonal spots in Figure 3.8(a) and the first local maximum of $\Delta(k)$ (appearing at $k \approx 2.693547$) in Fig. 3.8(b).

For our problem of vortices on the sphere we expect a rather complex structure factor if all points on the stereographic projection are included. However, if only

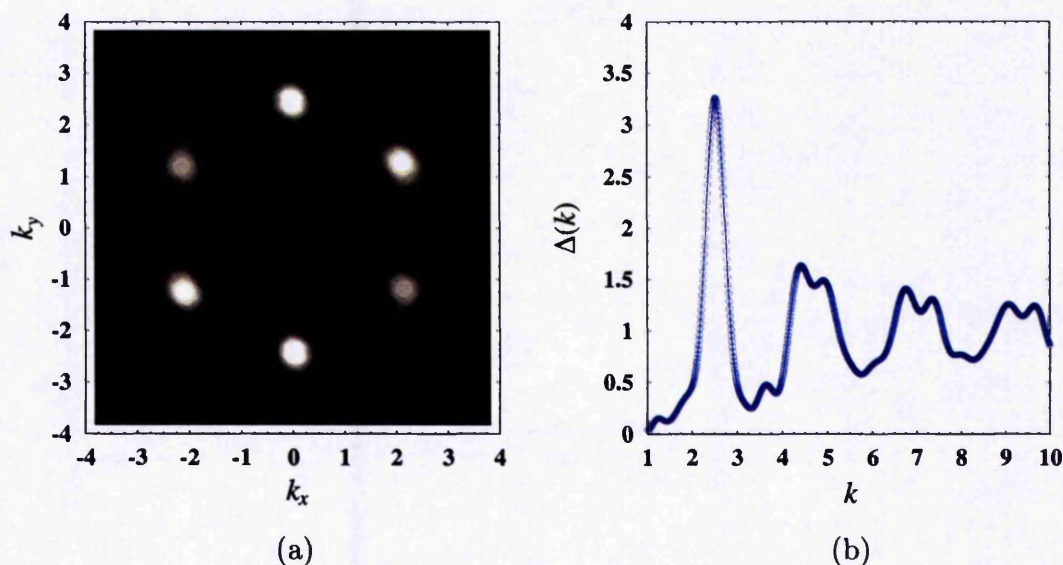


Figure 3.9: Scattering on the ground-state vortex positions (on stereographic projection) of the clean thin-film superconductor with spherical geometry for $N = 132$ vortices. (a) Structure factor. (b) Rotationally averaged structure function. [shown along with spline fit.]

projections of points near the north pole are considered, we expect a regular (quasi-hexagonal) ordering of the vortices for N sufficiently large. Figure 3.9 illustrates this fact by showing the ground state structure functions calculated on the points inside the square of side 0.8 about the origin in Figure 3.7(a).⁵ This section of the stereographic projection contains about $N/6$ vortices spaced almost homogeneously. For every system studied ($N = 12, 13, \dots, 230$) we find the same type of quasi-hexagonal ordering (with the twelve necessary disclinations from Euler's theorem [88], i.e. vortices with only five nearest neighbours). Sharper peaks on both $S(\mathbf{k})$ and $\Delta(k)$ are observed when less disclinations fall inside the square about the origin used to calculate the structure factor (and also as system size increases). This result appears consistent with the expected vortex lattice at $T = 0$ which should be perfectly triangular when $N \rightarrow \infty$.

⁵In fact after considering only points inside this square we have performed a scale transformation on the vortex positions, $\mathbf{x}'_i = b\mathbf{x}_i$, with b chosen so as to give an intervortex separation $\sim (4\pi/\sqrt{3})^{1/2}$. This makes the magnitude of the first reciprocal lattice vector to be approximately equal to the scaled intervortex separation, $(4\pi/\sqrt{3})^{1/2}$.

3.1.2 Finite Temperature Properties: Computer Simulations

The finite temperature properties of vortices in superconductors are found by numerical simulations. Throughout the whole of this thesis we use repeatedly the *Monte Carlo method* [89] under the *Metropolis algorithm* [90] for the different systems considered, so we shall describe this technique below. In this case we consider the pure thin-film superconductor (with spherical geometry), where a description in terms of the GL-LLL Hamiltonian as a function of the complex coefficients $\{v_q\} \equiv \mathbf{v}$ (as described in Section 3.1) is appropriate.⁶

We start by remarking that the aim in many problems of statistical physics, particularly of superconductivity, is to find the value of several thermodynamic variables: energy, magnetization, etc., whose thermal averages are defined in Eq. (2.3), and that within the LLL approximation read

$$\langle X(T, \mathbf{H}) \rangle = \frac{1}{Z(T, \mathbf{H})} \int \prod_{q=0}^N dv_q dv_q^* X(\mathbf{v}; T, \mathbf{H}) \exp[-\mathcal{H}(\mathbf{v})/k_B T], \quad (3.18)$$

where the partition function $Z(T, \mathbf{H})$ is given by

$$Z(T, \mathbf{H}) = \int \prod_{q=0}^N dv_q dv_q^* \exp[-\mathcal{H}(\mathbf{v})/k_B T]. \quad (3.19)$$

The Monte Carlo method in statistical physics provides a numerical solution to finding the value of such thermodynamic observables by accounting only of those configurations \mathbf{v} in phase space which contribute the most to the partition function, Eq. (3.19), and the thermal average itself. This technique is known as *importance sampling* and the set of states $\{\mathbf{v}\}$ in which the system spends most of its time are those describing thermodynamic equilibrium.

The problem for the Monte Carlo method turns out to find a way to generate those states \mathbf{v} describing thermodynamic equilibrium. Fortunately a rather straightforward solution is possible which makes use of a *Markov process* (i.e. a mechanism which,

⁶In a more general case, when extra energy terms for the pinning interactions studied in this thesis are added, the arguments of this section still hold (with \mathcal{H} denoting the total energy). For the layered system the only difference is that the number of complex coefficients gets multiplied by the number of layers. In that case $\mathbf{v} \equiv \{v_{n,q}\}$ (as described in Chapter 4) but the simulation method remains unchanged.

given a system in one state $\mathbf{v}_\mu \equiv \mu$, generates a new state $\mathbf{v}_\nu \equiv \nu$ of that system in a random fashion). The probability of generating the state ν given μ is called the *transition probability* $P(\mu \rightarrow \nu)$ for the transition from μ to ν . For a legitimate Markov process all the transition probabilities should depend only on the properties of the current states μ and ν , and not vary over time. They must also satisfy the normalization property

$$\sum_{\nu} P(\mu \rightarrow \nu) = 1. \quad (3.20)$$

This Markov process should be used repeatedly to generate a *Markov chain* of states: $\mathbf{v}_\mu, \mathbf{v}_{\mu+1}, \mathbf{v}_{\mu+2}, \dots$. For this Markov process to produce the correct succession of states appearing with probabilities given by the Boltzmann distribution, two further conditions are required on it. One, the *condition of ergodicity*, is the requirement that it should be possible for our Markov process to reach any state of the system from any other state. This implies that there must be at least one path of non-zero transition probabilities between any two states, even if in the rest of the possible paths the transition probabilities are zero. The other is called the *condition of detailed balance*

$$p_\mu P(\mu \rightarrow \nu) = p_\nu P(\nu \rightarrow \mu), \quad (3.21)$$

where $p_\mu = (1/Z)e^{-\mathcal{H}(\mathbf{v}_\mu)/k_B T}$ are the equilibrium occupation probabilities in the canonical ensemble (i.e. the probability to find the system in the state \mathbf{v}_μ). This ensures that it is the Boltzmann probability distribution which is generated after the system has come to equilibrium rather than any other distribution. The condition in Eq. (3.21) and the normalization property of Eq. (3.20) do not specify the transition probability uniquely. The choice often used in Monte Carlo simulations, which is the one we implement here, is the Metropolis algorithm: A subsequent state, $\mathbf{v}_{\mu+1}$, is chosen from a state \mathbf{v}_μ by changing one or more vortex coefficients. The probability that the system is allowed to move from μ to $\mu + 1$ is

$$P(\mu \rightarrow \mu+1) = \begin{cases} 1 & \text{if } \delta\mathcal{H} \leq 0, \\ e^{-\delta\mathcal{H}/k_B T} & \text{if } \delta\mathcal{H} > 0. \end{cases} \quad (3.22a)$$

$$(3.22b)$$

where $\delta\mathcal{H} = \mathcal{H}(\mathbf{v}_{\mu+1}) - \mathcal{H}(\mathbf{v}_\mu)$. In practice we change one complex coefficient at a time, $v_j \rightarrow v_j + \varepsilon$, and calculate the energy difference. If $\delta\mathcal{H} \leq 0$ we accept

the move and change the coefficient. If $\delta\mathcal{H} > 0$ we may still accept the move. The Metropolis algorithm tells us to change the coefficient with probability $P(\mu \rightarrow \mu+1) = e^{-\delta\mathcal{H}/k_B T}$. This can be achieved by evaluating the transition probability $e^{-\delta\mathcal{H}/k_B T}$ and then choosing a random number r between zero and one, $0 \leq r < 1$. If $r < e^{-\delta\mathcal{H}/k_B T}$ then we accept the change. If not, we keep our coefficient v_j unchanged; and that is the complete algorithm. Now we just keep on repeating the same calculations over and over again, choosing a coefficient, calculating the energy difference and then deciding whether to change it according to Eqs. (3.22). Here we define 1 Monte Carlo step (MCS) as $N + 1$ of those attempted moves (i.e. to the update of all the vortex coefficients v_j in the system) and choose the change of coefficient ε as a random number with real and imaginary parts between $-\tau$ and τ , where $\tau > 0$ is chosen so as to accept half of all MCS in each run.

To ensure that our Markov process has already generated a set of states $\{\mathbf{v}\}$ distributed according to the Boltzmann distribution (or in other words the system has reached equilibrium) we neglect the first 1/3 MCS in each run. (i.e. after each variation of α_T .) Then we use the remaining 2/3 MCS for measurements. We also supply the final configuration in each run as the initial for the next one. This helps the system in reaching equilibrium faster. Measurements are taken at constant intervals of MCS (usually ≥ 100) when the correlations between states \mathbf{v}_μ in the Markov chain (separated by a finite “distance”) have died out. We have chosen to update the vortex coefficients v_j randomly, which is more time-consuming than doing it sequentially but better in terms of avoiding spurious correlations.

This way we have made measurements of several physical quantities for each of the thin-film systems presented throughout Chapter 3. Normally we sampled the interval of effective temperatures $-13 \leq \alpha_T \leq 2$ (while cooling) with runs up to 7.68×10^6 MCS. The results of these measurements are presented in the following sections.

Fundamental Properties

In order to test our simulation codes we calculate thermal averages of basic properties such as energy, Abrikosov ratio, magnetization, etc., as functions of the effective

temperature parameter α_T . We obtain those quantities for the clean thin-film superconductor at system sizes $N = 72, 132, 432$. Figure 3.10 shows the “normalized” average energy, average Abrikosov ratio, and average magnetization per vortex as defined in Section 3.1.1 (for the different system sizes simulated). In this context (of finite temperature properties) we use E_0 to describe a normalization constant to the average energy $\langle E \rangle = \langle \mathcal{H}_c \rangle$ (also called internal energy in thermodynamics). E_0 is just the total energy function, \mathcal{H}_c , evaluated at the ground-state order parameter $\psi^{(0)}$ and the lowest α_T used in all simulations (usually -13). Therefore the quantity plotted in Fig. 3.10(a) is (up to a constant factor) the internal energy of the system. We observe a “parabolic” behaviour of this quantity with no appreciable system-size dependence, which should be contrasted with Eq. (2.28). [easily seen to be proportional to $-(\alpha_T)^2/\beta_{A,L}$ by the use of Eq. (2.34).] The dependence on α_T of the LLL-Abrikosov ratio, $\beta_{A,L}$, blurs the precise power of α_T appearing on the average energy. However, the analytic behaviour of $\langle \beta_A \rangle$ (as a function of α_T) and the fact that it is always positive (see Fig. 3.10(b)) confirms that $\langle E \rangle$ should not present singularities.⁷ Moreover, since $\langle \beta_A \rangle$ tends to a constant value for low enough temperatures, then we expect $\langle E \rangle \sim -(\alpha_T)^2$ in the limit of zero temperature, $\alpha_T \rightarrow -\infty$.

The Abrikosov ratio is an intensive quantity which varies between $\beta_{A,\min} = 1.15959527 \dots$ and 2. For small values, about its lower limit, it describes an order parameter with zeroes relatively evenly spaced which can be associated with a vortex lattice (perfectly triangular when $\langle \beta_A \rangle = \beta_{A,\min}$). For “considerably higher” values long-range correlations between vortex positions no longer exist, and this is usually interpreted as a vortex liquid state. Though this idea seems qualitatively natural, the value of $\langle \beta_A \rangle$ at which a phase transition should occur appears much less intuitive. We believe this value indeed exists, but must depend on each particular model (and approximations used, of course). For instance, we observe a rather close qualitative-behaviour of our plot of $\langle \beta_A \rangle$ in Fig. 3.10(b) with the “generalized Abrikosov ratio” of Ref. [76] (not shown) which appears from a diagrammatic resummation in the same thin-film model. Small numerical discrepancies can be noted (specially at low

⁷One should be careful with the change in sign of quantities like $\langle E \rangle$ because normalization “factors” depending on α_T might create spurious singularities.

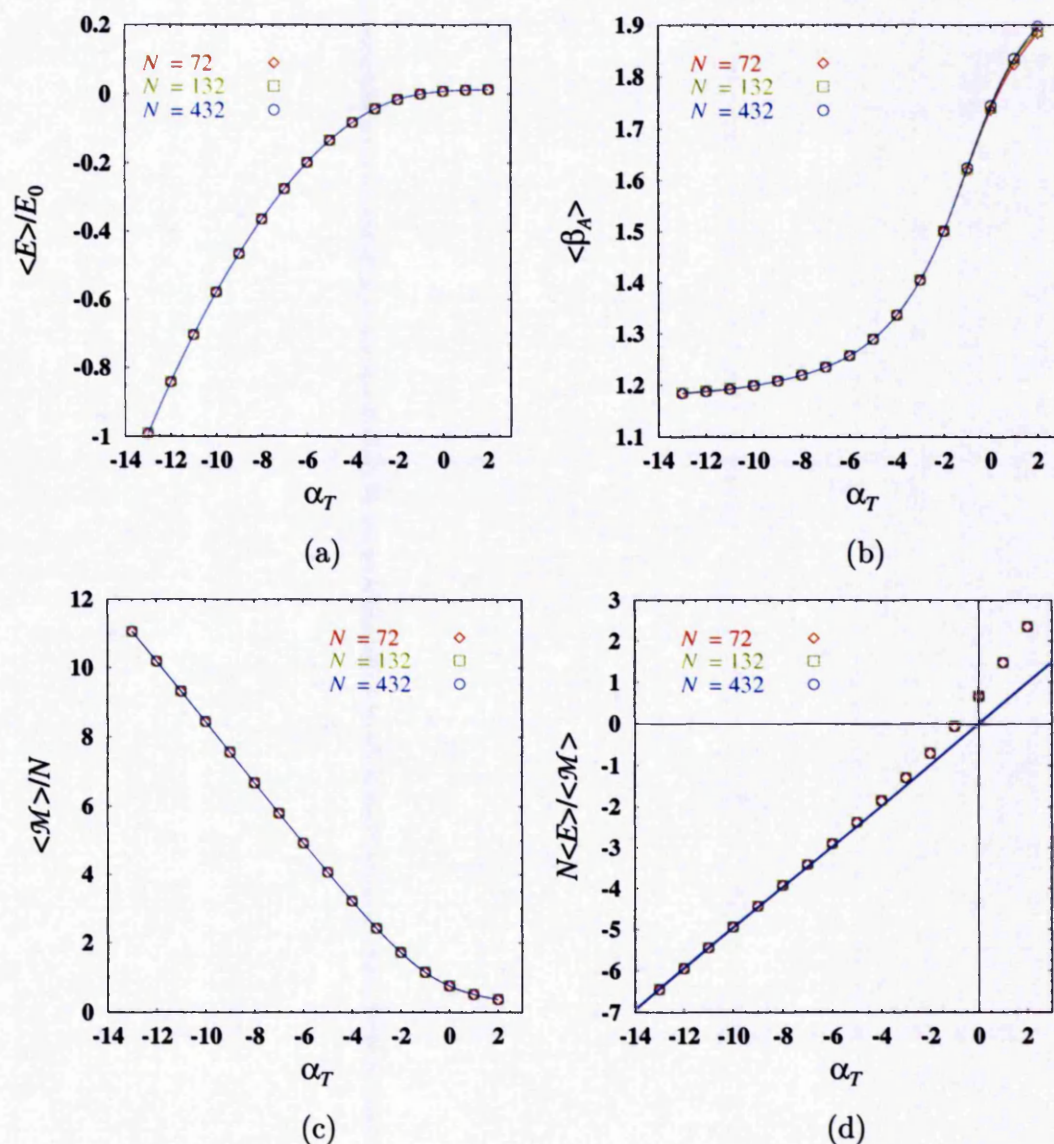


Figure 3.10: Finite-temperature properties of the clean thin-film superconductor with spherical geometry. (a) Normalized average energy. (b) Abrikosov ratio. (c) Magnetization per vortex. (d) Average energy divided by the magnetization per vortex. [(a,b,c) shown along with spline fits and (d) with linear fits for values of $\alpha_T \leq 10$.]

temperatures) which, we believe, arise from the difference in approximations.

Because of the way we have chosen to define the magnetization (per vortex), Eq. (3.8) and its LLL expression taken from Eq. (A.133), \mathcal{M}/N differs from $|\overline{\psi_L}|^2$ only by a constant factor. By using results from the end of Section 2.1.2 (and the relationship between α_H and α_T , Eq. (2.34)) it can be shown that $|\overline{\psi_L}|^2 \sim -\alpha_T/\beta_{A,L}$ (for $\alpha_T \leq 0$). The linear behaviour of our plot of $\langle \mathcal{M} \rangle/N$ at low temperatures (when β_A is tending to a constant) in Fig. 3.10(c) is in agreement with this. Though the intercept with the α_T -axis is expected at 0, this is not yet achieved for the range of temperatures investigated (the reason being that β_A is still decreasing considerably, even at $\alpha_T \sim -13$). An alternative way to see that (0,0) should lie on the asymptotic line of $\langle \mathcal{M} \rangle/N$ (as $\alpha_T \rightarrow -\infty$) appears by plotting the ratio of $\langle E \rangle$ to $\langle \mathcal{M} \rangle/N$ as a function of α_T . The dependence of this ratio on α_T is expected to be linear (see the end of Section 2.1.2) and independent of β_A . We find that a linear fit to the low-temperature values of this quantity is appropriate and gives the correct intercept at 0 (see Fig. 3.10(d)). With all this we see that the LLL analytical-forms of the energy and magnetization are recovered and therefore the ground-state properties regained in the limit $\alpha_T \rightarrow -\infty$. Moreover, we find all these quantities continuous and smooth at all values of $-13 \leq \alpha_T \leq 2$, in agreement with the lack of a phase transition at a non-zero finite temperature. This should be contrasted with results on the system with quasi-periodic boundary conditions: Kato and Nagaosa [91] report a weakly first order melting transition at $\alpha_{T,m} \approx -9.9$ which they deduce from a jump in the “normalized” internal energy and analysis of the structure factor. Hu and MacDonald [92] can also observe a first order melting transition, but at a higher temperature $\alpha_{T,m} \approx -9.3$. Strong evidence, in this case, appears from the double peak structure in the energy distribution function with increasing of peak heights as the system size increases. The structure factor also shows liquid-like correlations above the transition but Bragg peaks below $\alpha_{T,m}$.

Analysis of Structure

The structure factor reveals vortex motion as in a liquid even at low temperatures. In Fig. 3.11 we show contour plots of the structure factor, $S(\mathbf{k})$, at low temperatures for the pure system with $N = 132$ vortices. It can be observed the ring that characterises liquid-like correlations for $\alpha_T \geq -11$, and a sudden appearance of “hexatic-like” order at $\alpha_T = -12$ (marked by the appearance of quasi-Bragg peaks in the structure factor). Though this could be interpreted as the beginning of a freezing transition (as the temperature is lowered), we believe this apparent “breaking of ergodicity” is the effect of averaging over a not large-enough number of MCS for these low temperatures (where correlations between different states of the Markov chain are not negligible and therefore the system has not reached equilibrium). Each plot is obtained after a total of 2.4×10^5 MCS (thermalizing through the first 0.8×10^5 MCS, and averaging over the remaining 1.6×10^5 MCS). The authors of Ref. [91] have estimated a relaxation time of $2\text{--}5 \times 10^5$ MCS (which should increase with decrease of temperature). The upper bound of their result can be used to explain the quasi-Bragg peaks in Figs. 3.11(e) and 3.11(f) as effects of a not complete system-relaxation.

A quantitatively more rigorous way to show that the vortex phase remains a liquid down to low enough temperatures appears by plotting the density-density correlation length, ξ_D , as a function of α_T . As previously indicated [83], if a Lorentzian gives an accurate fit to the the first non-zero peak of the structure function $\Delta(k)$ (which is consistent with an exponential decay of density-density correlations in real space) then $\xi_D \sim \delta^{-1}$, where δ is the width of the peak at half its maximum.⁸ Figure 3.12 shows plots of the rotationally averaged structure function, $\Delta(k)$, at low temperatures (with a Lorentzian fit about the peak) and the extracted density correlation length. The Lorentzian function, defined as $L(k) = A\delta^2/[\delta^2 + 4(k - k_1)^2]$ (reaching its maximum value of A at $k = k_1$), clearly gives a proper fit to the first peak of $\Delta(k)$. The extracted

⁸The proof of this is straightforward. By calculating the Fourier transform of the symmetric Lorentzian-function, $L_s(k) = A\delta^2/[\delta^2 + 4k^2]$, one obtains $\tilde{L}_s(x) = (\pi/32)^{1/2} A\delta \exp(-x/2\delta^{-1})$. Then assuming $A \propto \delta^{-1}$ (which has been consistently shown before [80, 83, 85] and is also observed in our simulations) the required result, $\tilde{L}_s(x) \sim \exp(-x/2\delta^{-1})$, follows.

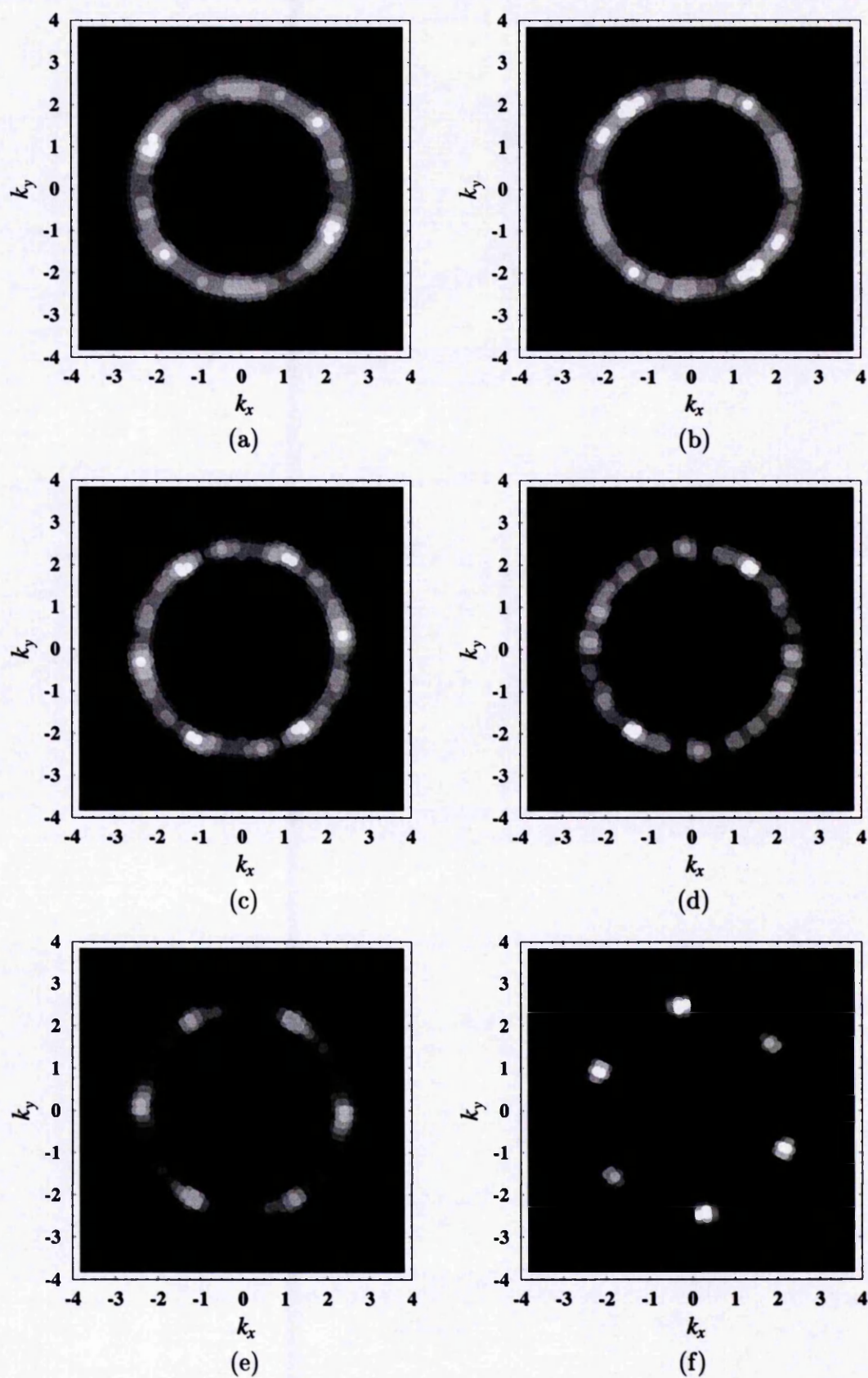


Figure 3.11: Structure factor of the clean thin-film HTSC for $N = 132$ vortices as the temperature is lowered: $\alpha_T = -8, -9, -10, -11, -12, -13$. [(a,b,c,d,e,f) respectively.]

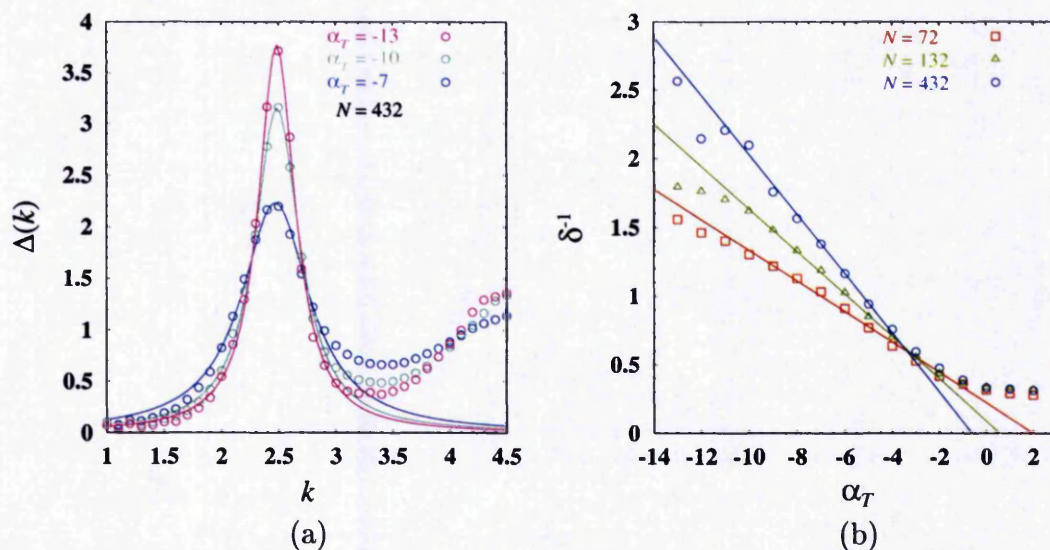


Figure 3.12: Density-density correlations for the clean thin-film HTSC as the temperature is lowered. (a) First peak of the rotationally averaged structure function (with Lorentzian fits) for the system with $N = 432$ vortices. (b) Extracted density correlation length, $\delta^{-1} \sim \xi_D$, (with linear fits) for all system sizes investigated.

density correlation length in Fig. 3.12(b) depends on system size but in all cases can be seen to increase linearly with $|\alpha_T|$ (diverging only when $\alpha_T \rightarrow -\infty$). This gives the same temperature dependence of ξ_D found since the work of O'Neill and Moore [79] for this thin-film model (consistent with a vortex liquid phase extending to all finite temperatures).

There is just one point that should be emphasized. In previous studies on the sphere different definitions of the “rotationally averaged structure function”, $\Delta(k)$, have been used (compare Eqs. (3.16) and (3.17) with their equivalent in Refs. [80], [83] or [85]). In the previous studies a “generalized” Fourier transform was defined so as to obtain the density-density correlation function in a “generalized” reciprocal space. In our case we used the usual Fourier transform and reciprocal space. This induced extra finite-size effects which can be observed in the early “splitting” of the lines $\delta^{-1}(\alpha_T)$ at $\alpha_T > -4$ (while in Ref. [83] the same effect appears about $\alpha_T = -8$). However, in the course of our investigation we became aware that none of the definitions of $S(\mathbf{k})$

in Refs. [80], [83] and [85] reproduce the six-fold Bragg-peaks expected for a “quasi-triangular lattice” (which should be the case in the ground state of the spherical geometry), and therefore we preferred to avoid using any of them. Our definition is expected to work efficiently for large enough systems ($N \sim 10^3$).

3.2 Pinning Due to Random Disorder

In this section we set up the theoretical framework for the consideration of pinning centres at random positions on the thin-film superconductor with spherical geometry introduced in Section 3.1. Afterwards we describe the implications of such random potential. As previously done by Moore and Newman [73], and Kienappel and Moore [84] we assume that pinning effects due to random disorder can be described, in general, by adding an extra energy-term to the original GL energy functional in Eq. (2.1). Within the thin-film limit this takes the form⁹

$$\mathcal{H}_{\text{rd}}[\psi; \Omega] = d_0 \int d^2r \Omega(\mathbf{r}) |\psi(\mathbf{r})|^2, \quad (3.23)$$

where the subindex “rd” stands for “random disorder” and $\Omega(\mathbf{r})$ is a real generalized-function, having a Gaussian distribution, which satisfies

$$\langle \Omega(\mathbf{r}) \rangle_{\text{dis}} = 0, \quad (3.24)$$

$$\langle \Omega(\mathbf{r}) \Omega(\mathbf{r}') \rangle_{\text{dis}} = \Delta_0 \delta(\mathbf{r} - \mathbf{r}'), \quad (3.25)$$

with $\langle \dots \rangle_{\text{dis}}$ representing an average over disorder. Here $\delta(\mathbf{r} - \mathbf{r}')$ is the two-dimensional Dirac delta function and Δ_0 a real parameter that measures the strength of the disorder.

In general the distribution Ω , on the spherical geometry, can be expanded in terms of the spherical harmonics $Y_l^m(\theta, \phi)$ with complex coefficients a_l^m drawn from a

⁹In the case of using the LLL scaled quantities this energy contribution becomes

$$\mathcal{H}_{\text{rd}}[\tilde{\psi}_L; \tilde{\Omega}] = d_0 \int d^2r \tilde{\Omega}(\mathbf{r}) |\tilde{\psi}_L(\mathbf{r})|^2,$$

with the order parameter $\tilde{\psi}_L$ given in Eq. (3.1) and all the other expressions, Eqs. (3.24)–(3.29), keeping the same form but with Q replaced by $\tilde{Q} = |2\pi/\alpha_T|^{1/2}$.

random Gaussian distribution as¹⁰

$$\Omega(\theta, \phi) = \frac{k_B T}{d_0 Q^2} \sum_{l=0}^{\infty} \sum_{m=-l}^l a_l^m Y_l^m(\theta, \phi), \quad (3.26)$$

and the conditions on the distribution Ω (being real, with a Gaussian distribution, zero mean, etc.) can be fully satisfied by imposing the following constraints on the expansion coefficients

$$a_l^{m*} = (-1)^m a_l^{-m}, \quad (3.27)$$

$$\langle a_l^m \rangle_{\text{dis}} = 0, \quad (3.28)$$

$$\langle a_l^m a_{l'}^{m'*} \rangle_{\text{dis}} = \sigma^2 \delta_{l,l'} \delta_{m,m'}, \quad (3.29)$$

which are valid for all $l = 0, 1, \dots$ and $-l \leq m \leq l$, with the variance of the coefficients a_l^m given by $\sigma^2 = (d_0 Q^2 / k_B T)^2 \Delta_0$.

The LLL-limit can be accounted by the substitution of the LLL order parameter in the spherical geometry, Eq. (2.24), and the spherical-harmonic expansion of the distribution Ω , Eq. (3.26), into the random disorder energy contribution, Eq. (3.23). By performing the integration over the sphere of radius R we obtain the random disorder energy contribution (per unit of thermal energy $k_B T$) given by

$$\frac{\mathcal{H}_{\text{rd}}(\mathbf{v}; \mathbf{a})}{k_B T} = \sum_{q=0}^N \left[\sum_{l=0}^{l_{\text{max}}} a_l^0 I_{q,l}^0 |v_q|^2 + 2\text{Re} \sum_{l=1}^{l_{\text{max}}} \sum_{m=1}^l a_l^m I_{q,l}^m v_{q+m}^* v_q \right], \quad (3.30)$$

where a factor $\Theta(q+m)\Theta(N-q-m)$ is implied in the second term and we have neglected terms with $l > l_{\text{max}} \approx 7R$. The dependence of \mathcal{H}_{rd} on the coefficients $\{a_l^m\}$ has also been made explicit by writing \mathbf{a} as one of its arguments. The coefficient $I_{q,l}^m$ is defined (and its LLL expression calculated) in Appendix A.4.

Therefore, within the LLL approximation the total energy function of the spherical thin-film in the presence of random disorder is

$$\mathcal{H}(\mathbf{v}; \mathbf{a}) = \mathcal{H}_{\text{c}}(\mathbf{v}) + \mathcal{H}_{\text{rd}}(\mathbf{v}; \mathbf{a}), \quad (3.31)$$

with the energy for the pure system given by Eq. (3.5) and the random disorder energy contribution taken from Eq. (3.30).

¹⁰In this notation the spherical harmonics are normalized on the sphere of radius R and its phase factor is chosen as described by Eqs. (A.43) and (A.44) in Appendix A.3.1.2.

In practice the energy contribution due to random disorder represents a difficult numerical-problem. The main trouble is the three-index coefficient $I_{q,l}^m$ which, because of its dependence on a generalized hypergeometric series (as shown in Appendix A.4), cannot be calculated accurately from within C. (This has been noticed previously by Kienappel [85].) Given this problem, we have decided to compute all the required values (using *Mathematica*) and to store them into data files (to be read at run time) following the method in Ref. [85]. The random disorder coefficients a_l^m (for different values of σ^2) are generated from within C and analogously stored into data files, noting that those with $m \neq 0$ must be complex, but those with $m = 0$ are purely real numbers. As for computing efficiency it must be stressed that the random disorder energy-contribution slows codes down by factors of two or more (depending on system sizes). We describe the results of our investigation in this problem next.

3.2.1 The System at $T = 0$

For this system we follow the same minimization technique as described in Section 3.1.1, but with the energy function given in Eq. (3.31) (written in terms of real variables) and its analytic gradient calculated in Appendix A.3.3.2. This time we just concentrate on the systems with $N = 12, 32, 50, 72$ and 132 vortices for two disorder strengths, given in terms of the variance on the disorder coefficients a_l^m , $\sigma^2 = 20/N$ and $200/N$, which range between 0.151515 and 16.666666 depending on system size.

In this case random disorder clearly destroys the quasi-hexagonal order (present in the pure system) even at the weakest pinning strength considered. We can see this effect, for instance, by looking at the vortex positions both on the sphere and on stereographic projection. The structure factor also reveals this loss of quasi-hexagonal order as the strength of the random disorder becomes bigger. Figure 3.13 shows the increasing of disorder on the vortex lattice as a function of the pinning strength, σ^2 , for the system with $N = 132$ vortices. In the pictures of vortex positions on the sphere we distinguish between vortices with different number of nearest neighbours (NNs): The green dots correspond to those with only four NNs. The big black-dots to those with five NNs. The small black-dots to those with six NNs; and the red dots to those

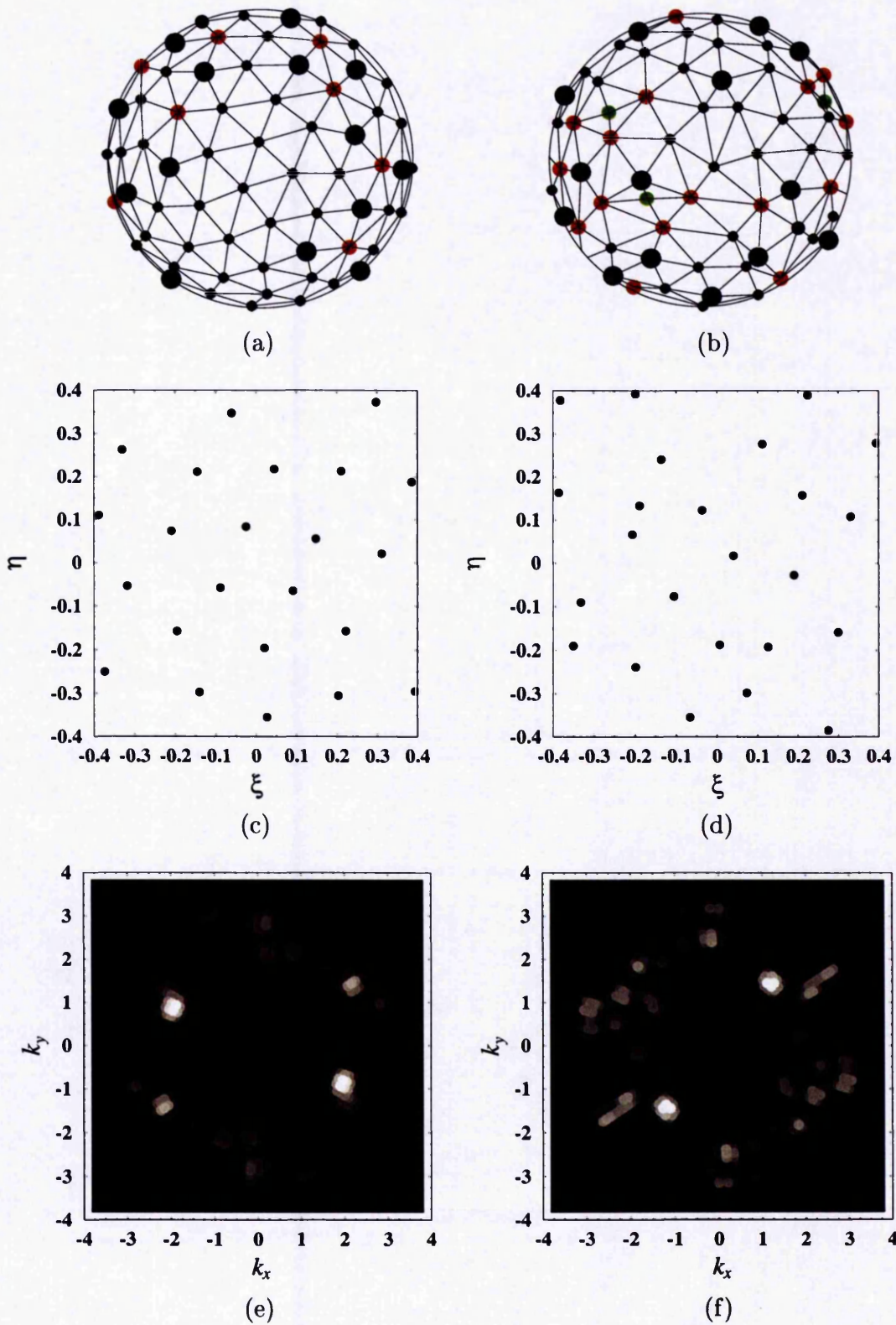


Figure 3.13: Vortex-solid structure in the ground state of the thin-film HTSC with random disorder for $N = 132$. (a,c,e) Positions on the sphere, section of the stereographic projection about the north pole, and structure factor for $\sigma^2 = 0.151515$. (b,d,f) *ibid.* for $\sigma^2 = 1.515151$.

with seven NNs. The plots of the stereographic projection and structure factor show the presence of a solid structure as that of a crystal with certain amount of disorder. This suggests an amorphous-solid phase at $T = 0$.

An interesting question, which remains to be answered, is whether a phase transition between the amorphous-solid phase and the quasi-hexagonal vortex lattice is possible for a (non-zero) strength of the random disorder (at $T = 0$). Such a phenomenon is not observed in our results for $\sigma^2 \geq 0.151515$, so we believe that in case it occurs it should appear at a $\sigma_c^2 < 0.151515$.

3.2.2 The System at $T > 0$

As in Section 3.1.2, we find several physical quantities of the thin superconducting film with random disorder by using the Monte Carlo method under the Metropolis algorithm. The treatment is completely analogous, but now with the total energy taken from Eq. (3.31). We carry out this investigation on systems with $N = 72$ and 132 vortices and a pinning strength of $\sigma^2 = 20/N$. It can be observed (see Fig. 3.14) that all fundamental quantities (normalized average energy, Abrikosov ratio and magnetization per vortex) as functions of α_T behave qualitatively the same way as those in the pure sample ($\sigma^2 = 0$).

In particular, we notice that as σ^2 increases the total energy of the system decreases. Contrarily, the Abrikosov ratio increases. As explained before, we associate high values of β_A to non-evenly spaced zeroes of the order parameter (i.e. to a non vortex lattice). By comparing the Abrikosov ratio in Fig. 3.14(b) for the system with disorder with the one for the pure system ($\sigma^2 = 0$), we can see that the system with pinning centres must present less “ordering” in vortex positions. This seems to indicate that the energy contribution to the pinning substrate favours a glassy state having a lower energy than that of the clean system.

By looking at the structure factor as the system is cooled down we observe the existence of amorphous-solid-like “structure” at temperatures as high as $\alpha_T = -4$. On the “noisy” background there is a set of quasi-hexagonal Bragg spots which become sharper and clearer for $\alpha_T \leq -8$ (as shown in Figure 3.15). This seems to indicate the

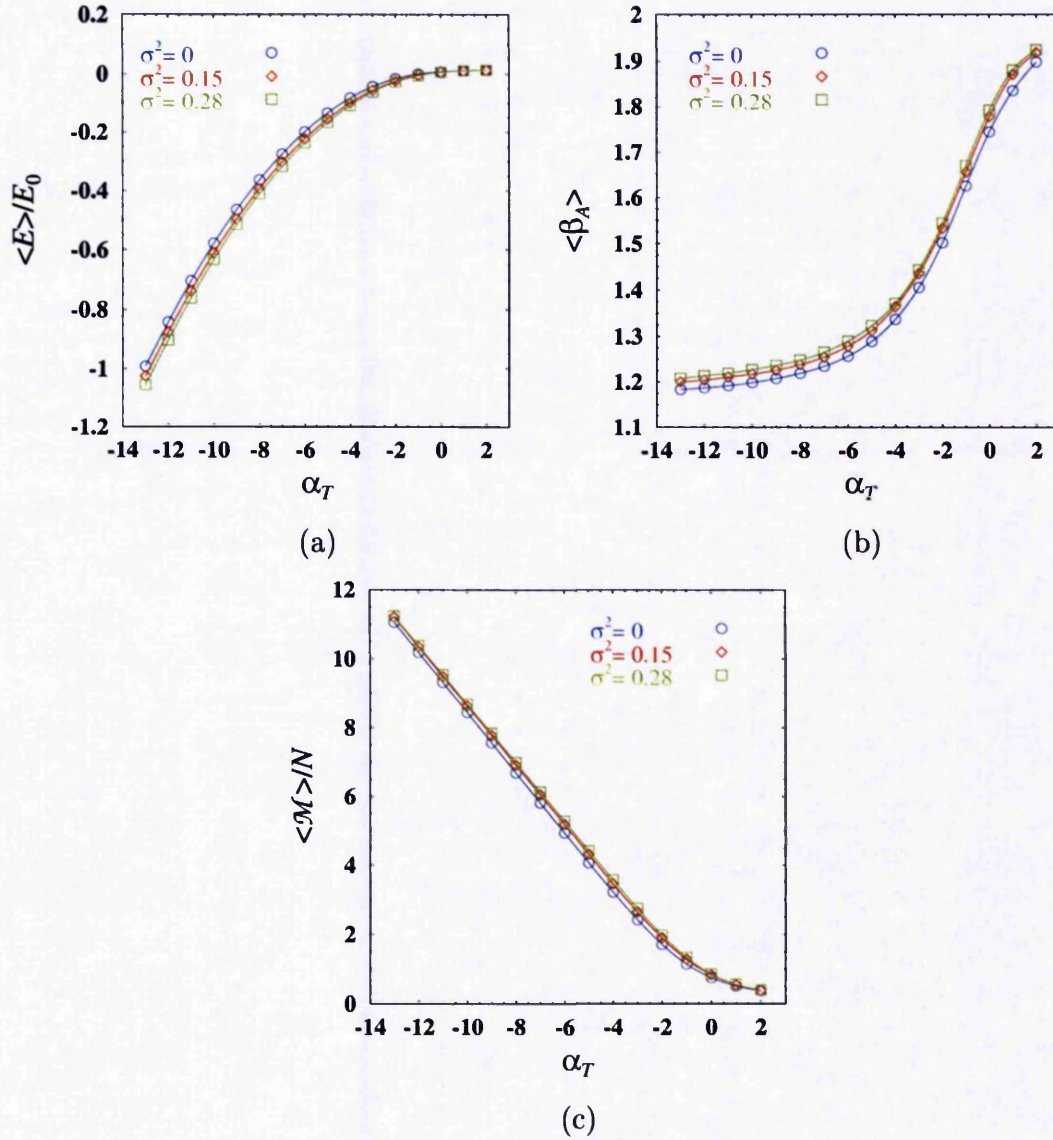


Figure 3.14: Finite-temperature properties of the thin-film HTSC with random disorder for $N = 72$ ($\sigma^2 = 0.277777$), $N = 132$ ($\sigma^2 = 0.151515$). [compared to the clean thin-film ($\sigma^2 = 0$).] (a) Average energy. (b) Abrikosov ratio. (c) Magnetization per vortex.

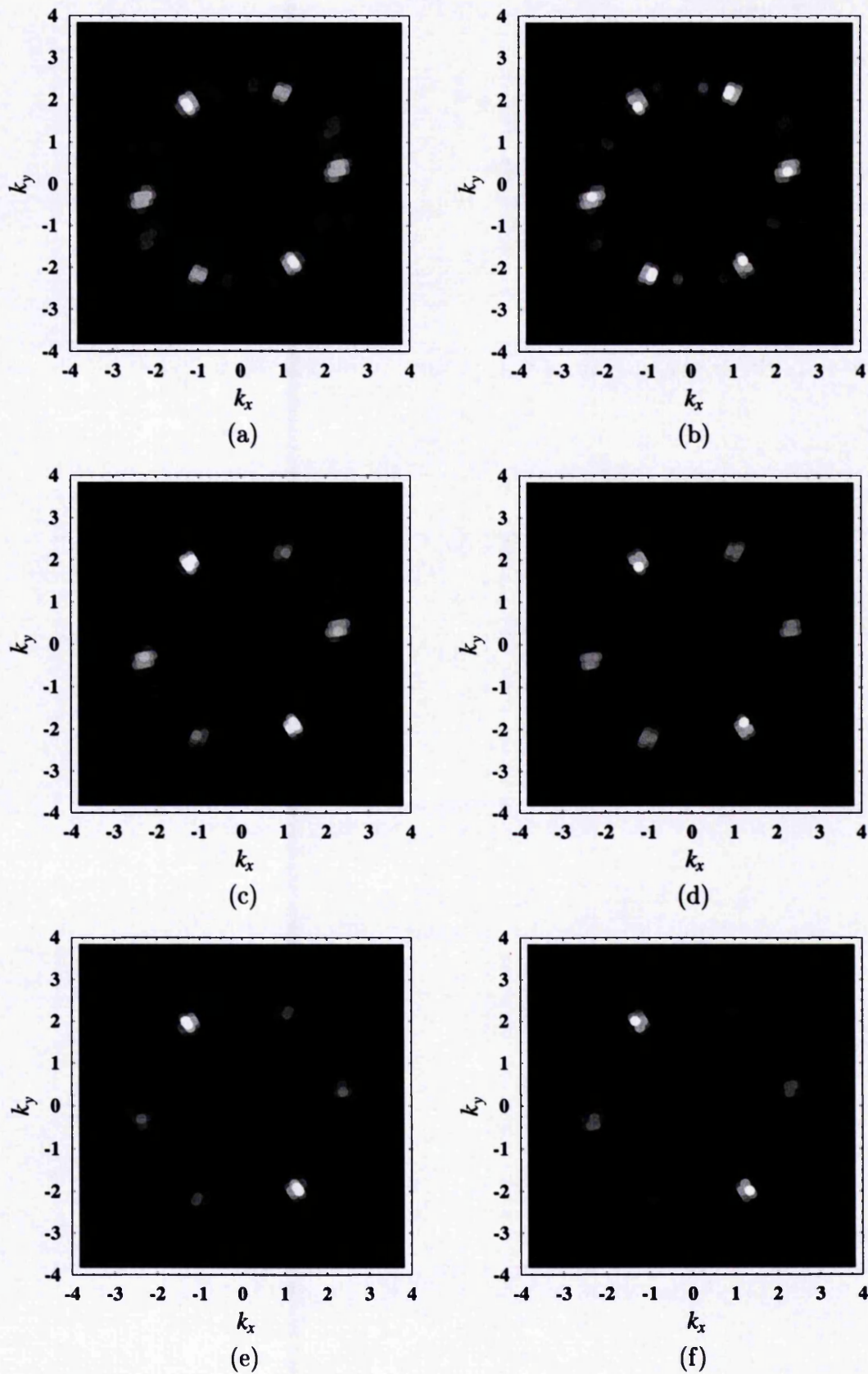


Figure 3.15: Structure factor of the thin-film HTSC with random disorder ($\sigma^2 = 0.151515$) for $N = 132$ vortices as the temperature is lowered: $\alpha_T = -8, -9, -10, -11, -12, -13$. [(a,b,c,d,e,f) respectively.]

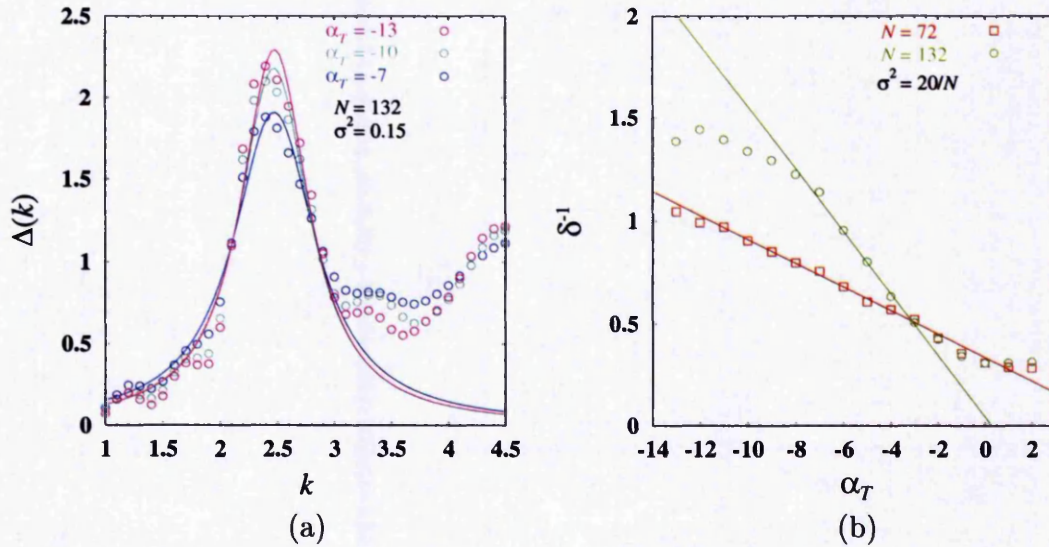


Figure 3.16: Density-density correlations for the thin-film HTSC with random disorder as the temperature is lowered. (a) First peak of the rotationally averaged structure function (with Lorentzian fits) for the system with $N = 132$ vortices ($\sigma^2 = 0.151515$). (b) Extracted density correlation length, $\delta^{-1} \sim \xi_D$, (with linear fits) for all system sizes investigated ($N = 72$ for $\sigma^2 = 0.277777$ and $N = 132$ for $\sigma^2 = 0.151515$).

possibility of a sort of vortex slow-reordering as a product of the pinning of vortices to randomly-distributed pinning centres. A quantitative study of the density correlation length (extracted from a Lorentzian fit to the first peak of $\Delta(k)$) shows no sign of a freezing transition (i.e. no rapid raise) at any finite temperature. Just as in the clean case, a straight line gives a reasonable good fit to the density correlation-length data (see Fig. 3.16) though finite size effects become pronounced for the system with $N = 132$ vortices at temperatures below $\alpha_T = -8$. As in the pure case, this appears consistent with an “absolute” freezing-transition only in the limit $\alpha_T \rightarrow -\infty$ (i.e. at $T = 0$).

3.3 Pinning Imposed by a Periodic Substrate

This section describes our the numerical study of the effects of regular arrays of pinning centres on the spherical thin-film superconductor. We follow, in part, the approach

used by Dodgson in Ref. [83] generalizing it to consider the two cases of most interest: those where the underlying pinning substrate and the vortex “lattice” are either commensurate or incommensurate.

We start this investigation by setting up the theoretical framework for the consideration of regular arrays of pinning centres on the spherical thin-film HTSC introduced in Section 3.1. In the rest of the Chapter we describe the consequences of that. As in the work of Dodgson [83] (and analogously to the case of the random disorder), we assume that it is possible to describe this kind of pinning effects by adding an extra energy contribution to the original GL energy functional in Eq. (2.1), which in the thin-film limit takes the form¹¹

$$\mathcal{H}_{\text{ps}}[\psi; \psi^{(0)}] = -g\beta d_0 \int d^2r |\psi^{(0)}(\mathbf{r})|^2 |\psi(\mathbf{r})|^2. \quad (3.32)$$

Here the subindex “ps” stands for “periodic substrate” and, in fact, the periodicity (though on the sphere) of this substrate of pinning centres comes from the geometrical nature of the ground-state order parameter $\psi^{(0)}$ for the pure system (as described in Section 3.1.1), that satisfies

$$\mathcal{H}[\psi^{(0)}(\mathbf{r})] \leq \mathcal{H}[\psi(\mathbf{r})], \quad (3.33)$$

with \mathcal{H} the GL energy functional defined in Eq. (2.1). This equation is valid for all possible order parameter configurations $\psi(\mathbf{r})$ with N' vortices. The periodic substrate of pinning centres is, therefore, defined by the function that minimizes the energy of the clean system with N' vortices present, $\psi^{(0)}(\mathbf{r})$.

In general the underlying periodic substrate and the vortex system can have different number of “elements”. This is set up by considering a system composed of N vortices, i.e. $\psi(\mathbf{r})$ being the order parameter describing N vortices, while the number of pinning centres is N' . The strength of the coupling of the superconducting order

¹¹In terms of the LLL scaled quantities this energy term is just

$$\mathcal{H}_{\text{ps}}[\tilde{\psi}_L; \tilde{\psi}^{(0)}] = -|\alpha_T|^2 k_B T g \int d^2\tilde{r} |\tilde{\psi}^{(0)}(\mathbf{r})|^2 |\tilde{\psi}_L(\mathbf{r})|^2,$$

with the LLL-GL order parameter $\tilde{\psi}_L$ taken from Eq. (3.1) and $\tilde{\psi}^{(0)}$ being the same as $\psi^{(0)}$ (in Eq. (3.34)) but with Q replaced by \tilde{Q} .

parameter $\psi(\mathbf{r})$ to the periodic substrate defined by $\psi^{(0)}(\mathbf{r})$ is measured by the real parameter g in Eq. (3.32). The positive parameter β is that of the GL theory in Eq. (2.1) and d_0 is the layer thickness.

Within the LLL approximation the order parameter is taken as that in Eq. (2.24) and, in a similar fashion, the ground-state order parameter for the periodic substrate expanded as

$$\psi^{(0)}(\theta, \phi) = Q \sum_{q=0}^{N'} v_q^{(0)} \psi_{q,N'}(\theta, \phi). \quad (3.34)$$

This is possible because at least one linear combination of the degenerate eigenfunctions of the LLL should minimize the GL energy functional for a suitable choice of coefficients $\mathbf{v}^{(0)} = \{v_q^{(0)}\}$.¹² After performing the quartic term integration, taking care of the presence of N and N' , we get the final form for the energy contribution of the periodic substrate of pinning centres (per unit of thermal energy $k_B T$) as

$$\frac{\mathcal{H}_{\text{ps}}(\mathbf{v}; \mathbf{v}^{(0)})}{k_B T} = -2g \frac{1}{2N} \sum_{p=0}^{N+N'} |U'_p(\mathbf{v}; \mathbf{v}^{(0)})|^2, \quad (3.35)$$

where the linear functions in the order parameter expansion coefficients v_q are defined by

$$U'_p(\mathbf{v}; \mathbf{v}^{(0)}) = N \gamma_{q,N+N'} \sum_{q=0}^N \mathcal{N}_{q,N} \mathcal{N}_{p-q,N'} \Theta(p-q) \Theta(N'-p+q) v_{p-q}^{(0)} v_q, \quad (3.36)$$

and the coefficient $\gamma_{q,N+N'}$ is that introduced in Section 3.1.

In this case the total energy function of the spherical thin-film in the presence of pinning centres forming a periodic array (on the sphere) is just

$$\mathcal{H}(\mathbf{v}; \mathbf{v}^{(0)}) = \mathcal{H}_c(\mathbf{v}) + \mathcal{H}_{\text{ps}}(\mathbf{v}; \mathbf{v}^{(0)}), \quad (3.37)$$

with the LLL energy for the pure system given in Eq. (3.5) and the pinning energy-contribution taken from Eq. (3.35). In practice the problem of considering this extra term of energy is much less CPU-time consuming than that of random disorder. Thus, systems of bigger size are accessible for periodic substrates of pinning centres.

¹²Though these coefficients are just constants once the ground state is found, it should be emphasized that they are not unique. Transformations of $\{v_q^{(0)}\}$ under which the energy and other physical quantities remain invariant are a global change of phase (of all coefficients) or a rotation of the whole system about a given axis. This has been noticed for general $\{v_q\}$ since the work of O'Neill and Moore [79].

Before going into specific results we introduce the concept of the *matching field*; useful to quantify the strength of the average magnetic-induction in the superconductor and to decide whether a periodic substrate and a vortex lattice (usually on the plane) are either commensurate or incommensurate. First we define a reference point for the average magnetic-induction, \overline{B}_Φ , (called the first matching field, or just the matching field) when there are N' vortices in the superconducting film of average radius R . Then, applying the Gauss law of electromagnetism to the flux through the sphere, we have $4\pi R^2 \overline{B}_\Phi = N' \Phi_0$, where $\Phi_0 = h/2|e|$ is the flux quantum. Analogously, for an arbitrary average magnetic-induction \overline{B} producing N vortices on the same film, we have $4\pi R^2 \overline{B} = N \Phi_0$. Taking the ratio of both equations we find the value of the arbitrary magnetic induction as

$$\overline{B} = \left(\frac{N}{N'} \right) \overline{B}_\Phi. \quad (3.38)$$

Notice that when the average induction \overline{B} in the superconductor is greater, less or equal to \overline{B}_Φ , then there are more, less or equal numbers of vortices and pinning centres respectively. In the following we describe the results of our investigation for some commensurate and incommensurate cases.

3.3.1 Commensurate Case

Unlike the relative simplicity of determining whether a periodic substrate and a vortex lattice are commensurate on the plane (see Ref. [58] for some examples), the analogous problem on the sphere turns out to be more difficult. For the regular substrates with N' pinning centres on the sphere, the easiest of all commensurate cases for the vortex lattice (with N sites) is that when $\overline{B} = \overline{B}_\Phi$ (i.e. when $N = N'$). This is valid for all system sizes. However, cases like $\overline{B} = p \overline{B}_\Phi$ with $p = 2, 3, \dots$ are non-commensurate in general. Other combinations are possible, and among them are those of ratios between $N = 32, 72, 132, \dots$ and $N' = 12$ (or viceversa). Both lattices are clearly commensurate because (as shown in Section 3.1.1) the vortex lattice of systems of size $N = 32, 72, 132, \dots$ is a projection onto the sphere of the icosadeltahedra (always commensurate to an icosahedron: $N' = 12$). These two cases: with the vortex system

at the matching field, $\bar{B} = \bar{B}_\Phi$, and with the icosahedral substrate, $\bar{B} = (N/12)\bar{B}_\Phi$ are reviewed next.

3.3.1.1 Pinning at the Matching Field: $\bar{B} = \bar{B}_\Phi$

We start by describing the zero-temperature properties of N vortices on the spherical thin-film with a regular array of the same number of pinning centres located at the ground-state vortex positions of the clean superconducting thin-film. As shown in Section 3.1.1, vortices on the clean system always arrange themselves so as to form a vortex lattice in their ground state. It is this regular array of pinning centres that we use to attract an equal number of vortices in our system.

Ground State Properties

To calculate the zero-temperature properties of this system we follow the same energy-minimization technique. In this case the total energy is given in Eq. (3.37). That is, again, written in terms of real variables and its analytic gradient taken from Appendix A.3.3.3.

Basic results are found qualitatively the same as those for the clean thin-film and therefore will be omitted. However, some comments will be made. We could observe that quantities like the Abrikosov ratio have exactly the same value (as in the pure case) for each of the systems studied: $12 \leq N \leq 230$. Numerical shifts in quantities like the ground state energy per vortex and the specific heat per vortex are expected from the extra energy term, and they actually appear to lower these quantities. They clearly depend on the pinning strength g . In this case we investigate vortex systems at weak ($g = 0.1$) and strong ($g = 100$) coupling to the periodic substrate. We notice that the vortex correlations which give rise to the system magnetization increase so as to produce a higher value: $\mathcal{M} \approx \mathcal{M}_{\text{clean}}(1 + g)$. In either case of weak or strong coupling, Figures 3.1 and 3.2 show faithfully the qualitative behaviour of these basic properties as functions of the system size.

Analogously to the pure case, a vortex lattice is found as the phase at zero temperature. Pictures of the vortex positions, both on the sphere and stereographic

projections show that at $T = 0$ vortices fall to the pinning centres (as expected). The same vortex lattice as for the pure sample is found for each system size, and this is also confirmed by the structure factor. In summary, we can extrapolate our result to suggest that the same vortex lattice found in the clean thin-film HTSC is the equilibrium phase at zero temperature of the thin-film superconductor with the periodic substrate (at the matching field) defined in Eq. (3.37) for any finite $g > 0$.

Expected XY -type Phase Transition

In the problem of the thin-film HTSC with a regular substrate of pinning centres at the matching field we can map the LLL-GL (plus pinning energy-term) onto a form of the XY model in two dimensions. Following closely the derivation of Dodgson [83], the physics of that is explained below.

By exploiting well known results on the GL theory of superconductivity, one can realise that the GL model should account for two symmetries. One is the symmetry of translational invariance associated with the existence of a low temperature vortex lattice. The other is the $U(1)$, XY -type, symmetry associated with the phase invariance of the order parameter. If we locate the pinning centres at the positions of the ground-state vortex-sites, then for low enough temperatures the symmetry of translational invariance has been broken. Therefore, we expect the remaining spontaneously broken symmetry to be associated with the XY -type phase transition.

This can be seen to arise naturally from the low temperature expansion of the GL energy functional provided by Eilenberger [75]. Let us consider the LLL-GL model for a thin-film with plane geometry in which the energy functional can be written as [83]

$$\mathcal{H}_{el}[\tilde{\psi}_L(\mathbf{r})] = |\alpha_T|^2 k_B T \int d^2 \tilde{r} \left[\text{sgn}(\alpha_T) |\tilde{\psi}_L|^2 + \frac{1}{2} |\tilde{\psi}_L|^4 \right], \quad (3.39)$$

where $\tilde{\psi}_L(\mathbf{r})$ is the rescaled superconducting order-parameter within the LLL approximation (written in terms of the original vector position \mathbf{r})¹³ and α_T is the two-dimensional field-temperature effective parameter from Eq. (2.34).

¹³It is not a problem to write expressions either in terms of \mathbf{r} or $\tilde{\mathbf{r}}$ as the scaling relationship in Eq. (2.30), $\mathbf{r} = \rho^{1/2} \tilde{\mathbf{r}}$, can be used. In fact, within this LLL scaling (and setting $l_m \equiv 1$) the constant $\rho = 2\pi$. [which, in addition, makes it clear why $d^2 \tilde{r} = (1/2\pi) d^2 r$.]

In order to consider the pinning potential due to the regular substrate we add an extra energy term given by

$$\mathcal{H}_{cd}[\tilde{\psi}_L(\mathbf{r}); \tilde{\psi}^{(0)}(\mathbf{r})] = -|\alpha_T|^2 k_B T g \int d^2\tilde{r} |\tilde{\psi}^{(0)}|^2 |\tilde{\psi}_L|^2, \quad (3.40)$$

in which $\tilde{\psi}^{(0)}$ is the ground-state order parameter of Eq. (3.39) and g measures the strength of the coupling of vortices to the pinning centres. In mean field approximation we just take into account the configuration $\tilde{\psi}_L(\mathbf{r}) = \tilde{\psi}_0$ that minimizes $\mathcal{H} = \mathcal{H}_{cl} + \mathcal{H}_{cd}$. In the Eilenberger notation, $\tilde{\psi}_0 = A\varphi(\mathbf{r}|\mathbf{0})$ [and $\tilde{\psi}^{(0)} = A^{(0)}\varphi(\mathbf{r}|\mathbf{0})$],¹⁴ so that the mean-field energy is

$$\mathcal{H}[\tilde{\psi}_0] = |\alpha_T|^2 k_B T L_x L_y (-A^2 + \frac{\beta_A}{2} A^4 - g\beta_A A^{(0)2} A^2), \quad (3.41)$$

where L_x and L_y are the lengths of the sample in the x and y direction respectively, and $\beta_A = 1/A^{(0)2}$. The energy in Eq. (3.41) is minimized by $A^2 = A^{(0)2}(1+g)$. Small fluctuations about mean field theory are calculated using a low temperature expansion that consists in writing the order parameter as

$$\tilde{\psi}_L(\mathbf{r}) \equiv \tilde{\psi}_0 + \delta\psi = A\varphi(\mathbf{r}|\mathbf{0}) + V^{-1/2} \sum_{\lambda,q} (a_{\lambda,q} + ib_{\lambda,q}) u_{\lambda,q}, \quad (3.42)$$

with $u_{\lambda,q} = Q_\lambda [e^{iqz} \varphi(\mathbf{r}|\mathbf{r}_\lambda) - e^{-iqz} \varphi(\mathbf{r}|\mathbf{r}_\lambda)]$ and $|Q_\lambda|^2 = 1/2$. Expanding the energy functional only to second order in $\delta\psi$, keeping terms up to $O(a_\lambda^2)$, we obtain

$$\mathcal{H}[\tilde{\psi}_L(\mathbf{r})] = \mathcal{H}[\tilde{\psi}_0] + \frac{|\alpha_T|^2 k_B T}{4\pi\beta_A} g(1+g) \sum_{k_x, k_y} \left(\frac{a_\lambda}{A}\right)^2 k^2. \quad (3.43)$$

The fluctuation spectrum therefore remains soft, but with a dispersion altered to k^2 that changes the low temperature properties of the system. This low temperature expansion, in fact, puts the system in the same universality class as the XY model. This is clearly seen if we consider the relation between the amplitude of the shear modes $(L_x L_y)^{-1/2} a_\lambda$ and the change of phase from the ground state $\Phi(\mathbf{r})$,

$$\Phi(\mathbf{r}) = \frac{2}{\pi} (L_x L_y)^{-1/2} \sum_{k_x, k_y} \left(\frac{a_\lambda}{A}\right) \sin(\mathbf{k} \cdot \mathbf{r}), \quad (3.44)$$

¹⁴Here $\varphi(\mathbf{r}|\mathbf{0}) = 3^{1/8} \exp(-y^2/2l_m^2) \vartheta_3(\pi z/l_0|\tau)$, where $\vartheta_3(\zeta|\mu)$ is a Jacobi theta function, $z = x + iy$ the complex variable, l_m the magnetic length, $l_0^2 = 4\pi l_m^2/\sqrt{3}$ and $\tau = (1+i\sqrt{3})/2$. The zeroes of $\varphi(\mathbf{r}|\mathbf{0})$ form a triangular lattice with a lattice spacing l_0 , and the functions satisfy $|\varphi(\mathbf{r}|\mathbf{0})|^2 = 1$. Analogously the functions $\varphi(\mathbf{r}|\pm\mathbf{r}_\lambda)$ are given by $\varphi(\mathbf{r}|\pm\mathbf{r}_\lambda) = \varphi(\mathbf{r} \pm \mathbf{r}_\lambda|\mathbf{0}) \exp(\pm i l_m^{-2} y_\lambda x)$.

from which we have

$$\frac{\pi^2}{2} \int d^2r (\nabla \Phi(\mathbf{r}))^2 \sim \sum_{k_x, k_y} \left(\frac{a_\lambda}{A} \right)^2 k^2, \quad (3.45)$$

to give the energy contribution for the large wavelength excitations at low temperatures of

$$\frac{\delta \mathcal{H}}{k_B T} = \frac{1}{2} \beta_{XY} \int d^2r (\nabla \Phi(\mathbf{r}))^2. \quad (3.46)$$

This has the same form as the large-wavelength limit of the XY model (where the phase Φ represents the angle of orientation of the spins), with an inverse temperature of $\beta_{XY} = \pi |\alpha_T|^2 g(1+g)/4\beta_A$. Therefore it is clear that the pinning potential imposed by the regular substrate of pinning centres makes this superconducting system behave as the XY model.

The XY model in two dimensions is expected to have a continuous Kosterlitz-Thouless (KT) phase transition due to the unbind of topological defects (dissociation of vortex-antivortex pairs). The superconducting counterpart of this should be a continuous KT transition resulting from vacancy-interstitial pairs unbinding in the Abrikosov vortex-lattice. Physically each vacancy can be associated with an antivortex and each interstitial with an XY vortex. Both, interstitials in the Abrikosov lattice and XY vortices are characterised for their phase change of 2π when going through a path around them, so they can be directly related. This explains why both models can be described by the same energy function. Kosterlitz and Thouless [93] have predicted a transition temperature T_{KT} when $\beta_{XY} \approx 2/\pi$. This gives the phase boundary $g = \left(\sqrt{1 + (32\beta_A/\pi^2 |\alpha_T|^2)} - 1 \right) / 2$ on the α_T - g plane.

The System at Finite Temperature

As in Sections 3.1.2 and 3.2.2, we find several physical properties of the thin-film HTSC with the periodic substrate of pinning centres (at the matching field) by using the Monte Carlo method under the Metropolis algorithm. The treatment is completely analogous, but now with the energy function given in Eq. (3.37) for $N' = N$. In this case the investigation is carried out on systems with $N = 72, 132$ and 432 vortices for pinning strengths of $g = 0.05, 0.1, 0.4, 1, 2, 10$ and 100 ; and each run started with the ground-state order parameter coefficients $\{v_q^{(0)}\}$. For weak couplings ($g \leq 0.1$) we

observe that quantities as the average energy (internal energy), Abrikosov ratio and magnetization per vortex (as functions of α_T) behave qualitatively in the same way as those for the pure system ($g = 0$), but with values slightly different (see Fig. 3.17). However, a much lower energy and Abrikosov ratio (as well as higher magnetization) is observed for all α_T at relatively strong coupling to the pinning substrate, $g \geq 0.4$. These results, specially the low (almost constant) values of β_A , seem to show the appearance of long-range quasi-hexagonal ordering of vortices at a sufficiently high temperature as the coupling $g \rightarrow 1$.

In addition to fundamental physical properties, Figure 3.17 also shows plots of two more quantities that are very sensitive to the pinning of vortices (as previously studied by Dodgson [83]). Here we call them the “pinning magnetization”, \mathcal{M}_g , defined as

$$\mathcal{M}_g = \frac{|\psi^{(0)}\psi^*|^2}{|\psi^{(0)}|^4}, \quad (3.47)$$

and the “pinning susceptibility”, χ_g , given by

$$\chi_g = \frac{|\psi^{(0)}\psi^*|^2}{|\psi^{(0)}|^2}. \quad (3.48)$$

Notice that these quantities actually measure phase coherence and that their thermal averages can be calculated, if preferred, only on the numerator because the denominator is just a constant.

In Figure 3.17(d) we observe that the pinning magnetization has a rather smooth behaviour (similar to the magnetization in Figure 3.17(c)), from where it gets its name. On the other hand, the pinning susceptibility in Figure 3.17(e) presents a nearly zero constant value at high temperatures with a sudden change to quasi-linear behaviour (going to higher values) as α_T decreases. As χ_g is rather sensitive to correlations between pinning centres and pancake vortices, we can associate the α_T at which the “sudden” change to quasi-linear behavior occurs with the temperature below which pinning by the periodic substrate becomes effective. This will happen when phase coherence is established. At $g = 0.1$, for instance, we can observe this to occur at about $\alpha_T = -4$ (see Fig. 3.17(e)).

Direct observations of the vortex positions (on the sphere, on stereographic projection or in angular coordinates) and structure factor as the system is cooled down

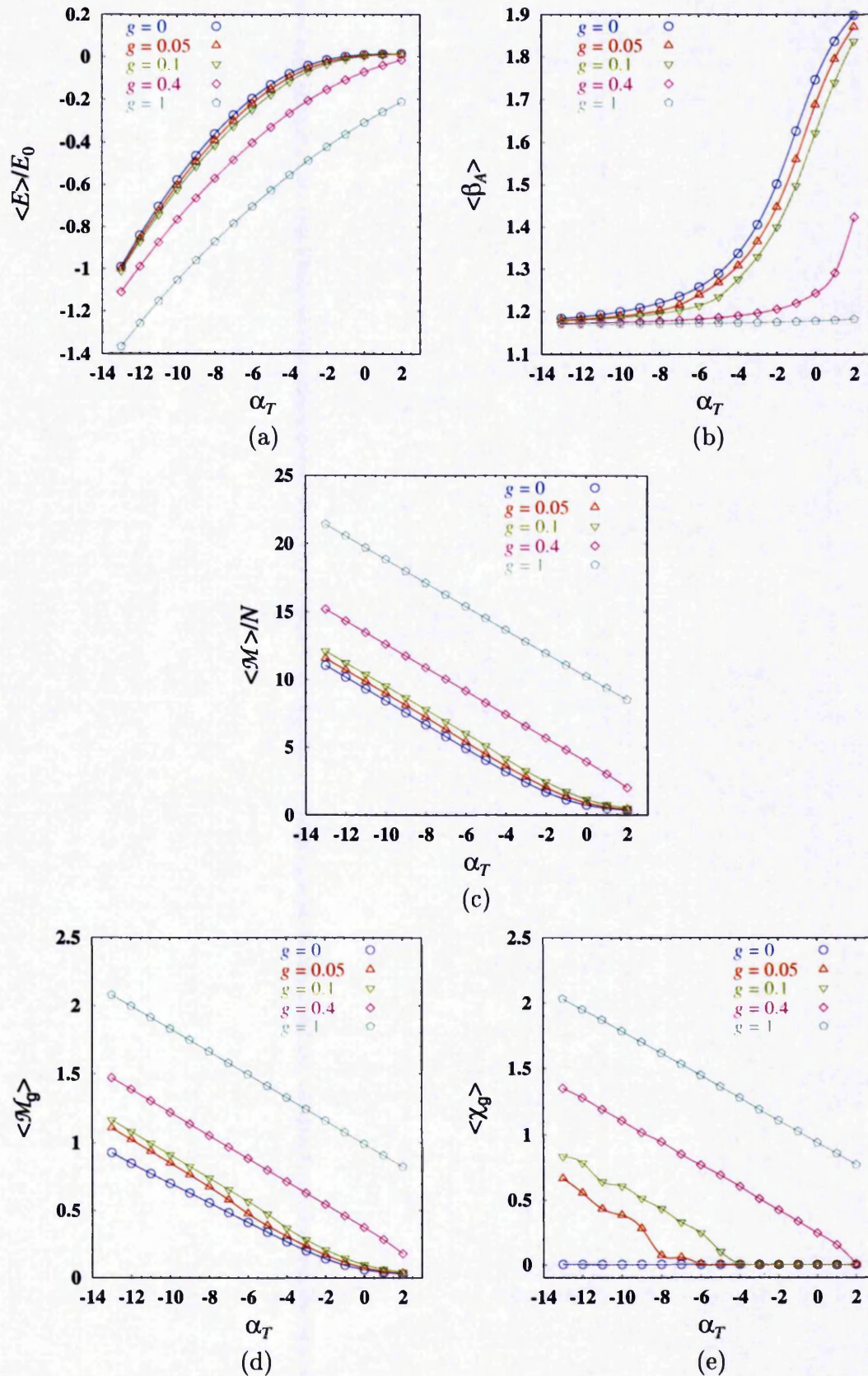


Figure 3.17: Finite-temperature properties of the thin-film HTSC with a regular array of pinning centres at the matching field ($N = N'$). (a) Average energy. (b) Abrikosov ratio. (c) Magnetization per vortex. (d,e) Pinning magnetization and susceptibility.

reveal the increase of quasi-hexagonal order at relatively high temperatures. Figure 3.18(a,c,e) shows this through the ordering of vortices to the pinning centres as temperature is lowered. There, results for the system with $N = 132$ vortices at $g = 0.1$ are shown, but similar features are observed also for $N = 72$ and 432 at the same coupling (not shown). It is clear from the pictures on angular vortex-positions, Fig. 3.18(a,c,e), that vortices tend to arrange with the periodic substrate so as to reach the ground-state vortex positions in the clean system (though with small fluctuations) at temperatures as high as $\alpha_T \sim -5$ (for $g = 0.1$). That is also confirmed by the structure factor contour-plots in Fig. 3.18(b,d,f). At any of the three temperatures shown an underlying set of quasi-hexagonal Bragg peaks is visible. We associate this to the fact that the pinning substrate has broken the symmetry of translational invariance at relatively high temperatures. Above $\alpha_T = -4$ (Fig. 3.18(d)) a certain amount of disorder in vortex positions can be still observed, but as the system cools down below this value (Fig. 3.18(f)) the Bragg peaks appear clearer and slightly sharper. By comparing the effective temperature α_T at which phase coherence appears (from the analysis of χ_g) to the temperature at which “clean Bragg peaks” are present, we can see this to occur about the same temperature. Therefore “clean Bragg peaks” will also indicate a coherent state of the order parameter in this case.

A final confirmation comes from detailed studies of the density-density correlations (see Fig. 3.19). Here, again, we find that a Lorentzian function gives a proper fit to the first peak of the structure function $\Delta(k)$ (shown for the system with $N = 432$ vortices at $g = 0.1$ in Fig. 3.19(a)), and from that we extract the density correlation length as $\delta^{-1} \sim \xi_D$. Contrarily to the clean thin-film, in this case δ^{-1} presents an abrupt increase about the temperature at which phase coherence is observed to appear. We associate this to as an effect of the expected continuous transition. Figure 3.19(b) shows this sudden raise in δ^{-1} as a function of α_T for the different system sizes at $g = 0.1$. A similar plot is shown in Fig. 3.19(c) but this one for the system with $N = 432$ vortices as g is varied. The arrow in this case marks the value of δ^{-1} in the ground state for this system size.

To summarize, the analysis of physical quantities of the thin-film HTSC with a

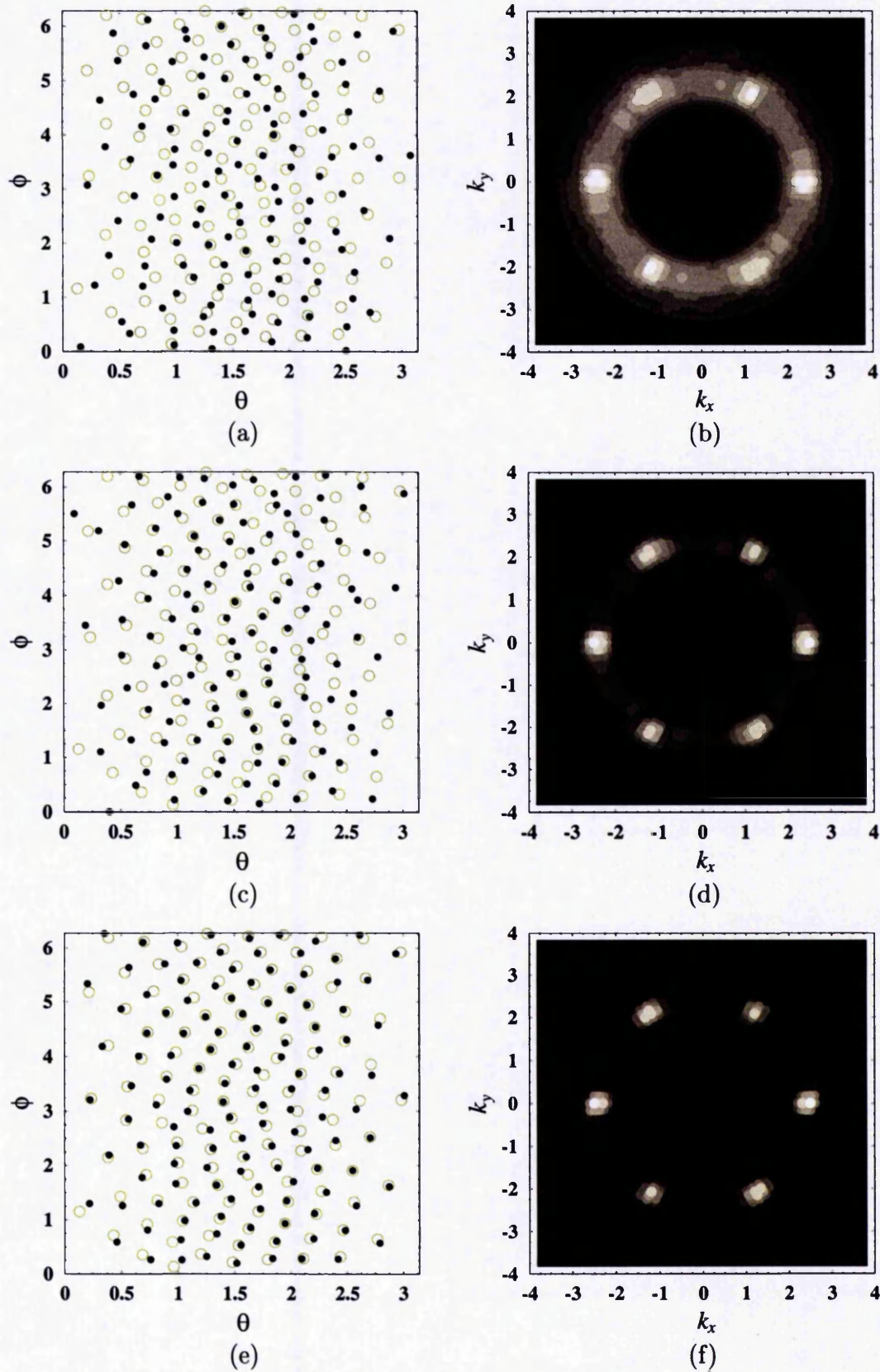


Figure 3.18: Angular vortex-positions and structure factor of the thin-film HTSC with a regular array of pinning centres at the matching field for $g = 0.1$ and $N = 132$ vortices as the temperature is lowered: $\alpha_T = -3, -4, -5$. [(a,b),(c,d),(e,f) respectively. In (a,c,e) open circles are the pinning centres, circles are the vortices.]

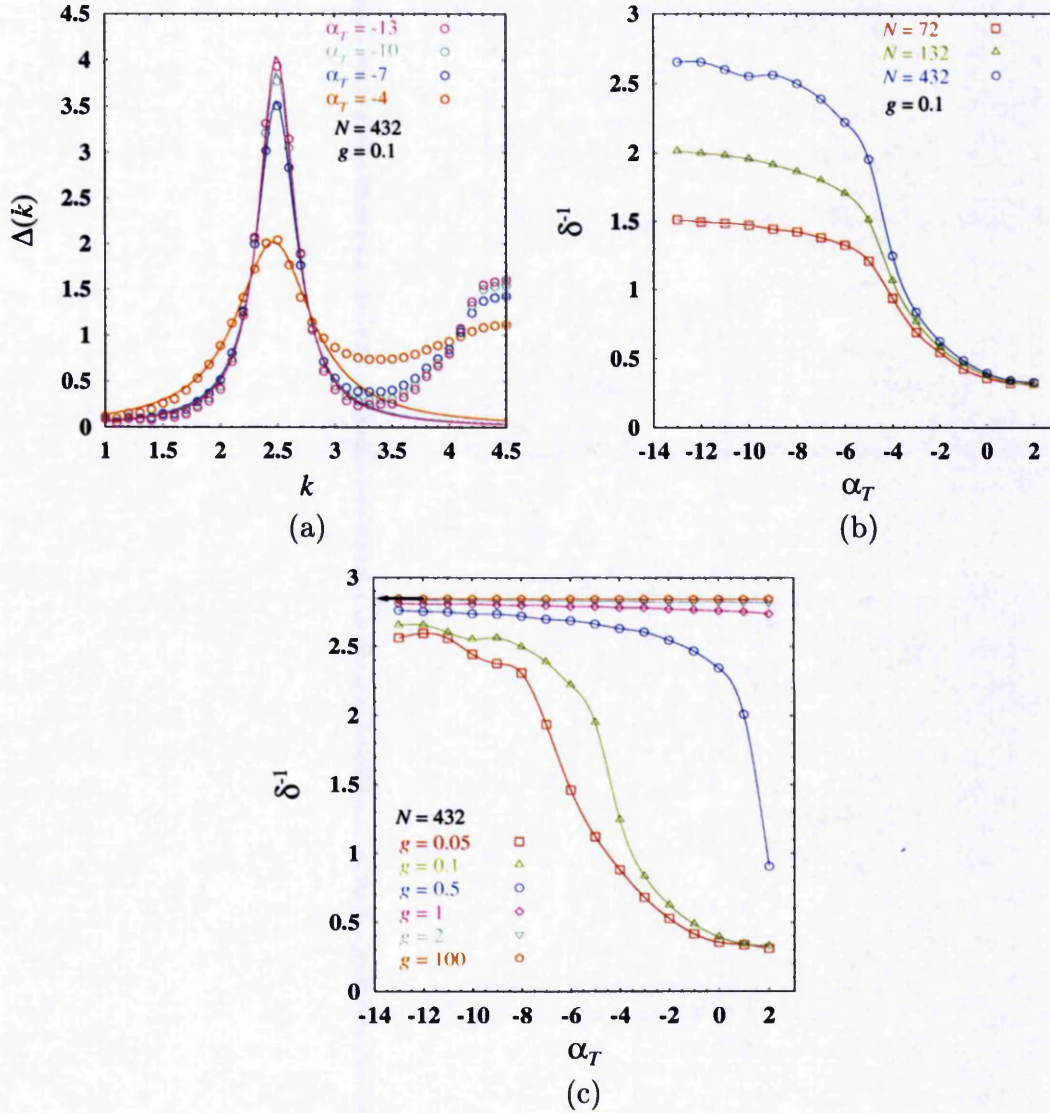


Figure 3.19: Density-density correlations for the thin-film HTSC with a regular substrate of pinning centres at the matching field as the temperature is lowered. (a) First peak of the rotationally averaged structure function (with Lorentzian fits) for the system with $N = 432$ vortices. (b) Extracted density correlation length, $\delta^{-1} \sim \xi_D$, (with spline fits) for all system sizes investigated (at $g = 0.1$). (c) Same as (b) but for $N = 432$ as g is varied. [The arrow marks the ground state value for this system size.]

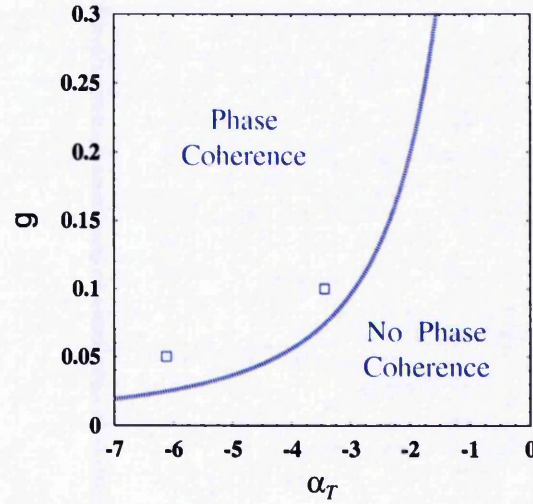


Figure 3.20: g - α_T phase diagram for vortices in the thin-film HTSC with a regular array of pinning centres at the matching field. The curve represents the predicted line of continuous phase transitions. The open squares are the values at which phase coherence appears (extracted from the linear fit of $\chi_g(\alpha_T)$ in the low temperature side).

periodic substrate at the matching field shows the existence of a “low temperature” superconducting state in which phase coherence exists and a phase with no phase coherence at higher temperatures. The estimated line of phase transitions clearly depends on the strength of the coupling to the substrate g . According to the analysis of the previous section, this should be a line of continuous phase transitions at which vacancy–interstitial vortex pairs unbind. Figure 3.20 shows our proposed phase diagram (in terms of the phenomenological parameters g and α_T) for the $B = B_\Phi$ case. In that the open squares correspond to the points (α_T, g) at which quasi-linear behavior appears in χ_g . The curve is the expected line of continuous phase transitions $g(\alpha_T)$ from the XY analysis in which we have assumed a constant value of $\beta_A = 1.16504$ (corresponding to the ground state in this geometry as a first approximation).

3.3.1.2 Pinning by the Icosahedral Substrate: $\bar{B} = (N/12)\bar{B}_\Phi$

In this case we observe the effects of an icosahedral substrate of pinning centres onto the vortices in the spherical thin-film. As described before, in Section 3.1.1, we find

that only systems of size $N(p, q) = 10(p^2 + pq + q^2) + 2$; with $p = 1, 2, \dots$ (and $N(1, 0) = N(0, 1) = 12$) have icosahedral symmetry. Therefore, system sizes in this set are the only ones commensurate to the icosahedral substrate.

Properties at Zero Temperature

This investigation has been carried out using the same energy-minimization technique as for the previous matching-field case (but for $N' = 12$). Though only systems of size $N(p, q)$ (above) are commensurate to the icosahedral substrate, we have studied system sizes $12 \leq N < 200$ for weak ($g = 0.1$) and strong ($g = 100$) pinning (that is for $\bar{B} \geq \bar{B}_\Phi$). In the “weak pinning” regime, for all these system sizes, we find essentially identical Abrikosov ratios to those of the clean system (compare Figs. 3.21(b) and 3.1(b)). However, quantities as the average energy, magnetization per vortex and specific heat per vortex become much smoother (as functions of N) and change slope (see Fig. 3.21(a,d,e)). It is noticeable that the commensurate cases $N = 12, 32$ and 72 still show lower energy and higher magnetization values than nearby N . The specific heat becomes so smooth that only a small kink (with a lower value) is evident at $N = 32$. This suggests that systems with $N = 12, 32$ and 72 vortices at weak couplings $g = 0.1$ are optimum to the icosahedral substrate in the $T \rightarrow 0$ limit.

On the “strong pinning” side ($g = 100$ here), the Abrikosov ratio becomes considerably higher for each system of size $N > 12$. Internal energy, magnetization and specific heat become almost completely smooth, suggesting that the icosahedral substrate acts in a similar fashion on all system sizes. In addition to this, interesting structural changes to the vortex lattice for system sizes $N' < N < 6N'$ are observed. In this case each pinning centre clearly pins a “bundle” of vortices around it, but none of them at its “core”. Figure 3.22 shows this effect by comparing the vortex positions (in stereographic projection) of systems of different size at $g = 0.1$ and $g = 100$. Although this might appear unimportant when the interest is on the thermodynamic limit, $N \rightarrow \infty$, it can be found useful in “quantum applications” where microscopic systems are relevant.

In this case it is remarkable the fact that a phase transition at $T = 0$ should

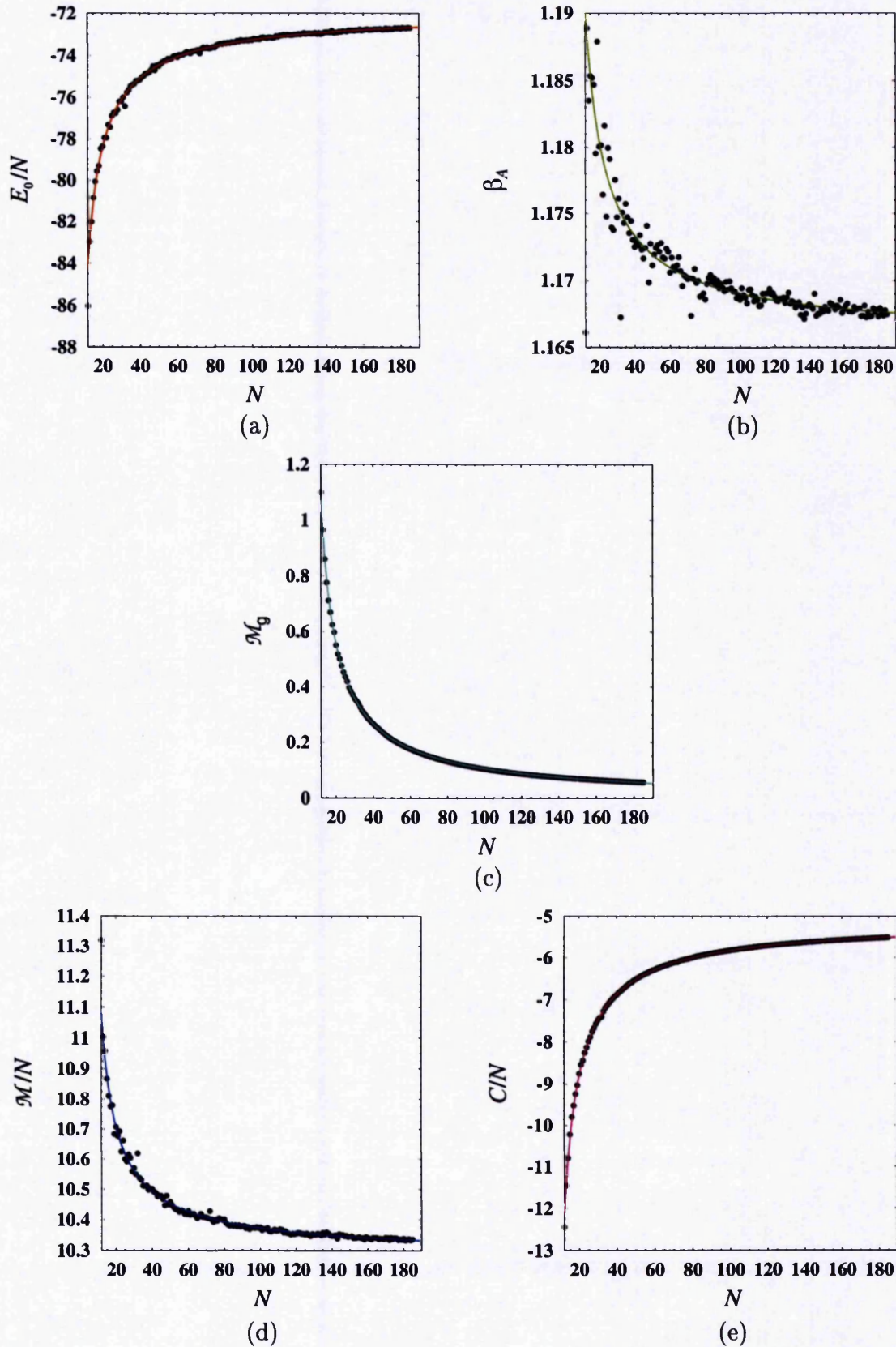


Figure 3.21: Ground-state properties of the thin-film HTSC with spherical geometry and an icosahedral ($N' = 12$) substrate of pinning centres at $g = 0.1$. (a) Energy per vortex. (b) Abrikosov ratio. (c) Pinning magnetization. (d) Magnetization per vortex. (e) Specific heat per vortex.

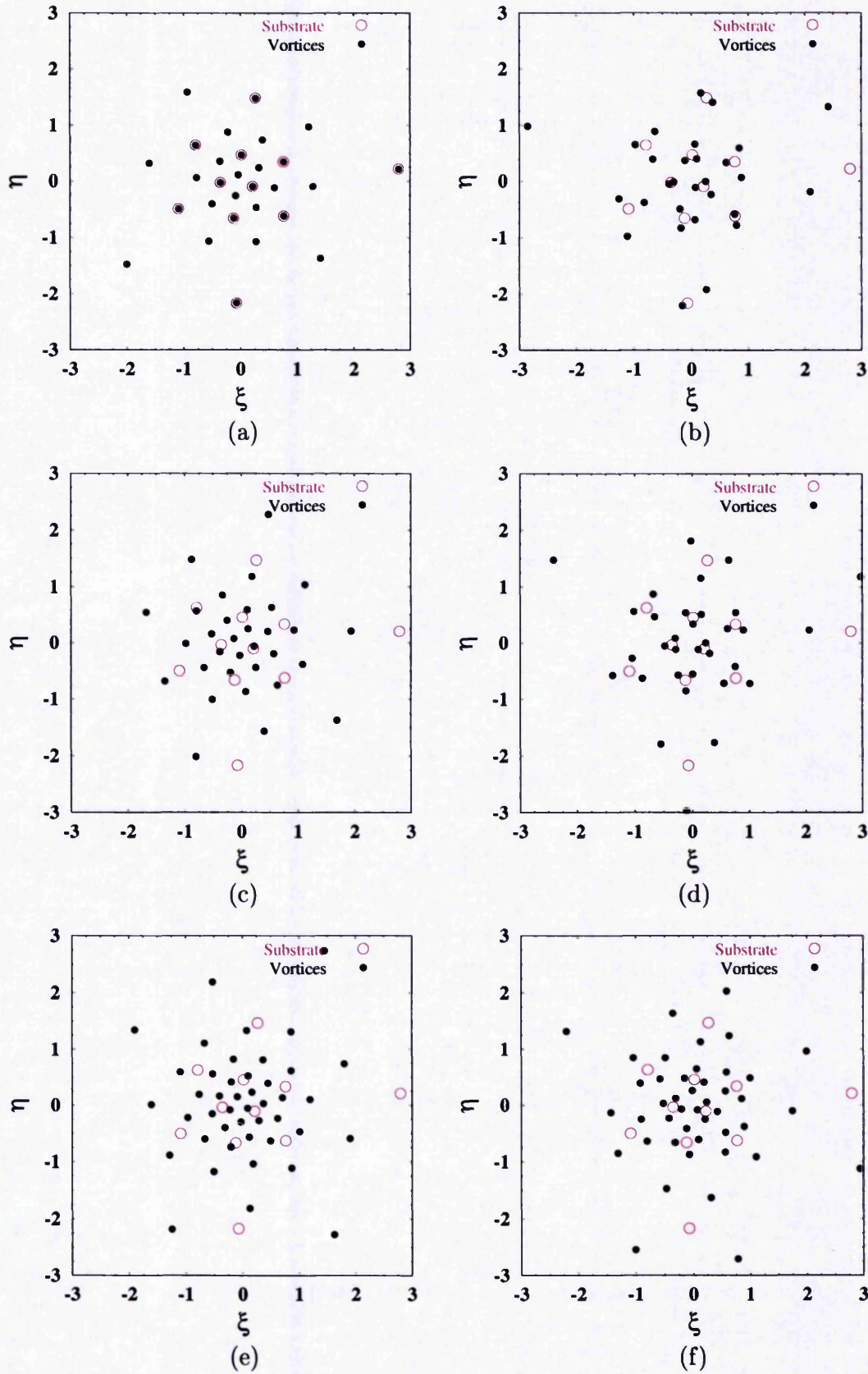


Figure 3.22: Ground-state vortex positions on the stereographic plane for the thin-film HTSC with icosahedral substrate. (a,c,e) for $g = 0.1$, $N = 32, 36, 48$. (b,d,f) for $g = 100$, $N = 32, 36, 48$ vortices respectively.

occur which allows the system to go from the usual vortex lattice (in the weak pinning regime) to the “vortex quasi-lattice” (observed in the strong pinning case). At weak pinning strengths, direct observations of the ground-state vortex positions on the sphere show that they coincide with the pictures in the pure case for all system sizes. This implies that the icosahedral substrate becomes negligible in the weak pinning regime. Also, in support of this is the fact that the Abrikosov ratio, which basically describes the ordering of vortices in the sample, is essentially identical to that in the clean case (having the same limit as $N \rightarrow \infty$). On the other hand, in both small and big systems (in the strong pinning regime), we observe that the icosahedral substrate cannot be neglected. In small-size systems ($N' < N < 6N'$) the substrate is responsible for the pinning of several vortices around each centre (as shown above). This is also observed directly on pictures of the vortex positions onto the sphere. Even in our biggest systems ($N \sim 230$) a disorder-like effect (as that of the randomly distributed pinning centres) can be seen, which we associate to pinning effects by the icosahedral substrate. The relatively-high limit of the Abrikosov ratio, 1.2863 ± 0.005079 as $N \rightarrow \infty$, that we obtain from the asymptotic behaviour of the power-law function fitted to the data is also in agreement with a non-conventional vortex lattice in the strong pinning regime.

At zero temperature, the transition between vortex lattices (as a function of the pinning strength g) has to be sharp as the states have different symmetry. We have not investigated this point at finite temperatures.

Properties at Finite Temperature

From Metropolis Monte Carlo simulations, as in previous Sections 3.1.2, 3.2.2 and the previous 3.3.1.1, we find thermal averages of several physical quantities. The treatment follows that in Eq. (3.37) but for $N' = 12$ pinning centres. This investigation is carried out on systems with $N = 72, 132$ and 432 vortices for pinning strengths of $g = 0.05, 0.1, 0.4, 1, 2, 10$ and 100 . We observe that usual quantities as the average energy and Abrikosov ratio (as functions of α_T) behave in the same qualitative fashion as those in the pure case; except that the values are slightly lower. The magnetization

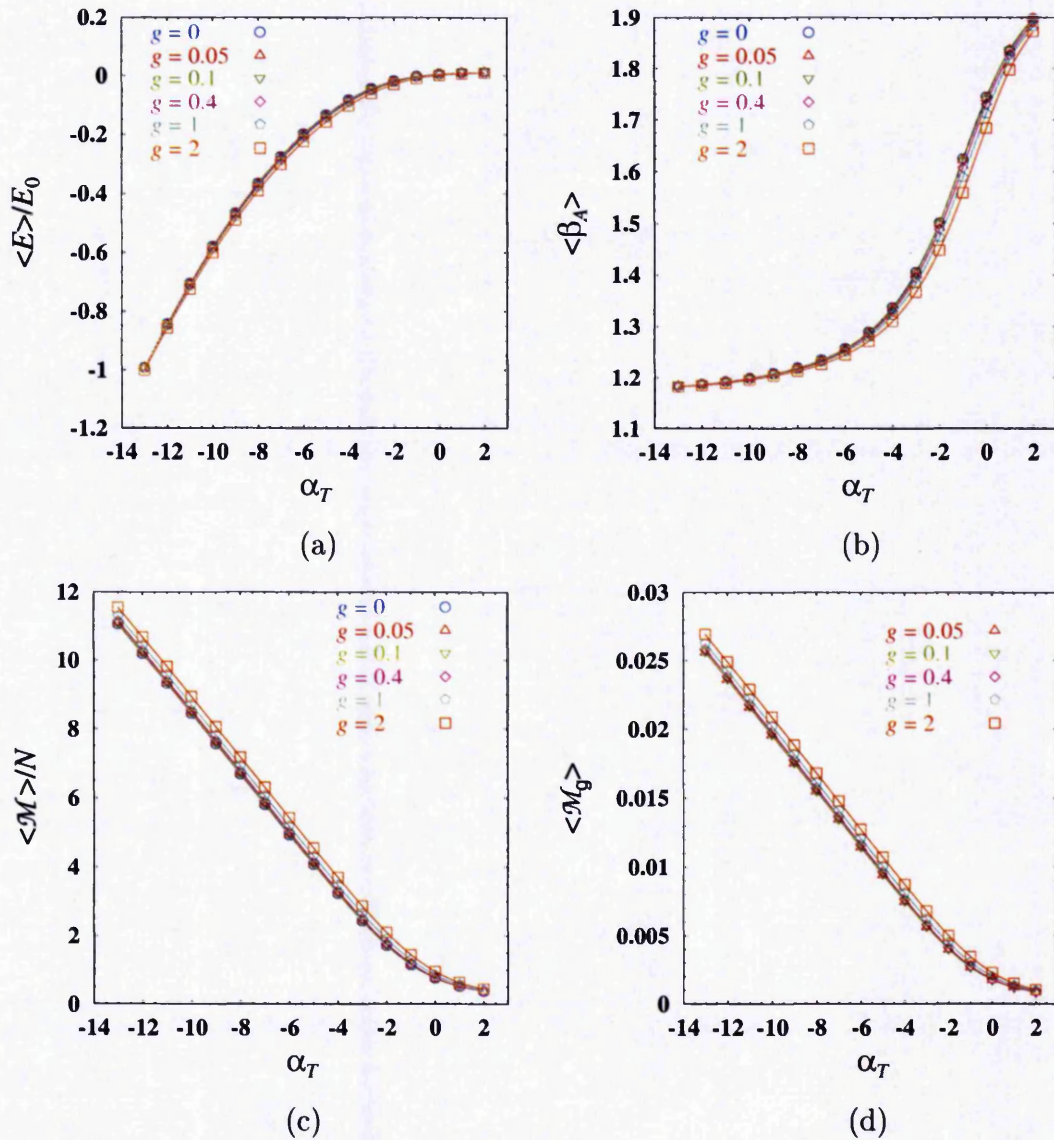


Figure 3.23: Finite-temperature properties of the thin-film HTSC with an icosahedral substrate of pinning centres for $N = 432$ vortices. (a) Average energy. (b) Abrikosov ratio. (c) Magnetization per vortex. (d) Pinning magnetization.

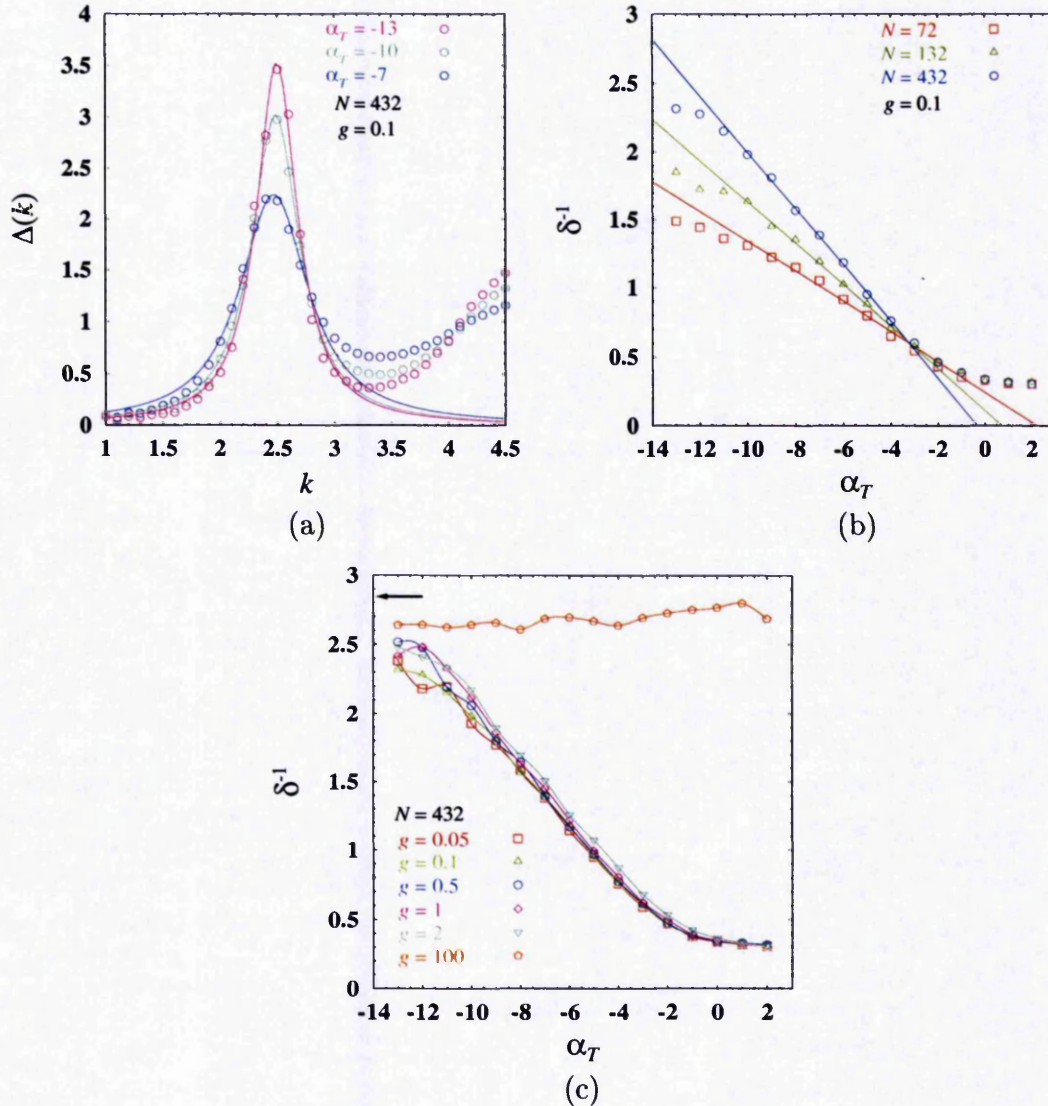


Figure 3.24: Density-density correlations for the thin-film HTSC with an icosahedral substrate of pinning centres as the temperature is lowered. (a) First peak of the rotationally averaged structure function (with Lorentzian fits) for the system with $N = 432$ vortices. (b) Extracted density correlation length, $\delta^{-1} \sim \xi_D$, (with spline fits) for all system sizes investigated (at $g = 0.1$). (c) Same as (b) but for $N = 432$ as g is varied. [The arrow marks the ground state value for this system size, δ_{\max}^{-1} .]

per vortex and pinning magnetization also present essentially identical behaviour, but these with slightly higher values (increasing for bigger g). As before, no system-size effects are observed. Figure 3.23 shows the analytical behaviour of these quantities as g is varied. Contrarily to the matching-field case, we notice that the variation with g of all properties is rather small in this case. This suggests that the effect of the icosahedral substrate on this system is somehow weak.

In addition, the structure factor does not show the same “signature” of quasi-hexagonal order (as in the case at the matching field) in the “weak” pinning regime ($g \leq 2$ in this case) for any accessible temperature. On the strong pinning side ($g = 10$ and 100 here), however, we observe the appearance of quasi-Bragg peaks (qualitatively the same as those in the matching-field case, but appearing at much higher pinning strengths). This is confirmed by plots of the extracted density correlation length (obtained by the usual Lorentzian fit method) in Figure 3.24. For weak pinning-strengths, $\delta^{-1} \sim |\alpha_T|$, but in the strong pinning regime $\delta^{-1} \sim \delta_{\max}^{-1}$ (where δ_{\max}^{-1} is the limit of δ^{-1} as $\alpha_T \rightarrow -\infty$). This seems to indicate that weak pinning is irrelevant on this system while for strong enough pinning the matching-field g - α_T phase diagram is expected to represent this sample but with the g -axis scaled to much higher values.

As the ratio N/N' increases we expect pinning effects to become rather local, and essentially non-relevant for any finite value of the pinning strength g . On the other hand, when $N \sim N'$ the behaviour of the vortex system at the matching field should be recovered.

3.3.2 Incommensurate Case

In the incommensurate case we study the effects of a regular array of 32 pinning centres onto the vortices in the spherical thin-film. As it is shown in Section 3.1.1, this periodic substrate coincides with the projection on the sphere of the icosadeltahedron with 32 vertices whose incommensurability to most system sizes can be shown by geometrical arguments. This is the only case to be described in the following.

System Properties at $T = 0$

Though it was not emphasized explicitly, several ground-state properties of the incommensurate case were already presented in Section 3.3.1.2. That is because most vortex lattices on the sphere are undoubtedly incommensurate to an icosahedral substrate. In our previous investigation, however, only the case $\bar{B} \geq \bar{B}_\Phi$ was considered. Here we extend that study to account for some values of $\bar{B} < \bar{B}_\Phi$. The ground state properties of this incommensurate case are found by the energy-minimization technique used for the previous icosahedral substrate (but for $N' = 32$). As in other cases we study system sizes $12 \leq N < 230$ for weak ($g = 0.1$) and strong ($g = 100$) pinning. In the weak pinning regime, we observe fairly similar results to those on the icosahedral substrate. In particular the Abrikosov ratios seem essentially identical (the same as for the clean case). Quantities as the average energy and specific heat (per vortex) are lower, but the magnetization per vortex and the pinning magnetization are higher. With the exception of the Abrikosov ratio, all properties show a visible kink at $N = 32$ (see Fig. 3.25). It appears interesting to us that this apparent non-analyticity in physical observables marks the system-size boundary between optimal and non-optimal pinning at weak coupling. That is, below $N = 32$ (which for this substrate with $N' = 32$ sites means $\bar{B} < \bar{B}_\Phi$), we observe that nonlinear fits in the region $12 \leq N < 32$ (using the same power-law function as in Sec. 3.1.1) tend asymptotically to lower energy and specific-heat values (but to higher magnetization and pinning-magnetization limits) than similar fits in the region $32 < N < 230$. This can be interpreted as that weak pinning is much more effective for $\bar{B} < \bar{B}_\Phi$ independently of whether the periodic substrate and the vortex lattice are either commensurate or incommensurate (i.e. what matters is the relative number of vortices to pinning centres, but not the arrangement). We believe that the region of optimal pinning, $\bar{B} < \bar{B}_\Phi$, should be independent of the particular choice of N' .

The values of quantities like the Abrikosov ratio become considerably high in the strong pinning regime ($g = 100$ here) for each system of size $N > 12$. Moreover, it develops a series of peaks of increasing height at particular values of $N < 132$, and after that decreases monotonously (rather similarly to that in the case with the

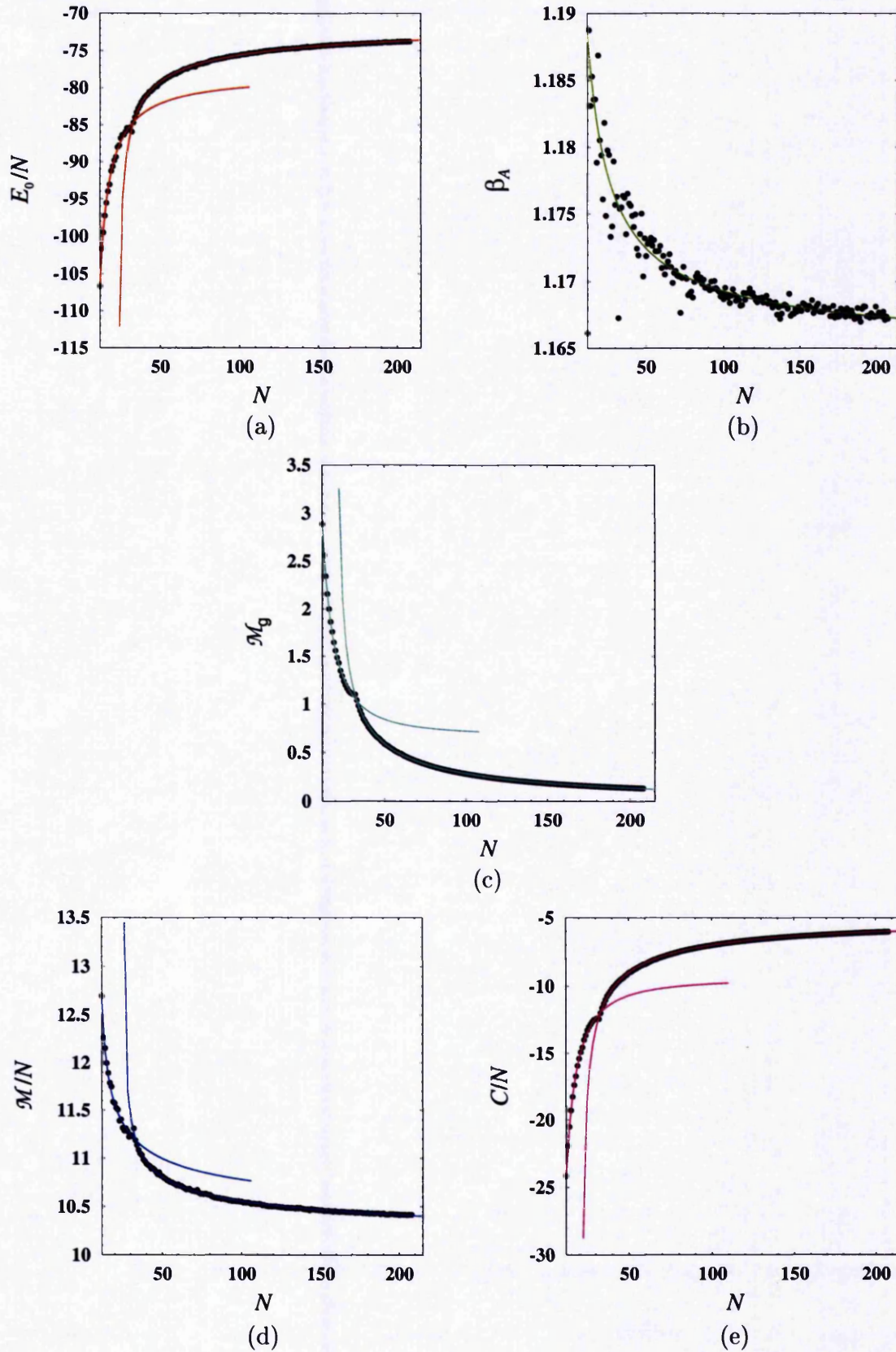


Figure 3.25: Ground-state properties of the thin-film HTSC with spherical geometry and a regular substrate of $N' = 32$ pinning centres ($g = 0.1$). (a) Energy per vortex. (b) Abrikosov ratio. (c) Pinning magnetization. (d) Magnetization per vortex. (e) Specific heat per vortex.

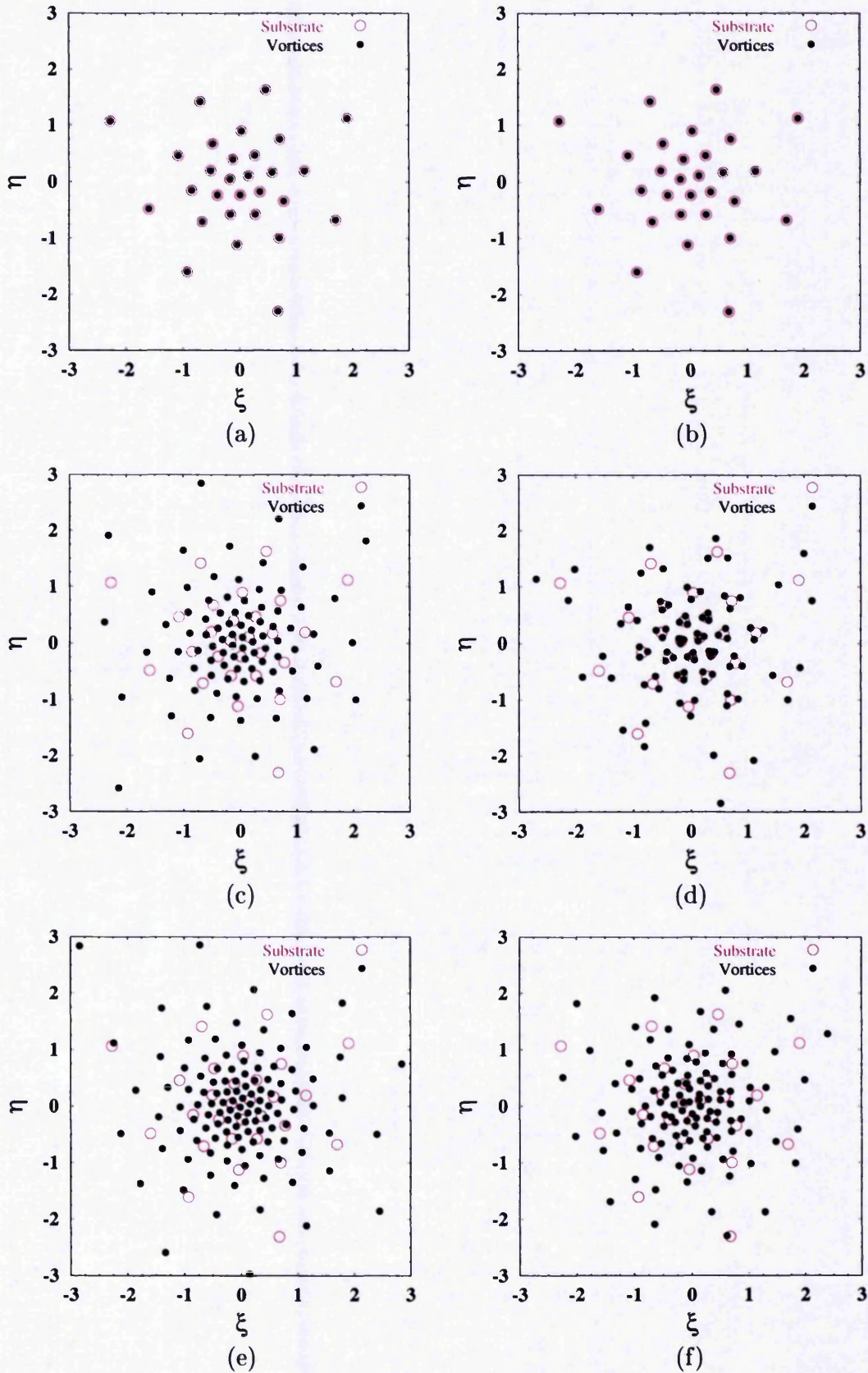


Figure 3.26: Ground-state vortex positions on the stereographic plane for the thin-film HTSC with a regular substrate of $N' = 32$ pinning centres. (a,c,e) for $g = 0.1$, $N = 32, 96, 128$. (b,d,f) for $g = 100$, $N = 32, 96, 128$ vortices respectively.

icosahedral substrate). The qualitative behaviour of the energy, specific heat and magnetization remains essentially the same as for weak pinning. This is in agreement with an optimal pinning-region, $\bar{B} < \bar{B}_\Phi$, also independent of pinning strength g .

Analogously to the case with the icosahedral substrate we find evidence for the existence of two different vortex phases as a function of the pinning strength (see Fig. 3.26). In the presence of weak pinning a vortex lattice (the same appearing in the pure system) is observed. This is consistent with the fact that weak pinning is not relevant in the $T \rightarrow 0$ limit. For the strong pinning case a vortex quasi-lattice is revealed where a bundle of vortices is pinned to each pinning centre (as long as $N' < N < 6N'$). Both, direct observations of vortex positions on the sphere and the high asymptotic-limit of the Abrikosov ratio, $\beta_A \rightarrow 1.30486 \pm 0.01403$ as $N \rightarrow \infty$, (extracted from a nonlinear fit to the data) are consistent with this. A sharp phase transition is expected to take place (about which the system changes symmetry) in the zero-temperature limit at a given pinning strength $g_c > 0.1$. No further investigation at finite temperatures has been carried out. Once again we remark the possible importance of this structural change in quantum applications, where microscopic systems are relevant.

System Properties at $T > 0$

The Metropolis Monte Carlo method is undertaken here to find thermal averages of several physical quantities. The treatment follows that in Eq. (3.37) but with $N' = 32$ pinning centres and systems with $N = 72, 132, 432$ vortices for pinning strengths of $g = 0.05, 0.1, 0.4, 1, 2, 10$ and 100. Figure 3.27 shows our results for the fundamental physical properties of this system.

We observe that quantities as the average energy and Abrikosov ratio behave not just in the same analytical fashion as those in the clean system ($g = 0$) but have basically the same values (though slightly lower) at any accessible α_T for pinning strengths $g \leq 2$. Both, the average magnetization and pinning magnetization are also quantitatively similar, but contrarily, become slightly higher.

For this incommensurate case, analogously to its counterpart with the icosahedral substrate, plots of the structure factor show no trace of quasi-hexagonal order in the

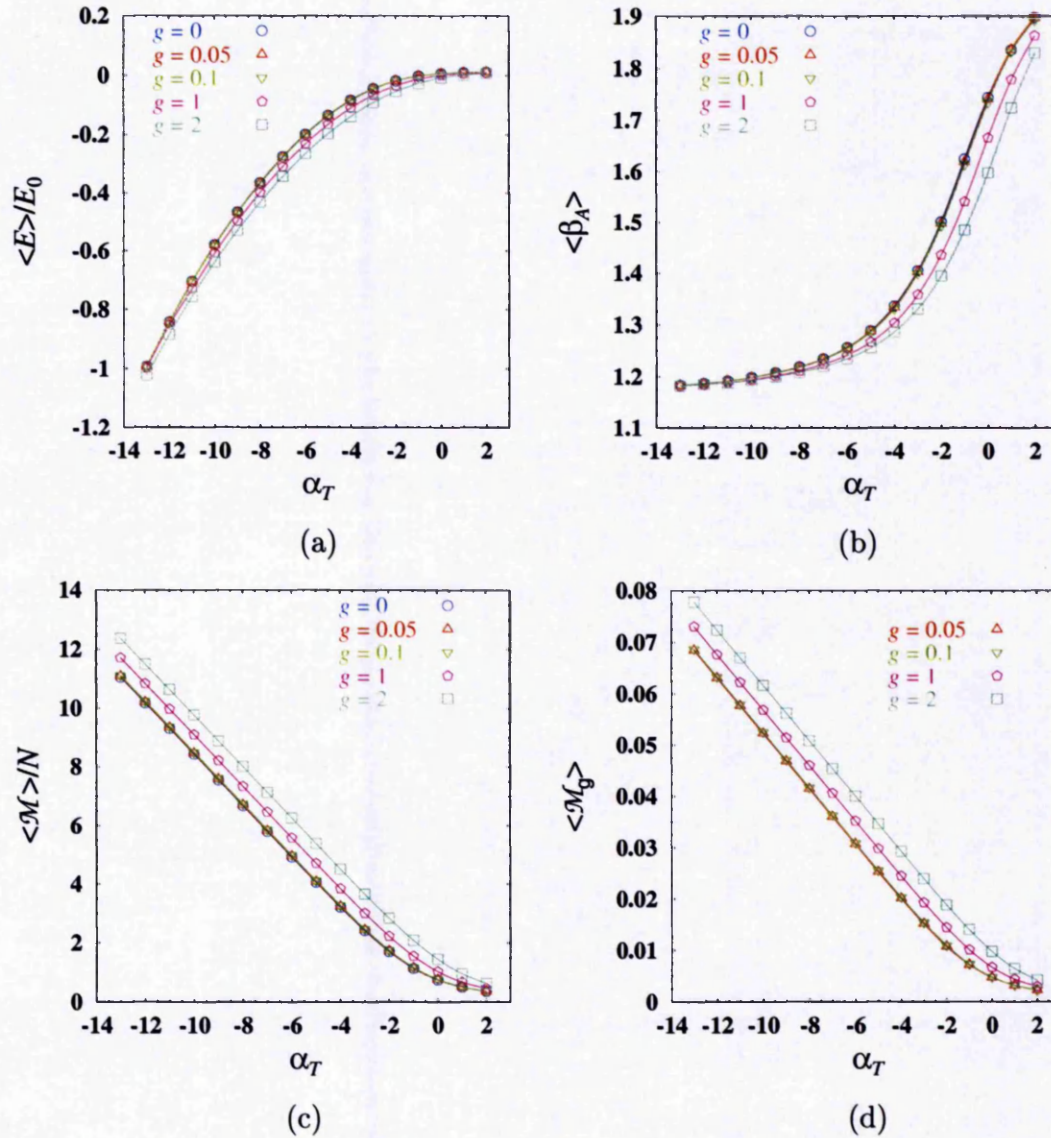


Figure 3.27: Finite-temperature properties of the thin-film HTSC with a regular substrate of $N' = 32$ pinning centres for $N = 432$ vortices. (a) Average energy. (b) Abrikosov ratio. (c) Magnetization per vortex. (d) Pinning magnetization.

weak pinning regime ($g \leq 2$ here) for any accessible temperature. In the strong pinning cases ($g = 10$ and 100), however, the appearance of quasi-Bragg peaks signals the appearance of a vortex state with phase coherence. This coherent phase appears at higher temperatures with stronger pinning, and fairly coincides with that in the commensurate-icosahedral case. Analysis of the density correlation length, $\xi_D \sim \delta^{-1}$, gives qualitatively (and almost quantitatively) the same behaviour as for the case with the icosahedral substrate (linear in $|\alpha_T|$ for weak pinning and nearly constant $\sim \delta_{\max}^{-1}$ in the strong pinning regime). Figure 3.24 represents qualitatively and to some extent quantitatively this result. This, again, seems to indicate that the same qualitative g - α_T phase diagram as for the case at the matching field (but with the g -axis scaled by a factor $\sim 10^2$) holds for this system. In this case, once again, as the ratio N/N' increases we expect pinning effects to become rather local, and essentially non-relevant for any finite value of the pinning strength g . However, when $N \sim N'$ we expect to recover the behaviour of the vortex system at the matching field.

3.4 Discussion

We devote this section to summarising the results of our investigation on the thin-film HTSC and comparing them with other studies.

The Thin Film without Disorder

It should be stressed, first of all, that the model considered in this part has been extensively investigated both on the spherical geometry [80, 83, 85] and on the flat plane with quasi-periodic or periodic boundary conditions [91, 92, 94, 95]. In the first case no indication of a vortex lattice has ever been observed at any non-zero finite temperature. This suggests a single vortex-liquid phase extending to all finite temperatures (where the vortices still exist) which freezes only at $T = 0$. We find our results consistent with this. On the other hand, essentially all kinds of studies concerning the model on the flat plane with quasi-periodic or periodic boundary conditions (PBCs) seem to agree with the existence of a low temperature vortex lattice

which melts to a vortex liquid at a finite temperature, and the phase boundary is usually claimed to be a first-order (or weakly first-order) phase transition. The results of other investigations [96, 97] have also been interpreted within the framework of the two-dimensional continuous melting mechanism [93, 98, 99, 100] proposed by Kosterlitz, Thouless, Berezinskii, Halperin, Nelson and Young (KTBHNY).

The effect of the boundary conditions appears to be one of the crucial points in the discrepancy in results, as pointed out by Dodgson [83]. While on the spherical thin-film no boundary conditions are required, the fact that each magnetic vortex interacts with the others via a long-range force (described by a logarithmic potential) makes the effect of the boundaries become relevant in finite-size systems with plane geometry. The question that still causes controversy is: why different boundary conditions give different results (as this should not make any difference in the thermodynamic limit)?

The most probable answer is that in the low-temperature (nearly crystalline) regime the system under study is not properly equilibrated. The differences in the reported behaviour probably reflect the differing effects of being out of equilibrium. On the sphere the twelve necessary disclinations seem to provide an extra degree of mobility for the vortices which appears to help to the vortex-system equilibration.

The Thin Film with Point Disorder Distributed Randomly

As for the “more realistic” thin-film model of HTSC with random disorder there have also been attempts to describe its phase diagram. On the model with spherical geometry the works of Kienappel [85], Kienappel and Moore [84], and Yeo and Moore [101] show no fundamental difference between the “pure case” and the one with random disorder. The results of those investigations seem to indicate the same type of vortex-liquid state as in the system without impurities (though with shorter density-density correlations) extending to the whole of the finite temperature mixed phase. No trace of any glassy phase is observed.

On the system with flat-plane geometry (including randomly-distributed point disorder) the consensus is that this quenched random disorder turns the vortex lattice into a Bragg-glass phase while the vortex liquid phase remains a liquid [102, 103, 104].

The results of our investigation seem to indicate the presence of a “vortex-glass” phase described by amorphous-solid correlations in the structure factor where previous studies [85, 84] report a vortex-liquid state. Even at the weakest pinning strength (which is smaller than all values investigated in Ref. [85]) our system appears “frozen” in this glassy state. This suggests that there is a fundamental disagreement between the approach followed here and in Refs. [85, 84] (see the fifth footnote in Appendix A.3.1.2), which should be re-examined.

The Thin Film with a Regular Substrate of Pinning Centres

The problem of the thin-film HTSC with an underlying regular-substrate of pinning centres in the spherical geometry was first considered (though only for the commensurate case at the matching field) in the work of Dodgson [83]. In that investigation an XY -type phase transition was predicted in the matching-field case, which our work seems to support. At the continuous transition-line pairs of vacancy-interstitial vortices unbind so as to lose phase coherence when the temperature is increased. This transition also shows a depinning-like behaviour, where vortices overcome the strength of the pinning potential and move freely as temperature is increased (which does cause a loss of phase coherence).

For magnetic-induction magnitudes different to the matching field, our investigation suggests that weak pinning becomes irrelevant down to low enough temperatures when $B > 6B_\Phi$. However, if pinning is strong enough then the system may behave as if it were tuned to the matching field. In this case a phase-coherent phase appears at low temperatures, but no pinning transition takes place. Though we did not report finite temperature results on the $B < B_\Phi$ case (i.e. when there are more pinning centres than vortices), we carried out a short investigation in very restricted system sizes ($N = 12, 32$ for $N' = 72, 132, 432$). The result from that study suggests that in this regime phase coherence sets in at higher temperatures (for the same pinning strength) than at the matching field (regardless of whether the vortex lattice and the pinning substrate are commensurate or incommensurate). This important result also seems to indicate that the only relevant parameter in the model (apart from α_T and

g) is the ratio of the magnetic induction to the matching field, $B/B_\Phi = N/N'$.

Finally, there are interesting observations even on the ground-state properties of the system for $B_\Phi < B < 6B_\Phi$. In the weak pinning regime the pure-system vortex lattice is present, but not for strong enough pinning. In the later case each pinning centre is able to pin several pancake vortices about it, but none at its core. The existence of two qualitatively different vortex “lattices” suggests a zero-temperature phase transition as g is increased above 0.1.

Chapter 4

Simulations on the Spherical Layered-Superconductor

The aim in this chapter is to extend the numerical work we have carried out on the thin-film high- T_c superconductor (HTSC) to the case of a strongly anisotropic layered-HTSC (in the same spherical geometry). Thus, the topics to be discussed here are essentially the layered counterparts of those described in Chapter 3. Again, our analysis starts with the introduction of the form of the energy function for an ideal pure-sample suitable to perform computer simulations within the LLL approximation. This is derived from the energy functional given by the Lawrence-Doniach (LD) model already introduced in Chapter 2. Afterwards we proceed to consider extra energy terms which describe columnar defects (along the c -axis) distributed both randomly and in regular patterns. In all cases only non-zero finite temperature properties are investigated. The chapter ends with a discussion on the main results of the layered HTSC, both with and without columnar defects. Derivations for the LLL expressions used throughout this chapter are provided in Appendix A.

4.1 Clean Layered-Superconductor

As in the thin-film model studied before, the theoretical framework for this numerical investigation is set up by defining precisely the physical model. In this case we assume a superconducting spherical-shell of average radius R composed by a set of M layers, each of thickness $d_0 \ll R$, separated by a distance $s \geq d_0$ from its adjacent neighbours. From the geometrical centre of the spherical-shell a radial magnetic field is applied, with a magnetic induction defined by the vector potential $\mathbf{A} = (\bar{B}R^2/r) \tan(\theta/2) \hat{\phi}$. We also suppose that the material composing this sample is a strongly anisotropic high- T_c superconductor, with the anisotropy in the radial direction. Thus, this sample should accept a description in terms of the LD-LLL model presented in Section 2.2.1. Again, within the LLL approximation we assume a “uniform” strength of the magnetic induction throughout the sample given by $B = \bar{B} \approx B(R)$ and use the LD-LLL energy functional in Eq. (2.50) with the scaled order parameter expanded in terms of the LLL energy eigenfunctions in the spherical geometry as

$$\tilde{\psi}_{n,L}(\theta, \phi) = \tilde{Q} \sum_{q=0}^N v_{n,q} \psi_{q,N}(\theta, \phi), \quad (4.1)$$

where $\tilde{Q} = |2\pi/\alpha_T|^{1/2}$, $\{\psi_{q,N}\}$ are the LLL eigenstates given in Eq. (3.2) and $v_{n,q}$ are the complex coefficients defined in Eq. (2.47).

By introducing the LLL expansion for the order parameter of Eq. (4.1) into the LD energy functional of Eq. (2.50), and calculating the integrals over the surface of the two-dimensional sphere of radius R (taking care of the scaled variables, as explained in Section 3.1), the energy functional of the clean layered-superconductor (per unit of thermal energy $k_B T$) is reduced to the function of $M(N+1)$ complex variables $\{v_{n,q}\}$, given by [85]

$$\frac{\mathcal{H}_c(\mathbf{v})}{k_B T} = \sum_{n=1}^M \left[\alpha_T \sum_{q=0}^N |v_{n,q}|^2 + \frac{1}{2N} \sum_{p=0}^{2N} |U_{n,p}(\mathbf{v})|^2 + \eta |\alpha_T| \sum_{q=0}^N |v_{n+1,q} - v_{n,q}|^2 \right], \quad (4.2)$$

where we have denoted $\{v_{n,q}\} = \mathbf{v}$ and the parameter for the interlayer coupling $\eta = 1/\bar{s}^2$. In a similar fashion to the thin-film limit, we have defined the quadratic

form on the coefficients \mathbf{v}

$$U_{n,p}(\mathbf{v}) = N\gamma_{p,2N} \sum_{q=0}^N \mathcal{N}_{q,N} \mathcal{N}_{p-q,N} \Theta(p-q) \Theta(N-p+q) v_{n,q} v_{n,p-q}, \quad (4.3)$$

with identical expressions for $\gamma_{p,2N}$ and $\Theta(x)$ as those in Section 3.1. Again this resummation makes computer calculations rather more efficient.

We perform computer simulations on the clean layered-superconductor defined in Eq. (4.2) using the Metropolis Monte Carlo (MC) method and report our results in the following.

4.1.1 Physical Properties and Order-Parameter Ratios

In this case, and throughout this chapter, we investigate the behaviour of different physical properties as functions of the effective temperature parameter α_T . Most of them have already been defined for the thin film in Chapter 3 and are derived in general for the layered system in Appendix A.6. We assume these expressions in the following sections. Most of the considerations remarked on the MC simulations in the thin-film case are also undertaken here. The only fundamental difference is the increase of the number of independent variables from $N+1$ (v_q , $q = 0, 1, \dots, N$) to $M(N+1)$ ($v_{n,q}$, $n = 1, 2, \dots, M$ and $q = 0, 1, \dots, N$).

For the clean layered-superconductor we have investigated systems with M layers and N vortices per layer in $\{(N, M) = (72, 18), (72, 12), (50, 15), (50, 10), (32, 12), (32, 8)\}$. The phase plane η - α_T (where η is the interlayer-coupling strength) has been sampled for $\eta = 0.14142, 0.5, 1, 2, 10$ and 100 , and $-13 \leq \alpha_T \leq 2$ (while cooling as in the thin film case). For this system we have calculated thermal averages of the total energy (normalized to E_0), Abrikosov ratio, magnetization per vortex, and the “Josephson-coupling ratio” defined as

$$\Gamma = \frac{\frac{1}{M} \sum_{n=1}^M |\psi_{n+1} - \psi_n|^2}{\frac{1}{M} \sum_{n=1}^M |\psi_n|^2}, \quad (4.4)$$

with LLL expression given in Appendix A.6. Figure 4.1 shows results for our biggest system, $(N, M) = (72, 18)$, as η increases. As before these quantities are defined so as to be intensive. Therefore they are not affected by finite-size effects but just by variations on temperature or interlayer-coupling parameter.

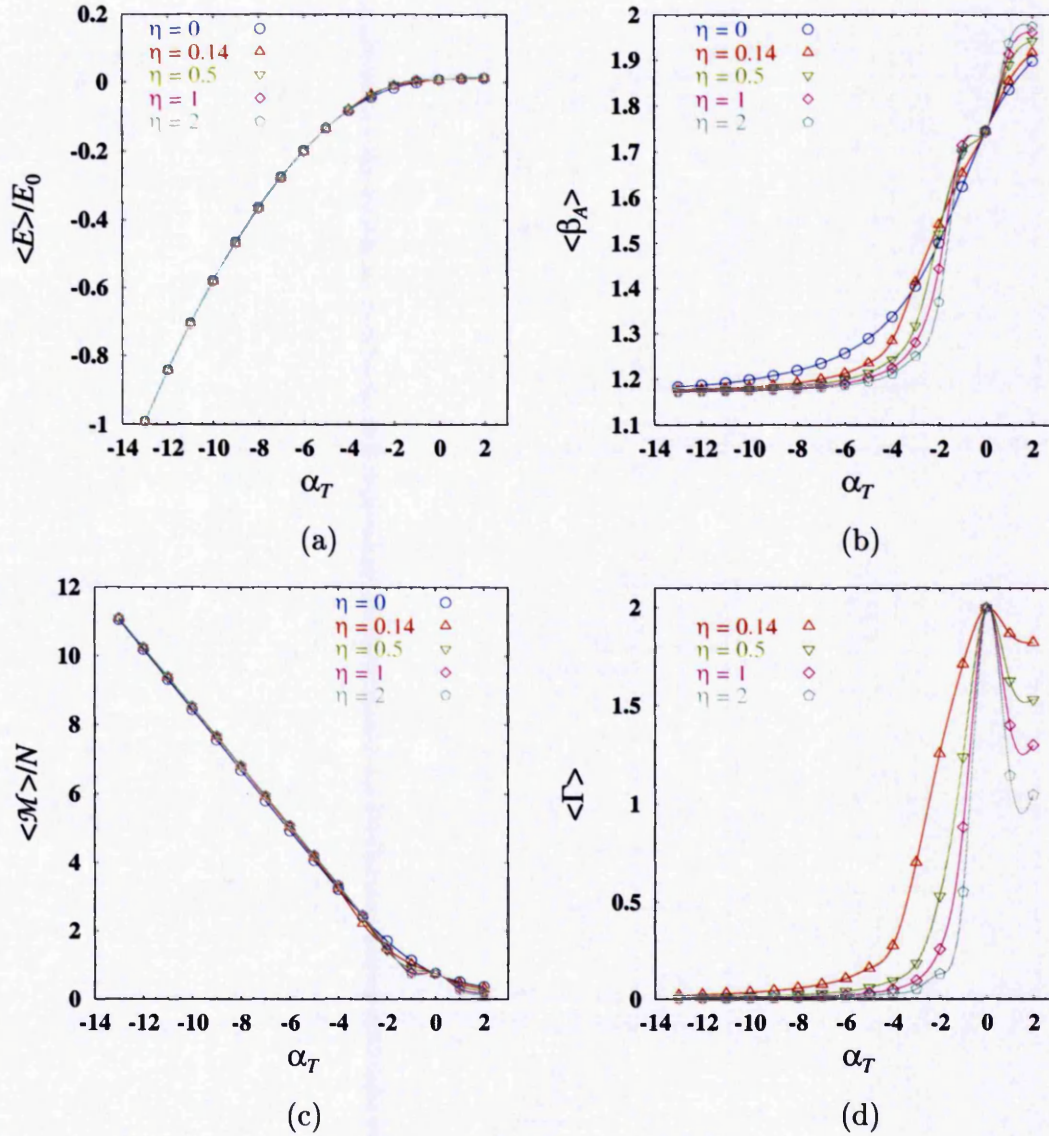


Figure 4.1: Finite-temperature properties of the clean layered-superconductor with spherical geometry. (a) Average energy. (b) Abrikosov ratio. (c) Magnetization per vortex. (d) Josephson-coupling ratio.

In contrast to the smoother behaviour of the similar curves in the thin-film case ($\eta = 0$ in all plots), we observe a faster drop in quantities like $\langle\beta_A\rangle$ and $\langle\Gamma\rangle$. This suggests a faster ordering (both intralayer and in this case interlayer) than in the clean thin-film. The intralayer quasi-hexagonal order is deduced from the low $\langle\beta_A\rangle$ values (compared to the thin-film limit), while the coupling of the order parameter in adjacent layers (associated with a phase of “disentangled” flux-lines) is concluded from the nearly zero values of $\langle\Gamma\rangle$.

At $\eta \leq 2$ we can still observe a region just below $\alpha_T = 0$ where $\langle\beta_A\rangle$ and $\langle\Gamma\rangle$ are considerably high. From the results on the thin film we can associate, a priori (though we will see that this does occur), this high temperature region to one with a vortex liquid-phase with entangled flux-lines (or rather a liquid of decoupled pancake-vortices). We expect this phase to exist in the phase diagram η - α_T , but a complete picture of the whole diagram is not revealed by these quantities.

It is worth mentioning that the apparent singular-behaviour of all quantities in Fig. 4.1 is just an artifact of the way we perform the sampling in the α_T - η plane. As we always vary the parameters α_T and η independently, the case $\alpha_T = 0$ appears for all values of η . At this point the term that couples layers in Eq. (4.2) vanishes and therefore the system behaves as a stack of decoupled layers (effectively two-dimensional). That is the reason why all curves have the same two-dimensional value at $\alpha_T = 0$.

4.1.2 Vortex Positions, Structure and Correlations

Aimed at determining the different phases of vortices, we study both the vortex positions (in all forms: angular coordinates, stereographic projection and directly on the sphere) and structure factor in each layer as the temperature is lowered. For all system sizes considered (at $\eta = 0.14142$) we find a phase of inter-layer decoupled-pancake-vortices on and above $\alpha_T = -3$, but a coupled phase for $\alpha_T \leq -4$ (with an increase of vortex coupling as temperature is lowered). This is shown in Figure 4.2 (a, c, e, respectively), where angular coordinates of the pancake vortices in all layers are plotted on the same θ - ϕ plane. Here symbols of the same type and colour correspond to the vortex positions in a given layer. The measurement of the vortex positions at each

temperature is taken after 1.2×10^5 MCS when the system is expected to have reached equilibrium at these considerably high temperatures. At $\alpha_T = -3$ (see Fig. 4.2(a)) a random distribution of pancake vortices about the plane can be observed. We associate this with a phase of decoupled pancake-vortices (also present for $\alpha_T > -3$, but not shown). At $\alpha_T = -4$ (see Fig. 4.2(c)), however, a structure of pancake-vortex domains appear (which we associate with a phase of disentangled flux-lines, though not completely straight).¹ Below $\alpha_T = -4$ a sharper localization of the pancake-vortex domains (here represented for $\alpha_T = -5$ in Fig. 4.2(e)) is visible. This is consistent with flux lines getting straighter with decrease of temperature, which we observe directly on all of our plots down to $\alpha_T = -13$. From similar qualitative-analyses we find that the phase of disentangled flux-lines extends to higher temperatures as the interlayer coupling η increases, but (at least for the systems studied here) seems not to depend on system size. For this case at $\eta = 0.14142$ the coupling transition-temperature is expected at an effective temperature between $\alpha_T = -4$ and -3 .

This qualitative argument is consistently confirmed by a change of behaviour of the interlayer phase-correlation-function, which on the layered system is defined as

$$C_p(m) = \frac{4\pi R^2}{Q^2} \left\langle \frac{1}{M} \sum_{n=1}^M \overline{\psi_n^*(\mathbf{r})} \psi_{n+m}(\mathbf{r}) \right\rangle, \quad (4.5)$$

with its LLL expression given in Appendix A.6. Figure 4.3(c,d) shows the decay in $\text{Re}[C_p(m)]$ as the distance along the c -axis, ms , increases. Phase correlations above the coupling transition ($\alpha_T \geq -3$), denoted by open symbols, decay exponentially (in agreement with short-ranged correlations), while below the transition (filled symbols) just decrease algebraically (consistent with a state with quasi-long-range order).

At first sight, the appearance of quasi-long-ranged inter-layer phase correlations seems to indicate XY -type behaviour (which should be consistent with the melting scenario). However, there exists a more natural explanation in terms of the effects of thermal fluctuations on phase order. Moore [77] and Chin and Moore [78] have predicted this kind of power-law decay of the phase correlation-function below certain

¹In the literature this kind of behaviour of vortices is also referred to phases of “decoupled” or “coupled” pancake-vortices instead of “entangled” or “disentangled” flux-lines (or viceversa).

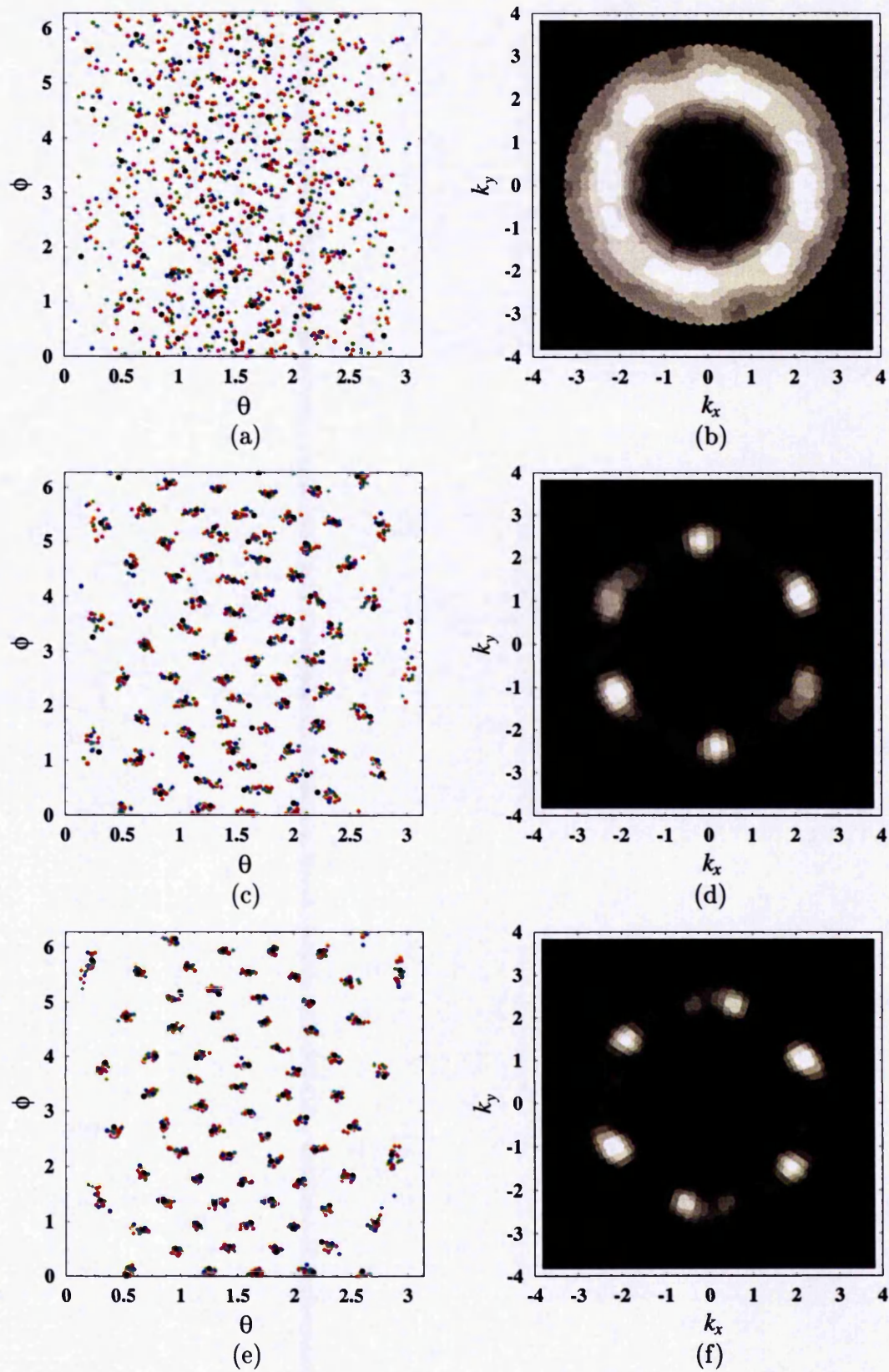


Figure 4.2: Angular vortex-positions (in all layers) and structure factor (at layer $M/2$) of the clean layered-superconductor with interlayer coupling $\eta = 0.14142$ for $(N, M) = (72, 18)$ as the temperature is lowered: $\alpha_T = -3, -4, -5$. [(a,b),(c,d),(e,f) respectively.] In (a,c,e) equal symbols (and colours) represent the same layer.

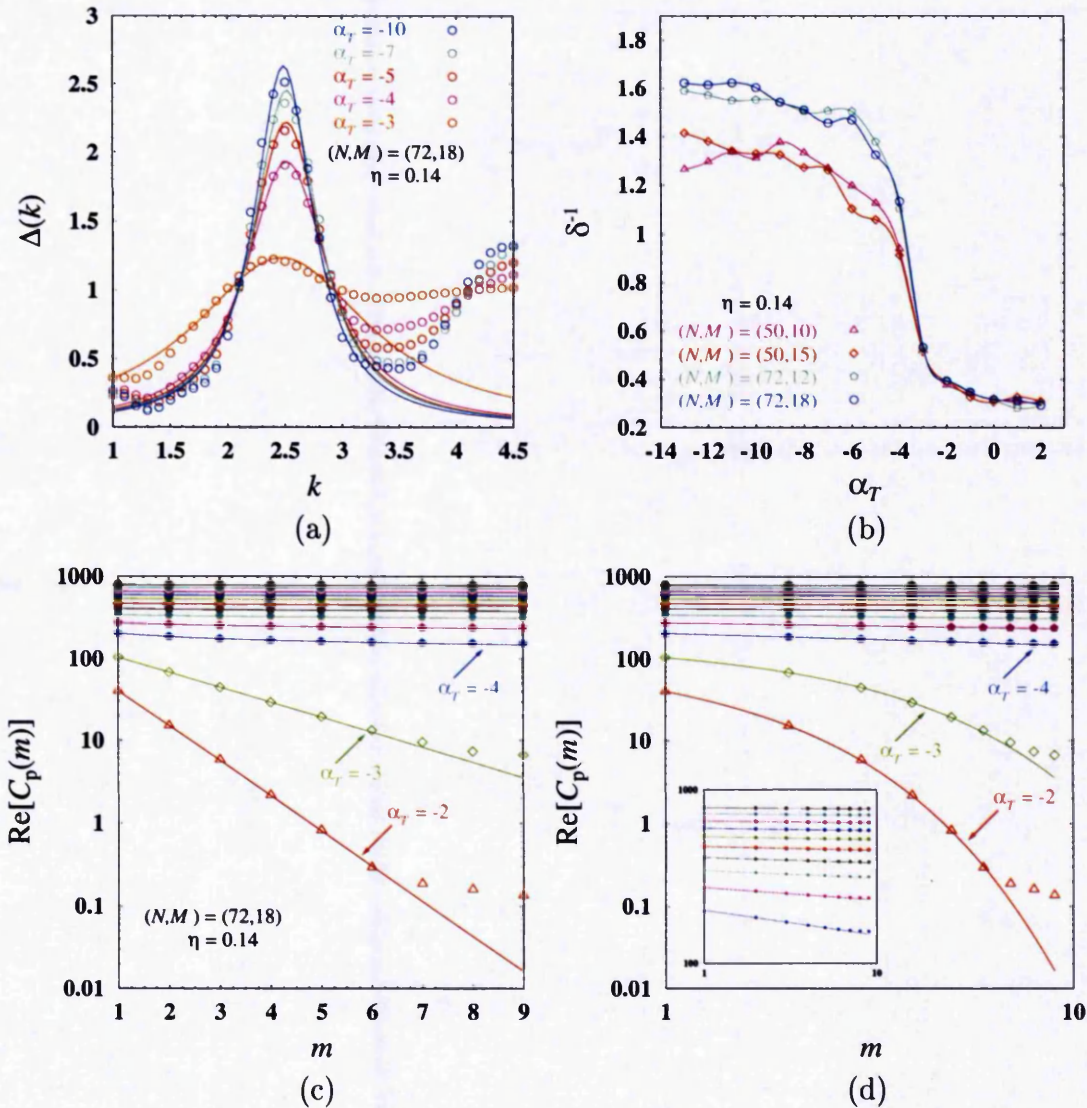


Figure 4.3: Intra- and inter-layer correlations on the clean layered-HTSC as the temperature is lowered. (a) First peak of the rotationally averaged structure function (with Lorentzian fits) for the system with $(N, M) = (72, 18)$ at $\eta = 0.14142$. (b) Extracted density correlation-length, $\delta^{-1} \sim \xi_D$, (with spline fits) for different system sizes at $\eta = 0.14142$. (c) Log-linear plot of the inter-layer phase-correlation-function, $\text{Re}[C_p(m)]$, as a function of the “distance” along the c -axis showing exponential decay of correlations above the transition (open symbols). (d) Log-log plot of $\text{Re}[C_p(m)]$ remarking power-law decrease of correlations below the transition (filled symbols). The inset is just a magnification of the curves below the transition. Fits are shown for $\alpha_T = -2, -3, -4, \dots, -13$ from bottom to top curves, except on the inset (there $\alpha_T = -4, -5, \dots, -13$ from bottom to top). The expected transition temperature lies between $\alpha_T = -4$ and -3 . The system in (c,d) is the same as in (a).

effective temperature for distances smaller than the relevant correlation length. In their calculations for a continuous three-dimensional sample the phase correlation function is expected to behave as $\text{Re}[C_p(m)] \sim 1/m^\tau$ with τ a temperature-dependent exponent. A straightforward calculation shows that the temperature dependence can be extracted as $\tau \sim 1/|\alpha_T|^2$. From the linear fits to the log-log data we have calculated $\tau = \tau(\alpha_T)$ for the different values of η and have found an exponent ranging between 2.2 and 2.02 for the dependence on $1/|\alpha_T|$ of τ . We find the value of this exponent to decrease with increasing of η , which is expected as the continuum limit corresponds to $\eta \rightarrow \infty$ (where the calculation of Moore [77] was done).

As for intralayer correlations we study the density-density correlation function in reciprocal space, $S(\mathbf{k})$, defined in Eq. (3.16). We measure numerically this quantity in each layer as temperature is lowered and find a sudden appearance of quasi-hexagonal Bragg-peaks at the temperature where the coupling transition is observed. Figure 4.2(b,d,f) shows this effect on the layer “at the middle” of the system. Above the coupling transition (at $\alpha_T = -3$, Fig. 4.2(b)) no clear quasi-hexagonal order is present, while below (for $\alpha_T \leq -4$, Figs. 4.2(d,f)) quasi-Bragg peaks are visible. At temperatures about the coupling transition these quasi-Bragg peaks still fluctuate in positions, and this can be taken as evidence for a vortex-liquid phase.

The rotationally averaged structure function, $\Delta(k)$, and its associated density correlation length, $\xi_D \sim \delta^{-1}$, (as defined in the part on structure of Section 3.1.2) give quantitative account of the rapid raise of intralayer correlations as the coupling transition is approached. Figure 4.3(a) shows plots of the first peak in $\Delta(k)$ for the system with $M = 18$ layers and $N = 72$ vortices per layer at $\eta = 0.14142$ (as temperature is lowered). There we can see that, despite the system size is relatively small, a Lorentzian again gives a proper fit to this peak (consistent with exponential decrease of density correlations in real space). For this, and for other system-sizes (at the same $\eta = 0.14142$), we extract the density correlation length shown in Fig. 4.3(b). An abrupt raise in intralayer density-correlations can be clearly observed at the temperature where coupling occurs ($-4 < \alpha_T < -3$). The vortex phase below the transition has been previously interpreted as a rather viscous liquid with quasi-crystal

correlations [85].

As the interlayer coupling-parameter η increases, the same qualitative abrupt-raise of density correlations is observed to appear at higher temperatures (parallel to the coupling transition). This suggests that rapid raise in both interlayer and intralayer correlations occurs simultaneously at the coupling transition.

All these features have been commonly interpreted as a first order melting-transition [105, 106] where decoupling of pancake-vortices in all layers occurs simultaneously (as the temperature is increased). In other simulations on a continuum model, Wilkin and Jensen [107] report a first-order transition associated with layer-decoupling and a further crossover to melting. Other investigations [108, 109] report a first order transition ending at a critical point which separates liquid phases of coupled and decoupled pancake-vortices. In our work we find quantitative agreement with the phase diagram on this scenario up to the claimed critical end-point. Beyond that we have not enough data to decide whether the point also appears in our simulations. This results in the possibility of interpreting our simulations in any of those scenarios (each case shown with an exponential fit to data from Ref. [85] in Fig. 4.4).

In the first case (Fig. 4.4(a)), no real phase boundary exists. The line of first order transitions separates coupled and decoupled vortex-liquid phases. On and above the critical point one can drive the vortex system continuously from a decoupled liquid to a coupled one (or viceversa). On the other hand, the second case (Fig. 4.4(b)) presents a phase boundary which separates a low-temperature coupled vortex-lattice from a decoupled vortex-liquid. The line is again of first order transitions, but in this case separating phases of different symmetry (in a fluid there is translational invariance, whereas in a solid this symmetry is broken). Our simulations show evidence for an interlayer coupling transition accompanied by an abrupt raise of in-layer density correlations. This later feature could also be interpreted as evidence for “freezing” allowing for the possibility of the diagram in Fig. 4.4(b). Notice, however, that any of those cases is congruent with a vortex-liquid phase extending to all finite temperatures in the thin-film limit, $\eta \rightarrow 0$.

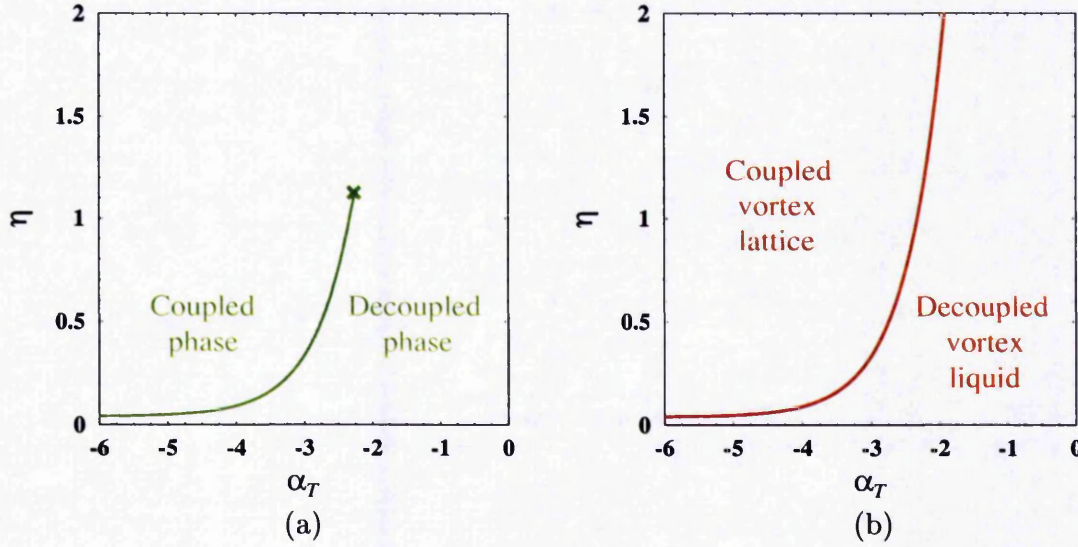


Figure 4.4: Possible η - α_T phase diagrams for vortices on the clean layered-HTSC with spherical geometry. (a) The coupling-decoupling scenario ending at a critical point. (b) The flux-lattice melting scenario. [In both cases the curve results from an exponential fit to the data in Ref. [85].]

4.2 Pinning by a Random Substrate of Columnar Defects

This section is concerned with a model of layered high- T_c superconductor in the presence of columnar defects distributed randomly about the a - b “planes” such as those first produced by irradiating samples with high-energy ions [110]. The numerical approach, for the spherical system we are investigating, suggests to consider the LD-LLL model for the clean layered-superconductor in Eq. (2.38) with the addition of a random disorder energy term given by

$$\mathcal{H}_{rs}[\psi_n; \Omega] = \sum_{n=1}^M d_0 \int d^2r \Omega(\mathbf{r}) |\psi_n(\mathbf{r})|^2, \quad (4.6)$$

(“rs” for random substrate) where the same random disorder function as that for its thin-film counterpart in Sec. 3.2, $\Omega(\mathbf{r})$, is assumed in every single layer n so as to describe columnar defects. This energy term is completely analogous to the one in the thin-film case, Eq. (3.23). Following the same integration as before we can write the

random columnar defect energy-contribution (within the LLL approximation) as

$$\frac{\mathcal{H}_{rs}(\mathbf{v}; \mathbf{a})}{k_B T} = \sum_{n=1}^M \sum_{q=0}^N \left[\sum_{l=0}^{l_{\max}} a_l^0 I_{q,l}^0 |v_{n,q}|^2 + 2\text{Re} \sum_{l=1}^{l_{\max}} \sum_{m=1}^l a_l^m I_{q,l}^m v_{n,q+m}^* v_{n,q} \right], \quad (4.7)$$

where a factor $\Theta(q+m)\Theta(N-q-m)$ is implied in the second sum and terms with $l > l_{\max} \approx 7R$ (with R the average radius of the sphere) have been neglected. Again, the coefficients a_l^m are those introduced in Section 3.2. Eq. (4.7) shows explicitly that this energy interaction has no interlayer contribution (it is purely intralayers) and does not depend on α_T . We add Eqs. (4.2) and (4.7) to obtain the total energy of the layered superconductor with randomly distributed columnar defects (parallel to the c -axis); and use the Metropolis Monte Carlo method to perform computer simulations on this model. Before describing our results we outline the theoretical expectation for this problem.

Theory of Pinning by Correlated Disorder

The phenomenon of pinning by correlated disorder can be found in cuprate high- T_c superconductors (HTSCs) as a consequence of the existence of twin boundaries, grain boundaries, etc. or to the introduction of columnar defects into the sample. In our description here, we shall concentrate on the effects of columnar defects only, and we will consider the cases when the distribution of such columnar pins (which are perpendicular to the copper-oxide layers) is either random or in a regular fashion. Nelson and Vinokur [111, 112] have performed a map between a system of flux lines in HTSCs pinned by columnar defects and the problem of boson localization in two dimensions. This theory predicts a low temperature Bose-glass phase, in which every magnetic vortex is trapped in a columnar defect, separated from a high temperature liquid of entangled flux-lines. The phase boundary is believed to be a line of continuous phase transitions, $T_{BG}(B)$ (see Figure 4.5). Within the Bose-glass state a “Mott insulator” phase is expected to be present when the magnetic induction equals the matching field, B_Φ . As the number of vortices matches the number of columnar defects in the Mott-insulator phase, then every single columnar defect should be occupied by a flux-line (with no free lines remaining).

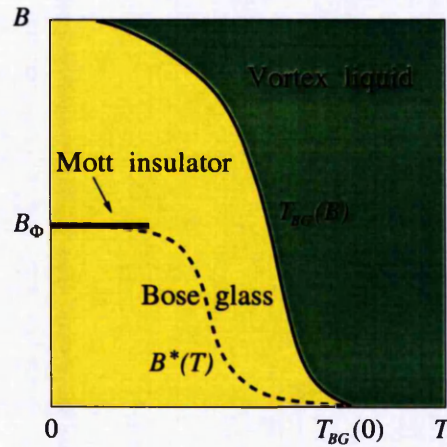


Figure 4.5: Phenomenological B - T phase diagram of a type-II superconductor in the presence of strong correlated disorder. [Adapted from Ref. [113].]

In the work of Wengel and Täuber [113] it is found that when columnar pins are distributed randomly about the Cu-O planes, the Mott insulator phase is suppressed. However, when columnar pins are introduced so as to form regular arrays (they refer to a nearly triangular defect distribution in their work), the Mott insulator phase can be observed.

In Fig. 4.5 the dashed line $B^*(T)$ represents a crossover between strongly (below) and weakly (above) pinned Bose-glass. A noteworthy feature is that the Bose-glass phase (product of the correlated disorder) is essentially different from the common vortex glass due to point-like pinning centres. The former is expected to be described by two phase correlation-lengths, ℓ_{\parallel} and ℓ_{\perp} , along and perpendicular to the columnar defects respectively which diverge at T_{BG} with critical exponents ν_{\parallel} and $\nu_{\perp} = \nu_{\parallel}/2$ respectively. However, the later should be described by just one phase correlation-length, ℓ , as point disorder is distributed isotropically. Since the work of Nelson and Vinokur [111, 112], a scaling relationship for the correlation lengths in the Bose-glass phase was predicted. Recently, the work of Lidmar and Wallin [114] has pointed out differences to the predictions to that scaling theory. This has lead to Nelson and Vinokur to a further revision, Ref. [115], to account for the distinction between \mathbf{B}_{\perp} and \mathbf{H}_{\perp} so as to obtain the correct scaling form.

4.2.1 Basic Quantities

As in the clean layered HTSC of the previous section, we first look at fundamental quantities like energy, magnetization, Abrikosov and Josephson-coupling ratios as functions of the effective temperature parameter α_T . For this case we study, again, systems of size $(N, M) = (72, 18), (72, 12), (50, 15), (50, 10), (32, 12)$ and $(32, 8)$ but only for the interlayer coupling $\eta = 0.14142$ and pinning strength $\sigma^2 = 20/N$ (as explained in Section 3.2). We sample the range of temperatures $-13 \leq \alpha_T \leq 2$ starting with a random configuration for $\{v_{n,q}\}$ at $\alpha_T = 2$ and cooling the system down. This way, thermal averages of these physical properties and order-parameter ratios are obtained. Figure 4.6 shows our results for the biggest systems $(N, M) = (72, 18), (50, 15)$ and $(32, 12)$ (that is, for pinning strengths $\sigma^2 = 0.277777, 0.4$ and 0.625 respectively) at Josephson interlayer-coupling $\eta = 0.14142$. All these are compared to the pure layered-system ($\sigma^2 = 0$) at the same $\eta = 0.14142$.

It can be observed that all four properties in Fig. 4.6 behave in the same qualitative fashion as those of the defects-free layered HTSC ($\sigma^2 = 0$). Both the “normalized” average energy and the magnetization per vortex have slightly different values depending on pinning strength. Though this must be connected with changes to the vortex lattice (imposed by columnar defects), the most revealing evidence of intralayer disordered-state of vortices (even at low temperatures) appears from the high $\langle\beta_A\rangle$ values at all temperatures (Fig. 4.6(b)). Compared to the clean system, coupling of pancake vortices seems to take place at higher temperatures. This can be inferred from the faster drop of the Josephson-coupling ratio (Fig. 4.6(d)), $\langle\Gamma\rangle$, at high temperatures (in agreement with the expectation that columnar defects should trap vortices favouring coupling). These quantitative differences can be interpreted as evidence for a possibly different vortex-phase in the case of the HTSC sample with randomly distributed columnar defects. However details of this are not fully revealed by these quantities. As in the clean layered-HTSC, the previous physical properties are defined so as to be intensive. There is no appreciable sensitivity to system size though quantitative changes as σ^2 is varied can be observed.

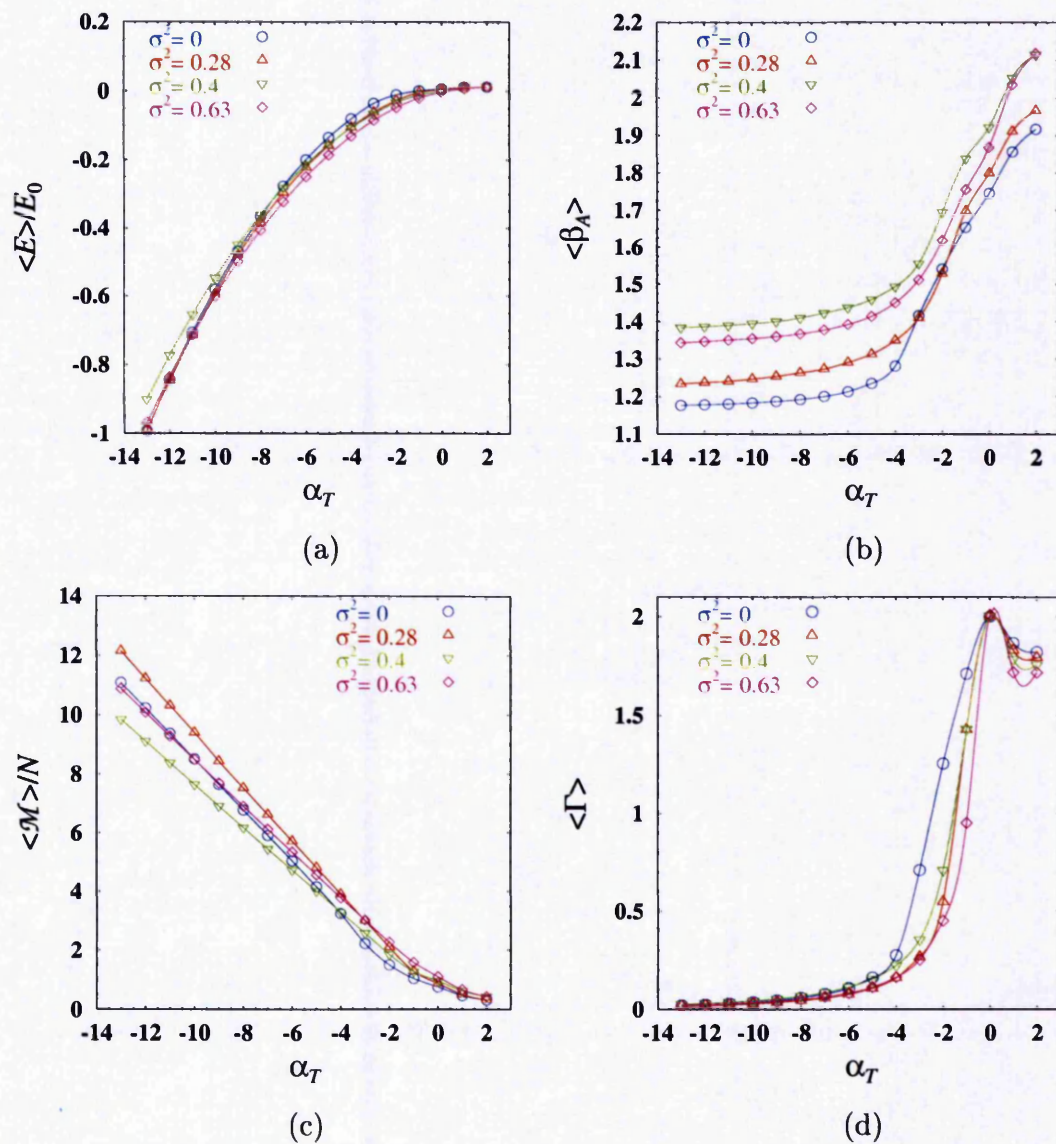


Figure 4.6: Finite-temperature properties of the layered superconductor with randomly distributed columnar defects along the c -axis. (a) Average energy. (b) Abrikosov ratio. (c) Magnetization per vortex. (d) Josephson-coupling ratio.

4.2.2 Structure and Vortex Correlations

From the study of both vortex positions and structure factor (in each layer) as temperature is lowered we are able to determine qualitatively the different phases of vortices. By plotting the angular coordinates of the pancake vortices in all layers (at each effective temperature as in the clean HTSC) we can observe the existence of a phase of coupled pancake-vortices for $\alpha_T \leq -3$ in our system with $(N, M) = (72, 18)$ at $\eta = 0.14142$ and $\sigma^2 = 0.27777$. Figure 4.7 (a,c,e) shows this result. Here points of the same type and colour represent the vortices on the same layer (calculated after 6×10^4 MCS). Unlike the clean layered-HTSC, we notice that interlayer coupling here is not total (even at $\alpha_T = -4$, Fig. 4.7(e)) as still some pairs of flux-lines remain entangled. In smaller systems we observe the same coupling at slightly higher temperatures. This is expected because as the number of vortices per layer, N , is reduced the coupling to columnar defects, $\sigma^2 = 20/N$, increases. As in the clean layered-HTSC we expect the coupled phase of vortices to extend to higher temperatures when both parameters η and σ^2 increase.

The layered superconductor with randomly distributed columnar defects shows a low temperature vortex-phase which behaves much like a glass, (i.e. neither intralayer quasi-hexagonal Bragg-spots nor liquid-like isotropic ring in the structure factor are visible) very similar to that in its thin-film counterpart. This is concluded from both, direct observations of the vortex positions on the sphere and structure factor (in each layer). Even in the high temperature regime ($\alpha_T \sim -1$), an amorphous solid structure appears from the structure factor, $S(\mathbf{k})$. This suggests that this type of columnar pins have, somehow, frozen the vortex system (see Fig. 4.7(b,d,f)). Plots of the vortex positions in each layer (as temperature is lowered) seem to indicate the existence of an effective temperature below which vortex movement is restricted (effectively as a glass) but above which vortices move slowly (as in an extremely viscous liquid). That temperature appears about the coupling-decoupling transition, but from this qualitative analysis seems more like a gradual crossover than a sharp transition.

A quantitative analysis of this can be given in terms of the intralayer and interlayer correlation functions. From the study of in-layer density correlations we can observe

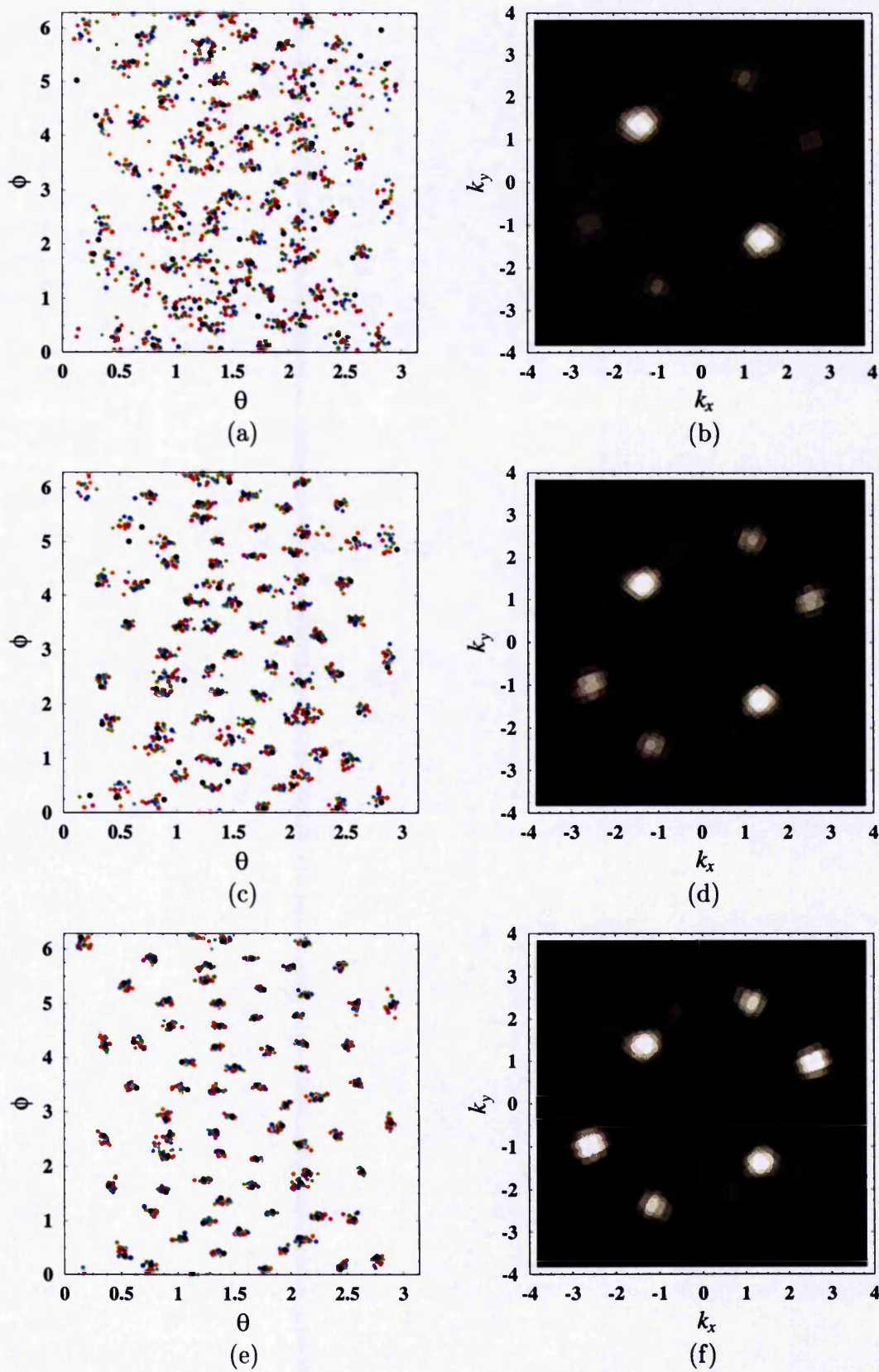


Figure 4.7: Angular vortex-positions (in all layers) and structure factor (at layer $M/2$) of the layered superconductor with randomly distributed columnar defects for $(N, M) = (72, 18)$, interlayer coupling $\eta = 0.14142$ and pinning strength $\sigma^2 = 0.27777$ as the temperature is lowered: $\alpha_T = -2, -3, -4$. [(a,b),(c,d),(e,f) respectively.]

4.2. Pinning by a Random Substrate of Columnar Defects

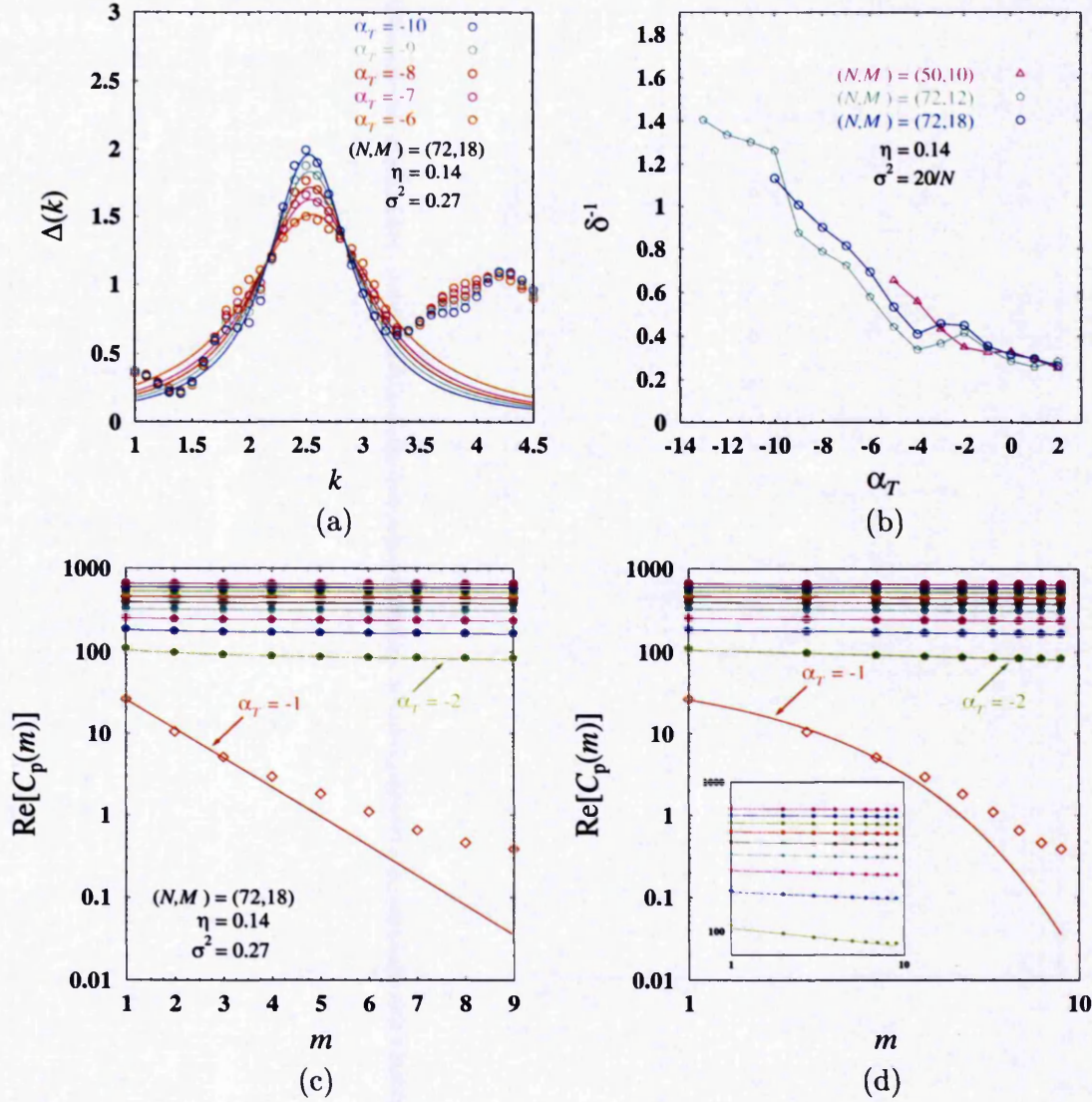


Figure 4.8: Intra- and inter-layer correlations on the layered-HTSC with a random substrate of columnar defects along the c -axis as the temperature is lowered. (a) First peak of the rotationally averaged structure function (with Lorentzian fits) for the system with $(N, M) = (72, 18)$ at $(\eta, \sigma^2) = (0.14142, 0.27777)$. (b) Extracted density correlation-length, $\delta^{-1} \sim \xi_D$, (with spline fits) for different system sizes at $(\eta, \sigma^2) = (0.14142, 20/N)$. (c) Log-linear plot of the inter-layer phase-correlation-function, $\text{Re}[C_p(m)]$, as a function of the “distance” along the c -axis showing quasi-exponential decay of correlations above the transition (open symbols). (d) Log-log plot of $\text{Re}[C_p(m)]$ remarking power-law decrease of correlations below the transition (filled symbols). The inset is just a magnification of the curves below the transition. Fits are shown for $\alpha_T = -1, -2, -3, \dots, -10$ from bottom to top curves, except on the inset (there $\alpha_T = -2, -3, \dots, -10$ from bottom to top). The expected transition temperature lies between $\alpha_T = -2$ and -1 . The system in (c,d) is the same as in (a).

that columnar defects change the smooth behaviour of $\Delta(k)$ (see Fig. 4.8(a)) reducing considerably the peak-height (in comparison to the pure sample). Nevertheless, a density correlation-length can be extracted which is seen to vary roughly linearly with α_T as in its thin-film counterpart (see Fig. 4.8(b)). This suggests no in-plane change in the vortex state (remaining a glass at any temperature below $\alpha_T = 0$). On the other hand, the interlayer phase-correlation-function clearly shows the appearance of quasi-long-range order along the c -axis below $\alpha_T = -1$. This is illustrated in Fig. 4.8(c,d), especially in Fig. 4.8(d), where the power-law decay of $\text{Re}[C_p(m)]$ at $\alpha_T \leq -2$ is clearly visible and supports the coupling-decoupling transition suggested above.

In summary, this system is seen to change its phase from a glassy state of decoupled pancake-vortices to a similar glass but with coupled pancake-vortices (or rather disentangled flux-lines) as temperature is lowered. In this case the transition mechanism for the system to carry out the change seems to coincide with a gradual crossover (rather than a sharp transition). This is in agreement with the expectation of two different length scales describing the system (parallel and perpendicular to the layered structure), but contrarily to the theoretical expectation (just above) the in-plane phase appears not to undergo a liquid-to-glass continuous transition.

4.3 Pinning by a Periodic Substrate of Columnar Defects

This section is devoted to the numerical study of a model of a layered high- T_c superconductor in the presence of a regular array of columnar defects in the direction perpendicular to the layered structure. The numerical approach, for the spherical system we are investigating, suggests considering the LD-LLL model for the clean layered-superconductor in Eq. (2.38) with the addition of the columnar-defect energy term given by

$$\mathcal{H}_{\text{ps}}[\psi_n; \psi_n^{(0)}] = -g\beta \sum_{n=1}^M d_0 \int d^2r |\psi_n^{(0)}(\mathbf{r})|^2 |\psi_n(\mathbf{r})|^2. \quad (4.8)$$

which is completely analogous to that for the thin-film HTSC introduced in Eq. (3.32). In this case the order parameter in each of the M layers, $\psi_n(\mathbf{r})$, describes N pancake vortices on the sphere, while the periodic substrate is defined by the set of functions $\{\psi_n^{(0)}(\mathbf{r})\}$ describing N' columnar defects. That is, $\{\psi_n^{(0)}(\mathbf{r})\}$ are the ground-state order parameters that minimize the LD-LLL model in Eq. (2.38) for a system of N' vortices.

Within the LLL approximation the order parameter in each layer is taken as that in Eq. (2.47) and the ground-state order parameter defining the periodic substrate expanded as

$$\psi_n^{(0)}(\theta, \phi) = Q \sum_{q=0}^{N'} v_{n,q}^{(0)} \psi_{q,N'}(\theta, \phi), \quad (4.9)$$

where the considerations in Section 3.3 apply. By inserting Eqs. (2.47) and (4.9) into Eq. (4.8) and performing the integration (analogous to the thin-film counterpart) we can write the energy contribution of this periodic substrate of columnar defects (per unit of thermal energy $k_B T$) as

$$\frac{\mathcal{H}_{\text{ps}}(\mathbf{v}; \mathbf{v}^{(0)})}{k_B T} = -2g \frac{1}{2N} \sum_{n=1}^M \sum_{p=0}^{N+N'} |U'_{n,p}(\mathbf{v}, \mathbf{v}^{(0)})|^2, \quad (4.10)$$

where $U'_{n,p}$ is the linear function on the expansion coefficients \mathbf{v} given by

$$U'_{n,p}(\mathbf{v}; \mathbf{v}^{(0)}) = N \gamma_{q,N+N'} \sum_{q=0}^N \mathcal{N}_{q,N} \mathcal{N}_{p-q,N'} \Theta(p-q) \Theta(N'-p+q) v_{n,p-q}^{(0)} v_{n,q}, \quad (4.11)$$

and $\gamma_{q,N+N'}$ is that defined in Section 3.1.

In the LLL approximation, the total energy (per unit of thermal energy) for this system is given by the sum of Eqs. (4.2) and (4.10). We use this model to perform MC simulations for some cases when the vortex system and the periodic substrate of columnar defects are either commensurate or incommensurate.

4.3.1 Commensurate Case

As in the thin-film counterpart of this problem, here we have investigated the effect of a substrate of columnar pins commensurate to the vortex system in the two most relevant cases: when the system is tuned at the matching field: $\overline{B} = \overline{B}_\Phi$ (that is when $N = N'$) and when an array of columnar defects with icosahedral radially-projected

symmetry acts on system sizes with $N = 32, 72, 132, \dots$ vortices per layer (i.e. when $\overline{B} = (N/12)\overline{B}_\Phi$). The results are presented in the following sections.

4.3.1.1 The Case of the Matching-Field

For the matching field case we, again, study systems with M layers and N vortices per layer in the set: $\{(N, M) = (72, 18), (72, 12), (50, 15), (50, 10), (32, 12), (32, 8)\}$, for interlayer coupling $\eta = 0.14142$ and pinning strength $g = 0.1$. After taking the LLL approximation, columnar defects are defined by the expansion coefficients $\{v_{n,q}^{(0)}\} = \mathbf{v}^{(0)}$ (being the same in each layer). We sample the usual range of effective temperatures $-13 \leq \alpha_T \leq 2$ starting with the initial configuration $\mathbf{v} = \mathbf{v}^{(0)}$ at $\alpha_T = 2$ and cooling the system down.

Thermodynamic Quantities and Order-Parameter Ratios

As in previous cases we consider first the fundamental quantities as functions of the effective temperature parameter α_T . For this system, in addition to the energy, magnetization and Abrikosov (and Josephson-coupling) ratio, we look at the pinning magnetization and susceptibility (with similar definitions to those in the thin-film case and LLL expressions given in Appendix A.6). Figure 4.9 shows our results for the system of size $(N, M) = (72, 18)$ for coupling constants in $\{(\eta, g) = (0, 0), (0.14142, 0), (0, 0.1), (0.14142, 0.1)\}$.

The upper four quantities in Fig. 4.9 present the same qualitative behaviour as those of the clean layered-HTSC, $(\eta, g) = (0.14142, 0)$. Quantitatively we find that the average energy, Abrikosov and Josephson-coupling ratios have lower values; though the average magnetization is slightly higher. This can be interpreted as that columnar defects at the matching field pin vortices so as to optimize quantities like energy at any α_T . In particular the low values of $\langle\beta_A\rangle$ and $\langle\Gamma\rangle$ at high temperatures seem to indicate both intralayer quasi-hexagonal order and interlayer coupling of pancake vortices, respectively.

From pictures of the pinning magnetization and susceptibility in Figs. 4.9(e) and 4.9(f) we can observe the temperature at which pinning starts to become effective.

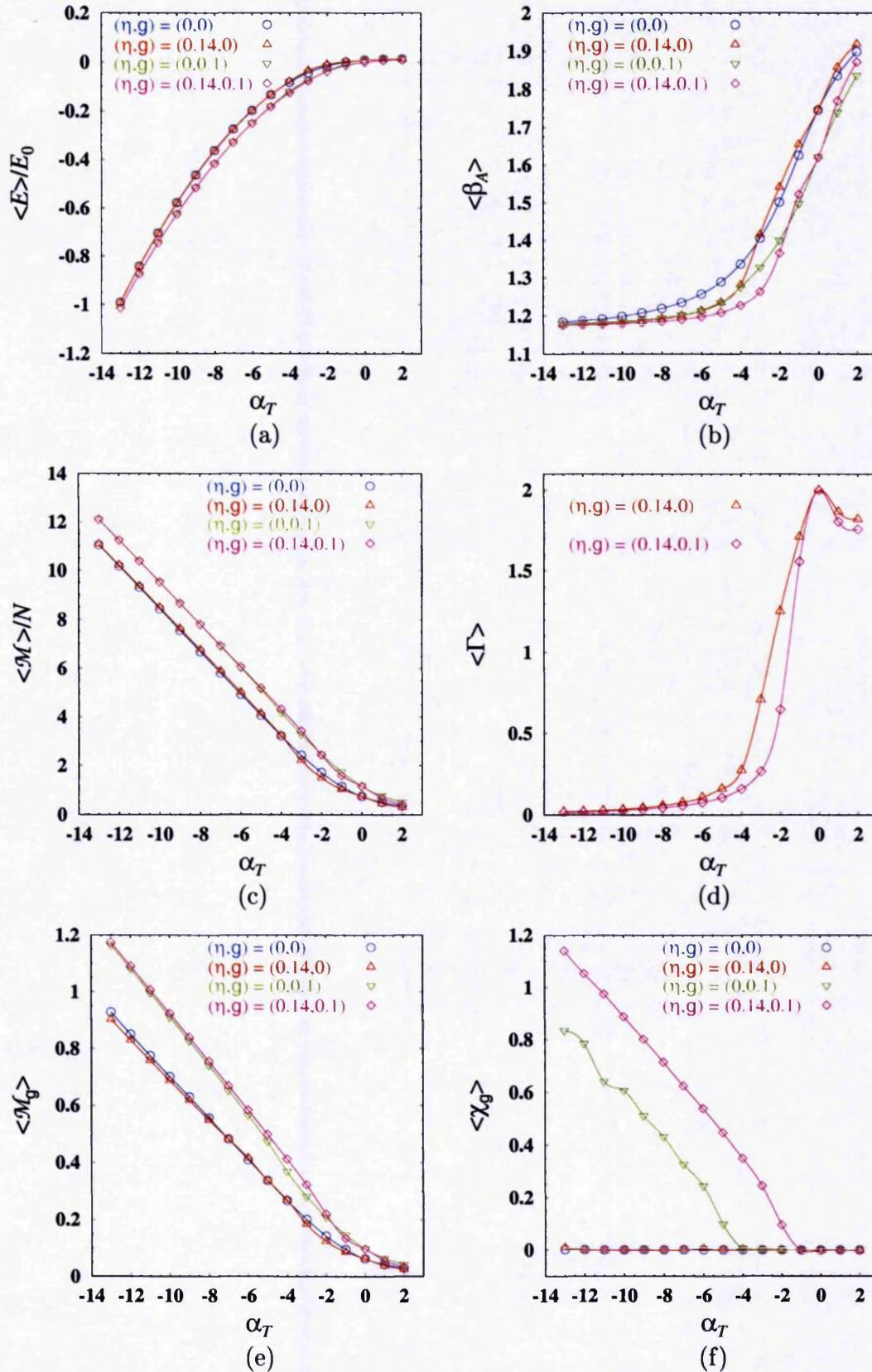


Figure 4.9: Finite-temperature properties of the layered HTSC with a periodic array of columnar defects along the c -axis for $(N, M) = (72, 18)$, $N' = 72$, $\eta = 0.14142$ and $g = 0.1$. (a) Average energy. (b) Abrikosov ratio. (c) Magnetization per vortex. (d) Josephson-coupling ratio. (e,f) Pinning magnetization and susceptibility.

4.3. Pinning by a Periodic Substrate of Columnar Defects

For our system with $M = 18$ layers and $N = 72$ vortices per layer (with the same number of columnar defects N') at $\eta = 0.14142$ and $g = 0.1$ we see that to take place at about $\alpha_T = -2$. That is more revealing from the pinning susceptibility which grows abruptly from its nearly zero value at $\alpha_T = -1$ to about 0.1 at $\alpha_T = -2$. In the pinning magnetization this shows up just as a small kink about the same temperatures. In all these intensive quantities no appreciable finite-size effects are noticed so quantitative differences are attributed to the variation of coupling parameters. A more detailed description of the vortex phases can be accounted by looking at the vortex positions, structure factor (in each layer) and correlations as temperature is lowered.

Vortex Positions, Correlations and Structure

From the study of both vortex positions and structure factor (in each layer) as temperature is lowered we determine qualitatively the different phases of vortices. By plotting the angular coordinates of the pancake vortices in all layers (at each effective temperature) we can observe the existence of a coupled phase just below $\alpha_T = -2$ in our system with $(N, M) = (72, 18)$ at $\eta = 0.14142$ and $g = 0.1$. Figure 4.10(a,c,e) shows this result. There the open circles represent the columnar pins. In smaller systems, but at the same coupling parameters, we observe interlayer vortex-coupling at the same temperature, confirming the system-size independence. In this case we expect the coupled phase of vortices to extend to higher temperatures when either η or g increases.

Analogously to its thin-film counterpart, the layered superconductor with the regular array of columnar defects at the matching field shows the appearance of phase coherence (in this case both intralayer and interlayer). In-layer phase coherence seems to take place at higher temperatures. This happens at about $\alpha_T = -2$ in our system with $(N, M) = (72, 18)$ at $\eta = 0.14142$ and $g = 0.1$, and shows up on the rapid raise of the in-layer density correlation length (see Fig. 4.11(b)). On the other hand, phase coherence along the c -axis sets in at a lower effective temperature, $-4 < \alpha_T < -3$, as shown by the appearance of quasi-long-ranged phase correlations in Fig. 4.11(c,d). The results of this section, therefore, suggest a “two step” transition to a vortex state

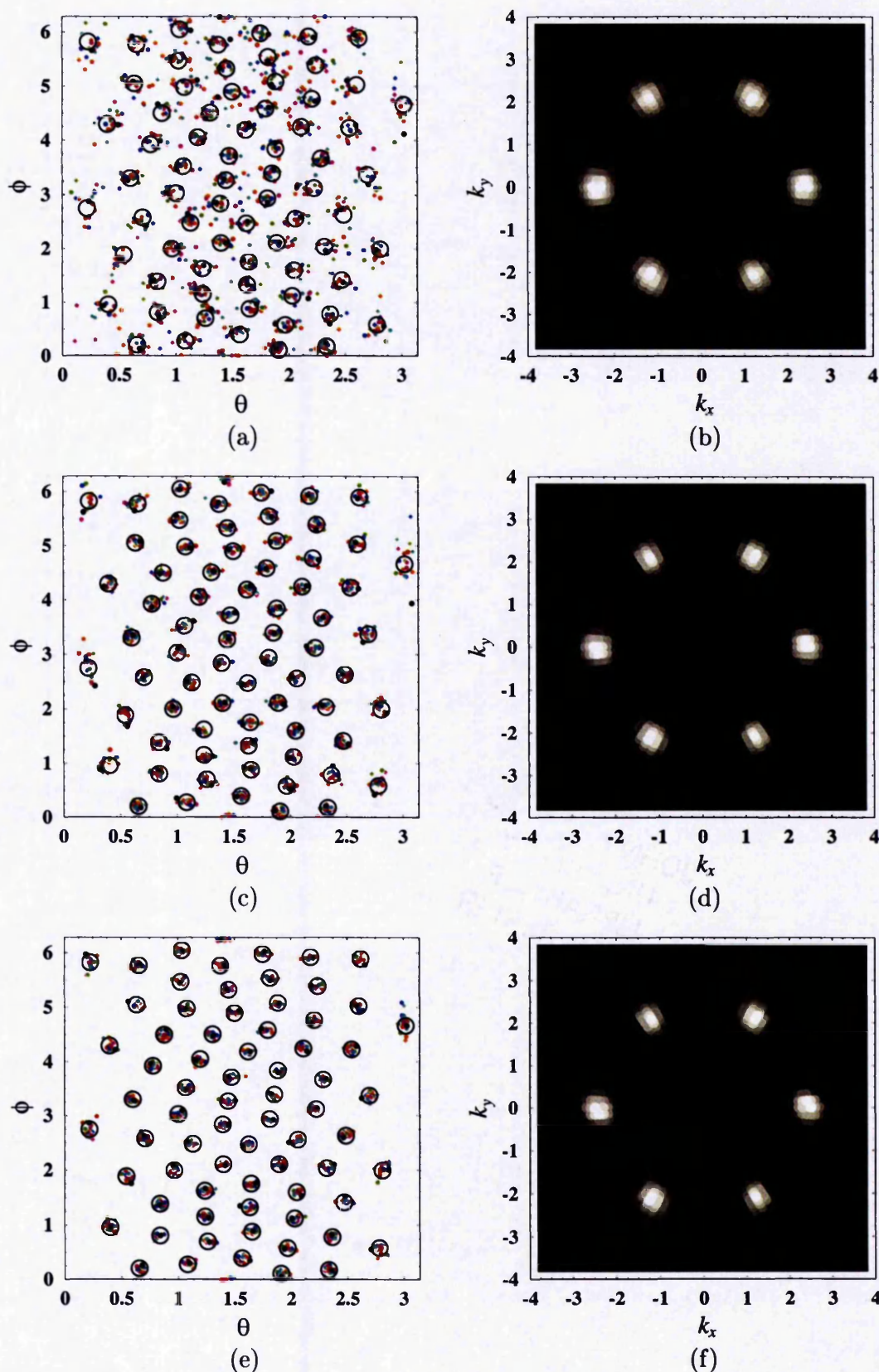


Figure 4.10: Angular vortex-positions (in all layers) and structure factor (at layer $M/2$) of the layered HTSC with a periodic array of columnar defects along the c -axis for $(N, M) = (72, 18)$, $N' = 72$, $\eta = 0.14142$ and $g = 0.1$ as the temperature is lowered: $\alpha_T = -2, -3, -4$. [(a,b),(c,d),(e,f) respectively.]

4.3. Pinning by a Periodic Substrate of Columnar Defects

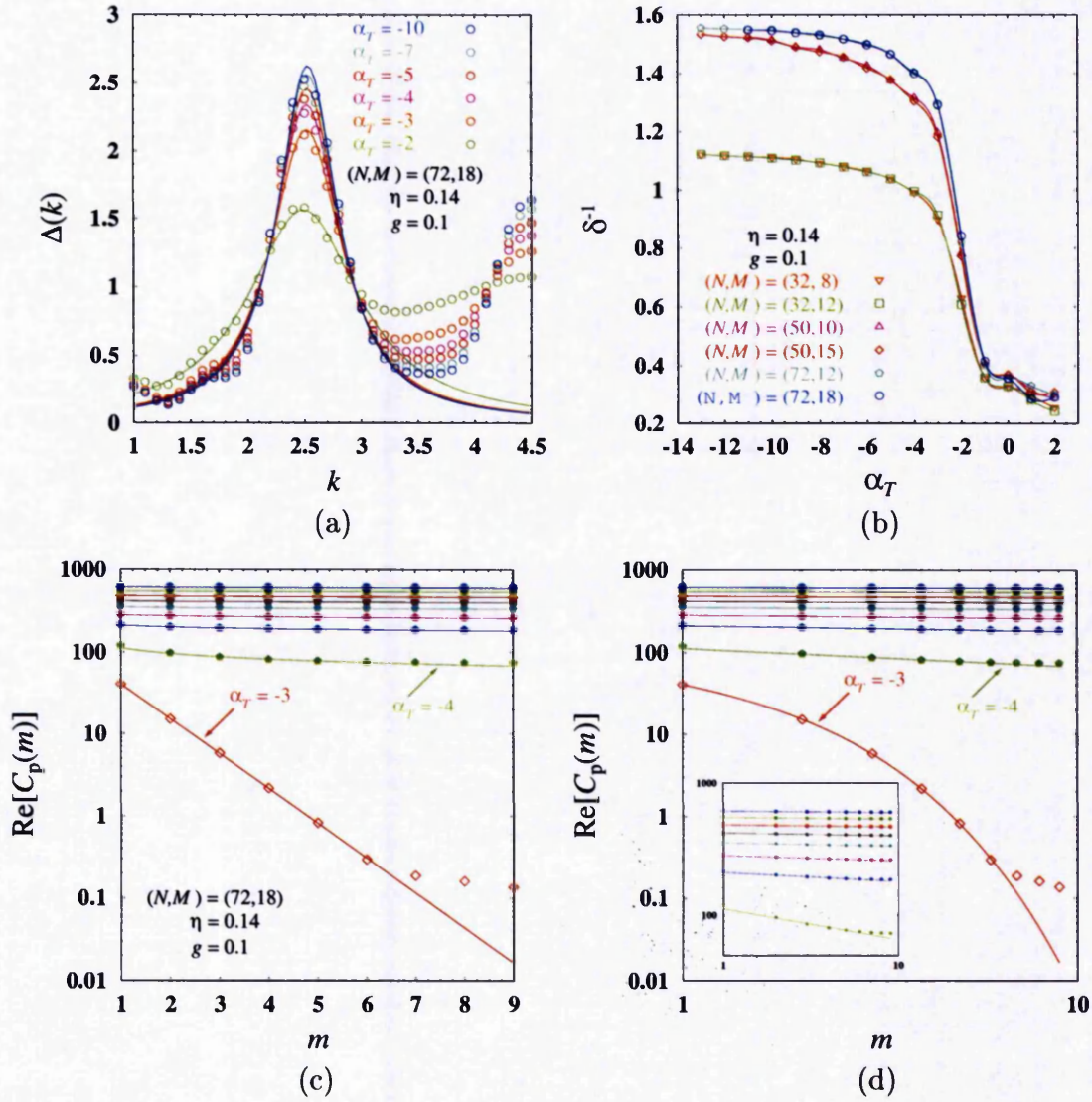


Figure 4.11: Intra- and inter-layer correlations for the layered-HTSC with a regular array of columnar defects at the matching field. (a) First peak of the rotationally averaged structure function (with Lorentzian fits) for the system with $(N, M) = (72, 18)$ at $(\eta, g) = (0.14142, 0.1)$. (b) Extracted density correlation-length, $\delta^{-1} \sim \xi_D$, (with spline fits) for different system sizes at $(\eta, g) = (0.14142, 0.1)$. (c) Log-linear plot of the inter-layer phase-correlation-function, $\text{Re}[C_p(m)]$, as a function of the “distance” along the c -axis showing exponential decay of correlations above the transition (open symbols). (d) Log-log plot of $\text{Re}[C_p(m)]$ remarking power-law decrease of correlations below the transition (filled symbols). The inset is just a magnification of the curves below the transition. Fits are shown for $\alpha_T = -3, -4, \dots, -11$ from bottom to top curves, except on the inset (there $\alpha_T = -4, -5, \dots, -11$ from bottom to top). The expected transition temperature lies between $\alpha_T = -4$ and -3 . The system in (c,d) is the same as in (a).

with superconducting phase coherence both intralayer and interlayer. As the system is cooled down below the upper critical field (defined by $\alpha_T = 0$) the onset of in-layer phase coherence is observed first, which then extends to all layers. By comparing the quantity that best describes in-layer phase coherence, $\chi_g(\alpha_T)$ for $(\eta, g) = (0.14, 0.1)$ in Fig. 4.9(f), to its counterpart in the thin film case $((\eta, g) = (0, 0.1)$ in the same figure) and extending the arguments on the predicted XY -type transition in Section 3.3.1 to the layered case, we can see that both transitions seem to be parallel. Therefore the first transition from high to low temperatures also appears to be XY -like. The later transition appears sharp as in the pure case and is also associated with coupling of pancake vortices along the c -axis. This should be a line of first order transitions which, in addition, seems to be simultaneous to flux-line “trapping” by columnar defects. Therefore, the low-temperature phase under consideration here could be well described as the Mott insulator, where every single columnar pin is occupied and no free flux-lines remain. The phase above these transitions certainly has no phase coherence and therefore should be a liquid of decoupled pancake-vortices (or possibly a glass, depending on the value of the pinning strength g).

4.3.1.2 The Case with the Icosahedral Substrate

For the vortex system with an icosahedral array of columnar defects parallel to the c -axis we study just a couple of examples with M layers and N vortices per layer in $\{(N, M) = (132, 12), (72, 12)\}$ for $N' = 12$ columnar defects, interlayer coupling $\eta = 0.14142$ and pinning strength $g = 0.1$. In this case the columnar defects are defined by the expansion coefficients $\{v_{n,g}^{(0)}\} = \mathbf{v}^{(0)}$ (being the same in each layer). We sample the usual range of effective temperatures $-13 \leq \alpha_T \leq 2$ starting at $\alpha_T = 2$ with the configuration which minimizes the energy of the clean system, $\mathbf{v} = \mathbf{v}_{\min}$, and cooling the system down. Measurements are taken, again, only at integer values of α_T .

Basic Physical Properties

As for previous cases we first look at the main physical quantities as functions of the effective temperature parameter, α_T . For this system we consider the average energy, magnetization, Abrikosov and Josephson-coupling ratios, and pinning magnetization. Figure 4.12 shows plots of those quantities for the system of size $(N, M) = (72, 12)$ with $N' = 12$ and coupling constants in $\{(\eta, g) = (0, 0), (0.14142, 0), (0, 0.1), (0.14142, 0.1)\}$.

It can be observed that all quantities (except the pinning magnetization) are not just qualitatively very similar to those of the clean layered-HTSC, $(\eta, g) = (0.14142, 0)$, but also quantitatively. This could be interpreted as that “weak” pinning by so small a number of columnar defects (compared to the number of vortices) is completely negligible at finite temperatures. This suggests that the results of this section should be essentially the same as for the clean layered-HTSC in Sections 4.1.1 and 4.1.2 (as long as the number of vortices per layer $N > 6N'$ so that the system is away of the matching field).

However, as in the thin-film counterpart of this model, interesting structural changes on the vortex lattice could take place at very low temperatures when the number of vortices $N' < N < 6N'$ for strong enough pinning. If that is the case, columnar defects should pin a bundle of magnetic vortices around them, but none of them at its “core”. Nevertheless, the clean layered-HTSC should be recovered for $N \gg N'$ even in the strong pinning regime as in the thin-film with the icosahedral substrate.

Vortex-System Structure and Correlations

From the study of both vortex positions and structure factor (in each layer) as the temperature is lowered we can estimate qualitatively the different phases of vortices. From plots of the angular coordinates of the pancake vortices in all layers (at each effective temperature) we can observe the existence of a coupled phase for $\alpha_T \leq -4$ in our system with $(N, M) = (132, 12)$ and $N' = 12$ at $\eta = 0.14142$ and $g = 0.1$. Figure 4.13(a,c,e) shows this result. In the smaller system $(N, M) = (72, 12)$ (for the same parameters) we observe interlayer vortex-coupling at the same temperature,

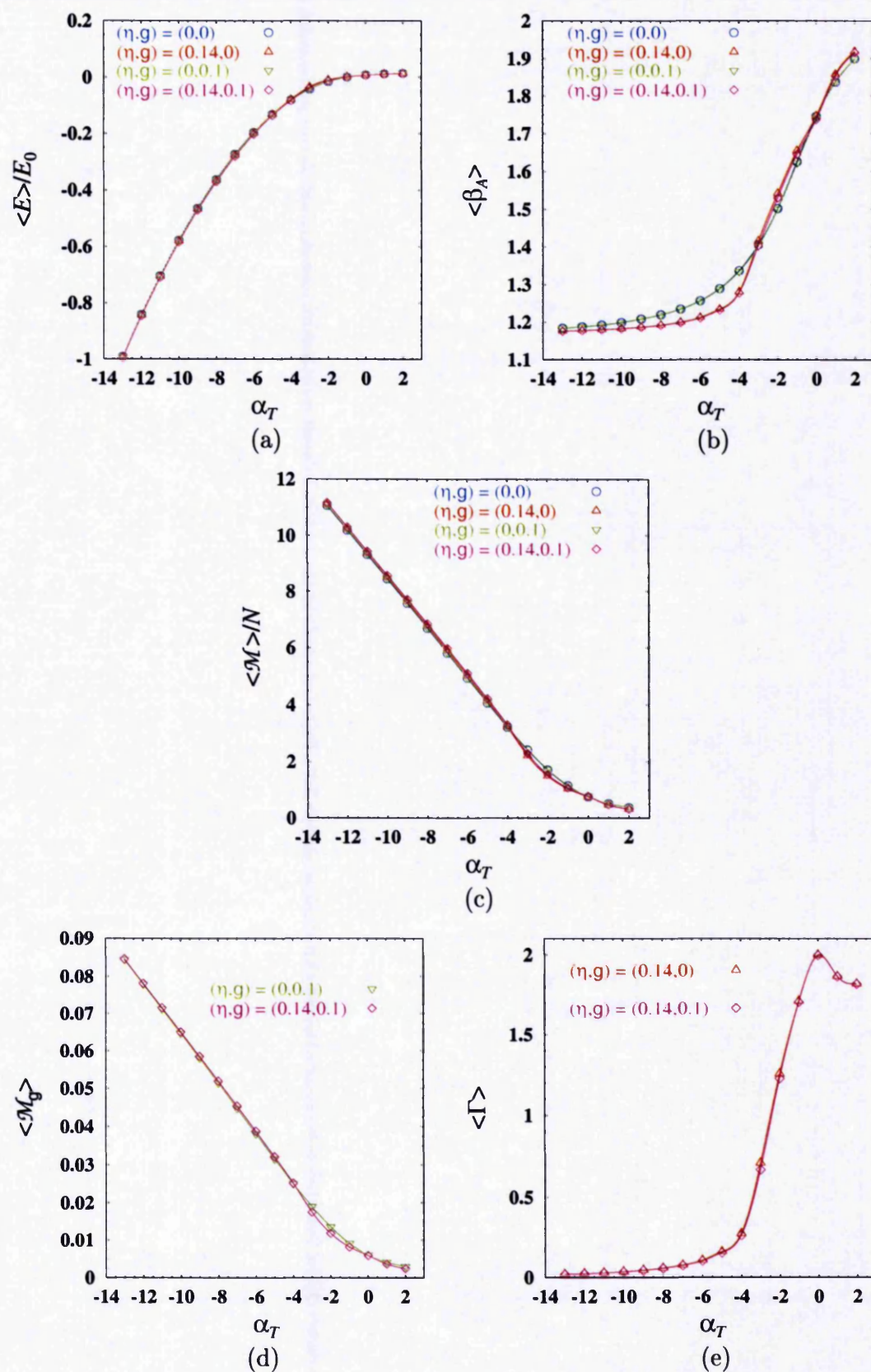


Figure 4.12: Finite-temperature properties of the layered HTSC with an icosahedral array of columnar defects along the c -axis for $(N, M) = (72, 12)$, $N' = 12$, $\eta = 0.14142$ and $g = 0.1$. (a) Average energy. (b) Abrikosov ratio. (c) Magnetization per vortex. (d) Pinning magnetization. (e) Josephson-coupling ratio.

4.3. Pinning by a Periodic Substrate of Columnar Defects

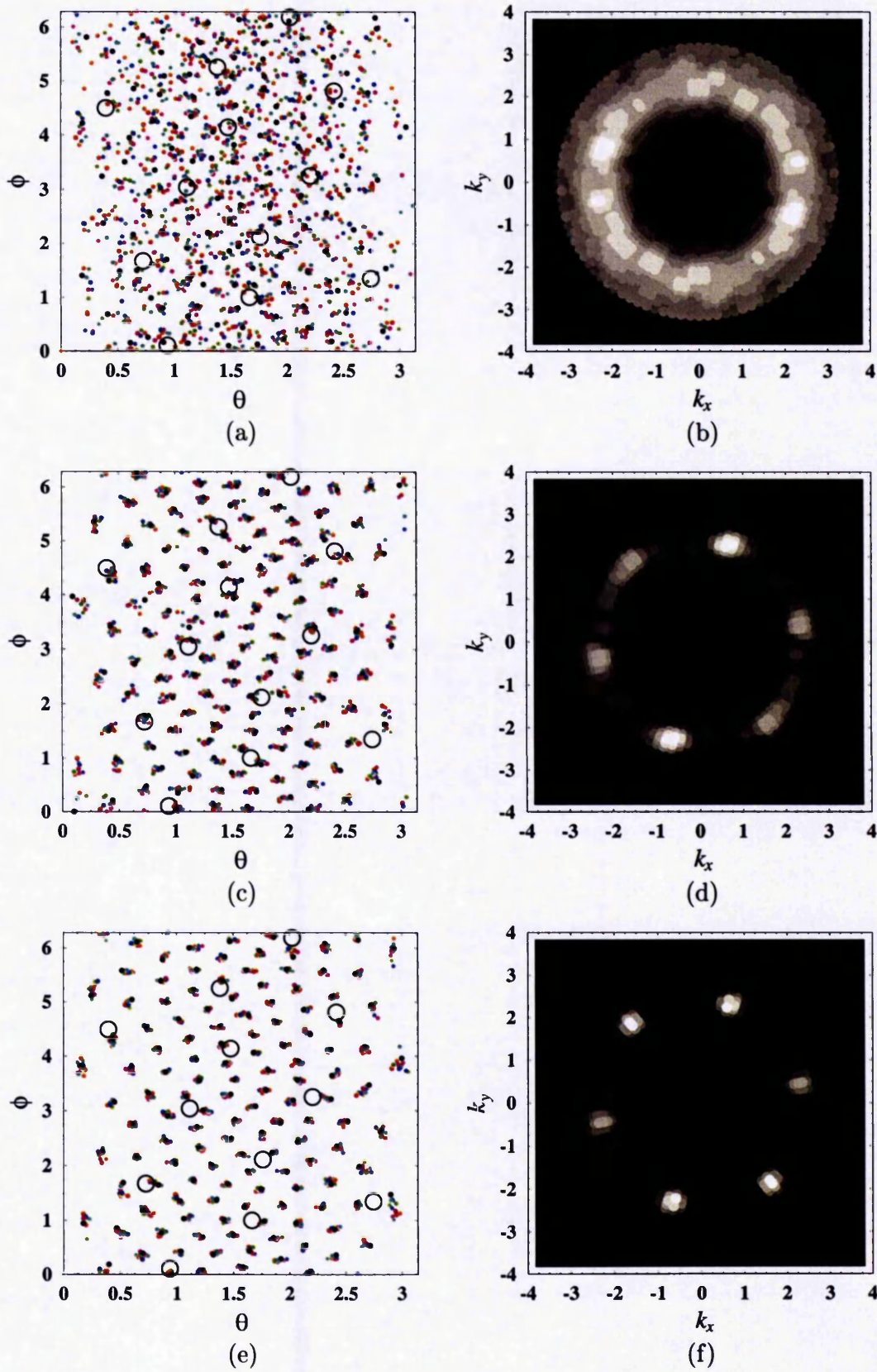


Figure 4.13: Angular vortex-positions (in all layers) and structure factor (at layer $M/2$) of the layered HTSC with an icosahedral array of columnar defects along the c -axis for $(N, M) = (132, 12)$, $N' = 12$, $\eta = 0.14142$ and $g = 0.1$ as the temperature is lowered: $\alpha_T = -3, -4, -5$. [(a,b),(c,d),(e,f) respectively.]

4.3. Pinning by a Periodic Substrate of Columnar Defects

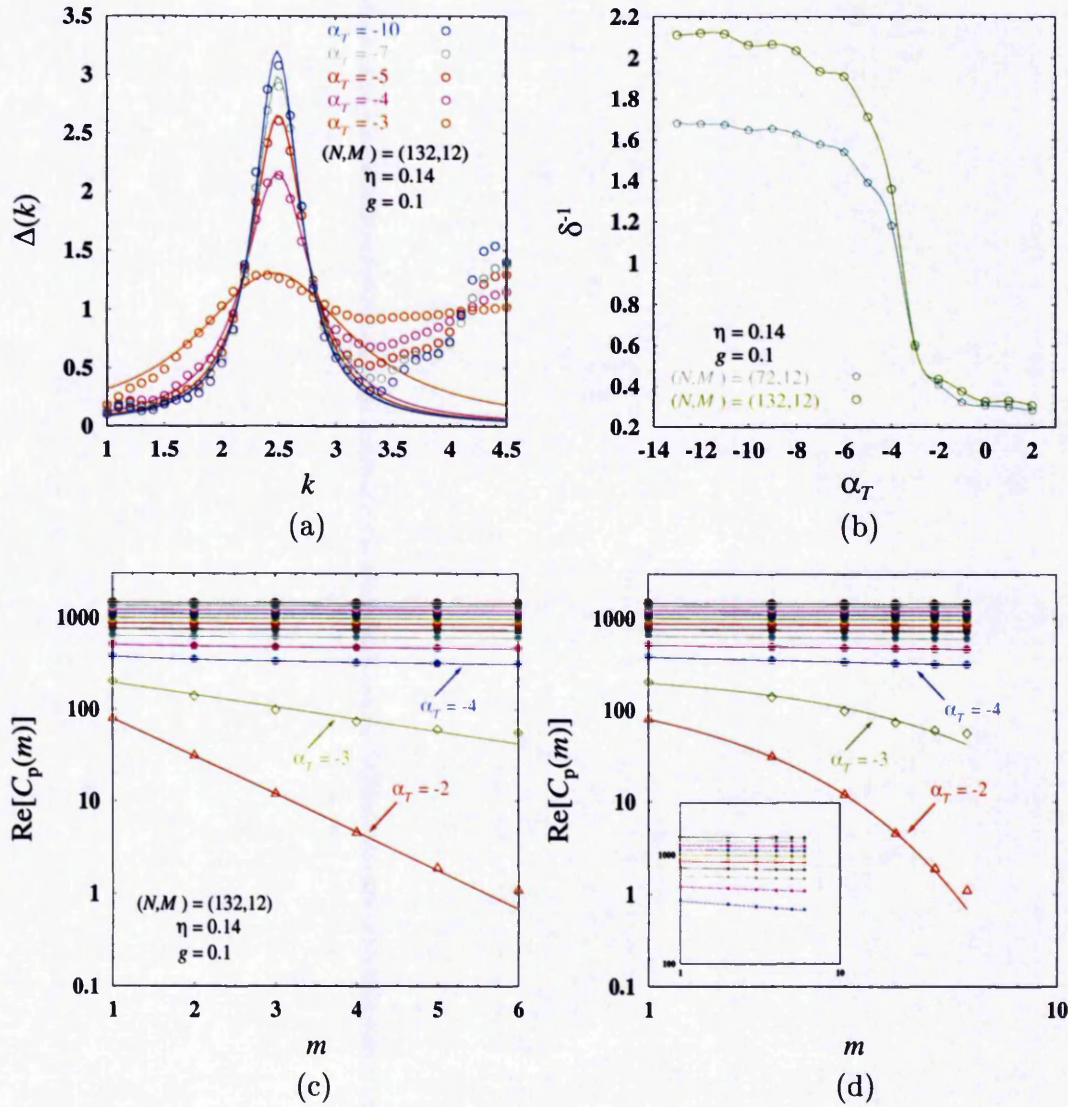


Figure 4.14: Intra- and inter-layer correlations for the layered-HTSC with an icosahedral array of columnar defects. (a) First peak of the rotationally averaged structure function (with Lorentzian fits) for the system with $(N, M) = (132, 12)$ at $(\eta, g) = (0.14142, 0.1)$. (b) Extracted density correlation-length, $\delta^{-1} \sim \xi_D$, (with spline fits) for different system sizes at $(\eta, g) = (0.14142, 0.1)$. (c) Log-linear plot of the inter-layer phase-correlation-function, $\text{Re}[C_p(m)]$, as a function of the “distance” along the c -axis showing exponential decay of correlations above the transition (open symbols). (d) Log-log plot of $\text{Re}[C_p(m)]$ remarking power-law decrease of correlations below the transition (filled symbols). The inset is just a magnification of the curves below the transition. Fits are shown for $\alpha_T = -2, -3, \dots, -13$ from bottom to top curves, except on the inset (there $\alpha_T = -4, -5, \dots, -13$ from bottom to top). The expected transition temperature lies between $\alpha_T = -4$ and -3 . The system in (c,d) is the same as in (a).

confirming system-size independence (for $N \geq 6N'$). Analogously to the clean layered-HTSC we expect the coupled phase of vortices to extend to higher temperatures when η increases.

The structure factor (calculated on the layer at the middle of the system) in Fig. 4.13(b,d,f) reveals appearance of quasi-hexagonal Bragg peaks at the temperature that interlayer vortex-coupling takes place. The mechanism for this seems to be the same as in the clean layered-case (i.e. rapid increase of correlations in all directions as the coupling transition is approached). In fact this qualitative description can be made quantitative by studying the associated in-layer and inter-layer correlation functions. We obtain information on the increase of in-layer density correlations by studying the rotationally averaged structure function, $\Delta(k)$. As in the clean-sample case we find a rather appropriate Lorentzian fit to its first peak, and from that extract the in-layer density correlation length, $\xi_D \sim \delta^{-1}$ (shown in Fig. 4.14(a,b)). We see δ^{-1} to increase abruptly about the coupling transition (in agreement with the qualitative description in terms of $S(k)$ given above). The temperature for the coupling transition itself is deduced from the behavior of the inter-layer phase correlation function. Very similarly to the clean layered-case a sudden appearance of algebraic decay in the phase correlation function is observed as the temperature is lowered through the qualitatively estimated coupling transition. This appearance of inter-layer phase coherence marks the onset of vortex coupling (shown in Fig. 4.14(c,d)). As expected from the previous analysis, pinning effects appear negligible in this case of weak pinning with a small number of columnar defects ($N' < N/6$). The transition to the coupled phase appears sharp as in the pure case and seems to be the same in nature. A noteworthy feature is that, as shown in the pictures of the structure factor (Fig. 4.13(b,d,f)), columnar defects do not actually pin flux lines individually but act collectively on the whole of the vortex system for this irradiated sample.

4.3.2 Incommensurate Case

To study the effects of a regular substrate of columnar defects incommensurate to a vortex system we choose (as in the thin-film case) to place the columnar defects on

the projections on the sphere of the icosadeltahedra with 32 vertices (as shown in Fig. 3.4(b)). As argued in Section 3.1.1, this substrate is incommensurate to almost any vortex lattice on the sphere. In particular for systems with $N = 132$ and 72 vortices per layer (the ones considered in this investigation). Here we study samples with M layers in $\{(N, M) = (132, 12), (72, 12)\}$ for $N' = 32$ columnar defects, interlayer coupling $\eta = 0.14142$ and pinning strength $g = 0.1$. The columnar defects are, once again, defined by the expansion coefficients $\{v_{n,q}^{(0)}\} = \mathbf{v}^{(0)}$ (being the same in each layer). We sample the usual range of effective temperatures $-13 \leq \alpha_T \leq 2$ at integer values of α_T only. The simulation starts at $\alpha_T = 2$ with the configuration that minimizes the energy of the pure system, $\mathbf{v} = \mathbf{v}_{\min}$ and measurements are taken as the system temperature is lowered.

Thermodynamic Quantities and Other Properties

We start the study of this system by looking at its basic properties as functions of the effective temperature parameter α_T . In this case we consider the average energy, magnetization, Abrikosov and Josephson-coupling ratios, and pinning magnetization. Figure 4.15 shows our results of those quantities for the system of size $(N, M) = (72, 12)$ with $N' = 32$ at couplings of $\{(\eta, g) = (0, 0), (0.14142, 0), (0, 0.1), (0.14142, 0.1)\}$.

It can be observed that all quantities (except the pinning magnetization) are not just qualitatively very similar to those of the clean layered-HTSC (and therefore to the ones for the case with the icosahedral substrate), but also numerically. This, again, can be taken as evidence to support that “weak” pinning by a relatively small number of columnar defects (compared to the number of vortices) is essentially negligible. This leads to the expectation that the results of this section should be in agreement with those of the clean layered-HTSC in Section 4.1.1 and also for the case with the icosahedral substrate considered just above. Once again, we expect this to be valid as long as the number of vortices per layer $N > 6N'$, so that the system is away of the matching field. Moreover, as in the thin-film counterpart of this model, the very low temperature structural changes on the vortex lattice could take place when the number of vortices $N < 6N'$ for strong enough pinning. As in that case, the expectation is

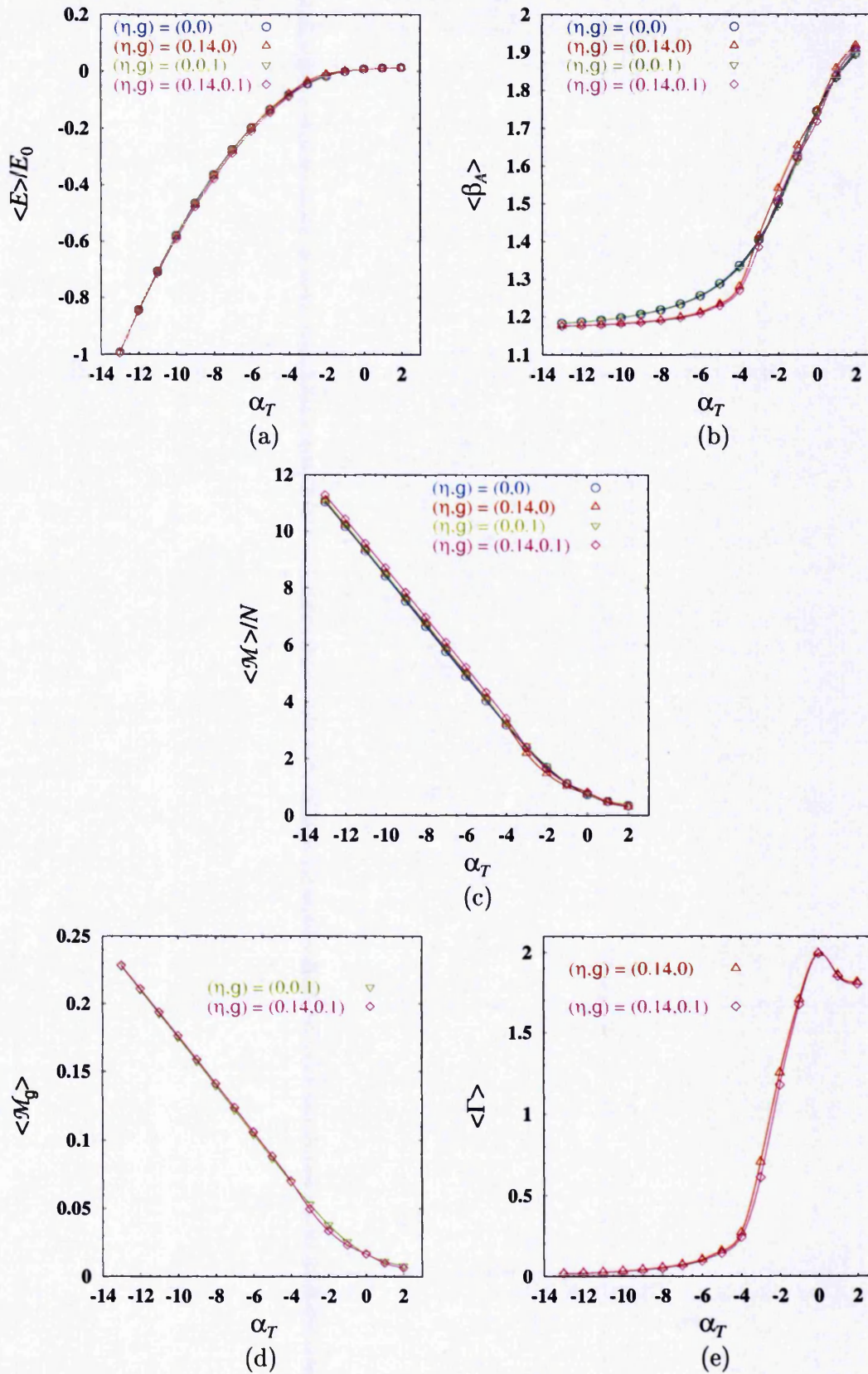


Figure 4.15: Finite-temperature properties of the layered HTSC with a regular array of columnar defects along the c -axis for $(N, M) = (72, 12)$, $N' = 32$, $\eta = 0.14142$ and $g = 0.1$. (a) Average energy. (b) Abrikosov ratio. (c) Magnetization per vortex. (d) Pinning magnetization. (e) Josephson-coupling ratio.

that each columnar defect should pin a bundle of vortices around them, but not to trap single flux-lines. Nevertheless, the clean layered-HTSC should be recovered for $N \gg N'$ even in the strong pinning regime as it happens in the thin-film counterpart of this case.

Vortex Positions and Structure

From the study of both vortex positions and structure factor (in each layer) as the temperature is lowered we determine qualitatively the different phases of vortices. From plots of the angular coordinates of the pancake vortices in all layers (at each effective temperature) we can observe the existence of a coupled phase for $\alpha_T \leq -4$ in both of our systems: $(N, M) = (132, 12), (72, 12)$ and $N' = 32$ at $\eta = 0.14142$ and $g = 0.1$. Figure 4.16(a,c,e) shows this result for $(N, M) = (132, 12)$. As previously discussed the phase of coupled vortices is expected to extend to higher temperatures when η increases.

Pictures of the structure factor show no qualitative difference to those of the clean layered-sample and therefore no to the case with the icosahedral substrate (see Fig. 4.16(b,d,f)). The appearance of quasi-hexagonal Bragg peaks is interpreted on basis of the same mechanism (abrupt increase of correlations in all directions as the coupling transition is approached). Once again we make our qualitative conjectures formal by studying correlation functions for in-layer density and inter-layer phase. The results we obtain for these quantities are again very much the same as those in the previous case with the icosahedral substrate. Figure 4.14 should provide an accurate enough account of them. In this case, again, the system is observed to behave effectively as the clean layered-HTSC. (at least for these coupling parameters $(\eta, g) = (0.14142, 0.1)$.) The numerical results on the correlations in this model appear essentially the same to those for the pure system. This means that the abrupt increase of correlations along the different system-axes takes place at a first-order transition associated with coupling along the c -axis.

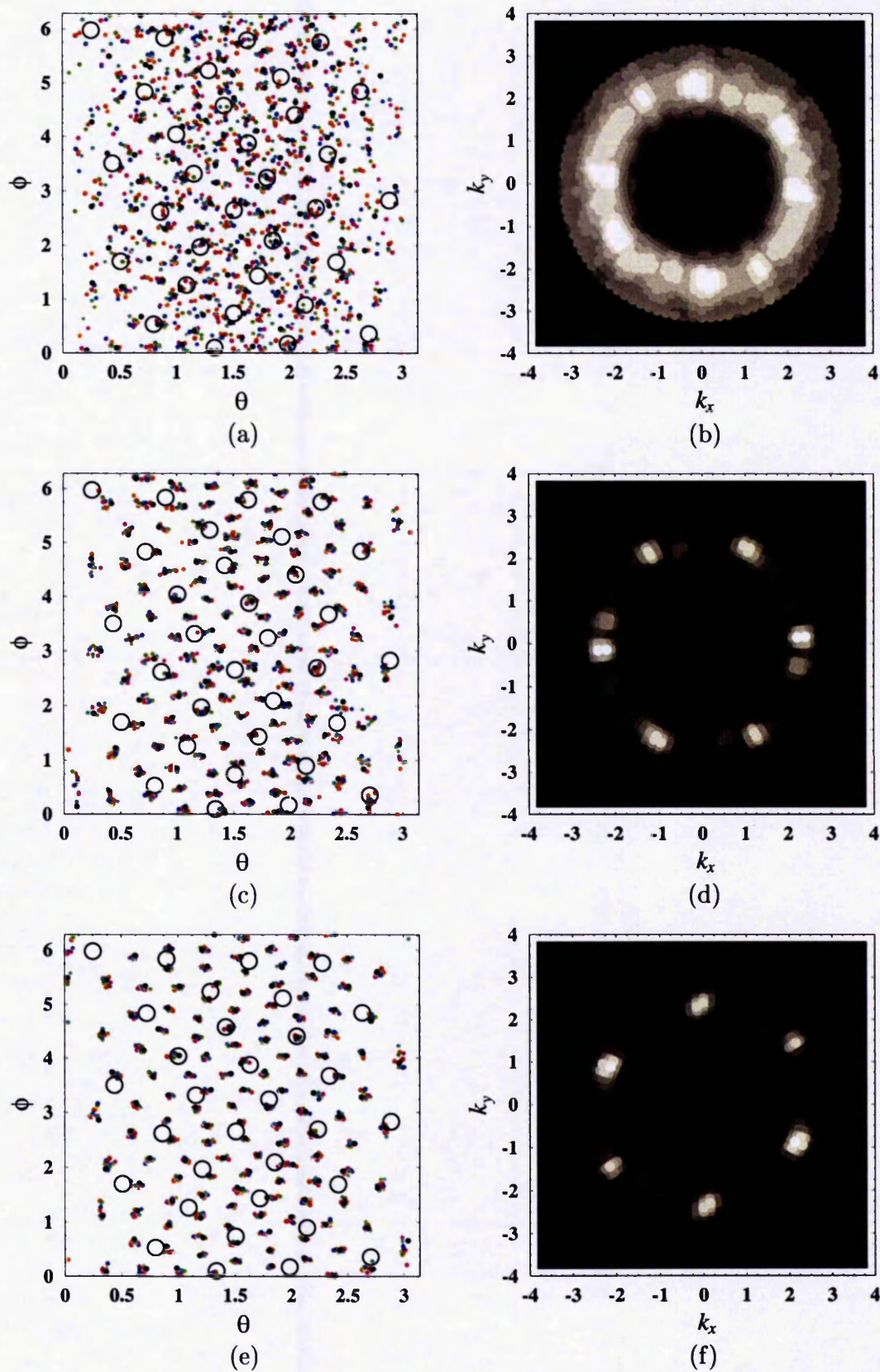


Figure 4.16: Angular vortex-positions (in all layers) and structure factor (at layer $M/2$) of the layered HTSC with a regular array of columnar defects along the c -axis for $(N, M) = (132, 12)$, $N' = 32$, $\eta = 0.14142$ and $g = 0.1$ as the temperature is lowered: $\alpha_T = -3, -4, -5$. [(a,b),(c,d),(e,f) respectively.]

4.3. Pinning by a Periodic Substrate of Columnar Defects

4.4 Discussion

Throughout this section the results of our investigation on the layered HTSC are summarised and compared to their similar as found in other studies.

The Clean Layered-HTSC

As the large majority of HTSCs having the highest critical temperature are the copper-oxide layered compounds, the problem of considering layered systems has been of great interest. Particularly, work has been carried out in pure systems both on the usual array of planes [105, 106] and on the spherical geometry [85, 108]. In the first case there is a claim that a first-order melting transition takes place on heating the system from the low temperature phase. This, according to the different investigations, can be simultaneous to (or followed by) a decoupling transition where flux lines break up to become pancake vortices. An alternative scenario [107] proposes that the first-order transition is associated with decoupling of layers and that melting takes place through a gradual crossover. On the spherical geometry a first-order transition is also observed, but this one appears to end at a critical point. The study of vortex correlations along the c -axis (orthogonal to the layers, but parallel to the applied magnetic field) seems to be consistent with a decoupling transition of flux lines. Then, the vanishing of hysteresis loops above a certain value of the inter-layer coupling parameter is taken as evidence for the existence of a critical point. The argument which follows is that as the line is ending at a critical point, the phase boundary must separate phases of the same symmetry. This leads to the conclusion that the phase should always be a vortex liquid. Recently Yeo and Moore [109], from a nonperturbative study on the plane geometry using the parquet approximation method, have reported the same result but appearing at higher temperatures (probably because of the restricted number of layers they can access).

In our investigation, we can spot the interlayer vortex-decoupling transition, and it appears sharp enough so that it might be a first-order transition. This rapid raise in correlations along the c -axis is simultaneous to an abrupt increase of in-layer density

correlations (making the system effectively as correlated as a vortex crystal). The phase boundary we are able to obtain is quantitatively in agreement with that in Ref. [108] up to the claimed critical point. About that region we have not a substantial amount of data so as to perform a detailed analysis. This makes our work inconclusive on whether a melting transition is possible or it is the critical end-point scenario which accounts for the correct description.

It appears that observing a first-order phase transition in both geometries (either on flat or spherical layers) is not a coincidence, though it is not clear why they are of different nature. What seems plausible is that perhaps the different investigations are dealing with essentially the same information but interpreting it in different ways.

The Layered HTSC with Randomly-Distributed Columnar Defects

The state of current research on this problem is restricted to the usual planar geometry, for which a Bose-glass phase is suggested to exist at low temperatures [111, 112, 113, 114, 115]. This should be separated from a higher-temperature liquid of decoupled pancake-vortices (as described in Sec. 4.2). No previous results on this problem have been presented on the spherical geometry.

In our investigation the study of the in-layer density correlation-length shows no signature of any abrupt change. That length scale remains roughly linear, increasing as α_T decreases. We interpret this as that the system undergoes no abrupt intralayer-change in symmetry. However, analysis of the phase correlation function along the c -axis reveals the appearance of phase coherence at a considerable high temperature. This and plots of the vortex positions as temperature is lowered seem to confirm that the transition is directly associated to coupling of pancake-vortices in different layers. Therefore it is clear that the low temperature phase of this system should be a glass of coupled pancake-vortices, while at high temperatures it is a liquid of decoupled vortices. All this takes place at high temperatures, suggesting that the pinning strength used in these simulations is rather strong. The possibility exists that this model is correctly described by the theory of pinning by correlated disorder (see Sec. 4.2), but in order to know whether this indeed happens we must be able to locate

the flux-line positions respect to the columnar defects. Unfortunately from the form of the pinning potential, $\Omega(\mathbf{r})$, it is not straightforward to determine the columnar-defect sites and thus the question of whether the low temperature phase of the system is a Bose-glass state remains unanswered.

The Layered HTSC with a Regular Substrate of Columnar Defects

As for the layered HTSC with randomly-distributed columnar defects, the theory of pinning by correlated disorder in Section 4.2 is also expected to describe this problem. In this case the usual approach has been considering arrays of columnar pins which are either commensurate or incommensurate to the low temperature vortex lattice. We have followed that approach and have found two main results: In the case when the magnitude of the magnetic induction equals the matching field, we can spot the Mott insulator phase below a given effective temperature α_T (which depends on the pinning strength g and interlayer coupling η). The Mott insulator phase is characterised by quasi-long-ranged phase correlations along the c -axis and disentangled flux-lines pinned at each columnar defect; and in this model seems to appear simultaneously with the coupling of vortices along the c -axis. One main difference between the model here and the usual planar systems [113] is that the transition to the Mott insulator phase seems to take place in “two steps”. From high to low temperatures, first in-layer density correlations are observed to increase abruptly and then phase correlations along the c -axis become quasi-long-ranged.

For the case $B > B_\Phi$ our investigation, carried out on weak pinning ($g = 0.1$), suggests that whether the pinning substrate and the flux-line lattice are commensurate or not is not a relevant issue. The only parameter which seems to play a role is the so called “filling fraction” $N/N' = B/B_\Phi$. At the accessible values here, $N/N' > 4$, we find that the system behaves as if no pinning were present (i.e. no appreciable difference between the pure sample and the one with columnar pins is observed). For stronger pinning strengths we cannot rule out the possibility of a low temperature Bose-glass phase.

Conclusions

The results of our numerical investigation in both thin-film and layered models of HTSCs in a perpendicular magnetic field have shown a “variety” of phases that the vortex system can experience as an interplay of temperature, inter-layer coupling and pinning strength.

For the thin-film model of a defect-free HTSC we find consistency with a single vortex-liquid phase which covers the mixed phase and freezes only in the zero temperature limit. This is in agreement with investigations on the same spherical geometry, but contrary to the studies on the flat-plane with quasi-periodic boundary conditions which generally claim the existence of a first-order melting transition of the Abrikosov vortex-lattice at a non-zero finite temperature. It has also been shown that the introduction of random impurities drive the vortex liquid to a vortex glass-like phase with density correlations that grow in the same fashion as if no disorder were present. Consistently, the ground state vortex lattice is replaced by an amorphous-solid phase of vortices. For the case where a periodic substrate of pinning centres is introduced in the film the behaviour of the system seems to be determined by the filling fraction $N/N' = B/B_\Phi$. At the matching field, $B/B_\Phi = 1$, the predicted XY-type continuous transition takes place. This phase boundary separates a low temperature region in which superconducting phase coherence exists from a non-phase-coherent state. The case $B/B_\Phi > 1$ appears not sensible to weak pinning, but beyond a large-enough strength shows qualitatively the same phase diagram as the case at the matching field. In the ground state this strongly pinned system shows a novel vortex quasi-lattice when $B_\Phi < B < 6B_\Phi$. As the usual vortex lattice is observed (at weak pinning) in the zero-temperature limit, the system is expected to have a sharp transition between these

vortex lattices (as they have different symmetry). This should take place at a pinning strength $g > 0.1$ as $T \rightarrow 0$.

In the layered HTSC our investigation shows evidence for a sharp first-order transition in which pancake-vortices couple along the c -axis. This is a common feature that appears regardless there are columnar defects or not. The phase above the line of phase transitions is found to have short-range correlations (both intralayer and interlayer), and therefore can be regarded as a liquid of decoupled pancake-vortices. The low temperature phase, however, is determined by pinning effects. For an ideally clean-sample, our investigation demonstrates that in the low-temperature phase the system behaves effectively as a crystal (with in-layer density correlation length which appears to diverge at a finite temperature in the thermodynamic limit). This, and the fact that we are unable to determine a critical end-point, suggests that flux-lattice melting could also take place at the coupling transition. In the case of the system with columnar defects randomly distributed through the layers, a low-temperature vortex glass can be observed. No signature of a sharp transition to the vortex liquid suggests that the system just crosses over to liquid behaviour at the decoupling transition. This is not consistent with the expected continuous transition from the theory of pinning by correlated disorder. The question whether the vortex glass is in fact a Bose-glass remains to be answered. Finally, for the system with a regular array of columnar defects the most interesting effects are observed. At the matching field, $B/B_\Phi = 1$, the Mott insulator phase (where all columnar pins are occupied and no free flux-lines remain) appears at low temperatures. The mechanism for the system to achieve this appears to be setting of lattice-like vortex ordering within each layer and then inter-layer coupling (the last simultaneous with flux-line trapping by columnar defects). The case $B/B_\Phi > 1$ shows no signature of a Bose-glass phase down to temperatures $\alpha_T = -13$ in the weak pinning regime.

Perhaps the most important conclusion of this work is that it shows that pinning by regular arrays appears to depend on the parameter B/B_Φ , but not on whether the pinning substrate and the vortex system are commensurate or not. This result could be used to enhance properties of the layered HTSC by introducing the maximum

amount of columnar defects. That would happen when a nearly closed-pack array of cylindrical columns (of radius of the ground-state size of the vortex core) were introduced with axes forming a triangular lattice (on the planar geometry) or the appropriate icosahedral structure (on the spherical structure). In such a case, for any applied magnetic field below the H_{c2} line, the ratio B/B_{Φ} will be maximized and pinning effects should be optimum even at strong magnetic fields.

Proposition for Further Work

This numerical investigation has been based on phenomenological parameters only. One piece of theoretical information which would be desirable to have is a consistent map between the effective temperature, inter-layer coupling, pinning strengths, etc., and the parameters used in experiments: temperature, applied magnetic field, etc., so as to be able to compare numerical results with a variety of compounds.

Numerically, the major problem seems to be the difficulty to access system sizes of (at least!) one order of magnitude bigger, which may resolve controversies arising from finite-size effects. The only way out in this appears to be to make use of more sophisticated computer power (either vector, parallel, super-computers or the novel “Linux-clusters” that can be comparable in speed to some of the others). Making use of all possible CPU resources, finer numerical-measurements could be carried out about the raw estimations provided here (aimed at determining the precise nature of the transitions). This seems to be a high-priority task, but perhaps the first step is still to resolve the controversy of the phase diagram of an ideally clean thin-film of HTSC.

Appendix A

Notation, Conventions and Derivations

In this appendix we set up the notation and conventions, and derive the most important expressions used throughout this thesis. Readers interested in details of the model may be benefited by reading Section A.1 before going through the whole manuscript.

A.1 Notation and Conventions

In general we employ the usual symbols to denote physical (or mathematical) functions, variables, parameters or constants as follows: \mathcal{H} for Hamiltonian, \mathbf{H} or H for external magnetic field, \mathbf{B} for magnetic induction (though B is used for the Beta function). T is the temperature (with T_c denoting the “critical temperature”, when one exists). $H_c(T)$, $H_{c1}(T)$ and $H_{c2}(T)$ are the “critical fields” (thermodynamical, lower and upper, respectively). $\lambda(T)$ stands for the magnetic penetration depth and $\xi(T)$ is the coherence length. κ is the Ginzburg-Landau parameter. \mathbf{j} or j denote a transport current density. \mathbf{A} is the magnetic vector potential, etc. . . .

Vectors are, as usual, typed in boldface. Unit vectors, in addition, will have a hat on them (e.g. the orthonormal triad in Cartesian coordinates: $\{\hat{\mathbf{i}}, \hat{\mathbf{j}}, \hat{\mathbf{k}}\}$, or the one in spherical polar coordinates: $\{\hat{\mathbf{r}}, \hat{\boldsymbol{\theta}}, \hat{\boldsymbol{\phi}}\}$). Notice, however, that the use of the hat is not exclusive for unit vectors, but also applies to “quantum mechanical”

operators (when appropriate). Some other sets of coefficients with two indices (that could be written as matrices) are also typed in boldface. Functionals are recognised by writing their arguments in square brackets while for functions we use just common parenthesis. Measure elements in functional integrations are denoted by $\mathcal{D}[f]$, where f is an argument of the functional (which can be complex in general). First arguments (separated by commas) of both functionals and functions will denote “variables”, but if there is a semicolon then all arguments after it will represent “parameters” (except for the generalized hypergeometric functions ${}_pF_q$). In the case of the functions ${}_pF_q$ the arguments will be arranged in a two-row matrix with the upper vector containing the p upper parameters of the hypergeometric expansion and the lower one containing the q lower parameters plus (separated by a semicolon) the argument of the function, z .

Within the Ginzburg-Landau (GL) theory of superconductivity, $\psi(\mathbf{r})$ denotes the superconducting order parameter. $\alpha(T)$ and β are the phenomenological GL parameters. In the derivative operator, $\mathbf{D} = -i\hbar\nabla - 2e\mathbf{A}$, we write explicitly the charge of the Cooper pair, $2e$, and for consistency set $m = 2m_e$ (i.e. the mass of the Cooper pair). The energy Landau levels (LL) are denoted as $\psi_{n,\dots}$ and the highly degenerated ($n = 0$) lowest Landau level (LLL) written just as ψ_{\dots} , where “ \dots ” denotes k_x in the plane geometry but “ q, N ” on the sphere. The LLL expansion for the superconducting order parameter, ψ , will be denoted as ψ_L (with L an abbreviation for *LLL*). In this Q represents a temperature-dependent amplitude factor for ψ_L and $\{v_q\} \equiv \mathbf{v}$ are complex expansion-coefficients weighting each degenerate function of the LLL subset. $\alpha_H(T)$ and β_κ represent the “phenomenological GL parameters” within the LLL approximation (analogous to the $\alpha(T)$ and β above). $\tilde{\psi}_L(\tilde{\mathbf{r}})$ stands for the rescaled order parameter (depending on the rescaled vector $\tilde{\mathbf{r}}$). This defines a new rescaled order-parameter amplitude, \tilde{Q} , and both parameters (α_H and β_κ) can be combined to define effective temperature (and magnetic field) parameters: α_T in two dimensions, and $\alpha_T^{(3D)}$ in three dimensions.

The Lawrence-Doniach model for layered superconductors follows parallel notation, except that the order parameter in each layer is labeled by an index n . That is, $\psi_n(\mathbf{r})$ is the order parameter in layer n . This layered structure introduces anisotropy

to the model. The case investigated in this thesis is that of the magnetic field applied perpendicular to the layers, and we always refer the anisotropic quantities to the direction of the field (e.g. m_{\parallel} and m_{\perp} are the masses parallel and perpendicular to the applied magnetic field respectively). The same LLL eigenfunctions for the thin film in the GL theory (ψ_{\dots} above) apply in each layer. Thus the LLL expansion of the order parameter in layer n is now denoted $\psi_{n,L}$ (and the complex expansion coefficients $\{v_{n,q}\} \equiv \mathbf{v}$). With the appropriate replacement of m by either m_{\parallel} or m_{\perp} , the same definitions of α_H , β_K , etc. apply in this case. This, therefore, affects the GL definitions of α_T and $\alpha_T^{(3D)}$. In analogy to the thin film, a rescaled order parameter per layer, $\tilde{\psi}_{n,L}(\tilde{\mathbf{r}})$ with amplitude \tilde{Q} , is also defined.

We follow the usual notation on averages: \overline{X} represents the spatial average of the quantity “ X ” over the ‘volume’ under consideration, $\langle X \rangle$ denotes its thermal average, and $\langle X \rangle_{\text{dis}}$ an average over disorder. As for the numerical model we have: R denotes the average radius of the spherical sample (both for the thin film and the layered system), d_0 the layer thickness and (in the layered case) s the interlayer spacing. l_m is the magnetic length (mean distance between magnetic vortices) and \overline{B} the average magnetic flux through the sample. Interlayer coupling in the layered case is measured by the parameter η (to be distinguished from the vortex coordinate in stereographic projection, (ξ, η)). σ^2 stands for the strength of the coupling between magnetic vortices and randomly distributed pinning centres (or columnar defects in the layered case). g represents the analogous to σ^2 but for regular arrays of pinning centres.

At last, we choose to write our expressions in the SI (or MKS) unit-system. In this each of the physical constants appearing throughout the thesis have the value:¹

e	charge of the electron (including sign)	$[e = -1.60217733 \times 10^{-19} \text{ C}]$.
m	mass of the Cooper pair (i.e. twice m_e)	$[m = 1.8218779 \times 10^{-30} \text{ Kg}]$.
\hbar	Planck’s constant h divided by 2π	$[\hbar = 1.05457266 \times 10^{-34} \text{ J}\cdot\text{s}]$.
k_B	Boltzmann’s constant	$[k_B = 1.380658 \times 10^{-23} \text{ J/K}]$.
μ_0	Permeability of the vacuum	$[\mu_0 = 4\pi \times 10^{-7} \text{ H/m}]$.

And the usual mathematical constants $\pi = 3.14159265 \dots$ and $e = 2.71828182 \dots$.

¹Taken from Ref. [116]. (In all cases the standard error is $\leq 6 \times 10^{-7}$, except for k_B where it is $< 9 \times 10^{-6}$.)

A.2 Landau Levels

In this part we derive the energy eigenfunctions of a particle of charge $2e$ and mass m moving on a two-dimensional surface with a magnetic field perpendicular to it. The problem is to find the spectrum of eigenstates and eigenvalues of the operator $\mathbf{D}^2 = (-i\hbar\nabla - 2e\mathbf{A})^2$ for a given surface and vector potential \mathbf{A} . We consider two geometries here, a plane surface with a perpendicular magnetic field and a spherical surface with a radial magnetic field coming out of its centre. In any of these cases we see that the eigensolutions of this problem are the same as those of the operator $\mathbf{D}_{\hat{n}}^2 = (\hat{n} \times \mathbf{D})^2$; where \hat{n} is a vector perpendicular to the surface where the particle moves (that is, parallel to the applied magnetic field). This new operator can be written in general as

$$\mathbf{D}_{\hat{n}}^2 = -\hbar^2 \nabla_{\perp}^2 + 2ei\hbar(\nabla_{\perp} \cdot \mathbf{A}_{\perp}) + 4ei\hbar\mathbf{A}_{\perp} \cdot \nabla_{\perp} + 4e^2\mathbf{A}_{\perp}^2, \quad (\text{A.1})$$

where we have introduced the direction “perpendicular” relative to the applied magnetic field.

Plane Geometry: Landau’s Gauge

In the plane geometry we assume the particle moving on the xy -plane with a uniform magnetic field pointing in the positive direction of the z -axis defined by the Landau’s gauge: $\mathbf{A} = -\bar{B}y\hat{i}$. Thus $\hat{n} = \hat{k}$ and the eigenfunctions of the operator in Eq. (A.1) will be functions $\psi(x, y)$. We notice immediately that this gauge satisfies $\nabla \cdot \mathbf{A} = \nabla_{\perp} \cdot \mathbf{A}_{\perp} = 0$ and substituting it in Eq. (A.1) we obtain for this geometry

$$\mathbf{D}_{\hat{k}}^2 = -\hbar^2 \left(\frac{\partial^2}{\partial x^2} + \frac{\partial^2}{\partial y^2} \right) - 4ei\hbar\bar{B}y \frac{\partial}{\partial x} + 4e^2\bar{B}^2 y^2. \quad (\text{A.2})$$

Following arguments by Landau [117] we notice that the momentum operator in the x -direction, $\hat{p}_x = -i\hbar\partial/\partial x$, commutes with $\mathbf{D}_{\hat{k}}^2$ (because the coordinate x is not contained explicitly in $\mathbf{D}_{\hat{k}}^2$). Therefore $\mathbf{D}_{\hat{k}}^2$ and \hat{p}_x share the same set of eigenfunctions, and $\psi(x, y)$ can be written in the form

$$\psi(x, y) = \exp(ik_x x) \varphi(y), \quad (\text{A.3})$$

where $\hbar k_x$ are the eigenvalues of the momentum operator \hat{p}_x (which take all real values from $-\infty$ to $+\infty$) and the function $\varphi(y)$ is to be determined. In fact, substituting Eq. (A.3) into the energy eigenvalues equation

$$\frac{1}{2m} \mathbf{D}_{\mathbf{k}}^2 \psi(x, y) = E \psi(x, y), \quad (\text{A.4})$$

reveals that the function $\varphi(y)$ must satisfy

$$\varphi''(y) + \frac{2m}{\hbar^2} \left[E - \frac{1}{2} m \omega^2 (y - y_0)^2 \right] \varphi(y) = 0, \quad (\text{A.5})$$

where $y_0 = \hbar k_x / 2|e|\bar{B}$ and $\omega = 2|e|\bar{B}/m$. Eq. (A.5) is formally the equation of a quantum linear oscillator, oscillating with frequency ω about the coordinate y_0 . Therefore we conclude that the energy levels of this particle moving on a plane perpendicular to a uniform magnetic field (called the Landau levels) are given by

$$E_n = \hbar \omega \left(n + \frac{1}{2} \right), \quad (\text{A.6})$$

for $n = 0, 1, 2, \dots$; and the solutions of Eq. (A.5) given by [117]

$$\varphi_n(y) = C_n \exp \left[-\frac{1}{2} \left(\frac{y - y_0}{l_m} \right)^2 \right] H_n \left(\frac{y - y_0}{l_m} \right), \quad (\text{A.7})$$

where $H_n(x)$ are the Hermite polynomials of order n , $C_n = [\pi^{1/4} l_m^{1/2} \sqrt{2^n n!}]^{-1}$ is the normalization constant for this solution and we have written the magnetic length as $l_m = \sqrt{\hbar/m\omega}$.

The normalized Landau level eigenfunctions for this geometry can be obtained by normalizing the x -component solution. For a finite-sized system (of length L_x along the x direction) and periodic boundary condition (PBC), $\exp(ik_x x) = \exp(ik_x[x + L_x])$, the x -component of the wave vector is quantized so that $k_x = 2\pi n_x / L_x$ for $n_x = 0, \pm 1, \pm 2, \dots$. In this case the normalization constant for the x solution is just $L_x^{-1/2}$. For an infinite system a generalized “normalization” to a Dirac delta function is common [118]. For this k_x can take any real value, $-\infty < k_x < \infty$, and if k_x is chosen as the argument of the Dirac delta function then the normalization factor in the x -direction is $1/\sqrt{2\pi}$. In any case the eigenfunctions can be written as

$$\psi_{n,k_x}(x, y) = \mathcal{N}_n \exp \left[ik_x x - \frac{1}{2} \left(\frac{y - y_0}{l_m} \right)^2 \right] H_n \left(\frac{y - y_0}{l_m} \right), \quad (\text{A.8})$$

where $\mathcal{N}_n = [\pi^{1/4} l_m^{1/2} L_x^{1/2} \sqrt{2^n n!}]^{-1}$ in the finite-sized system (in the infinite case it takes the value $\mathcal{N}_n = [\pi^{3/4} l_m^{1/2} \sqrt{2^{n+1} n!}]^{-1}$).² Notice that y_0 can also be written as $y_0 = k_x l_m^2$. In particular the lowest Landau level ($n = 0$) has energy $E_0 = |e| \bar{B} \hbar / m$ and is spanned by the degenerate set of states

$$\psi_{k_x}(x, y) = \mathcal{N} \exp \left[i k_x x - \frac{1}{2} \left(\frac{y - y_0}{l_m} \right)^2 \right], \quad (\text{A.9})$$

with finite-system normalization $\mathcal{N} = [\pi^{1/4} l_m^{1/2} L_x^{1/2}]^{-1}$. ($\mathcal{N} = [2^{1/2} \pi^{3/4} l_m^{1/2}]^{-1}$ in the infinite case.) From Eq. (A.9) on in this Appendix we assume the convention on the fifth footnote in Chapter 2. That is, the $n = 0$ index in the LLL expressions will be dropped to compact the notation.

Spherical Geometry: Magnetic Monopole

Here we assume the particle moving on the sphere of radius R with a radial magnetic field coming out of its centre (as produced by a magnetic monopole) defined by the gauge $\mathbf{A} = (\bar{B} R^2 / r) \tan(\theta/2) \hat{\phi}$, where $\bar{B} = B(R)$. Therefore $\hat{\mathbf{n}} = \hat{\mathbf{r}}$ and the eigenfunctions of the operator in Eq. (A.1) will be functions $\psi(\theta, \phi)$. This gauge also satisfies $\nabla \cdot \mathbf{A} = \nabla_{\perp} \cdot \mathbf{A}_{\perp} = 0$ and substituting it in Eq. (A.1) we obtain

$$[\mathbf{D}_{\hat{\mathbf{r}}}^2]_{r=R} = -\frac{\hbar^2}{R^2} \left[\frac{1}{\sin \theta} \frac{\partial}{\partial \theta} \left(\sin \theta \frac{\partial}{\partial \theta} \right) + \frac{1}{\sin^2 \theta} \frac{\partial^2}{\partial \phi^2} - iN \frac{1}{1 + \cos \theta} \frac{\partial}{\partial \phi} - \frac{N^2}{4} \frac{1 - \cos \theta}{1 + \cos \theta} \right], \quad (\text{A.10})$$

where Gauss' law of electromagnetism, $4\pi R^2 \bar{B} = N \Phi_0$ ($\Phi_0 = \pi \hbar / |e|$), has been used.

In a similar fashion to the plane geometry, as the coordinate ϕ does not appear explicitly in the operator $[\mathbf{D}_{\hat{\mathbf{r}}}^2]_{r=R}$, we conclude immediately that this operator

²When the particle is allowed to move in a three-dimensional space with the uniform magnetic field pointing in the z -direction the energy eigenvalues get a contribution from the momentum component in this direction. They are in this case: $E_{n,k_z} = \hbar \omega \left(n + \frac{1}{2} \right) + \hbar^2 k_z^2 / 2m$ and the eigenstates become

$$\psi_{n,k_x,k_z}(x, y, z) = \mathcal{N}_n^{(3D)} \exp \left[i(k_x x + k_z z) - \frac{1}{2} \left(\frac{y - y_0}{l_m} \right)^2 \right] H_n \left(\frac{y - y_0}{l_m} \right).$$

with normalization constant for the finite-sized system (with PBCs in the x and z directions) given by $\mathcal{N}_n^{(3D)} = [\pi^{1/4} l_m^{1/2} L_x^{1/2} L_z^{1/2} \sqrt{2^n n!}]^{-1}$. For the infinite system $\mathcal{N}_n^{(3D)} = [\pi^{5/4} l_m^{1/2} \sqrt{2^{n+2} n!}]^{-1}$.

commutes with the angular momentum operator in the z -direction, $\hat{l}_z = -i\partial/\partial\phi$. Therefore $[\mathbf{D}_{\mathbf{f}}^2]_{r=R}$ and \hat{l}_z have common eigenfunctions which can be written in the form

$$\psi(\theta, \phi) = \exp(iq\phi)f(\theta), \quad (\text{A.11})$$

where we are denoting by q the eigenvalues of \hat{l}_z and the function $f(\theta)$ is yet to be determined. If the function ψ is to be single valued, it must be periodic, with period 2π . This implies that $q = 0, \pm 1, \pm 2, \dots$. By substituting Eq. (A.11) into the energy eigenvalues equation [analogous to Eq. (A.4)]

$$\frac{1}{2m} [\mathbf{D}_{\mathbf{f}}^2]_{r=R} \psi(\theta, \phi) = E\psi(\theta, \phi), \quad (\text{A.12})$$

we see that the function $f(\theta)$ must satisfy the equation

$$f''(\theta) + \frac{\cos\theta}{\sin\theta} f'(\theta) + \left[E' - \frac{q^2}{\sin^2\theta} + \frac{qN}{1+\cos\theta} - \frac{N^2}{4} \frac{1-\cos\theta}{1+\cos\theta} \right] f = 0, \quad (\text{A.13})$$

where $E' = (2mR^2/\hbar^2)E$. Now we perform the change of variable $x = \cos\theta$, with which the equation becomes

$$(1-x^2) f''(x) - 2xf'(x) + \left[E' - \left(\frac{N}{2}(1-x) - q \right)^2 (1-x^2)^{-1} \right] f(x) = 0. \quad (\text{A.14})$$

The form of this equation suggests to try a solution of the form

$$f(x) = (1-x)^\mu (1+x)^\nu g(x), \quad (\text{A.15})$$

which in fact, for $\mu = q/2$ and $\nu = (N-q)/2$, reduces it to

$$(1-x^2) g''(x) + [(N-2q) - (N+2)x]g'(x) + \left(E' - \frac{N}{2} \right) g(x) = 0. \quad (\text{A.16})$$

The solutions of this equation are the Jacobi polynomials [119] $P_n^{(q, N-q)}(x)$ with energy eigenvalue

$$E_n = \hbar\omega \left(\frac{n(n+N+1)}{N} + \frac{1}{2} \right), \quad (\text{A.17})$$

where we have used $\hbar^2/2mR^2 = \hbar\omega/N$ and $\omega = 2|e|\overline{B}/m$ as before. Combining the results of Eqs. (A.11) and (A.15), with $x = \cos\theta$, we write the normalized Landau

level eigenfunctions for this geometry as³

$$\psi_{n,q,N}(\theta, \phi) = \mathcal{N}_{n,q,N} e^{iq\phi} \sin^q(\theta/2) \cos^{N-q}(\theta/2) P_n^{(q,N-q)}(\cos \theta), \quad (\text{A.18})$$

with the normalization constant $\mathcal{N}_{n,q,N} = \left[\frac{(N+1+2n)n!(N+n)!}{(q+n)!(N-q+n)!4\pi R^2} \right]^{1/2}$.

The Landau levels are, once again, labelled by the index $n = 0, 1, 2, \dots$. From the properties of the Jacobi polynomials and the finite value of the normalization constant, $\mathcal{N}_{n,q,N}$, the number of degenerate states in each level is found to be $N+1+2n$. The angular momentum values that the particle may take within the level n are $q = -n, -n+1, \dots, n+N$. Analogously to the plane geometry, the lowest Landau level ($n=0$) has energy $E_0 = |e|\bar{B}\hbar/m$ and, in this case, is composed by the degenerate set of $N+1$ states

$$\psi_{q,N}(\theta, \phi) = \mathcal{N}_{q,N} e^{iq\phi} \sin^q(\theta/2) \cos^{N-q}(\theta/2), \quad (\text{A.19})$$

with $q = 0, 1, \dots, N$ and normalization factor $\mathcal{N}_{q,N} = [(N+1)C_N^q/4\pi R^2]^{1/2}$, where $C_N^q = N!/q!(N-q)!$ is the binomial coefficient.

Notice, however, that the equidistant spacing between successive energy levels on the plane does not apply on a finite radius sphere. In this case the spacing increases quadratically with n as shown in Fig. 2.1.

A.3 LLL Calculations on Energy Terms

In this part we derive expressions for the energy terms used in numerical calculations and simulations. We concentrate on the general case of the spherical layered superconductor within the LLL approximation as described in Chapter 4 (the thin-film case

³Once again, if the particle is allowed to move in a three-dimensional space with the radial magnetic field $\bar{\mathbf{B}} = \bar{B}\hat{\mathbf{r}}$ the energy eigenvalues become: $E_{n,k} = \hbar\omega \left(\frac{n(n+N+1)}{N} + \frac{1}{2} \right) + \hbar^2 k^2 / 2m$, and the energy eigenstates can be approximated by

$$\psi_{n,q,N,k}(r, \theta, \phi) = \mathcal{N}_{n,q,N,k}^{(3D)} K_k(r) e^{iq\phi} \sin^q(\theta/2) \cos^{N-q}(\theta/2) P_n^{(q,N-q)}(\cos \theta),$$

where $K_k(r) = r^{-1/2} [C_1 J_{1/2}(kr) + C_2 H_{1/2}^{(2)}(kr)]$, with $J_{1/2}(z)$ the Bessel function of the first kind, $H_{1/2}^{(2)}(z)$ the second Hankel function and C_1, C_2 integration constants [120]. $\mathcal{N}_{n,q,N,k}^{(3D)}$ is a normalization constant.

is regained by setting the interlayer terms to zero and dropping the sum over n and the index from the intralayer terms).

A.3.1 Expansion Coefficients Representation

First we concentrate on the derivation of the energy functions, within the LLL approximation, in terms of the complex expansion coefficients $\{v_{n,q}\}$. We start with the different terms in the energy of the clean system and then the pinning contributions are calculated.

A.3.1.1 Clean Energy Term: Three Integrals

To begin with, we consider the LD-LLL energy functional for the scaled parameters given in Eq. (2.50) with the order parameter expanded in terms of the LLL energy eigenfunctions in the spherical geometry as in Eq. (4.1). This substitution leads to the calculation of three integrals.

First Integral: Quadratic Intralayer Contribution

The first energy term (quadratic intralayer contribution) per unit of thermal energy, after substitution of the scaled order parameter in Eq. (4.1), becomes

$$\frac{\mathcal{H}_c^{(1)}(\mathbf{v})}{k_B T} = \alpha_T \sum_{n=1}^M \sum_{p,q=0}^N v_{n,p}^* v_{n,q} \int d^2 r \psi_{p,N}^* \psi_{q,N}. \quad (\text{A.20})$$

After introducing the LLL eigenstates, the integral can be written as

$$\int d^2 r \psi_{p,N}^* \psi_{q,N} = \mathcal{N}_{p,N} \mathcal{N}_{q,N} R^2 \int_0^{2\pi} d\phi e^{i(q-p)\phi} \int_0^\pi d\theta \sin \theta \sin^{p+q}(\theta/2) \cos^{2N-p-q}(\theta/2). \quad (\text{A.21})$$

The integration over ϕ is immediate and, for this case of integers p and q , gives a factor $2\pi \delta_{p,q}$. The remaining integral over θ can be evaluated by using the Beta function form

$$B(x+1, y+1) = \frac{1}{2} \int_0^\pi d\theta \sin \theta \sin^{2x}(\theta/2) \cos^{2y}(\theta/2), \quad (\text{A.22})$$

to give

$$\int d^2 r \psi_{p,N}^* \psi_{q,N} = \mathcal{N}_{p,N} \mathcal{N}_{q,N} 4\pi R^2 \delta_{p,q} B\left(\frac{p+q}{2} + 1, \frac{2N-p-q}{2} + 1\right). \quad (\text{A.23})$$

If $p \neq q$ the integral is zero, but if $p = q$ the result is

$$\int d^2r \psi_{p,N}^* \psi_{q,N} = (\mathcal{N}_{p,N})^2 4\pi R^2 B(p+1, N-p+1), \quad (\text{A.24})$$

which, by using $(\mathcal{N}_{p,N})^2 = (N+1)!/4\pi R^2 p!(N-p)!$ and $B(p+1, N-p+1) = p!(N-p)!/(N+1)!$, is clearly one. Therefore we have derived the orthonormal relationship for the LLL eigenfunctions:

$$\int d^2r \psi_{p,N}^* \psi_{q,N} = \delta_{p,q}, \quad (\text{A.25})$$

which when used in Eq. (A.20), reduces it to

$$\frac{\mathcal{H}_c^{(1)}(\mathbf{v})}{k_B T} = \alpha_T \sum_{n=1}^M \sum_{q=0}^N |v_{n,q}|^2. \quad (\text{A.26})$$

Second Integral: Quartic Intralayer Contribution

The second term in Eq. (2.50) gives another intralayer contribution, but this time of fourth order in the LLL eigenfunctions. After substitution of the scaled order parameter, Eq. (4.1), it takes the form

$$\frac{\mathcal{H}_c^{(2)}(\mathbf{v})}{k_B T} = \pi \sum_{n=1}^M \sum_{p,q,r,s=0}^N v_{n,p} v_{n,q} v_{n,r}^* v_{n,s}^* \int d^2r \psi_{p,N} \psi_{q,N} \psi_{r,N}^* \psi_{s,N}^*. \quad (\text{A.27})$$

By introducing the LLL eigenstates, the integral can be written as

$$\begin{aligned} \int d^2r \psi_{p,N} \psi_{q,N} \psi_{r,N}^* \psi_{s,N}^* &= \mathcal{N}_{p,N} \mathcal{N}_{q,N} \mathcal{N}_{r,N} \mathcal{N}_{s,N} \\ &\times R^2 \int_0^{2\pi} d\phi e^{i(p+q-r-s)\phi} \int_0^\pi d\theta \sin \theta \sin^{p+q+r+s}(\theta/2) \cos^{4N-(p+q+r+s)}(\theta/2). \end{aligned} \quad (\text{A.28})$$

Analogously to the previous case, the integration over ϕ gives a factor $2\pi \delta_{p+q,r+s}$. The integration over θ follows directly from Eq. (A.22) to give

$$\begin{aligned} \int d^2r \psi_{p,N} \psi_{q,N} \psi_{r,N}^* \psi_{s,N}^* &= \mathcal{N}_{p,N} \mathcal{N}_{q,N} \mathcal{N}_{r,N} \mathcal{N}_{s,N} \\ &\times 4\pi R^2 \delta_{p+q,r+s} B\left(\frac{p+q+r+s}{2} + 1, \frac{4N-(p+q+r+s)}{2} + 1\right). \end{aligned} \quad (\text{A.29})$$

The Kronecker delta function forces the indices to satisfy $p+q=r+s$ (otherwise the integral is zero). In this case the value can be written in the symmetric form

$$\begin{aligned} \int d^2r \psi_{p,N} \psi_{q,N} \psi_{r,N}^* \psi_{s,N}^* &= \mathcal{N}_{p,N} \mathcal{N}_{q,N} \mathcal{N}_{r,N} \mathcal{N}_{s,N} 4\pi R^2 \delta_{p+q,r+s} \\ &\times B^{1/2}(p+q+1, 2N-p-q+1) B^{1/2}(r+s+1, 2N-r-s+1), \end{aligned} \quad (\text{A.30})$$

which after simplifications on the factors $\mathcal{N}_{k,N}$ and $B^{1/2}(x, y)$, using $4\pi R^2 = 2\pi N$, can be reduced to

$$\int d^2r \psi_{p,N} \psi_{q,N} \psi_{r,N}^* \psi_{s,N}^* = \frac{(N+1)^2}{2\pi N(2N+1)} \left[\frac{C_N^p C_N^q C_N^r C_N^s}{C_{2N}^{p+q} C_{2N}^{r+s}} \right]^{1/2} \delta_{p+q, r+s}. \quad (\text{A.31})$$

Then, by defining the coefficient

$$\mathcal{W}_{pqrs} = \frac{(N+1)^2}{2N(2N+1)} \left[\frac{C_N^p C_N^q C_N^r C_N^s}{C_{2N}^{p+q} C_{2N}^{r+s}} \right]^{1/2}, \quad (\text{A.32})$$

the quartic intralayer term of energy can be written as

$$\frac{\mathcal{H}_c^{(2)}(\mathbf{v})}{k_B T} = \sum_{n=1}^M \sum_{p,q,r,s=0}^N \mathcal{W}_{pqrs} v_{n,p} v_{n,q} v_{n,r}^* v_{n,s}^* \delta_{p+q, r+s}. \quad (\text{A.33})$$

An important resummation, for the purpose of numerical calculations and simulations, can be made on this energy term by performing one of the sums on an index appearing in the Kronecker delta function. We choose p , which reduces the sums to

$$\frac{\mathcal{H}_c^{(2)}(\mathbf{v})}{k_B T} = \sum_{n=1}^M \sum_{q,r,s=0}^N \mathcal{W}_{r+s-q, qrs} v_{n, r+s-q} v_{n,q} v_{n,r}^* v_{n,s}^*, \quad (\text{A.34})$$

where a factor $\Theta(r+s-q)\Theta(N-r-s+q)$ is implied.

Now we define a “new” dummy index $p = r + s$ which varies between 0 and $2N$, and at the same time determines $r = p - s$ varying between 0 and N . The energy term just above can be written in terms of these new indices as

$$\frac{\mathcal{H}_c^{(2)}(\mathbf{v})}{k_B T} = \sum_{n=1}^M \sum_{p=0}^{2N} \sum_{q,s=0}^N \mathcal{W}_{p-q, q, p-s, s} v_{n, p-q} v_{n,q} v_{n, p-s}^* v_{n,s}^*, \quad (\text{A.35})$$

with a factor $\Theta(p-q)\Theta(N-p+q)\Theta(p-s)\Theta(N-p+s)$ implied.

By combining Eqs. (A.32), (A.31) and (A.29), the coefficient $\mathcal{W}_{p-q, q, p-s, s}$ can be rewritten as

$$\mathcal{W}_{p-q, q, p-s, s} = \frac{1}{2N} \mathcal{N}_{p-q, N} \mathcal{N}_{q, N} \mathcal{N}_{p-s, N} \mathcal{N}_{s, N} (N \gamma_{p, 2N})^2, \quad (\text{A.36})$$

with $\gamma_{p, 2N} = 2\pi / [(2N+1)C_{2N}^p]^{1/2}$ as defined at the end of Section 3.1. Then, with the quadratic form on the coefficients defined as

$$U_{n,p}(\mathbf{v}) = N \gamma_{p, 2N} \sum_{q=0}^N \mathcal{N}_{p-q, N} \mathcal{N}_{q, N} \Theta(p-q) \Theta(N-p+q) v_{n, p-q} v_{n,q}, \quad (\text{A.37})$$

the resummed energy term reads

$$\frac{\mathcal{H}_c^{(2)}(\mathbf{v})}{k_B T} = \frac{1}{2N} \sum_{n=1}^M \sum_{p=0}^{2N} |U_{n,p}(\mathbf{v})|^2. \quad (\text{A.38})$$

Third Integral: Quadratic Interlayer Contribution

The integration of the third term in Eq. (2.50), which couples the order parameter in adjacent layers, follows in a similar fashion to the first case. We first substitute the scaled order parameter, Eq. (4.1), to get

$$\frac{\mathcal{H}_c^{(3)}(\mathbf{v})}{k_B T} = \eta |\alpha_T| \sum_{n=1}^M \sum_{p,q=0}^N (v_{n+1,p}^* - v_{n,p}^*) (v_{n+1,q} - v_{n,q}) \int d^2 r \psi_{p,N}^* \psi_{q,N}. \quad (\text{A.39})$$

where we have defined $\eta = 1/\tilde{s}^2$. The integration is straightforward from Eq. (A.25), and after performing the sum over p we obtain

$$\frac{\mathcal{H}_c^{(3)}(\mathbf{v})}{k_B T} = \eta |\alpha_T| \sum_{n=1}^M \sum_{q=0}^N |v_{n+1,q} - v_{n,q}|^2. \quad (\text{A.40})$$

A.3.1.2 Random Disorder Energy Term

Next we derive the expression for the energy of the random disorder extra term (again in the context of the layered superconductor). We consider Eq. (4.6) with $\Omega(\mathbf{r})$ given by Eq. (3.26) and the order parameter constrained to the LLL, Eq. (2.47). With all this the energy term becomes

$$\frac{\mathcal{H}_{\text{rs}}(\mathbf{v}; \mathbf{a})}{k_B T} = \sum_{n=1}^M \sum_{l=0}^{\infty} \sum_{m=-l}^l \sum_{p,q=0}^N a_l^m J_{p,q,l}^m v_{n,p}^* v_{n,q}, \quad (\text{A.41})$$

where the coefficient $J_{p,q,l}^m$ is defined by the integral

$$J_{p,q,l}^m = \int d^2 r \psi_{p,N}^*(\theta, \phi) \psi_{q,N}(\theta, \phi) Y_l^m(\theta, \phi). \quad (\text{A.42})$$

We take the spherical harmonics, normalized on the sphere of radius R and defined without the usual phase factor $(-1)^m$, as⁴

$$Y_l^m(\theta, \phi) = \left[\frac{(2l+1)(l-m)!}{4\pi R^2(l+m)!} \right]^{1/2} P_l^m(\cos \theta) e^{im\phi}, \quad (\text{A.43})$$

⁴This choice of phases of the spherical harmonics and the associated Legendre functions, Eqs. (A.43) and (A.44), makes the spherical harmonics to satisfy

$$Y_l^{-m}(\theta, \phi) = (-1)^m Y_l^{m*}(\theta, \phi),$$

which translates into, for instance, $J_{p,q,l}^{-m} = (-1)^m J_{q,p,l}^m$ (because $J_{q,p,l}^m$ is real).

with the associated Legendre functions for negative m values satisfying

$$P_l^{-m}(x) = (-1)^m \frac{(l-m)!}{(l+m)!} P_l^m(x), \quad (\text{A.44})$$

and the LLL subspace composed by the $N+1$ functions in Eq. (3.2) [which are also normalized on the sphere of radius R , Eq. (A.25)].

The sum over m in Eq. (A.41) can be reduced to only non-negative values by considering the properties of $J_{p,q,l}^{-m}$ and a_l^{-m} [$J_{p,q,l}^{-m} = (-1)^m J_{p,q,l}^m$ and $a_l^{-m} = (-1)^m a_l^{m*}$].

This gives

$$\frac{\mathcal{H}_{\text{rs}}(\mathbf{v}; \mathbf{a})}{k_B T} = \sum_{n=1}^M \sum_{p,q=0}^N \left[\sum_{l=0}^{\infty} a_l^0 J_{p,q,l}^0 v_{n,p}^* v_{n,q} + \sum_{l=1}^{\infty} \sum_{m=1}^l (a_l^m J_{p,q,l}^m + a_l^{m*} J_{p,q,l}^m) v_{n,p}^* v_{n,q} \right]. \quad (\text{A.45})$$

Next, by using the result of Eq. (A.118), the sum over the first lower-index of $J_{r,s,t}^u$ above can be performed to give

$$\begin{aligned} \frac{\mathcal{H}_{\text{rs}}(\mathbf{v}; \mathbf{a})}{k_B T} = & \sum_{n=1}^M \sum_{q=0}^N \sum_{l=0}^{\infty} a_l^0 I_{q,l}^0 v_{n,q}^* v_{n,q} + \\ & + \sum_{n=1}^M \left[\sum_{q=0}^N \sum_{l=0}^{\infty} \sum_{m=0}^l a_l^m I_{q,l}^m v_{n,q+m}^* v_{n,q} + \sum_{p=0}^N \sum_{l=1}^{\infty} \sum_{m=1}^l a_l^{m*} I_{p,l}^m v_{n,p}^* v_{n,p+m} \right]. \quad (\text{A.46}) \end{aligned}$$

Then the dummy index p in the second term can be set to q and the sums can be compressed as

$$\frac{\mathcal{H}_{\text{rs}}(\mathbf{v}; \mathbf{a})}{k_B T} = \sum_{n=1}^M \sum_{q=0}^N \left[\sum_{l=0}^{\infty} a_l^0 I_{q,l}^0 |v_{n,q}|^2 + 2\text{Re} \sum_{l=1}^{\infty} \sum_{m=1}^l a_l^m I_{q,l}^m v_{n,q+m}^* v_{n,q} \right]. \quad (\text{A.47})$$

Finally, as the expression for the energy is intended to be used in numerical simulations, we are forced to set a bound for the index l . A general choice is $l \leq l_{\text{max}}$ so that⁵

$$\frac{\mathcal{H}_{\text{rs}}(\mathbf{v}; \mathbf{a})}{k_B T} \simeq \sum_{n=1}^M \sum_{q=0}^N \left[\sum_{l=0}^{l_{\text{max}}} a_l^0 I_{q,l}^0 |v_{n,q}|^2 + 2\text{Re} \sum_{l=1}^{l_{\text{max}}} \sum_{m=1}^l a_l^m I_{q,l}^m v_{n,q+m}^* v_{n,q} \right]. \quad (\text{A.48})$$

We set $l_{\text{max}} = 7R$ (where $R = (N/2)^{1/2}$ is the radius of the sphere). This accounts for all relevant values. Notice that a factor $\Theta(q+m)\Theta(N-q-m)$ is implied in the second term.

⁵Kienappel and Moore [85] set $l_{\text{max}} = N$ and propose a further reduction by defining new coefficients $g_{q,m}$ which result basically from the sum $\sum_{l=0}^{l_{\text{max}}} a_l^m I_{q,l}^m$. We find the resummation unwieldy and prefer not to use it here.

A.3.1.3 Periodic Substrate Energy Term

Now we derive the expression for the energy contribution of a periodic substrate in the case of a layered superconductor. We consider Eq. (4.8) with the LLL order parameter in each layer ψ_n describing N vortices, Eq. (2.47), and the periodic substrate defined by the order parameter which minimizes the energy of the clean system with N' vortices, $\psi_n^{(0)}$ in Eq. (4.9). Substitution of the order parameter functions into the energy form gives

$$\frac{\mathcal{H}_{\text{ps}}(\mathbf{v}; \mathbf{v}^{(0)})}{k_B T} = -2\pi g \sum_{n=1}^M \sum_{p,r=0}^{N'} \sum_{q,s=0}^N v_{n,p}^{(0)} v_{n,q} v_{n,r}^{(0)*} v_{n,s}^* \int d^2 r \psi_{p,N'} \psi_{q,N} \psi_{r,N'}^* \psi_{s,N}^*, \quad (\text{A.49})$$

where the relationships $Q = (\Phi_0 k_B T / \beta d_0 \bar{B})^{1/4}$ and $\Phi_0 / \bar{B} = 2\pi$ (valid in our case of $l_m = 1$) have been used to simplify the prefactor. This shows a quadratic form on the complex variables $\{v_{n,k}\}$ (since the coefficients $\{v_{n,k}^{(0)}\}$ are fixed) with a slightly generalized integral involving four LLL eigenstates. Therefore the procedure to follow is completely analogous to that on the second integral, in Section A.3.1.1. The integral in terms of the LLL eigenfunctions is in this case

$$\begin{aligned} \int d^2 r \psi_{p,N'} \psi_{q,N} \psi_{r,N'}^* \psi_{s,N}^* &= \mathcal{N}_{p,N'} \mathcal{N}_{q,N} \mathcal{N}_{r,N'} \mathcal{N}_{s,N} \\ &\times R^2 \int_0^{2\pi} d\phi e^{i(p+q-r-s)\phi} \int_0^\pi d\theta \sin \theta \sin^{p+q+r+s}(\theta/2) \cos^{2(N'+N)-(p+q+r+s)}(\theta/2), \end{aligned} \quad (\text{A.50})$$

which after integrating over ϕ and θ becomes

$$\begin{aligned} \int d^2 r \psi_{p,N'} \psi_{q,N} \psi_{r,N'}^* \psi_{s,N}^* &= \mathcal{N}_{p,N'} \mathcal{N}_{q,N} \mathcal{N}_{r,N'} \mathcal{N}_{s,N} \\ &\times 4\pi R^2 \delta_{p+q,r+s} B \left(\frac{p+q+r+s}{2} + 1, \frac{2(N+N')-(p+q+r+s)}{2} + 1 \right). \end{aligned} \quad (\text{A.51})$$

The constriction imposed by the Kronecker delta function makes it possible for the integral to be written in the symmetric form

$$\begin{aligned} \int d^2 r \psi_{p,N'} \psi_{q,N} \psi_{r,N'}^* \psi_{s,N}^* &= \mathcal{N}_{p,N'} \mathcal{N}_{q,N} \mathcal{N}_{r,N'} \mathcal{N}_{s,N} 4\pi R^2 \delta_{p+q,r+s} \\ &\times B^{1/2}(p+q+1, N+N'-p-q+1) B^{1/2}(r+s+1, N+N'-r-s+1), \end{aligned} \quad (\text{A.52})$$

which after simplifications on the factors $\mathcal{N}_{k,J}$ and $B^{1/2}(x, y)$, using $4\pi R^2 = 2\pi N$, can be reduced to

$$\int d^2 r \psi_{p,N'} \psi_{q,N} \psi_{r,N'}^* \psi_{s,N}^* = \frac{(N'+1)(N+1)}{2\pi N(N+N'+1)} \left[\frac{C_{N'}^p C_N^q C_{N'}^r C_N^s}{C_{N+N'}^{p+q} C_{N+N'}^{r+s}} \right]^{1/2} \delta_{p+q,r+s}. \quad (\text{A.53})$$

In a similar fashion we define the coupling coefficient

$$\mathcal{W}'_{pqrs} = \frac{(N' + 1)(N + 1)}{2N(N + N' + 1)} \left[\frac{C_{N'}^p C_N^q C_{N'}^r C_N^s}{C_{N+N'}^{p+q} C_{N+N'}^{r+s}} \right]^{1/2}, \quad (\text{A.54})$$

with which the energy term becomes

$$\frac{\mathcal{H}_{\text{ps}}(\mathbf{v}; \mathbf{v}^{(0)})}{k_B T} = -2g \sum_{n=1}^M \sum_{p,r=0}^{N'} \sum_{q,s=0}^N \mathcal{W}'_{pqrs} v_{n,p}^{(0)} v_{n,q} v_{n,r}^{(0)*} v_{n,s}^* \delta_{p+q,r+s}. \quad (\text{A.55})$$

A similar resummation can be made on this energy term with the assistance of the Kronecker delta function. We choose p , which reduces the sums to

$$\frac{\mathcal{H}_{\text{ps}}(\mathbf{v}; \mathbf{v}^{(0)})}{k_B T} = -2g \sum_{n=1}^M \sum_{r=0}^{N'} \sum_{q,s=0}^N \mathcal{W}'_{r+s-q,qr s} v_{n,r+s-q}^{(0)} v_{n,q} v_{n,r}^{(0)*} v_{n,s}^*, \quad (\text{A.56})$$

where a factor $\Theta(r + s - q)\Theta(N' - r - s + q)$ is implied.

We define a “new” dummy index $p = r + s$ which varies between 0 and $N' + N$, and at the same time determines $r = p - s$ varying between 0 and N' . The energy term just above can be written in terms of these new indices as

$$\frac{\mathcal{H}_{\text{ps}}(\mathbf{v}; \mathbf{v}^{(0)})}{k_B T} = -2g \sum_{n=1}^M \sum_{p=0}^{N+N'} \sum_{q,s=0}^N \mathcal{W}'_{p-q,q,p-s,s} v_{n,p-q}^{(0)} v_{n,q} v_{n,p-s}^{(0)*} v_{n,s}^*, \quad (\text{A.57})$$

with a factor $\Theta(p - q)\Theta(N' - p + q)\Theta(p - s)\Theta(N' - p + s)$ implied.

By combining Eqs. (A.54), (A.53) and (A.51), the coefficient $\mathcal{W}'_{p-q,q,p-s,s}$ can be rewritten as

$$\mathcal{W}'_{p-q,q,p-s,s} = \frac{1}{2N} \mathcal{N}_{p-q,N'} \mathcal{N}_{q,N} \mathcal{N}_{p-s,N'} \mathcal{N}_{s,N} (N \gamma_{p,N'+N})^2, \quad (\text{A.58})$$

with $\gamma_{p,N'+N} = 2\pi / [(N' + N + 1) C_{N'+N}^p]^{1/2}$ as defined before. Then, defining the linear function on the coefficients $\{v_{n,q}\}$ as

$$U'_{n,p}(\mathbf{v}; \mathbf{v}^{(0)}) = N \gamma_{p,N'+N} \sum_{q=0}^N \mathcal{N}_{p-q,N'} \mathcal{N}_{q,N} \Theta(p - q) \Theta(N' - p + q) v_{n,p-q}^{(0)} v_{n,q}, \quad (\text{A.59})$$

the resummed energy term becomes

$$\frac{\mathcal{H}_{\text{ps}}(\mathbf{v}; \mathbf{v}^{(0)})}{k_B T} = -2g \frac{1}{2N} \sum_{n=1}^M \sum_{p=0}^{N'+N} |U'_{n,p}(\mathbf{v}; \mathbf{v}^{(0)})|^2. \quad (\text{A.60})$$

A.3.2 Energy Differences

This part is concerned with the calculation of the energy differences (after the update of an order-parameter expansion coefficient) which are required to perform Monte Carlo (MC) simulations. Again, we concentrate on the layered case only.

A.3.2.1 Energy Difference on the Clean Energy Term

We start with the energy of the clean layered system in terms of the order parameter coefficients, $\mathcal{H}_c(\mathbf{v})$ in Eq. (4.2), which after updating the arbitrary coefficient $v_{i,j} \rightarrow v_{i,j} + \varepsilon$ becomes $\mathcal{H}_c(\mathbf{v}; \varepsilon)$. We will call $\delta\mathcal{H}_c = \mathcal{H}_c(\mathbf{v}; \varepsilon) - \mathcal{H}_c(\mathbf{v})$, the energy difference. Now we calculate the contributions term by term.

Difference in the Quadratic Intralayer Term

From Eq. (A.26) we determine, by inspection, that the only terms which change after the update of the coefficient $v_{i,j}$ are given by

$$\frac{\delta\mathcal{H}_c^{(1)}}{k_B T} = \alpha_T \sum_{n=1}^M \sum_{q=0}^N \left[|v_{n,q} + \varepsilon|^2 - |v_{n,q}|^2 \right] \delta_{n,i} \delta_{q,j}. \quad (\text{A.61})$$

Expanding the first term and performing the sums over n and q , the energy difference becomes

$$\frac{\delta\mathcal{H}_c^{(1)}}{k_B T} = \alpha_T \left[2\text{Re}(v_{i,j}^* \varepsilon) + |\varepsilon|^2 \right]. \quad (\text{A.62})$$

Difference in the Quartic Intralayer Term

The energy change in Eq. (A.38), after the update of the same arbitrary coefficient $v_{i,j}$, is completely determined by calculating the change in the quadratic form, $\delta U_{i,p} = U_{i,p}(\mathbf{v}; \varepsilon) - U_{i,p}(\mathbf{v})$, from Eq. (A.37). In order to simplify expressions we define the symmetric factor

$$w_{r,s} = N \gamma_{r+s, 2N} \mathcal{N}_{r,N} \mathcal{N}_{s,N} \Theta(r) \Theta(N-r) \Theta(s) \Theta(N-s), \quad (\text{A.63})$$

which allows us to write the change in the quadratic form, after the update, as

$$\delta U_{i,p} = \sum_{q=0}^N w_{p-q,q} \left[\{ (v_{i,p-q} + \varepsilon) v_{i,q} - v_{i,p-q} v_{i,q} \} \delta_{p-q,j} (1 - \delta_{q,j}) \right]$$

$$\begin{aligned}
& + \{ (v_{i,p-q} + \varepsilon)(v_{i,q} + \varepsilon) - v_{i,p-q}v_{i,q} \} \delta_{q,j} \delta_{p-q,j} \\
& + \{ v_{i,p-q}(v_{i,q} + \varepsilon) - v_{i,p-q}v_{i,q} \} \delta_{q,j} (1 - \delta_{p-q,j}) \}.
\end{aligned} \tag{A.64}$$

Carrying out some simplifications, the expression becomes

$$\delta U_{i,p} = \sum_{q=0}^N w_{p-q,q} \left[\varepsilon v_{i,p-q} \delta_{q,j} + v_{i,q} \varepsilon \delta_{p-q,j} + \varepsilon^2 \delta_{q,j} \delta_{p-q,j} \right], \tag{A.65}$$

which after summing over q gives

$$\delta U_{i,p} = 2w_{j,p-j}v_{i,p-j}\varepsilon + w_{j,j}\varepsilon^2\delta_{p,2j}. \tag{A.66}$$

Difference in the Quadratic Interlayer Term

In a similar fashion to the quadratic intralayer case we determine by inspection the energy terms which change after the update of the coefficient $v_{i,j}$. From Eq. (A.40), we have in this case

$$\begin{aligned}
\frac{\delta \mathcal{H}_c^{(3)}}{k_B T} &= \eta |\alpha_T| \sum_{n=1}^M \sum_{q=0}^N \left[\left\{ |(v_{n+1,q} + \varepsilon) - v_{n,q}|^2 - |v_{n+1,q} - v_{n,q}|^2 \right\} \delta_{n+1,i} \delta_{q,j} \right. \\
&\quad \left. + \left\{ |v_{n+1,q} - (v_{n,q} + \varepsilon)|^2 - |v_{n+1,q} - v_{n,q}|^2 \right\} \delta_{n,i} \delta_{q,j} \right].
\end{aligned} \tag{A.67}$$

which after the usual simplifications is reduced to

$$\frac{\delta \mathcal{H}_c^{(3)}}{k_B T} = \eta |\alpha_T| \sum_{n=1}^M \sum_{q=0}^N \left[2\text{Re} \left\{ (v_{n+1,q}^* - v_{n,q}^*) \varepsilon \right\} \delta_{q,j} (\delta_{n+1,j} - \delta_{n,j}) + |\varepsilon|^2 \delta_{q,j} (\delta_{n+1,j} + \delta_{n,j}) \right]. \tag{A.68}$$

Carrying out the sums over n and q , the energy difference simply becomes

$$\frac{\delta \mathcal{H}_c^{(3)}}{k_B T} = 2\eta |\alpha_T| \left[\text{Re} \left\{ (2v_{i,j}^* - v_{i+1,j}^* - v_{i-1,j}^*) \varepsilon \right\} + |\varepsilon|^2 \right], \tag{A.69}$$

with the usual periodic boundary conditions: $M+1 \rightarrow 1$ and $0 \rightarrow M$.

A.3.2.2 Energy Difference on the Random Disorder Term

Now we calculate the energy difference on the random disorder term after updating the arbitrary coefficient $v_{i,j} \rightarrow v_{i,j} + \varepsilon$. The expression for the energy difference is taken directly from Eq. (A.48). We consider first the term with $m = 0$, for which

$$\frac{\delta \mathcal{H}_{rd}^{(m=0)}}{k_B T} = \sum_{n=1}^M \sum_{q=0}^N \sum_{l=0}^{l_{\max}} a_l^0 I_{q,l}^0 \left[|v_{n,q} + \varepsilon|^2 - |v_{n,q}|^2 \right] \delta_{n,i} \delta_{q,j}. \tag{A.70}$$

Expanding the first term and performing the sums over n and q this energy difference becomes

$$\frac{\delta\mathcal{H}_{rd}^{(m=0)}}{k_B T} = \sum_{l=0}^{l_{\max}} a_l^0 I_{j,l}^0 \left[2\text{Re}(v_{i,j}^* \varepsilon) + |\varepsilon|^2 \right]. \quad (\text{A.71})$$

Now, since the random disorder energy term is purely intralayer, we just look at the projection of the sum on $n = i$. In this case the energy difference on the term with $m > 0$ reads

$$\begin{aligned} \frac{\delta\mathcal{H}_{rd}^{(m>0)}}{k_B T} = 2\text{Re} \sum_{q=0}^N \sum_{l=1}^{l_{\max}} \sum_{m=1}^l a_l^m I_{q,l}^m & \left[\left\{ (v_{i,q+m} + \varepsilon)^* v_{i,q} - v_{i,q+m}^* v_{i,q} \right\} \delta_{q+m,j} (1 - \delta_{q,j}) \right. \\ & + \left\{ (v_{i,q+m} + \varepsilon)^* (v_{i,q} + \varepsilon) - v_{i,q+m}^* v_{i,q} \right\} \delta_{q,j} \delta_{q+m,j} \\ & \left. + \left\{ v_{i,q+m}^* (v_{i,q} + \varepsilon) - v_{i,q+m}^* v_{i,q} \right\} \delta_{q,j} (1 - \delta_{q+m,j}) \right], \end{aligned} \quad (\text{A.72})$$

which after some simplifications becomes

$$\frac{\delta\mathcal{H}_{rd}^{(m>0)}}{k_B T} = 2\text{Re} \sum_{q=0}^N \sum_{l=1}^{l_{\max}} \sum_{m=1}^l a_l^m I_{q,l}^m \left[\varepsilon^* v_{i,q} \delta_{q+m,j} + v_{i,q+m}^* \varepsilon \delta_{q,j} + |\varepsilon|^2 \delta_{q,j} \delta_{q+m,j} \right]. \quad (\text{A.73})$$

Carrying out the sum over q we finally obtain

$$\frac{\delta\mathcal{H}_{rd}^{(m>0)}}{k_B T} = 2\text{Re} \sum_{l=1}^{l_{\max}} \sum_{m=1}^l a_l^m \left[I_{j-m,l}^m \varepsilon^* v_{i,j-m} + I_{j,l}^m v_{i,j+m}^* \varepsilon \right], \quad (\text{A.74})$$

with the appropriate factors $\Theta(j-m)\Theta(N-j+m)$ and $\Theta(j+m)\Theta(N-j-m)$ implied in the first and second terms respectively.

The total energy difference in the random disorder term is given by the contributions $m = 0$ and $m > 0$ in Eqs. (A.71) and (A.74).

A.3.2.3 Energy Difference on the Periodic Substrate Term

To conclude the calculations on energy differences we carry out the one on the periodic substrate term after updating the arbitrary coefficient $v_{i,j} \rightarrow v_{i,j} + \varepsilon$. As in the quartic term we notice that the energy difference is determined by the difference in the function $U'_{i,p}(\mathbf{v}; \mathbf{v}^{(0)})$, from Eq. (A.59). In a similar fashion we define the non-symmetric quantity

$$w'_{r,s} = N \gamma_{r+s, N'+N} \mathcal{N}_{r, N'} \mathcal{N}_{s, N} \Theta(r) \Theta(N' - r) \Theta(s) \Theta(N - s), \quad (\text{A.75})$$

which allows us to write the difference in the function $U'_{i,p}(\mathbf{v}; \mathbf{v}^{(0)})$ as

$$\delta U'_{i,p} = \sum_{q=0}^N w'_{p-q,q} v_{i,p-q}^{(0)} [(v_{i,q} + \varepsilon) - v_{i,q}] \delta_{q,j}. \quad (\text{A.76})$$

Thus, after performing the sum over q , the expression is reduced to

$$\delta U'_{i,p} = w'_{p-j,j} v_{i,p-j}^{(0)} \varepsilon. \quad (\text{A.77})$$

A.3.3 First Order Derivatives

The calculation of the first order derivatives of the energy terms, with respect to the real and imaginary parts of an arbitrary expansion coefficient, $v_{i,j} = x_{i,j} + iy_{i,j}$, is outlined here. These quantities are used in the minimization routines to find the ground states. Once again we work with the layered superconductor expressions.

A.3.3.1 Derivatives of the Clean Energy Term

To carry out this calculation we regard the energy terms as functions of the real variables $\{x_{n,q}, y_{n,q}\}$. We start with each of the terms of the energy of the clean layered system.

Derivatives of the Quadratic Intralayer Term

The first term, in Eq. (A.26), can be written in terms of the real independent variables (\mathbf{x}, \mathbf{y}) as

$$\frac{\mathcal{H}_c^{(1)}(\mathbf{x}, \mathbf{y})}{k_B T} = \alpha_T \sum_{n=1}^M \sum_{q=0}^N [x_{n,q}^2 + y_{n,q}^2]. \quad (\text{A.78})$$

Its derivative with respect to $x_{i,j}$ is

$$\frac{\partial}{\partial x_{i,j}} \left[\frac{\mathcal{H}_c^{(1)}(\mathbf{x}, \mathbf{y})}{k_B T} \right] = \alpha_T \sum_{n=1}^M \sum_{q=0}^N 2x_{n,q} \delta_{n,i} \delta_{q,j}, \quad (\text{A.79})$$

which after carrying out the sums over n and q gives

$$\frac{\partial}{\partial x_{i,j}} \left[\frac{\mathcal{H}_c^{(1)}(\mathbf{x}, \mathbf{y})}{k_B T} \right] = 2\alpha_T x_{i,j}. \quad (\text{A.80})$$

Analogously the derivative with respect to $y_{i,j}$ is

$$\frac{\partial}{\partial y_{i,j}} \left[\frac{\mathcal{H}_c^{(1)}(\mathbf{x}, \mathbf{y})}{k_B T} \right] = 2\alpha_T y_{i,j}. \quad (\text{A.81})$$

Derivatives of the Quartic Intralayer Term

To calculate these derivatives we realise, from Eq. (A.38), that the derivative with respect to $x_{i,j}$ can be written as

$$\frac{\partial}{\partial x_{i,j}} \left[\frac{\mathcal{H}_c^{(2)}(\mathbf{x}, \mathbf{y})}{k_B T} \right] = \frac{1}{2N} 2\text{Re} \sum_{n=1}^M \sum_{p=0}^{2N} U_{n,p}^*(\mathbf{x}, \mathbf{y}) \frac{\partial U_{n,p}(\mathbf{x}, \mathbf{y})}{\partial x_{i,j}}, \quad (\text{A.82})$$

with its analogous counterpart for the derivative with respect to $y_{i,j}$. This means that only derivatives of the function $U_{n,p}(\mathbf{x}, \mathbf{y})$ are needed. We write the function $U_{n,p}$ in terms of the variables \mathbf{x} and \mathbf{y} first

$$U_{n,p}(\mathbf{x}, \mathbf{y}) = \sum_{q=0}^N w_{p-q,q} [(x_{n,p-q} x_{n,q} - y_{n,p-q} y_{n,q}) + i(x_{n,p-q} y_{n,q} + y_{n,p-q} x_{n,q})], \quad (\text{A.83})$$

and, using chain's rule, calculate its derivative with respect to $x_{i,j}$

$$\frac{\partial U_{n,p}(\mathbf{x}, \mathbf{y})}{\partial x_{i,j}} = \delta_{n,i} \sum_{q=0}^N w_{p-q,q} [(\delta_{p-q,j} x_{n,q} + x_{n,p-q} \delta_{q,j}) + i(\delta_{p-q,j} y_{n,q} + y_{n,p-q} \delta_{q,j})]. \quad (\text{A.84})$$

Performing the sum over q and simplifying common terms, we obtain

$$\frac{\partial U_{n,p}(\mathbf{x}, \mathbf{y})}{\partial x_{i,j}} = 2\delta_{n,i} w_{j,p-j} (x_{n,p-j} + i y_{n,p-j}). \quad (\text{A.85})$$

Introducing this result and the complex conjugate of $U_{n,p}$, from Eq. (A.83), into Eq. (A.82) and carrying out further simplifications the expression reads

$$\begin{aligned} \frac{\partial}{\partial x_{i,j}} \left[\frac{\mathcal{H}_c^{(2)}(\mathbf{x}, \mathbf{y})}{k_B T} \right] &= \frac{1}{2N} 4 \sum_{p=0}^{2N} \sum_{q=0}^N w_{p-q,q} w_{j,p-j} [x_{i,q} (x_{i,p-q} x_{i,p-j} + y_{i,p-q} y_{i,p-j}) \\ &\quad + y_{i,q} (x_{i,p-q} y_{i,p-j} - y_{i,p-q} x_{i,p-j})]. \end{aligned} \quad (\text{A.86})$$

Analogously the calculation with $y_{i,j}$ gives

$$\frac{\partial U_{n,p}(\mathbf{x}, \mathbf{y})}{\partial y_{i,j}} = 2\delta_{n,i} w_{j,p-j} (-y_{n,p-j} + i x_{n,p-j}), \quad (\text{A.87})$$

which when used with the complex conjugate of $U_{n,p}$, from Eq. (A.83), into the analogous form for $y_{i,j}$ in Eq. (A.82), becomes

$$\begin{aligned} \frac{\partial}{\partial y_{i,j}} \left[\frac{\mathcal{H}_c^{(2)}(\mathbf{x}, \mathbf{y})}{k_B T} \right] &= \frac{1}{2N} 4 \sum_{p=0}^{2N} \sum_{q=0}^N w_{p-q,q} w_{j,p-j} [y_{i,q} (x_{i,p-q} x_{i,p-j} + y_{i,p-q} y_{i,p-j}) \\ &\quad - x_{i,q} (x_{i,p-q} y_{i,p-j} - y_{i,p-q} x_{i,p-j})]. \end{aligned} \quad (\text{A.88})$$

It is worth noticing that a factor $\Theta(p-q)\Theta(N-p+q)\Theta(p-j)\Theta(N-p+j)$ is present both in Eqs. (A.86) and (A.88) through the definition of $w_{r,s}$.

Derivatives of the Quadratic Interlayer Term

We first write the quadratic interlayer energy in Eq. (A.40) in terms of the real independent variables (\mathbf{x}, \mathbf{y}) as

$$\frac{\mathcal{H}_c^{(3)}(\mathbf{x}, \mathbf{y})}{k_B T} = \eta |\alpha_T| \sum_{n=1}^M \sum_{q=0}^N \left[(x_{n+1,q} - x_{n,q})^2 + (y_{n+1,q} - y_{n,q})^2 \right]. \quad (\text{A.89})$$

Taking the partial derivative with respect to $x_{i,j}$ of this expression we find

$$\frac{\partial}{\partial x_{i,j}} \left[\frac{\mathcal{H}_c^{(3)}(\mathbf{x}, \mathbf{y})}{k_B T} \right] = \eta |\alpha_T| \sum_{n=1}^M \sum_{q=0}^N 2(x_{n+1,q} - x_{n,q}) \delta_{q,j} (\delta_{n+1,i} - \delta_{n,i}), \quad (\text{A.90})$$

from which, after summing over q and n , we finally obtain

$$\frac{\partial}{\partial x_{i,j}} \left[\frac{\mathcal{H}_c^{(3)}(\mathbf{x}, \mathbf{y})}{k_B T} \right] = 2\eta |\alpha_T| [2x_{i,j} - x_{i+1,j} - x_{i-1,j}]. \quad (\text{A.91})$$

Analogously the derivative with respect to $y_{i,j}$ is

$$\frac{\partial}{\partial y_{i,j}} \left[\frac{\mathcal{H}_c^{(3)}(\mathbf{x}, \mathbf{y})}{k_B T} \right] = 2\eta |\alpha_T| [2y_{i,j} - y_{i+1,j} - y_{i-1,j}], \quad (\text{A.92})$$

where the boundary conditions $M+1 \rightarrow 1$ and $0 \rightarrow M$ apply.

A.3.3.2 Derivatives of the Random Disorder Term

Now we go on to the calculation of the derivatives with respect to $x_{i,j}$ and $y_{i,j}$ of the random disorder energy contribution. We start by rewriting this energy term, Eq. (A.48), as a function of the real independent-variables (\mathbf{x}, \mathbf{y}) . The $m=0$ term is

$$\frac{\mathcal{H}_{rs}^{(m=0)}(\mathbf{x}, \mathbf{y})}{k_B T} = \sum_{n=1}^M \sum_{q=0}^N \sum_{l=0}^{l_{\max}} a_l^0 I_{q,l}^0 [x_{n,q}^2 + y_{n,q}^2], \quad (\text{A.93})$$

and following a similar calculation to that on the quadratic intralayer term, its derivative with respect to $x_{i,j}$ is immediately found to be

$$\frac{\partial}{\partial x_{i,j}} \left[\frac{\mathcal{H}_{rs}^{(m=0)}(\mathbf{x}, \mathbf{y})}{k_B T} \right] = 2 \sum_{l=0}^{l_{\max}} a_l^0 I_{j,l}^0 x_{i,j}. \quad (\text{A.94})$$

The analogous counterpart for the derivative respect to $y_{i,j}$,

$$\frac{\partial}{\partial y_{i,j}} \left[\frac{\mathcal{H}_{rs}^{(m=0)}(\mathbf{x}, \mathbf{y})}{k_B T} \right] = 2 \sum_{l=0}^{l_{\max}} a_l^0 I_{j,l}^0 y_{i,j}, \quad (\text{A.95})$$

also holds. Then the $m > 0$ energy contribution, written in terms of (\mathbf{x}, \mathbf{y}) , is

$$\frac{\mathcal{H}_{\text{rs}}^{(m>0)}(\mathbf{x}, \mathbf{y})}{k_B T} = 2\text{Re} \sum_{n=1}^M \sum_{q=0}^N \sum_{l=1}^{l_{\max}} \sum_{m=1}^l a_l^m I_{q,l}^m [(x_{n,q+m} x_{n,q} + y_{n,q+m} y_{n,q}) + i(x_{n,q+m} y_{n,q} - y_{n,q+m} x_{n,q})], \quad (\text{A.96})$$

and its derivative with respect to $x_{i,j}$

$$\frac{\partial}{\partial x_{i,j}} \left[\frac{\mathcal{H}_{\text{rs}}^{(m>0)}(\mathbf{x}, \mathbf{y})}{k_B T} \right] = 2\text{Re} \sum_{n=1}^M \sum_{q=0}^N \sum_{l=1}^{l_{\max}} \sum_{m=1}^l a_l^m I_{q,l}^m \delta_{n,i} [(\delta_{q+m,j} x_{n,q} + x_{n,q+m} \delta_{q,j}) + i(\delta_{q+m,j} y_{n,q} - y_{n,q+m} \delta_{q,j})]. \quad (\text{A.97})$$

After performing the sums over n and q , and carrying out some simplifications, it becomes

$$\frac{\partial}{\partial x_{i,j}} \left[\frac{\mathcal{H}_{\text{rs}}^{(m>0)}(\mathbf{x}, \mathbf{y})}{k_B T} \right] = 2 \sum_{l=1}^{l_{\max}} \sum_{m=1}^l [b_l^m (I_{j-m,l}^m x_{i,j-m} + I_{j,l}^m x_{i,j+m}) - c_l^m (I_{j-m,l}^m y_{i,j-m} - I_{j,l}^m y_{i,j+m})], \quad (\text{A.98})$$

where we have written explicitly $a_l^m = b_l^m + i c_l^m$.

The derivative with respect to $y_{i,j}$ follows in exactly the same way. It gives

$$\frac{\partial}{\partial y_{i,j}} \left[\frac{\mathcal{H}_{\text{rs}}^{(m>0)}(\mathbf{x}, \mathbf{y})}{k_B T} \right] = 2\text{Re} \sum_{n=1}^M \sum_{q=0}^N \sum_{l=1}^{l_{\max}} \sum_{m=1}^l a_l^m I_{q,l}^m \delta_{n,i} [(\delta_{q+m,j} y_{n,q} + y_{n,q+m} \delta_{q,j}) + i(x_{n,q+m} \delta_{q,j} - \delta_{q+m,j} x_{n,q})], \quad (\text{A.99})$$

which after performing the sums over n and q , and carrying out simplifications, becomes

$$\frac{\partial}{\partial y_{i,j}} \left[\frac{\mathcal{H}_{\text{rs}}^{(m>0)}(\mathbf{x}, \mathbf{y})}{k_B T} \right] = 2 \sum_{l=1}^{l_{\max}} \sum_{m=1}^l [b_l^m (I_{j-m,l}^m y_{i,j-m} + I_{j,l}^m y_{i,j+m}) - c_l^m (I_{j,l}^m x_{i,j+m} - I_{j-m,l}^m x_{i,j-m})]. \quad (\text{A.100})$$

A.3.3.3 Derivatives of the Periodic Substrate Term

To conclude this section we carry out the calculation of the derivatives, respect to $x_{i,j}$ and $y_{i,j}$, of the periodic substrate term. We start by noticing that the coefficients $\mathbf{v}^{(0)}$ are fixed and therefore the functions $U'_{n,p}(\mathbf{v}, \mathbf{v}^{(0)})$ are linear in the complex variables

v. Again, as in the quartic energy term calculation, we realise that the derivative respect to $x_{i,j}$ is

$$\frac{\partial}{\partial x_{i,j}} \left[\frac{\mathcal{H}_{ps}(\mathbf{x}, \mathbf{y})}{k_B T} \right] = -2g \frac{1}{2N} 2\text{Re} \sum_{n=1}^M \sum_{p=0}^{N'+N} U'_{n,p}(\mathbf{x}, \mathbf{y}) \frac{\partial U'_{n,p}(\mathbf{x}, \mathbf{y})}{\partial x_{i,j}}, \quad (\text{A.101})$$

with its analogous counterpart for the $y_{i,j}$ variable. In a similar fashion we write the function $U'_{n,p}$ in terms of the variables \mathbf{x} and \mathbf{y} , which in this case is

$$U'_{n,p}(\mathbf{x}, \mathbf{y}) = \sum_{q=0}^N w'_{p-q,q} \left[(x_{n,p-q}^{(0)} x_{n,q} - y_{n,p-q}^{(0)} y_{n,q}) + i(x_{n,p-q}^{(0)} y_{n,q} + y_{n,p-q}^{(0)} x_{n,q}) \right]. \quad (\text{A.102})$$

The partial derivative of this, respect to $x_{i,j}$, is calculated directly to give

$$\frac{\partial U'_{n,p}(\mathbf{x}, \mathbf{y})}{\partial x_{i,j}} = \delta_{n,i} \sum_{q=0}^N w'_{p-q,q} \left[x_{n,p-q}^{(0)} + i y_{n,p-q}^{(0)} \right] \delta_{q,j}, \quad (\text{A.103})$$

which, after performing the sum over q , becomes

$$\frac{\partial U'_{n,p}(\mathbf{x}, \mathbf{y})}{\partial x_{i,j}} = \delta_{n,i} w'_{p-j,j} \left[x_{n,p-j}^{(0)} + i y_{n,p-j}^{(0)} \right]. \quad (\text{A.104})$$

Introducing this result and the complex conjugate of $U'_{n,p}$, from Eq. (A.102), into Eq. (A.101) and carrying out further simplifications the derivative reads

$$\begin{aligned} \frac{\partial}{\partial x_{i,j}} \left[\frac{\mathcal{H}_{ps}(\mathbf{x}, \mathbf{y})}{k_B T} \right] = & -4g \frac{1}{2N} \sum_{p=0}^{N'+N} \sum_{q=0}^N w'_{p-q,q} w'_{p-j,j} \left[x_{i,q} (x_{i,p-q}^{(0)} x_{i,p-j}^{(0)} + y_{i,p-q}^{(0)} y_{i,p-j}^{(0)}) \right. \\ & \left. + y_{i,q} (x_{i,p-q}^{(0)} y_{i,p-j}^{(0)} - y_{i,p-q}^{(0)} x_{i,p-j}^{(0)}) \right]. \end{aligned} \quad (\text{A.105})$$

Analogously the calculation with $y_{i,j}$ gives

$$\frac{\partial U'_{n,p}(\mathbf{x}, \mathbf{y})}{\partial y_{i,j}} = \delta_{n,i} w'_{p-j,j} \left[-y_{n,p-j}^{(0)} + i x_{n,p-j}^{(0)} \right], \quad (\text{A.106})$$

which when used with the complex conjugate of $U'_{n,p}$, from Eq. (A.102), into the analogous form for $y_{i,j}$ in Eq. (A.101), becomes

$$\begin{aligned} \frac{\partial}{\partial y_{i,j}} \left[\frac{\mathcal{H}_{ps}(\mathbf{x}, \mathbf{y})}{k_B T} \right] = & -4g \frac{1}{2N} \sum_{p=0}^{N'+N} \sum_{q=0}^N w'_{p-q,q} w'_{p-j,j} \left[y_{i,q} (x_{i,p-q}^{(0)} x_{i,p-j}^{(0)} + y_{i,p-q}^{(0)} y_{i,p-j}^{(0)}) \right. \\ & \left. - x_{i,q} (x_{i,p-q}^{(0)} y_{i,p-j}^{(0)} - y_{i,p-q}^{(0)} x_{i,p-j}^{(0)}) \right]. \end{aligned} \quad (\text{A.107})$$

Again a factor $\Theta(p-q)\Theta(N'-p+q)\Theta(p-j)\Theta(N'-p+j)$ is present both in Eqs. (A.105) and (A.107) through the definition of $w'_{r,s}$.

A.4 The Integral $J_{p,q,l}^m$ and its Reduced Form $I_{q,l}^m$

The aim of this part is to show a simple derivation of the integral in Eq. (A.42). Direct substitution of the LLL eigenfunctions, Eq. (3.2), and the spherical harmonics in Eq. (A.43), into Eq. (A.42), gives us the following expression

$$J_{p,q,l}^m = C_1 \int_0^{2\pi} d\phi e^{i(q-p+m)\phi} \int_0^\pi d\theta \sin \theta \sin^{p+q}(\theta/2) \cos^{2N-p-q}(\theta/2) P_l^m(\cos \theta), \quad (\text{A.108})$$

where we have defined the factor C_1 as

$$C_1 = \left[\frac{(2l+1)(l-m)!}{4\pi R^2(l+m)!} \right]^{1/2} \mathcal{N}_{p,N} \mathcal{N}_{q,N} R^2. \quad (\text{A.109})$$

The integration over ϕ is immediate, and for this case of integer numbers p, q and m , gives

$$J_{p,q,l}^m = C_1 2\pi \delta_{q,p-m} \int_0^\pi d\theta \sin \theta \sin^{p+q}(\theta/2) \cos^{2N-p-q}(\theta/2) P_l^m(\cos \theta). \quad (\text{A.110})$$

Then, rewriting the integrand to allow the use of the trigonometric identities for the cosine and sine of the “double angle”, the integral becomes

$$J_{p,q,l}^m = C_1 2\pi \delta_{q,p-m} \left(\frac{-1}{2^N} \right) \int_0^\pi d(\cos \theta) \sin^{p+q} \theta (1 + \cos \theta)^{N-p-q} P_l^m(\cos \theta). \quad (\text{A.111})$$

The integrand can now be written completely in terms of $x = \cos \theta$ by using $\sin \theta = (1 - \cos^2 \theta)^{1/2}$ [$0 \leq \theta \leq \pi$]. After some further simplifications and using the constriction $q = p - m$ from the Kronecker delta function, the integral reads

$$J_{p,q,l}^m = C_1 2\pi \delta_{q,p-m} \left(\frac{1}{2^N} \right) \int_{-1}^1 dx (1+x)^{N-p+\frac{m}{2}} (1-x)^{p-\frac{m}{2}} P_l^m(x). \quad (\text{A.112})$$

At this point we find it more convenient to use the representation of the associated Legendre functions $P_l^m(x)$ in terms of the hypergeometric function [119], ${}_2F_1$

$$P_l^m(x) = \frac{(-1)^m \Gamma(l+m+1)}{2^m \Gamma(m+1) \Gamma(l-m+1)} (1-x^2)^{\frac{m}{2}} {}_2F_1 \left[\begin{matrix} m-l, & m+l+1 \\ m+1; & \frac{1-x}{2} \end{matrix} \right], \quad (\text{A.113})$$

which substituted into Eq. (A.112), and after performing the change of variable $y = (1-x)/2$, reduces the integral to

$$J_{p,q,l}^m = C_1 C_2 \delta_{q,p-m} \int_0^1 dy (1-y)^{N-p+m} y^p {}_2F_1 \left[\begin{matrix} m-l, & m+l+1 \\ m+1; & y \end{matrix} \right], \quad (\text{A.114})$$

where C_2 is given by

$$C_2 = \frac{(-1)^m 4\pi(l+m)!}{m!(l-m)!}. \quad (\text{A.115})$$

The last form of the integral, Eq. (A.114), has been calculated in general [119] to give

$$\int_0^1 dx (1-x)^{\mu-1} x^{\nu-1} {}_pF_q \left[\begin{matrix} a_1, & \dots, & a_p \\ b_1, & \dots, & b_q; & cx \end{matrix} \right] = \frac{\Gamma(\mu)\Gamma(\nu)}{\Gamma(\mu+\nu)} {}_{p+1}F_{q+1} \left[\begin{matrix} \nu, & a_1, & \dots, & a_p \\ \mu+\nu, & b_1, & \dots, & b_q; & c \end{matrix} \right]. \quad (\text{A.116})$$

Using this result on Eq. (A.114) and making further simplifications we finally obtain

$$J_{p,q,l}^m = (-1)^m \delta_{q,p-m} \left[\frac{(2l+1)(l+m)!}{4\pi R^2(l-m)!} \right]^{1/2} \mathcal{N}_{p,N} \mathcal{N}_{p-m,N} \times \frac{4\pi R^2(N-p+m)!p!}{m!(N+m+1)!} {}_3F_2 \left[\begin{matrix} m-l, & l+m+1, & p+1 \\ m+1, & N+m+2; & 1 \end{matrix} \right]. \quad (\text{A.117})$$

The Kronecker delta function in Eq. (A.117) suggest to carry out one of the sums (either respect to the p or q indices) in the expressions where $J_{p,q,l}^m$ appears so that the expressions simplify. This way we define the reduced form $I_{q,l}^m$ by

$$I_{q,l}^m f(q+m) = \sum_{p=0}^N J_{p,q,l}^m f(p), \quad (\text{A.118})$$

where $f(p)$ is any function of the parameter p [e.g. the complex coefficient $v_{n,p}^*$ in Eq. (A.41)]. Performing the previous sum over p , using the form of $J_{p,q,l}^m$ given in Eq. (A.117), we obtain directly

$$I_{q,l}^m = (-1)^m \left[\frac{(2l+1)(l+m)!}{4\pi R^2(l-m)!} \right]^{1/2} \mathcal{N}_{q+m,N} \mathcal{N}_{q,N} \times \frac{4\pi R^2(N-q)!(q+m)!}{m!(N+m+1)!} {}_3F_2 \left[\begin{matrix} m-l, & l+m+1, & q+m+1 \\ m+1, & N+m+2; & 1 \end{matrix} \right]. \quad (\text{A.119})$$

which, by simplifying the $\mathcal{N}_{k,N} = [(N+1)!/4\pi R^2 k!(N-k)!]^{1/2}$ factors, becomes

$$I_{q,l}^m = (-1)^m \left[\frac{(2l+1)(l+m)!}{4\pi R^2(l-m)!} \right]^{1/2} \left[\frac{(N-q)!(q+m)!}{q!(N-q-m)!} \right]^{1/2} \times \frac{(N+1)!}{m!(N+m+1)!} {}_3F_2 \left[\begin{matrix} m-l, & l+m+1, & q+m+1 \\ m+1, & N+m+2; & 1 \end{matrix} \right]. \quad (\text{A.120})$$

where $R^2 = N/2$ in units of the magnetic length l_m .

A.5 LD-LLL Energy Function in Terms of the Original Variables

In this part we derive the LD energy function in terms of the complex coefficients of the LLL order-parameter expansion given in the original variables. We show that, in the HTSC limit ($\kappa \gg 1$), this gives the same result as that with the scaled variables. As before, the thin-film case is regained by setting the interlayer terms to zero and dropping the sum over n and the index from the intralayer terms. Thus, we consider the LD energy functional in Eq. (2.38) with $\mathbf{B} = \mu_0 \mathbf{H}$, which we rewrite in the form

$$\mathcal{H}_{LD}[\psi_n] = \sum_{n=1}^M d_0 \int d^2r \left[\alpha |\psi_n|^2 + \frac{\beta}{2} |\psi_n|^4 + \frac{1}{2m_{\perp}} \psi_n^* \mathbf{D}_{\perp}^2 \psi_n + \frac{\hbar^2}{2m_{\parallel} s^2} |\psi_{n+1} - \psi_n|^2 \right], \quad (\text{A.121})$$

and directly substitute the LLL order parameter expansion in Eq. (2.47). This, again, leads to the calculation of three energy terms.

The Quadratic Intralayer Contribution

This comes from the first and third terms in Eq. (A.121) and gives

$$\frac{\mathcal{H}_{LD}^{(1)}(\mathbf{v})}{k_B T} = \alpha_H \frac{d_0 Q^2}{k_B T} \sum_{n=1}^M \sum_{p,q=0}^N v_{n,p}^* v_{n,q} \int d^2r \psi_{p,N}^* \psi_{q,N}, \quad (\text{A.122})$$

where $\alpha_H = \alpha + |e| \hbar \mu_0 H / m_{\perp}$. By using $Q = (\Phi_0 k_B T / \beta d_0 \bar{B})^{1/4}$, with $\Phi_0 = \pi \hbar / |e|$ and $\bar{B} = \mu_0 H$, we see that the prefactor in this intralayer term becomes $(\beta_{\kappa} / \beta)^{1/2} \alpha_T$. In the HTSC limit ($\kappa \gg 1$), $(\beta_{\kappa} / \beta) \rightarrow 1$, which gives the same result as in the first integral in Appendix A.3.1.1. Therefore, we conclude that

$$\frac{\mathcal{H}_{LD}^{(1)}(\mathbf{v})}{k_B T} = \alpha_T \sum_{n=1}^M \sum_{q=0}^N |v_{n,q}|^2, \quad (\text{A.123})$$

as in Eq. (A.26).

The Quartic Intralayer Contribution

This comes from the second term in Eq. (A.121) and gives

$$\frac{\mathcal{H}_{LD}^{(2)}(\mathbf{v})}{k_B T} = \frac{\beta}{2} \frac{d_0 Q^4}{k_B T} \sum_{n=1}^M \sum_{p,q,r,s=0}^N v_{n,p} v_{n,q} v_{n,r}^* v_{n,s}^* \int d^2r \psi_{p,N} \psi_{q,N} \psi_{r,N}^* \psi_{s,N}^*. \quad (\text{A.124})$$

Again we use $Q = (\Phi_0 k_B T / \beta d_0 \overline{B})^{1/4}$, but now with $\Phi_0 / \overline{B} = 2\pi$ (in units of l_m). The prefactor becomes just π as in the second integral in Appendix A.3.1.1. From the results in that Appendix we conclude that

$$\frac{\mathcal{H}_{LD}^{(2)}(\mathbf{v})}{k_B T} = \frac{1}{2N} \sum_{n=1}^M \sum_{p=0}^{2N} |U_{n,p}(\mathbf{v})|^2. \quad (\text{A.125})$$

as in Eq. (A.38).

The Quadratic Interlayer Contribution

This comes from the last term in Eq. (A.121) and gives

$$\frac{\mathcal{H}_{LD}^{(3)}(\mathbf{v})}{k_B T} = \frac{\hbar^2}{2m_{\parallel} s^2} \frac{d_0 Q^2}{k_B T} \sum_{n=1}^M \sum_{p,q=0}^N (v_{n+1,p}^* - v_{n,p}^*)(v_{n+1,q} - v_{n,q}) \int d^2 r \psi_{p,N}^* \psi_{q,N}. \quad (\text{A.126})$$

From its definition in Eq. (4.2), and Eq. (2.49), we write the interlayer-coupling parameter $\eta = \hbar^2 / 2m_{\parallel} s^2 |\alpha_H|$. When this expression is inserted into the prefactor above, it becomes $(\beta \kappa / \beta)^{1/2} \eta |\alpha_T|$. Once again, in the HTSC limit ($\kappa \gg 1$), this gives the same expression as in the third integral in Appendix A.3.1.1. Therefore, we conclude that

$$\frac{\mathcal{H}_{LD}^{(3)}(\mathbf{v})}{k_B T} = \eta |\alpha_T| \sum_{n=1}^M \sum_{q=0}^N |v_{n+1,q} - v_{n,q}|^2. \quad (\text{A.127})$$

as in Eq. (A.40). This shows the equivalence of LLL formulations in terms of the original and scaled parameters.

A.6 Physical Properties in the LLL Approximation

In this part we obtain LLL expressions for the physical quantities used in the numerics of Chapters 3 and 4. They are found, in general, by substituting the LLL order-parameter expansion of Eq. (2.47) and performing the surface integrations (over the sphere of radius R) when required. Here we consider the layered case only since the thin-film counterpart is obtained by setting $M = 1$ and dropping the index n (or any function of n) from all expressions.

Average Energy

The first quantity of interest is the average energy of the system, also called the internal energy in thermodynamics. For all layered HTSCs considered throughout this thesis, the average energy can be written in general as

$$\langle E \rangle = \langle \mathcal{H}_c[\psi_n] + \mathcal{H}_{\text{dis}}[\psi_n] \rangle, \quad (\text{A.128})$$

where \mathcal{H}_c is the energy of the clean system in Eq. (2.38) and \mathcal{H}_{dis} denotes the pinning-interaction energy. The last one can be either of a random substrate as in Eq. (4.6) or set by a regular array of pinning centres, Eq. (4.8).

The LLL form of the clean part is written explicitly in Eq. (4.2) and pinning contributions to both random and regular arrays of columnar defects given in Eqs. (4.7) and (4.10) respectively. Therefore the LLL expression for the average energy can be written in the compact form

$$\langle E \rangle = \langle \mathcal{H}_c(\mathbf{v}) + \mathcal{H}_{\text{dis}}(\mathbf{v}; \mathbf{p}) \rangle, \quad (\text{A.129})$$

with \mathbf{p} denoting the parameters the pinning energy depends upon (e.g. $\mathbf{a} \equiv \{a_l^m\}$ for random disorder or $\mathbf{v}^{(0)} \equiv \{v_{n,q}^{(0)}\}$ for a regular substrate). That should be the “absolute” average energy. Throughout all MC studies in this manuscript we will be referring its value to a constant energy, E_0 , which in fact coincides with the total energy evaluated at the ground state order parameter of the clean system, $\psi_n^{(0)}$, and at the minimum α_T used in the numerics (usually -13 for both energy minimizations and MC simulations).

Specific Heat and Magnetization

The specific heat of the layered HTSC is calculated directly from its thermodynamical definition

$$C = \frac{\partial \langle E \rangle}{\partial T}, \quad (\text{A.130})$$

where $E = \mathcal{H}$ is the total energy of the system appearing in Eq. (A.128). Differentiation of the LLL form of this energy, Eq. (A.129), gives directly

$$C = \frac{\langle E \rangle}{k_B T} - \frac{\alpha_T}{2} \left\langle \sum_{n=1}^M \sum_{q=0}^N |v_{n,q}|^2 \right\rangle - \frac{\eta |\alpha_T|}{2} \left\langle \sum_{n=1}^M \sum_{q=0}^N |v_{n+1,q} - v_{n,q}|^2 \right\rangle. \quad (\text{A.131})$$

This is the LLL expression for the specific heat (with the total energy E replaced by the proper expression).

The average magnetization (per vortex) is defined as the electrodynamic spatially-averaged magnetization, $|(1/\mu_0)\mathbf{B} - \mathbf{H}| = |\mathbf{M}|$, (with the expression taken from the first Abrikosov's identity in Eq. (2.25)) multiplied by the factor $4\pi R^2 m/Q^2 |e/\hbar|$. Therefore its thermal average is just

$$\frac{1}{N}\langle \mathcal{M} \rangle = \frac{4\pi R^2}{Q^2} \frac{1}{N} \left\langle \frac{1}{M} \sum_{n=1}^M |\psi_n|^2 \right\rangle. \quad (\text{A.132})$$

Within the LLL approximation the two-dimensional spatial average is calculated by using the orthonormal property of the LLL eigenfunctions. That gives

$$\frac{1}{N}\langle \mathcal{M} \rangle = \frac{1}{NM} \left\langle \sum_{n=1}^M \sum_{q=0}^N |v_{n,q}|^2 \right\rangle. \quad (\text{A.133})$$

Abrikosov and Josephson-Coupling Ratios

The Abrikosov ratio has already been defined before in the thin-film case (see the end of Section 2.1.2). The same definition applies in a bulk superconductor, but for the layered HTSC it has to be slightly modified. Its thermal average in that case is

$$\langle \beta_A \rangle = \left\langle \frac{\frac{1}{M} \sum_{n=1}^M |\psi_n|^4}{\left(\frac{1}{M} \sum_{n=1}^M |\psi_n|^2\right)^2} \right\rangle. \quad (\text{A.134})$$

Calculation the two-dimensional spatial averages (within the LLL approximation) simply reduces it to

$$\langle \beta_A \rangle = \left\langle \frac{M \sum_{n=1}^M \sum_{q=0}^N |U_{n,p}(\mathbf{v})|^2}{\left(\sum_{n=1}^M \sum_{q=0}^N |v_{n,q}|^2\right)^2} \right\rangle. \quad (\text{A.135})$$

There is another quantity, useful to describe vortex correlations along the c -axis (associated with entangled and disentangled vortex lines), called the *Josephson-coupling ratio*. Its thermal average is defined as

$$\langle \Gamma \rangle = \left\langle \frac{\frac{1}{M} \sum_{n=1}^M |\psi_{n+1} - \psi_n|^2}{\frac{1}{M} \sum_{n=1}^M |\psi_n|^2} \right\rangle, \quad (\text{A.136})$$

which within the LLL approximation becomes

$$\langle \Gamma \rangle = \left\langle \frac{\sum_{n=1}^M \sum_{q=0}^N |v_{n+1,q} - v_{n,q}|^2}{\sum_{n=1}^M \sum_{q=0}^N |v_{n,q}|^2} \right\rangle. \quad (\text{A.137})$$

Pinning Magnetization and Susceptibility

To measure the pinning strength of the periodic substrate, defined by the order parameter $\psi_n^{(0)}$, Dodgson [83] has defined two more quantities.⁶ One is

$$\langle \mathcal{M}_g \rangle = \frac{\left\langle \frac{1}{M} \sum_{n=1}^M |\psi_n^{(0)} \psi_n^*|^2 \right\rangle}{\frac{1}{M} \sum_{n=1}^M |\psi_n^{(0)}|^4}, \quad (\text{A.138})$$

which, for its similar behaviour to the average magnetization in Eq. (A.132), has been called the “magnetization” corresponding to the field defining the pinning potential. Its LLL expression is easily obtained by performing the two-dimensional spatial averages and reads

$$\langle \mathcal{M}_g \rangle = \frac{\left\langle \sum_{n=1}^M \sum_{p=0}^{N+N'} |U'_{n,p}(\mathbf{v}; \mathbf{v}^{(0)})|^2 \right\rangle}{\left(\frac{N}{N'} \right)^2 \sum_{n=1}^M \sum_{p=0}^{2N'} |U_{n,p}(\mathbf{v}^{(0)})|^2}, \quad (\text{A.139})$$

where the fact that there are N' columnar defects and N vortices per layer has been taken into account.

The other quantity, called the “susceptibility” corresponding to the field defining the pinning potential, is defined as

$$\langle \chi_g \rangle = \frac{\left\langle \left| \frac{1}{M} \sum_{n=1}^M \overline{\psi_n^{(0)} \psi_n^*} \right|^2 \right\rangle}{\left(\frac{1}{M} \sum_{n=1}^M |\psi_n^{(0)}|^2 \right)^2}, \quad (\text{A.140})$$

with a LLL expression given by

$$\langle \chi_g \rangle = \frac{\left\langle \left| \sum_{n=1}^M \sum_{q=0}^{N_m} A_q^{(N,N')} v_{n,q}^{(0)} v_{n,q}^* \right|^2 \right\rangle}{\left(\sum_{n=1}^M \sum_{q=0}^{N'} |v_{n,q}^{(0)}|^2 \right)^2}, \quad (\text{A.141})$$

where $N_m = \min(N, N')$ and we have denoted

$$A_q^{(N,N')} = \int d^2r \psi_{q,N'} \psi_{q,N}^*. \quad (\text{A.142})$$

After the integration (and further simplifications), using the LLL eigenfunctions in the spherical geometry in Eq. (3.2), $A_q^{(N,N')}$ becomes

$$A_q^{(N,N')} = \left[\frac{(N+1)!(N'+1)!}{(N-m)!(N'-m)!} \right]^{1/2} \frac{\left(\frac{N+N'}{2} - m \right)!}{\left(\frac{N+N'}{2} + 1 \right)!}. \quad (\text{A.143})$$

⁶Because they measure vortex correlations to the pinning substrate it should probably be appropriate to call them, in short: “pinning magnetization” and “pinning susceptibility” respectively. Notice, however, that the definitions used in this thesis are slightly different from those in Ref. [83].

Notice that the trivial result $A_q^{(N,N)} = 1$, from the orthonormality property of the LLL subspace, appears directly from both Eqs. (A.143) and (A.142). It is also remarkable that as $\psi_n^{(0)}$ is the order parameter (in layer n) which minimizes the energy of the clean system, then $v_{n,q}^{(0)}$ are the expansion coefficients of this order parameter.

Interlayer Phase-Correlation-Function

To measure phase coherence along the c -axis in a layered superconductor with order parameter $\psi_n(\mathbf{r})$ at layer n , we define the interlayer phase-correlation-function

$$C_p(m) = \frac{4\pi R^2}{Q^2} \left\langle \frac{1}{M} \sum_{n=1}^M \overline{\psi_n^*(\mathbf{r}) \psi_{n+m}(\mathbf{r})} \right\rangle. \quad (\text{A.144})$$

For $m = 0, 1, \dots, M$. Here we impose periodic boundary conditions on the order parameter: $\psi_{M+p} = \psi_p$. By calculating the spatial average within the LLL approximation one obtains

$$C_p(m) = \frac{1}{M} \left\langle \sum_{n=1}^M \sum_{q=0}^N v_{n,q}^* v_{n+m,q} \right\rangle. \quad (\text{A.145})$$

The periodic boundary condition turns this quantity a symmetric function of m (i.e. symmetric about the middle of the system). Therefore only values up to $m = [(M+1)/2]$ are required, where the notation $[K]$ means the lower-integer of K (i.e. the closest integer less-than or equal-to K).

References

- [1] B. S. Chandrasekhar in *Superconductivity*, edited by R. D. Parks (Dekker, New York, 1969), Vol. 1.
- [2] A. A. Golubov in *Handbook of Applied Superconductivity*, edited by B. Seeber (IOP-Arrowsmith, Bristol, 1998), Vol. 1.
- [3] J. B. Ketterson and S. N. Song, *Superconductivity* (Cambridge University Press, Cambridge, 1999).
- [4] Shu-Ang Zhou, *Electrodynamic Theory of Superconductors* (Peter peregrinus, England, 1991).
- [5] V. V. Schmidt, *The Physics of Superconductors*, edited by P. Müller and A. V. Ustinov (Springer-Verlag, Berlin, 1997).
- [6] L. D. Landau and V. L. Ginzburg, Zh. Eksp. Teor. Fiz. **20**, 1064 (1950) [English translation in *Collected Papers of L. D. Landau* (Pergamon Press, Oxford, 1965) p. 546].
- [7] J. Bardeen, L. N. Cooper and J. R. Schrieffer, Phys. Rev. **108**, 1175 (1957).
- [8] H. Kamerlingh Onnes, Commun. Phys. Lab. Univ. Leiden, **119b** (1911).
- [9] H. Kamerlingh Onnes, Commun. Phys. Lab. Univ. Leiden, **139f** (1914).
- [10] W. H. Keesom, Rapp. et Disc. 4^e Congr. Phys. Solvay, p. 288 (1924).
- [11] A. J. Rutgers, Physica **1**, 1055 (1934).

-
- [12] C. J. Gorter and H. B. G. Casimir, *Phys. Z.* **35**, 963 (1934); *Physica* **1**, 306 (1934).
- [13] F. London and H. London, *Proc. Roy. Soc. A* **149**, 71 (1935).
- [14] W. Meissner and R. Ochsenfeld, *Naturwissenschaften* **21**, 787 (1933).
- [15] F. London, *Superfluids* (Wiley, New York, 1950), Vol. 1.
- [16] R. Peierls, *Proc. Roy. Soc. A* **155**, 613 (1936).
- [17] L. D. Landau, *Zh. Eksp. Teor. Fiz.* **7** 371 (1937) [English translation in *Collected Papers of L. D. Landau* (Pergamon Press, Oxford, 1965) p. 217].
- [18] A. B. Pippard, *Proc. Roy. Soc. A* **216**, 547 (1953).
- [19] L. V. Shubnikov *et al.*, *Zh. Eksp. Teor. Fiz.* **7**, 221 (1937).
- [20] A. A. Abrikosov, *Zh. Eksp. Teor. Fiz.* **32**, 1442 (1957); *Soviet Phys. JETP* **5**, 1174 (1957).
- [21] U. Essmann and H. Träuble, *Phys. Lett. A* **24**, 526 (1967).
- [22] P. G. de Gennes, *Superconductivity of Metals and Alloys* (Addison-Wesley, USA, 1989).
- [23] L. P. Gor'kov, *Soviet Phys. JETP* **9**, 1364 (1959).
- [24] I. Giaever, *Phys. Rev. Lett* **15**, 825 (1965).
- [25] A. M. Campbell and J. E. Evetts, *Adv. Phys.* **21**, 199 (1972).
- [26] H. Ullmaier, C. Papastaikoudis, S. Takács and W. Schilling in *Proc. 12th Int. Conf. on Low-Temp. Phys. (Kyoto)* p. 369 (1972).
- [27] C. P. Bean, *Phys. Rev. Lett.* **8**, 250 (1962).
- [28] Y. B. Kim *et al.*, *Phys. Rev. Lett.* **9**, 306 (1962).
- [29] R. Labusch, *Phys. Status Solidi* **32**, 439 (1969).
-

- [30] A. I. Larkin and Yu N. Ovchinnikov, J. Low. Temp. Phys. **34**, 409 (1979).
- [31] P. W. Anderson, Phys. Rev. Lett. **9**, 309 (1962).
- [32] P. W. Anderson and Y. B. Kim, Rev. Mod. Phys. **36**, 39 (1964).
- [33] M. R. Beasley, M. Labusch and W. W. Webb, Phys. Rev. **181**, 682 (1969).
- [34] R. G. Mints and A. L. Rakhmanov, Rev. Mod. Phys. **53**, 551 (1981).
- [35] V. L. Ginzburg, Sov. Solid State Phys. **2**, 1824 (1960).
- [36] A. A. Varlamov and M. Ausloos in *Fluctuation phenomena in high temperature superconductors*, edited by M. Ausloos and A. A. Varlamov (Kluwer, Dordrecht, 1997).
- [37] A. V. Nikulov in *Fluctuation phenomena in high temperature superconductors*, edited by M. Ausloos and A. A. Varlamov (Kluwer, Dordrecht, 1997).
- [38] J. G. Bednorz and K. A. Müller, Z. Phys. B **64**, 189 (1986).
- [39] M. K. Wu *et al.*, Phys. Rev. Lett. **58**, 908 (1987).
- [40] Z. X. Zhao *et al.*, Kexue Tongbao **32**, 422 (1987).
- [41] A. Schilling *et al.*, Nature **363**, 56 (1993).
- [42] D. R. Harshman and A. P. Millis, Phys. Rev. B **45**, 10684 (1992).
- [43] R. C. Dynes, Solid State Commun. **92**, 53 (1994).
- [44] D. J. Van Harlingen, Rev. Mod. Phys. **67**, 515 (1995).
- [45] B. Goss Levi, Phys. Today **49**, 19 (1996).
- [46] D. J. Scalapino, Phys. Rep. **250**, 329 (1995).
- [47] A. A. Abrikosov, Phys. Rev. B **51**, 11955 (1995).
- [48] M. Tinkham, *Introduction to Superconductivity* (McGraw-Hill, USA, 1996).

-
- [49] W. E. Lawrence and S. Doniach in *Proc. 12th Int. Conf. on Low-Temp. Phys. (Kyoto)* p. 361 (1972).
- [50] R. Kleiner *et al.*, Phys. Rev. Lett. **68**, 2394 (1992).
- [51] S. N. Artemenko and A. N. Kruglov, Phys. Lett. A **143**, 485 (1990).
- [52] A. Buzdin and D. Feinberg, J. Physique **51**, 1971 (1990).
- [53] J. R. Clem, Phys. Rev. B **43**, 7837 (1991).
- [54] G. Blatter *et al.*, Rev. Mod. Phys. **66**, 1125 (1994).
- [55] M. V. Feigel'man, V. B. Geshkenbein and A. I. Larkin, Physica C **167**, 177 (1990).
- [56] V. M. Vinokur, P. H. Kes and A. E. Koshelev, Physica C **168**, 29 (1990).
- [57] L. Miu *et al.*, Phys. Rev. B **57**, 3151 (1998); A. E. Koshelev and V. M. Vinokur, *ibid.* **57**, 8026 (1998); B. W. Kang *et al.*, *ibid.* **60**, 3088 (1999).
- [58] B. Y. Zhu, Jinming Dong and D. Y. Xing, Phys. Rev. B **57**, 5063 (1998); C. Reichhardt, C. J. Olson and Franco Nori, *ibid.* **57**, 7937 (1998); C. Reichhardt, C. J. Olson and Franco Nori, Phys. Rev. Lett. **78**, 2648 (1997).
- [59] L. N. Bulaevskii, M. P. Maley and V. M. Vinokur, Phys. Rev. B **57**, 5626 (1998); N. Morozov *et al.*, Phys. Rev. Lett. **82**, 1008 (1999); C. J. van der Beek *et al.*, Phys. Rev. B **61**, 4259 (2000).
- [60] P. M. Chaikin and T. C. Lubensky, *Principles of Condensed Matter Physics* (Cambridge University Press, UK, 1997).
- [61] R. J. Baxter, *Exactly Solved Models in Statistical Mechanics* (Academic Press, London, 1989).
- [62] J. Zinn-Justin, *Quantum Field Theory and Critical Phenomena* (Clarendon Press, Oxford, 1989).
- [63] G. J. Ruggeri and D. J. Thouless, J. Phys. F: Metal Phys. **6**, 2063 (1976).
-

-
- [64] A. L. Fetter and P. C. Hohenberg in *Superconductivity*, edited by R. D. Parks (Dekker, New York, 1969), Vol. 2.
- [65] W. H. Kleiner, L. M. Roth and S. H. Autler, Phys. Rev. **133**, 1226 (1964).
- [66] R. A. Klemm, A. Luther and M. R. Beasley, Phys. Rev. B **12**, 877 (1975).
- [67] A. Houghton, R. A. Pelcovits and A. Sudbø, Phys. Rev. B **40**, 6763 (1989).
- [68] Z. Tešanović *et al.*, Phys. Rev. Lett. **69**, 3563 (1992).
- [69] I. D. Lawrie, Phys. Rev. B **50**, 9456 (1994).
- [70] E. Brezin, A. Fujita and S. Hikami, Phys. Rev. Lett. **65**, 1949 (1990); *ibid.* **65**, 2921 (1990).
- [71] J. Hu, A. H. MacDonald and B. D. McKay, Phys. Rev. B **49**, 15263 (1994).
- [72] E. Brezin, D. R. Nelson and A. Thiaville, Phys. Rev. B **31**, 7124 (1985).
- [73] M. A. Moore and T. J. Newman, Phys. Rev. Lett. **75**, 533 (1995).
- [74] A. N. Berker, Physica A **194**, 72 (1993).
- [75] G. Eilenberger, Phys. Rev. **164**, 628 (1967).
- [76] J. Yeo and M. A. Moore, Phys. Rev. Lett. **76**, 1142 (1996).
- [77] M. A. Moore, Phys. Rev. B **45**, 7336 (1992).
- [78] S-K. Chin and M. A. Moore, preprint cond-mat/9709347.
- [79] J. A. O'Neill and M. A. Moore, Phys. Rev. Lett. **69**, 2582 (1992); Phys. Rev. B **48**, 374 (1993).
- [80] J. A. O'Neill, PhD thesis, The University of Manchester (1992).
- [81] H. H. Lee and M. A. Moore, Phys. Rev. B **49**, 9240 (1994).
- [82] M. J. W. Dodgson and M. A. Moore, Phys. Rev. B **55**, 3816 (1997).

-
- [83] M. J. W. Dodgson, PhD thesis, The University of Manchester (1996).
- [84] A. K. Kienappel and M. A. Moore, Phys. Rev. B **56**, 8313 (1997).
- [85] A. K. Kienappel, PhD thesis, The University of Manchester (1998).
- [86] S. M. Roy and V. Singh, Phys. Rev. Lett. **51**, 2069 (1983).
- [87] W. H. Press, S. A. Teukolsky, W. T. Vetterling and B. P. Flannery, *Numerical Recipes in C*, 2nd Ed. (Cambridge University Press, Cambridge, 1992).
- [88] E. A. Lord and C. B. Wilson, *The Mathematical Description of Shape and Form* (John Wiley and Sons, N.Y., 1984).
- [89] K. Binder and D. W. Heerman, *Monte Carlo Simulation in Statistical Physics*, 2nd Ed. (Springer-Verlag, Berlin, 1992).
- [90] N. Metropolis *et al.*, J. Chem. Phys. **21**, 1087 (1953).
- [91] Y. Kato and N. Nagaosa, Phys. Rev. B **47**, 2932 (1993); *ibid.* **48**, 7383 (1993).
- [92] J. Hu and A. H. MacDonald, Phys. Rev. Lett. **71**, 432 (1993); Phys. Rev. B **52**, 1286 (1995).
- [93] J. M. Kosterlitz and D. J. Thouless, J. Phys. C **6**, 1181 (1973); J. M. Kosterlitz, *ibid.* **7**, 1046 (1974).
- [94] R. Šášik and D. Stroud, Phys. Rev. B **49**, 16074 (1994); R. Šášik, D. Stroud and Z. Tešanović, Phys. Rev. B **51**, 3042 (1995).
- [95] M. Franz and S. Teitel, Phys. Rev. Lett. **73**, 480 (1994); Phys. Rev. B **51**, 6551 (1995).
- [96] S. Hikami, A. Fujita and A. I. Larkin, Phys. Rev. B **44**, 10400 (1991).
- [97] Z. Tešanović, Phys. Rev. B **44**, 12635 (1991); Z. Tešanović and L. Xing, Phys. Rev. Lett. **67**, 2729 (1991).
-

- [98] V. L. Berezinskii, Zh. Eksp. Teor. Fiz. **59**, 907 (1970) [Sov. Phys. JETP **32**, 493 (1971)].
- [99] B. I. Halperin and D. R. Nelson, Phys. Rev. Lett. **41**, 121 (1978); D. R. Nelson and B. I. Halperin, Phys. Rev. B **19**, 2457 (1979).
- [100] A. P. Young, Phys. Rev. B **19**, 1855 (1979).
- [101] J. Yeo and M. A. Moore, Phys. Rev. B **54**, 4218 (1996).
- [102] D. R. Nelson and P. Le Doussal, Phys. Rev. B **42**, 10113 (1990).
- [103] T. Giamarchi and P. Le Doussal, Phys. Rev. B **52**, 1242 (1995).
- [104] D. Carpentier and P. Le Doussal, Phys. Rev. B **55**, 12128 (1997); preprint cond-mat/9712227.
- [105] R. Šášik and D. Stroud, Phys. Rev. B **48**, 9938 (1993); R. Šášik and D. Stroud, Phys. Rev. Lett. **72**, 2462 (1994); R. Šášik and D. Stroud, *ibid.* **75**, 2582 (1995); Ing-Jye Hwang, R. Šášik and D. Stroud, Phys. Rev. B **54**, 12010 (1996).
- [106] J. Hu and A. H. MacDonald, Phys. Rev. B **56**, 2788 (1997).
- [107] N. K. Wilkin and H. J. Jensen, Europhys. Lett. **40**, 423 (1997).
- [108] A. K. Kienappel and M. A. Moore, Phys. Rev. B **60**, 6795 (1999); *ibid.* **61**, 3748 (2000).
- [109] J. Yeo and M. A. Moore, preprint cond-mat/0012421.
- [110] L. M. Paulius *et al.*, Phys. Rev. B **56**, 913 (1997).
- [111] D. R. Nelson and V. M. Vinokur, Phys. Rev. Lett. **68**, 2398 (1992).
- [112] D. R. Nelson and V. M. Vinokur, Phys. Rev. B **48**, 13060 (1993).
- [113] Carsten Wengel and Uwe Claus Täuber, Phys. Rev. B **58**, 6565 (1998).
- [114] J. Lidmar and M. Wallin, Europhys. Lett. **47**, 494 (1999).

- [115] D. R. Nelson and V. M. Vinokur, *Phys. Rev. B* **61**, 5917 (2000).
- [116] G. W. C. Kaye and T. H. Laby, *Tables of Physical and Chemical Constants*, 16th Ed. (Longman, England, 1995).
- [117] L. D. Landau and E. M. Lifshitz, *Quantum Mechanics (Non-relativistic Theory)* (Pergamon, Oxford, 1977), pp. 456-458.
- [118] E. Merzbacher, *Quantum Mechanics*, 3rd Ed. (John Wiley, New York, 1998), pp. 62-68.
- [119] I. S. Gradshteyn and I. M. Ryzik, *Table of Integrals, Series and Products* (Academic Press, USA, 1994).
- [120] N. N. Lebedev, *Special Functions and their Applications* (Prentice-Hall, USA, 1965).

JOHN RYLANDS
UNIVERSITY
LIBRARY OF
MANCHESTER